MPM SCIENTIFIC JOURNAL

ISSN 1605-2730
E-ISSN 1605-8119

MATERIALS PHYSICS AND MECHANICS

Vol. 50, No. 1, 2022

MATERIALS PHYSICS AND MECHANICS

"Materials Physics and Mechanics" Editorial Office:
Phone: +7(812)552 77 78, ext. 224 **E-mail:** mpmjournal@spbstu.ru **Web-site:** http://www.mpm.spbstu.ru

International scientific journal "**Materials Physics and Mechanics**" is published by Peter the Great St.Petersburg Polytechnic University in collaboration with Institute of Problems of Mechanical Engineering of the Russian Academy of Sciences in both hard copy and electronic versions.

The journal provides an international medium for the publication of reviews and original research papers written in English and focused on the following topics:

- Mechanics of composite and nanostructured materials.
- Physics of strength and plasticity of composite and nanostructured materials.
- Mechanics of deformation and fracture processes in conventional materials (solids).
- Physics of strength and plasticity of conventional materials (solids).
- Physics and mechanics of defects in composite, nanostructured, and conventional materials.
- Mechanics and physics of materials in coupled fields.

Owner organizations: Peter the Great St. Petersburg Polytechnic University; Institute of Problems of Mechanical Engineering RAS.

Materials Physics and Mechanics is indexed in Chemical Abstracts, Cambridge Scientific Abstracts, Web of Science Emerging Sources Citation Index (ESCI) and Elsevier Bibliographic Databases (in particular, SCOPUS).

MPM MATERIALS PHYSICS AND MECHANICS

МЕХАНИКА И ФИЗИКА МАТЕРИАЛОВ

Materials Physics and Mechanics

Том 50, номер 1, 2022 год

Учредители:
ФГАОУ ВО «Санкт-Петербургский политехнический университет Петра Великого»
ФГБУН «Институт проблем машиноведения Российской Академии Наук»

Тел.: +7(812)552 77 78, доб. 224 **E-mail:** mpmjournal@spbstu.ru **Web-site:** http://www.mpm.spbstu.ru

Тематика журнала

Международный научный журнал "Materials Physics and Mechanics" издается Санкт-Петербургским политехническим университетом Петра Великого в сотрудничестве с Институтом проблем машиноведения Российской Академии Наук в печатном виде и электронной форме. Журнал публикует обзорные и оригинальные научные статьи на английском языке по следующим тематикам:

- Механика композиционных и наноструктурированных материалов.
- Физика прочности и пластичности композиционных и наноструктурированных материалов.
- Механика процессов деформации и разрушения в традиционных материалах (твердых телах).
- Физика прочности и пластичности традиционных материалов (твердых тел).
- Физика и механика дефектов в композиционных, наноструктурированных и традиционных материалах.
- Механика и физика материалов в связанных полях.

Редколлегия принимает статьи, которые нигде ранее не опубликованы и не направлены для опубликования в другие научные издания. Все представляемые в редакцию журнала "Механика и физика материалов" статьи рецензируются. Статьи могут отправляться авторам на доработку. Не принятые к опубликованию статьи авторам не возвращаются.

Журнал "Механика и физика материалов" ("Materials Physics and Mechanics") включен в систему цитирования Web of Science Emerging Sources Citation Index (ESCI), SCOPUS и РИНЦ.

Contents

Materials Physics and Mechanics. 2022;50(1): 1-19
Research article
http://dx.doi.org/10.18149/MPM.5012022_1

Submitted: September 25, 2021
Approved: May 23, 2022
Accepted: June 24, 2022

Dispersion analysis of electrically actuated hygro-magneto-thermo-flexo electric nanobeam embedded on silica aerogel foundation

R. Selvamani[1]✉, L. Rubine[1], J. Rexy[1], F. Ebrahimi[2]

[1]Department of Mathematics, Karunya Institute of Technology and Sciences, Coimbatore-641114, Tamilnadu, India

[2]Department of Mechanical Engineering, Imam Khomieni International University, Qazvin34148-96818, Iran

✉ selvam1729@gmail.com

Abstract. This paper accesses the performance of applied electric voltage in a hygro thermo magneto flexo electric nanobeams embedded on a silica aerogel foundation based on nonlocal elasticity theory. Higher-order refined beam theory via Hamilton's principle is utilized to arrive at the governing equations of nonlocal nanobeams and solved by an analytical solution. A parametric study is presented to analyze the effect of the applied electric voltage on dimensionless deflection via nonlocal parameters, slenderness, moisture constant, critical temperature, and foundation constants. It is found that physical variants and beam geometrical parameters have significant effects on the dimensionless deflection of nanoscale beams. The accuracy and efficiency of the presented model are verified by comparing the results with that of published research. A good agreement has arrived.
Keywords: applied voltage, hygro thermo magnetic effect, flexoelectric nanobeam, nonlocal elasticity, refined beam theory, silica aerogel foundation

Acknowledgements. *No external funding was received for this study.*

Citation: Selvamani R, Rubine L, Rexy J, Ebrahimi F. Dispersion analysis of electrically actuated hygro-magneto-thermo-flexo electric nano beam embedded on silica aerogel foundation. *Materials Physics and Mechanics*. 2022;50(1): 1-19. DOI: 10.18149/MPM.5012022_1.

1. Introduction

Structural monitoring of nanobeams, nanoplates, and nanomembranes are recent novel field for many researchers due to their improvement of the quality properties. The classical continuum theory is aptly practical in the mechanical behavior of the macroscopic structures, but it is improperly for the size effect on the mechanical treatments on micro or nanoscale structures. Nevertheless, the classical continuum theory needs to be extended to factor in the nanoscale effects. The prime magneto-electro-elastic (MEE) was used in the 1970s, and MEE composite consisting of the piezoelectric and piezo magnetic phase was discovered this year. Van den Boomgard et al. [1] the MEE nano-materials, (BiFeO3, BiTiO3-CoFe2O4, NiFe2O4-PZT) and their nanostructures became a significant role in research (Zheng et al. [2], Martinet al. [3], Wang et al. [4], Prashanthi et al. [5]). For this reason to the major potential of nanostructure for amplification of many applications, their mechanical behavior

Publisher: Peter the Great St. Petersburg Polytechnic University

should be investigated and well-identified before new designs can be proposed. The classical mechanic continuum theories demonstrate to predict the response of structures up to a minimum size sub which they fail to provide accurate predictions. The nonlocal theories add a size parameter in the modeling of the continuum. This paper studied models that developed according to the greatly used nonlocal elasticity theory (Eringen [6], Eringen [7], Eringen [8], Eringen [9], Eringen [10]). Timoshenko beam theory and nonlocal elasticity theory were investigated in their study. So based on an elastic medium, the stability response of SWCNT is described. Winkler and Pasternak parameter, an aspect ratio of the SWCNT, and nonlocal parameter was studied. Yang et al. [11] studied nonlinear free vibration of SWCNTs based on strains Eringen's nonlocal elasticity theory. Ehyaei and Akbarizadeh [12] illustrated the vibration analysis of micro composite thin beam based on modified couple stress theory.

A unified formulation for modeling the inhomogeneous nonlocal beams is developed by Ebrahimi and Barati [13]. Free vibration analysis of chiral double-walled carbon nanotube embedded in an elastic medium using nonlocal elasticity theory and Euler Bernoulli beam model was studied by Dihaj et al. [14]. Vibration and buckling of piezoelectric and piezomagnetic nanobeams based on third-order beam model are verified by Ebrahimi and Barati [16,17,18]. The vibration, buckling, and bending, free of Timoshenko nanobeams based on a meshless method were investigated by Roque et al. [19]. Embedded in the nonlocal component relevance of Eringen, a major of articles published searching to enlarge nonlocal beam models for nanostructures. Peddieson et al. [20] proposed the nonlocal Euler-Bernoulli and Timoshenko beam theory, accepted by many studies to verify bending (Civalek and Demir [21], Wang [22], Wang et al. [23]). During the years of research, the small size agents in SWCNTs were studied by Murmu and Pradhan [24]. Karami et al. [25] studied the wave propagation of functionally graded anisotropic nanoplates resting on the Winkler-Pasternak foundation. Ebrahimi and Rostami [26] analyzed the propagation of elastic waves in thermally affected embedded carbon-nanotube-reinforced composite beams via various shear deformation plate theories.

Free vibration analysis of a piezoelectric nanobeam using nonlocal elasticity theory is verified by Ali Hajnayeb and Foruzande [27]. Large amplitude forced vibration of the functionally graded nanocomposite plate with piezoelectric layers resting on the nonlinear elastic foundation was investigated by Yazdi [28]. Thermo-magneto-electro-elastic analysis of a functionally graded nanobeam integrated with functionally graded piezomagnetic layers was studied by Arefi and Zenkour [29]. Ebrahimi and Barati [30] investigated the wave propagation analysis of smart strain gradient piezo-magneto-elastic nonlocal beams. Arefi [31] checked the static analysis of laminated piezo-magnetic size-dependent curved beam based on modified couple stress theory. Jiang et al. [32] studied the analytical solutions to magneto-electro-elastic beams.

Furthermore, in recent years many researchers have presented the static and dynamic characteristics of beams and plates exposed to hygro-thermal environments because of the considerable effects of these environments on the structure's behavior. Gayen and Roy [33] presented an analytical method to determine the stress distributions in circular tapered laminated composite beams under hygro and thermal loadings. Kurtinaitiene et al. [34] investigated the effect of additives on the hydrothermal synthesis of manganese ferrite nanoparticles. Alzahrani et al. [35] investigated the size effects on the static behavior of nanoplates resting on elastic foundation subjected to hygro-thermal loadings. They extended the nonlocal constitutive relations of Eringen to contain the hygro-thermal effects. Also, Sobhy [36] studied the frequency response of simply-supported shear deformable orthotropic graphene sheets exposed to hygro-thermal loading.

Bending of Electro-mechanical sandwich nanoplate based on silica Aerogel foundation examined by Ghorbanpour et al. [37]. They described the influence of parameters on

nanostructure such as applied voltage, porosity index, foundation characteristics, parameter, plate aspect ratio, and thickness ratio on the bending response of sandwich nanoplate. Simsek et al. [38] presented three unknown shear and normal deformations nonlocal beam theories for the bending analysis of the problem. Ke et al. [39] studied the free vibration of size-dependent magneto-electro-elastic nanoplates based on the nonlocal theory. Selvamani and Ponnusamy [41-49] have proposed novel ideas in wave propagation analysis of different structures. Ramirez [50] investigated the discrete layer solution to free vibrations of functionally graded magneto-electro-elastic plates. Forooghi et al. [51] reported the thermal instability analysis of nanoscale FG porous plates embedded on the Kerr foundation coupled with fluid flow. Safarpour et al. [52] analyzed the theoretical and numerical solution for the bending and frequency response of graphene reinforced nanocomposite rectangular plates. Forooghi and Alibeigloo [53] studied the hygro-thermo-magnetically induced vibration of FG-CNTRC small-scale plate incorporating nonlocality and strain gradient size dependency. Vibrational frequencies of FG-GPLRC viscoelastic rectangular plate subjected to different temperature loadings based on higher-order shear deformation theory were proposed by Huang et al. [54].

This paper studies the bending of HMEE nanobeams bedded on a silica aerogel foundation based on nonlocal elasticity theory. Governing equations of a nonlocal nanobeam on Winkler-Pasternak substrate are derived via Hamilton's principle. Galerkin method is implemented to solve the governing equations. Effects of different factors such as nonlocal parameter, slenderness, moisture constant, critical temperature, applied voltage, magnet potential, and Young's modulus, and height of silica aerogel foundation on the deflection characteristics of a nanobeam are investigated.

2. Problem formulation

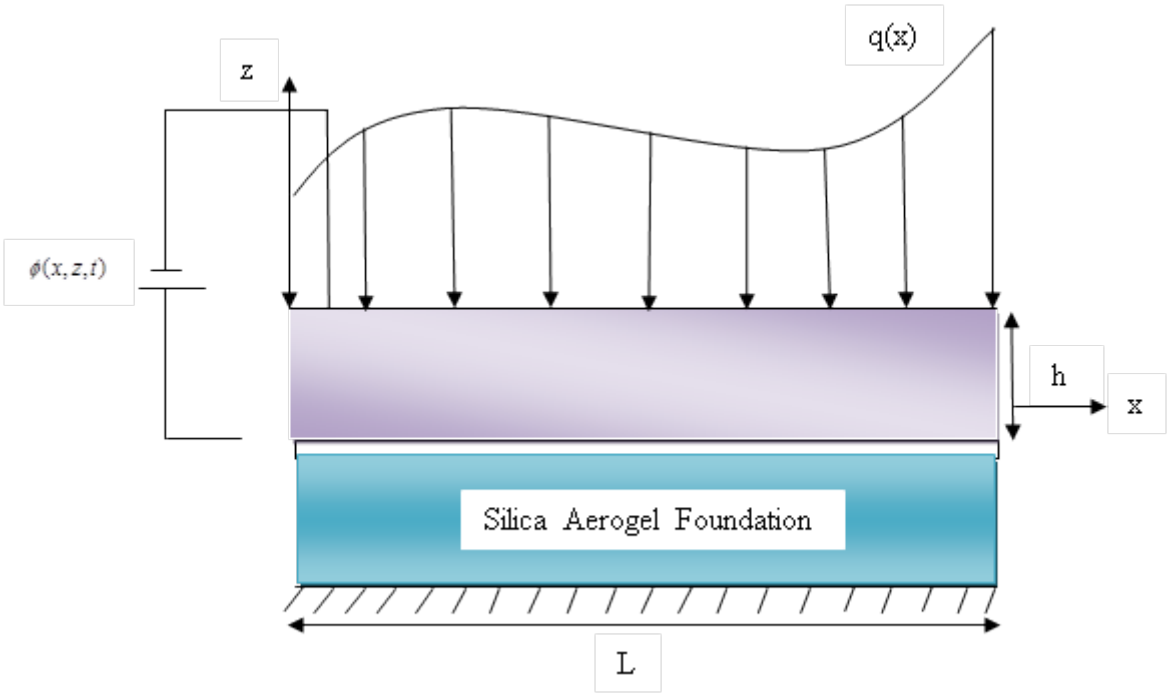

Fig. 1. Geometry of nanobeam resting on silica aerogel foundation

The component of displacement via refined shear deformable beam can be expressed by:

$$\boldsymbol{u_x(x,z) = u(x) - z\frac{\partial w_b}{\partial x} - f(z)\frac{\partial w_s}{\partial x}}, \tag{1}$$

$$\boldsymbol{u_z(x,z) = w_b(x) + w_s(x)}, \tag{2}$$

where u is axial mid-plane displacement and w_b, w_s denote the bending and shear components of transverse displacement, respectively. Also, $f(z)$ is the shape function representing the shear stress/strain distribution through the beam thickness which for the present study has a trigonometric essence, thus a shear correction factor is not required.

$$\boldsymbol{f(z)} = z + h_0 - tan[0.03(z + h_0)]. \tag{3}$$

Non-zero strains of the suggested beam model can be expressed as follows:

$$\varepsilon_{xx} = \frac{\partial u}{\partial x} - z\frac{\partial^2 w_b}{\partial x^2} - f(z)\frac{\partial^2 w_s}{\partial x^2}, \tag{4}$$

$$\gamma_{xz} = \mathrm{g}(z)\frac{\partial w_s}{\partial x}, \tag{5}$$

where $\mathrm{g}(z) = 1 - \partial f(z)/\partial z$.

According to Maxwell's equation, the relation between electric field (E_x, E_z) and electric potential (ϕ) and magnet field (Q_x, Q_z) and magnet potential (ψ), can be obtained as Ke et al. [39]:

$$E_x = -\phi_{,x} = \cos(\xi z)\frac{\partial \phi}{\partial x}\ , Q_x = -\psi_{,x} = \cos(\xi z)\frac{\partial \psi}{\partial x}, \tag{6}$$

$$E_z = -\phi_{,z} = \xi\sin(\xi z) - \frac{2v}{h}, Q_z = -\psi_{,z} = \xi\sin(\xi z) - \frac{2v}{h}, \tag{7}$$

where $\xi = \pi / h$. Also, V is the external electricity applied to the nanobeam.

Through extended Hamilton's principle, the governing equations can be derived as follows:

$$\int_0^t \delta(\Pi_S - \Pi_W)\mathrm{d}t = 0, \tag{8}$$

where Π_S is the total strain energy, Π_W is the work done by externally applied forces. The first variation of strain energy Π_S can be calculated as:

$$\delta\Pi_S = \int \sigma_{ij}\delta\varepsilon_{ij}dv = \int \sigma_x\delta\varepsilon_x + \sigma_{xz}\delta\gamma_{xz}. \tag{9}$$

Substituting equations (1) - (2) into equation (6) yields:

$$\begin{aligned}\Pi\mathrm{s} = {} & \int_0^a (N\frac{\partial \delta u}{\partial x} - M_b\frac{\partial^2 \delta w_b}{\partial x^2} - M_s\frac{\partial^2 \delta w_s}{\partial x^2} + Q\frac{\partial \delta w_s}{\partial x})dx + \\ & \int_0^a \int_{-h/2}^{h/2}\Big[-D_x\cos(\xi z)\frac{\partial \delta\phi}{\partial x} + D_z\xi\sin(\xi z)\,\delta\phi - \\ & B_x\cos(\xi z)\frac{\partial \delta\psi}{\partial x} + B_z\xi\sin(\xi z)\,\delta\varphi\psi\Big]\,dx\,dz,\end{aligned} \tag{10}$$

in which the forces and moments expressed in the above equation are defined as follows:

$$\begin{aligned}&(N, M_b, M_s) = \int_A (1, z, f)\sigma_i dA\ , i = (x, y, xy),\\ &Q_i = \int_A \mathrm{g}\sigma_i dA\ , i = (xz, yz)\ .\end{aligned} \tag{11}$$

The first variation of the work done by applied forces can be written in the form:

$$\delta\Pi_w = \int_0^l [(-N_x^0)\frac{\partial w}{\partial x}\frac{\partial \delta w}{\delta x} + (N^T + N^H)\frac{\partial (w_b + w_s)}{\partial x}\frac{\partial \delta (w_b + w_s)}{\delta x} - k_1\delta(w_b + w_s) + k_2\frac{\partial^2 (w_{b+}w_s)}{\partial x^2}]dx, \tag{12}$$

k_1, k_2 foundation parameters are as follows:

$$k_1 = \int_{-h/2-h_0}^{h/2-h_0} c_{11}\left(\frac{dx}{dz}\right)^2 dz,$$

$$k_2 = b\int_{-h/2-h_0}^{h/2-h_0} c_{44}x^2 dz.$$

Shape function of the foundation can be considered as:

$$x(z) = \frac{\sinh\gamma\left(1 - \dfrac{z}{H}\right)}{\sinh\gamma}.$$

In addition, γ is calculated by $\gamma^2 = H^2 \dfrac{c_{11}\int_{-\infty}^{\infty} \nabla w dxdy}{\int_{-\infty}^{\infty} w^2 dxdy}$,

where N^E, N^B electric, and magnet, loading respectively.

$N_x^0 = N^E + N^B$,

$$N^E = -\int_{-h/2}^{h/2} e_{31} \frac{2V}{h} \mathrm{d}z, \tag{13}$$

$$N^B = -\int_{-h/2}^{h/2} e_{31} \frac{2\Omega}{h} \mathrm{d}z, \tag{14}$$

where N^T, N^H are applied forces due to variation of temperature and moisture as

$$N^T = \int_{-h/2}^{h/2} \mathrm{E(z)\alpha(z)\Delta T}\, dz, \tag{15}$$

$$N^H = \int_{-h/2}^{h/2} \mathrm{E(z)\beta(z)\Delta H}\, dz. \tag{16}$$

The following Euler-Lagrange equations are obtained by inserting equations (10)-(12) in equation (8) when the coefficients of $\partial u, \partial w_b, \partial w_s, \emptyset, \psi$ are equal to zero:

$$\frac{\partial N_x}{\partial x} = 0, \tag{17}$$

$$\frac{\partial^2 M_b}{\partial x^2} + (-N^E - N^B)\nabla^2(w_b + w_s) - (N^T + N^H)\frac{\partial^2 (w_{b+} w_s)}{\partial x^2} + k_1(w_b + w_s) - k_2\nabla^2(w_b + w_s) = 0, \tag{18}$$

$$\frac{\partial^2 M_s}{\partial x^2} - \frac{\partial Q}{\partial x} + (-N^E - N^B)\nabla^2(w_b + w_s) - (N^T + N^H)\frac{\partial^2 (w_{b+} w_s)}{\partial x^2} + k_1(w_b + w_s) - k_2\nabla^2(w_b + w_s) = 0, \tag{19}$$

$$\int_{-h/2}^{h/2} \left[\cos(\xi z)\frac{\partial D_x}{\partial x} + \xi \sin(\xi z)\, D_z\right] \mathrm{d}z = 0, \tag{20}$$

$$\int_{-h/2}^{h/2} \left[B_x \cos(\xi z)\frac{\partial \delta\psi}{\partial x} + B_z \xi \sin(\xi z)\, \delta\psi\right] \mathrm{d}z = 0. \tag{21}$$

3. Nonlocal elasticity theory

The nonlocal theory can be extended for the piezo magnetic nanobeams as:

$$\sigma_{ij-}(ea)^2\nabla^2\sigma_{ij} = \left[c_{ijkl}\varepsilon_{kl} - e_{mij}E_m - q_{nij}H_n - \alpha_{ij}T - \beta_{ij}H\right], \tag{22}$$

$$D_{ij-}(ea)^2\nabla^2 D_{ij} = [e_{ikl}\varepsilon_{kl} + k_{im}E_m + d_{in}H_n], \tag{23}$$

$$B_{i-}(ea)^2\nabla^2 B_i = [q_{ikl}\varepsilon_{kl} + d_{im}E_m + \varkappa_{in}H_n], \tag{24}$$

$$p_{i-}(ea)^2\nabla^2 p_i = \left[\varepsilon_0\chi_{ij}E_j + e_{ikl}\varepsilon_{kl}\right]. \tag{25}$$

Also, χ_{ij} is the relative dielectric susceptibility and f_{ijkl} is the flexoelectric coefficient. Also, $e_0 a$ is nonlocal parameter which is introduced to describe the size-dependency of nanostructures. ∇^2 is the Laplacian operator. The stress relations can be expressed by:

$$(1 - \mu\nabla^2)\sigma_{xx} = (1 - \lambda^2\nabla^2)\left[C_{11}\varepsilon_{xx} - e_{31}E_z - q_{31}H_z - \alpha\Delta T - \beta\Delta H\right], \tag{26}$$

$$(1 - \mu\nabla^2)\sigma_{xz} = (1 - \lambda^2\nabla^2)[C_{55}\gamma_{xz} - e_{15}E_x - q_{15}H_x], \tag{27}$$

$$(1 - \mu\nabla^2)D_x = (1 - \lambda^2\nabla^2)[e_{15}\gamma_{xz} + k_{11}E_x + d_{11}H_x], \tag{28}$$

$$(1 - \mu\nabla^2)D_z = (1 - \lambda^2\nabla^2)[e_{31}\varepsilon_{xx} + k_{33}E_z + d_{33}H_z], \tag{29}$$

$$(1 - \mu\nabla^2)B_x = (1 - \lambda^2\nabla^2)[q_{15}\gamma_{xz} + d_{11}E_x + \varkappa_{11}H_x], \tag{30}$$

$$(1 - \mu\nabla^2)B_z = (1 - \lambda^2\nabla^2)[q_{31}\varepsilon_{xx} + d_{33}E_z + \varkappa_{33}H_x]. \tag{31}$$

Integrating equation (26-31) over the cross-section area of nanobeam provides the following nonlocal relations for a refined beam model as:

$$M_x = \int_{-h/2}^{h/2} \left(e_{31} \frac{2V}{h} + q_{31} \frac{2V}{h} \right) Z dz, \tag{32}$$

$$\int_{-h/2}^{h/2} (1 - \mu\nabla^2) \{D_x\} \cos(\xi z)\, dz = F_{11}^e \left\{ \frac{\partial \phi}{\partial x} \right\}, \tag{33}$$

$$\int_{-h/2}^{h/2} (1 - \mu\nabla^2) \{B_x\} \cos(\xi z)\, dz = R_{11}^e \left\{ \frac{\partial \psi}{\partial x} \right\}, \tag{34}$$

$$(1 - \mu\nabla^2) \int_{-h/2}^{h/2} \xi \sin(\xi z)\, D_z dz = \left[A_{31} \left(\frac{\partial u}{\partial x} \right) - E_{31} \nabla^2 w \right], \tag{35}$$

$$(1 - \mu\nabla^2) \int_{-h/2}^{h/2} \xi \sin(\xi z)\, B_z dz = \left[G_{31} \left(\frac{\partial u}{\partial x} \right) - Q_{31} \nabla^2 w \right], \tag{36}$$

in which:

$$\{A_{11}, B_{11}, B_{11}^s, D_{11}, D_{11}^s, H_{11}^s\} = \int_{-\frac{h}{2}}^{\frac{h}{2}} c11\, (1, z, f, z^2, fz, f^2) dz, \tag{37}$$

$$(A_{31}, E_{31}) = \int_{-h/2}^{h/2} e_{31} \xi \sin(\xi z) \{1, z, f\}_z dz, \tag{38}$$

$$(F_{11}, F_{33}) = \int_{-h/2}^{h/2} \{s_{11}\, cos^2(\xi z)\,, s_{33} \xi^2\, sin^2(\xi z)\} dz, \tag{39}$$

$$(R_{11}, R_{33}) = \int_{-h/2}^{h/2} \{d_{11}\, cos^2(\xi z)\,, d_{33} \xi^2\, sin^2(\xi z)\} dz, \tag{40}$$

$$(G_{31}, Q_{31}) = \int_{-h/2}^{h/2} q_{31} \xi \sin(\xi z) \{1, z\}_z dz, \tag{41}$$

$$(\varkappa_{11}, \varkappa_{33}) = \int_{-h/2}^{h/2} \{\varkappa_{11}\, cos^2(\xi z)\,, \varkappa_{33} \xi^2\, sin^2(\xi z)\} dz. \tag{42}$$

The governing equations of nonlocal strain gradient nanoplate under electrical field in terms of the displacement can be derived by substituting equations (32) -(36), into equations (17) -(20) as follows:

$$\left[A_{11} \frac{\partial^2 u}{\partial x^2} - B_{11} \frac{\partial^3 w^b}{\partial x^3} - B_{11}^s \frac{\partial^3 w^s}{\partial x^3} + A_{31} \frac{\partial \phi}{\partial x} + G_{31} \frac{\partial \psi}{\partial x} \right] = \frac{\partial N_x}{\partial x}, \tag{43}$$

$$\begin{aligned} \left[[B_{11} \frac{\partial^3 u}{\partial x^3} - D_{11} \frac{\partial^4 w^b}{\partial x^4} - D_s^{11} \frac{\partial^4 w^s}{\partial x^4}] + E_{31} \frac{\partial^2 \phi}{\partial x^2} + Q_{31} \frac{\partial^2 \psi}{\partial x^2} + k_1 (w_b + w_s) - k_2 \nabla^2 (w_b \right. \\ + w_s)] - \mu [(-N^E - N^B) + (N^T + N^H) \frac{\partial^2 (w_{b+} w_s)}{\partial x^2}) + k_1 (w_b + w_s) \\ \left. - k_2 \nabla^2 (w_b + w_s)] \right] = \frac{\partial^2 M_b}{\partial x^2}, \end{aligned} \tag{44}$$

$$\begin{aligned} \left[\left[B_{11}^s \frac{\partial^3 u}{\partial x^3} - D_{11}^s \frac{\partial^4 w^b}{\partial x^4} - H_{11}^s \frac{\partial^4 w^s}{\partial x^4} \right] + F_{11} \frac{\partial^2 \phi}{\partial x^2} + R_{11} \frac{\partial^2 \psi}{\partial x^2} + k_1 (w_b + w_s) - k_2 \nabla^2 (w_b \right. \\ + w_s)) - \mu [(-N^E - N^B) + (N^T + N^H) \frac{\partial^2 (w_{b+} w_s)}{\partial x^2} + k_1 (w_b + w_s) \\ \left. - k_2 \nabla^2 (w_b + w_s)] \right] = \frac{\partial^2 M_s}{\partial x^2} - \frac{\partial Q}{\partial x}, \end{aligned} \tag{45}$$

$$[A_{31} \frac{\partial u}{\partial x} - E_{31} \frac{\partial^2 w^b}{\partial x^2} - Q_{31} \frac{\partial^2 w^s}{\partial x^2} + F_{11} \frac{\partial^2 \phi}{\partial x^2} + R_{11} \frac{\partial^2 \psi}{\partial x^2} - F_{33} \phi - R_{33} \psi = 0, \tag{46}$$

$$[A_{31} \frac{\partial u}{\partial x} - E_{31} \frac{\partial^2 w^b}{\partial x^2} - Q_{31} \frac{\partial^2 w^s}{\partial x^2} + F_{11} \frac{\partial^2 \phi}{\partial x^2} + \varkappa_{11} \frac{\partial^2 \psi}{\partial x^2} - F_{33} \phi - \varkappa_{33} \psi = 0. \tag{47}$$

4. Solution procedure

To satisfy the above-mentioned boundary conditions, the displacement quantities are presented in the following form:

$$u = \sum_{n=1}^{\infty} U_n \frac{\partial X_n(x)}{\partial x} e^{i\omega_n t}, \tag{48}$$

$$w_b = \sum_{n=1}^{\infty} W_{bn} X_n(x) e^{i\omega_n t}, \tag{49}$$

$$w_s = \sum_{n=1}^{\infty} W_{sn} X_n(x) e^{i\omega_n t}, \tag{50}$$

$$\emptyset = \sum_{n=1}^{\infty} \emptyset_n X_n(x) e^{i\omega_n t}, \quad (51)$$

$$\psi = \sum_{n=1}^{\infty} \psi_n X_n(x) e^{i\omega_n t}, \quad (52)$$

where (U_{mn} ,W_{bmn}, W_{zmn},$\emptyset, \psi$) are the unknown coefficients and for different boundary conditions ($\alpha = m\pi / a$, $\beta = n\pi / b$).

$$[K]\begin{Bmatrix} u_n \\ w_{bn} \\ w_{sn} \\ \phi \\ \psi \end{Bmatrix} = \begin{Bmatrix} 0 \\ Q_n(1+\mu\frac{n^2\pi^2}{L^2}) \\ Q_n\left(1+\mu\frac{n^2\pi^2}{L^2}\right) \\ 0 \\ 0 \end{Bmatrix}, \quad (53)$$

where [K], [F] are the stiffness, loading matrixes for nanobeam, respectively.

$$k_{1,1} = A_{11}\alpha_1, \quad K_{1,2} = B_{11}\alpha_2, \quad K_{1,3} = B_{11}^s\alpha_2, \quad K_{1,4} = A_{31}\alpha_3, \quad K_{1,5} = G_{31}\alpha_3 \quad (54)$$

$$K_{2,1} = B_{11}\alpha_{11}, \quad k_{2,2} = -D_{11}\alpha_7 + k_1\alpha_5 - k_2\alpha_6 + \mu[(-N^E - N^B + (N^T + N^H) + k_2)\alpha_6 - k_1\alpha_5], \quad K_{2,3} = D_{11}^s\alpha_7 + k_1\alpha_5 - k_2\alpha_6 + \mu[(-N^E - N^B + (N^T + N^H) + k_2)\alpha_6 - k_1\alpha_5],$$

$$k_{2,4} = E_{31}\alpha_6, \quad k_{2,5} = Q_{31}\alpha_6,$$

$$K_{3,1} = B_{11}^s\alpha_{11}, \quad K_{3,2} = -D_{11}^s\alpha_7 + \mu[(-N^E - N^B + (N^T + N^H) + k_2)\alpha_6 - k_1\alpha_5], \quad K_{3,3} = -H_{11}^s\alpha_7 + k_1\alpha_5 - k_2\alpha_6 + \mu[(-N^E - N^B + (N^T + N^H) + k_2)\alpha_6 - \left(k_1 + \frac{e_{31}}{2k_{33}}\right)f_{13}\alpha_5],$$

$$k_{3,4} = F_{11}\alpha_6, \quad k_{3,5} = R_{11}\alpha_6,$$

$$k_{4,1} = A_{31}\alpha_3, \quad k_{4,2} = -E_{31}\alpha_6, \quad k_{4,3} = -Q_{31}\alpha_6, \quad k_{4,4} = F_{11}\alpha_6 - F_{33}\alpha_5, \quad k_{4,5} = R_{11}\alpha_6 - R_{33}\alpha_5,$$

$$k_{5,1} = A_{31}\alpha_3, \quad k_{5,2} = -E_{31}\alpha_6, \quad 5 = -Q_{31}\alpha_6, \quad k_{4,4} = F_{11}\alpha_6 - F_{33}\alpha_5, \quad k_{4,5} = \varkappa_{11}\alpha_6 - \varkappa_{33}\alpha_5,$$

$$F_{1,1} = N\alpha_3,$$

$$F_{2,2} = M_b(1-\mu\alpha_6),$$

$$F_{3,3} = M_s(1-\mu\alpha_6) - Q(1-\mu\alpha_3),$$

in which (Table 1):

$$\alpha_1 = \int_0^a X'(x)X''(x)\,dx, \ \alpha_2 = \int_0^a X(x)X'''(x)\,dx, \ \alpha_7 = \int_0^a X(x)X''''(x)\,dx, \quad (55)$$

$$\alpha_5 = \int_0^a X(x)\,X(x)dx, \ \alpha_3 = \int_0^a X(x)\,X'(x)dx, \ \alpha_{11} = \int_0^a X'(x)X'''(x)\,dx,$$

$$\alpha_6 = \int_0^a X(x)X''(x)\,dx.$$

The uniform load is supposed that lead to bending and is expressed by the following form:

$$q_{dynamics} = \sum_{n=1}^{\infty} Q_n \sin[\frac{n\pi}{L}x]\sin\omega t, \quad (56)$$

$$Q_n = \frac{2}{L}\int_{x_0-c}^{x_0+c} \sin[\frac{n\pi}{L}x]q_x dx, \quad (57)$$

in which Q_n are the Fourier coefficients and $q(x) = q_0$ is the uniform load density and x_0 is the centroid coordinate. Also, in the case of concentrated point load the following expression for the harmonic load intensity can be written:

$$q(x) = p\delta(x - x_0)\sin\omega t, \quad (58)$$

$$Q_n = \frac{2p}{L}\sin\left[\frac{n\pi}{L}x_0\right], \quad (59)$$

in which δ is the Dirac delta.

Table 1. The admissible functions $X_m(x)$ Sobhy [36]

	Boundary conditions	The functions X_m
	At x=0, a	$X_m(x)$
SS	$X_m(0) = X_m''(0) = 0$	$Sin(\alpha x)$
	$X_m(a) = X_m''(a) = 0$	

5. Numerical results and discussions

The bending of hygro magneto thermo piezoelectric nanobeam is analyzed in this section. The material properties are shown in Table 2 (Ramirez et al. [50]). The validity of the present study is proved by the means of comparing the bending of this model with those of Arefi and Zenkour [29]. Arefi and Zenkour [29] for various nonlocal parameters are presented in Table 3.

Table 2. Material properties of $BiTiO_3$-$CoFe_2O_4$ composite materials

Properties	$BiTiO_3$-$CoFe_2O_4$
Elastic (GPa)	c_{11} = 226, c_{12} = 125, c_{13} = 124, c_{33} = 216, c_{44} = 44.2, c_{66} = 50.5
Piezoelectric/(C ⋅ m^{-2})	e_{31} = −2.2, e_{33} = 9.3, e_{15} = 5.8
Dielectric/(10^{-9}C ⋅ V^{-1} ⋅ m^{-1})	k_{11} = 5.64, k_{33} = 6.35
Piezomagnetic/(N ⋅ A^{-1} ⋅ m−1)	q_{15} = 275, q_{31} = 290.1, q_{33} = 349.9
Magnetoelectric/(10^{-12}Ns ⋅ V^{-1} ⋅ C^{-1})	s_{11} = 5.367, s_{33} = 2 737.5
Magnetic ($10^{-6}\ Ns^2\ c^{-2}/2$)	$\varkappa_{11}$ = -297, $\varkappa_{33}$ = 83.5
Mass density(10^3Kg/m^3)	ρ=5.55
Hygrothermal(/K)	$\alpha_{eff} = 1.6\times10^{-6}$ $\beta_{eff} = 26\times10^{-4}$

Table 3. Comparison of dimensionless deflections of nanobeam for electric voltage and magnet potential

L/h	μ(nm^2)	$\psi = 0.001$		L/h	μ(nm^2)	$\phi = 0.001$	
		Arefi and Zenkour [29]	present			Arefi and Zenkour [29]	Present
10	1	3.68	3.5781	10	0	3.68	3.59892
	2	3.71	3.6482		1	1.3333	3.66921
	3	3.77	3.7302		2	1.3645	3.74018
	4	3.84	3.79011		3	1.3958	3.80234
	5	3.94	3.8952		4	1.4270	3.92011

The role of various parameters like magnetic potential (Ω), electric voltage (V), moisture constant (ΔH), and nonlocal parameter (μ) on the non-dimensional frequencies of the simply supported higher-order magneto-electro-elastic nanobeams at L/h =20 and L/h =30 are exposed in Tables 4 and Table 5. Here, it is noticeable that with the rise of nonlocal parameters the natural frequencies of hygro magneto-electro-elastic nanobeam reduces for all magnetic potentials and external voltages due to the fact that the existence of nonlocality weakens the beam. Also, it is referred that when the moisture constant arose the

non-dimensional frequencies of hygro magneto-electro-elastic nanobeam decrease, especially for lower moisture constant. Moreover, it is concluded that negative values of magnetic potential and external electric voltage produce lower/higher frequencies compared to those of positive ones, respectively.

Table 4. Variation of the third dimensionless frequency of FG nanobeam for the various nonlocal parameters, magnetic potentials, and electric voltages (L/h =30)

μ		Ω=-0.05			Ω=0			Ω=+0.05		
		ΔH	ΔH =1	ΔH =5	ΔH	ΔH =1	ΔH =5	ΔH=0.	ΔH =1	ΔH =5
0	V=-	78.077	71.962	68.082	78.967	72.525	68.275	79.848	73.084	68.467
	V=0	77.941	71.532	67.345	78.833	72.099	67.540	79.715	72.661	67.735
	V=+	77.804	71.100	66.600	78.698	71.670	66.797	79.582	72.235	66.994
1	V=-	56.325	52.280	49.892	57.553	53.053	50.156	58.756	53.814	50.417
	V=0	56.136	51.687	48.882	57.369	52.468	49.151	58.575	53.238	49.418
	V=+	55.947	51.087	47.850	57.184	51.877	48.125	58.394	52.655	48.397
2	V=-	46.039	43.041	41.429	47.534	43.976	41.746	48.983	44.891	42.060
	V=0	45.808	42.318	40.207	47.310	43.269	40.533	48.766	44.199	40.856
	V=+	45.576	41.583	38.946	47.085	42.550	39.282	48.548	43.496	39.616
3	V=-	39.712	37.400	36.307	41.436	38.472	36.668	43.091	39.515	37.025
	V=0	39.444	36.566	34.905	41.179	37.662	35.280	42.844	38.727	35.651
	V=+	39.174	35.712	33.445	40.921	36.834	33.836	42.596	37.922	34.223

Table 5. Dispersion of dimensionless frequency of nanobeam for the various nonlocal parameters, magnetic potentials, and electric voltages (L/h =20)

μ		Ω=-0.05			Ω=0			Ω=+0.05		
		ΔH	ΔH =1	ΔH =5	ΔH	ΔH =1	ΔH =5	ΔH	ΔH =1	ΔH =5
0	V=-	35.608	32.956	31.424	36.477	33.504	31.611	37.325	34.044	31.797
	V=0	35.474	32.534	30.705	36.346	33.089	30.896	37.198	33.635	31.087
	V=+	35.340	32.107	29.968	36.215	32.669	30.164	37.070	33.222	30.359
1	V=-	29.900	27.860	26.782	30.929	28.506	27.002	31.926	29.139	27.219
	V=0	29.741	27.360	25.934	30.775	28.018	26.161	31.777	28.661	26.385
	V=+	29.581	26.850	25.058	30.621	27.520	25.292	31.627	28.174	25.524
2	V=-	26.174	24.556	23.798	27.344	25.287	24.044	28.466	25.998	24.288
	V=0	25.992	23.987	22.839	27.170	24.735	23.096	28.299	25.461	23.350
	V=+	25.808	23.404	21.838	26.994	24.170	22.107	28.130	24.912	22.372
3	V=-	23.487	22.191	21.678	24.784	22.997	21.948	26.017	23.776	22.215
	V=0	23.284	21.559	20.621	24.592	22.388	20.905	25.834	23.188	21.185
	V=+	23.079	20.909	19.507	24.398	21.763	19.806	25.650	22.584	20.102

The length of nanobeam is considered to be L = 10 nm. Also, the dimensionless deflection is adopted as

$$W = 100\frac{C_{11}I}{q_0L^4}. \quad (60)$$

Figures 2 and 3 investigated for the effect of nonlocal parameters on a dimensionless deflection through various magnetic potential, it is found that increasing the value of the nonlocal parameters caused the increase in dimensionless deflection but positive electric voltage leads to a reduction in deflection and negative potential rise the dimensionless deflection. We understand from this subject that magnetic potential has a significant role under dimensionless deflection and also dimensionless deflection null effect during zero electric voltage. The effect of humidity is observed in Fig. 3 through the rise in dimensionless deflection.

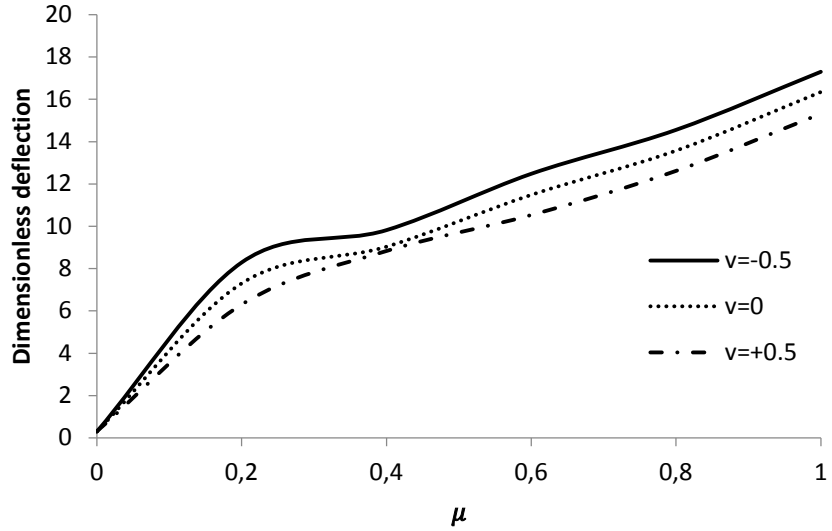

Fig. 2. Effect of nonlocal parameters on dimensionless deflection via $\Omega = 0.5$ (L/*h*=10, $K_w = K_p$=20, ΔH=1.5)

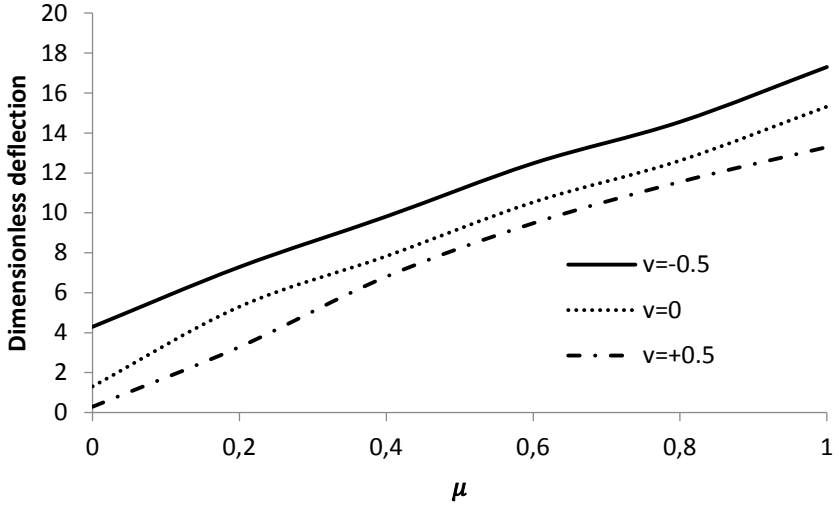

Fig. 3. Effect of nonlocal parameters on dimensionless deflection via $\Omega = 1.5$ (L/*h*=10, $K_w = K_p$=20, ΔH=1.5)

Dimensionless deflection of the nanobeam with respect to slenderness ratio through various electric voltages are presented in Figs. 4 and 5. It is found that the external electric voltage caused that softening deflection of nanobeam for positive values and external voltage for negative values of nanobeam demonstrated a hardening effect. From this, the axial tensile and compressive forces are exposed in the nanobeams via the constructed positive and negative voltages, respectively. In addition, it is lightly observed that the dimensionless

deflection is approximately independent of the slenderness ratio for zero electric voltages ($V=0$**)**. The increase in magnetic potential hardens the deflection.

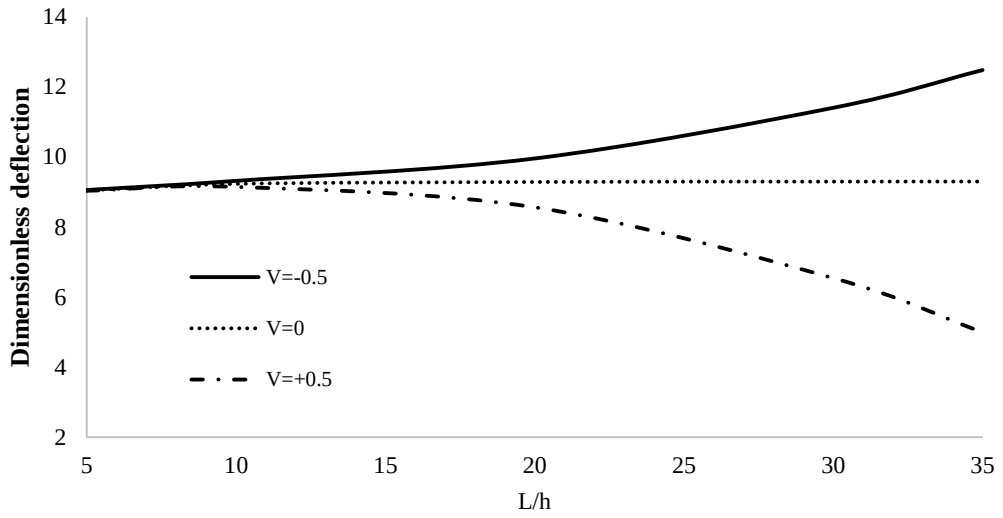

Fig. 4. Effect of slenderness ratio on dimensionless deflection via $\Omega = 0.5$ (L/*h*=10, K_w= K_p=20, ΔH=1.5)

.

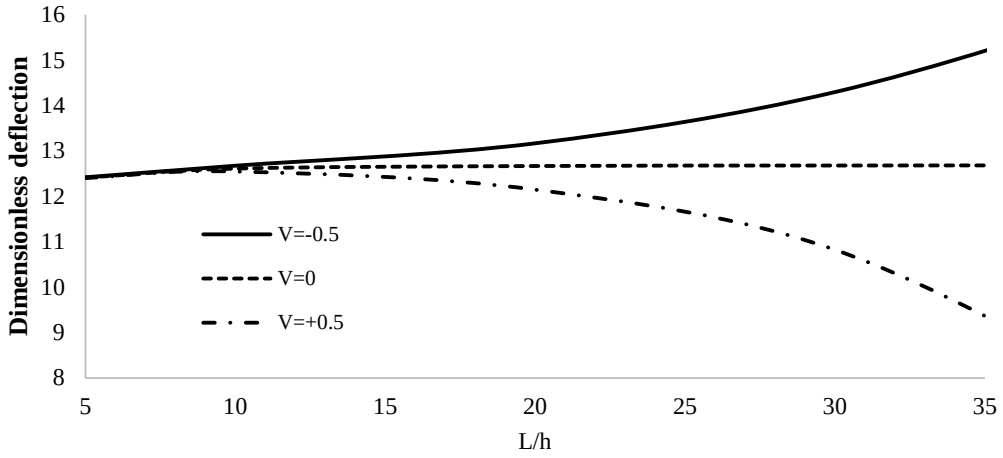

Fig. 5. Effect of slenderness ratio on dimensionless deflection via $\Omega = 1.5$ (L/*h*=10, K_w= K_p=20, ΔH=1.5)

Figures 6 and 7 are demonstrated for the variation of dimensionless deflection of nanobeam with the moisture constant via various magnetic potentials. In this example, the rise in moisture constants improves the value of deflection. Also, it is referred that the positive voltage values stiffen the deflection more than the negative voltage. This result also indicates that the effect of moisture weakens the nanobeam. The obtained results of these figures indicate that the maximum deflection increases with increasing the magnetic potential of the nanobeam.

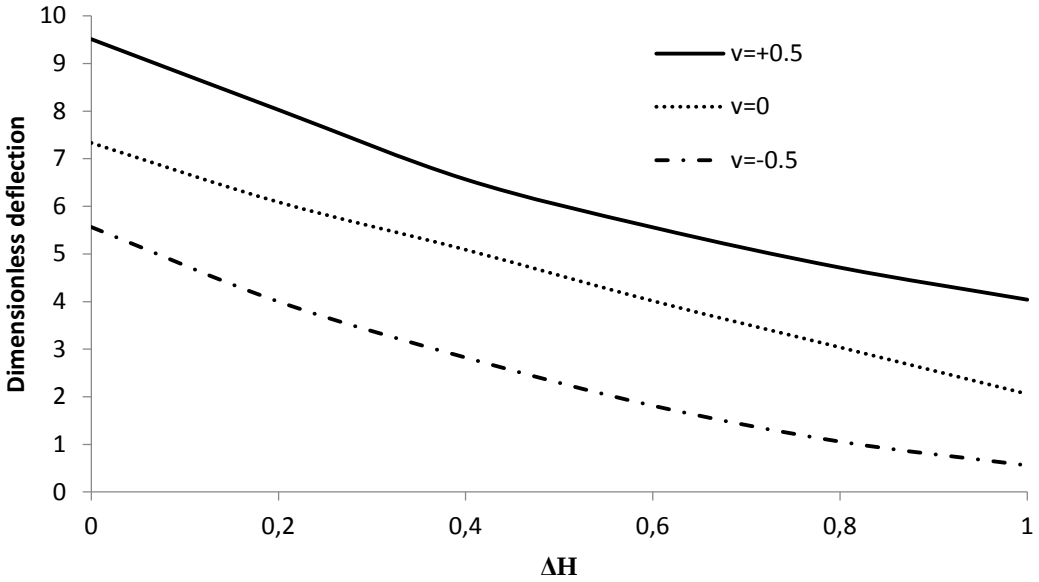

Fig. 6. Effect of moisture constant versus dimensionless deflection via $\Omega = 0.5$ (L/h=10, K_p =K_w=20)

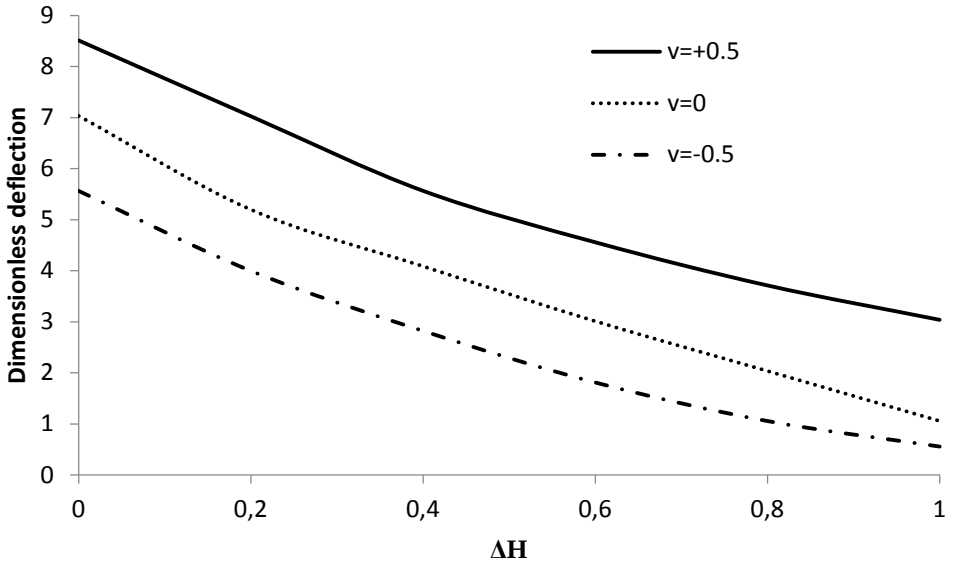

Fig. 7. Effect of moisture constant versus dimensionless deflection via $\Omega = 1.5$ (L/h=10, K_p =K_w=20)

Figures 8-9 expresses the effect of critical temperature on the dimensionless deflection via moisture coefficient rise with different electric voltage values. It can be noticed that the rise in critical temperature drives to reduce the dimensionless deflection. Also, the moisture coefficient rise expose the less amount of magnitude rise in dimensionless deflection while an increase in temperature values. The results expose the truth that the moisture coefficient variations soften the variant values via critical temperature.

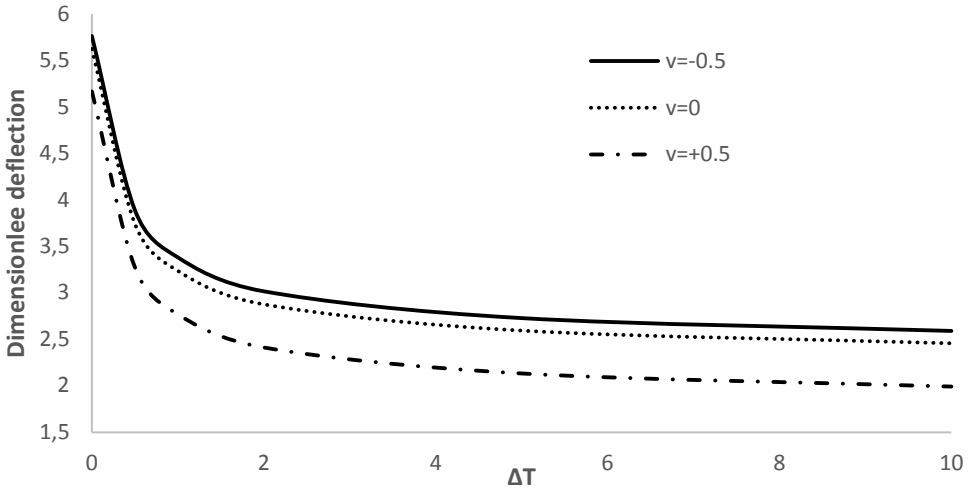

Fig. 8. Effect of critical temperature versus dimensionless deflection via ΔH=0.5 (*L/h*=10, K_p =K_w=20, $\Omega = 0$)

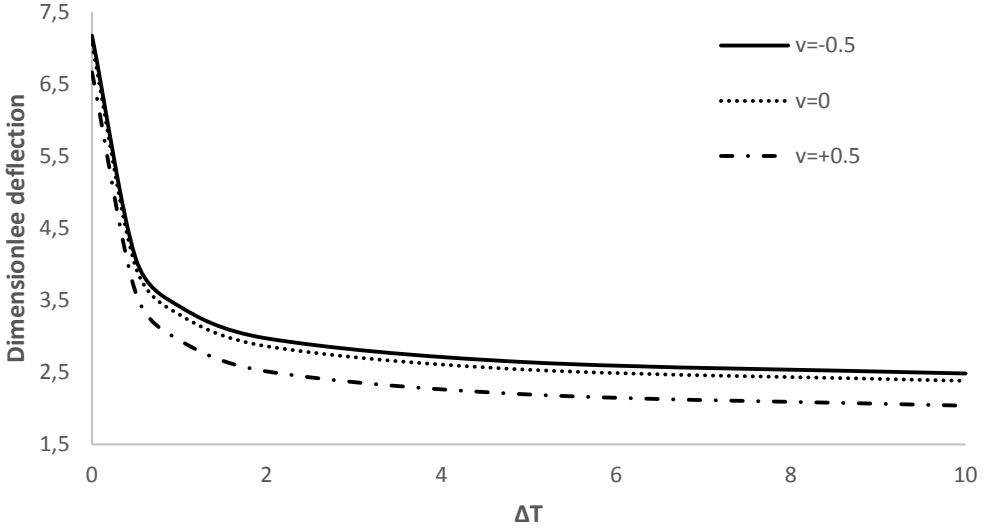

Fig. 9. Effect of critical temperature versus dimensionless deflection via ΔH=1.5 (*L/h*=10, K_p =K_w=20, $\Omega = 0$)

The variations of the dimensionless deflection of nanobeams versus Young's modulus of silica aerogel foundation for various electric voltages are shown in Figs. 10 and 11, respectively. It is found from this figure that regardless of the sign and magnitude of electric voltage, the dimensionless deflection decreases with the increase of Young's modulus of silica aerogel foundation, so the stiffness weakens of the nanobeam. It must be mentioned that the rise in magnetic potential provides higher deflection.

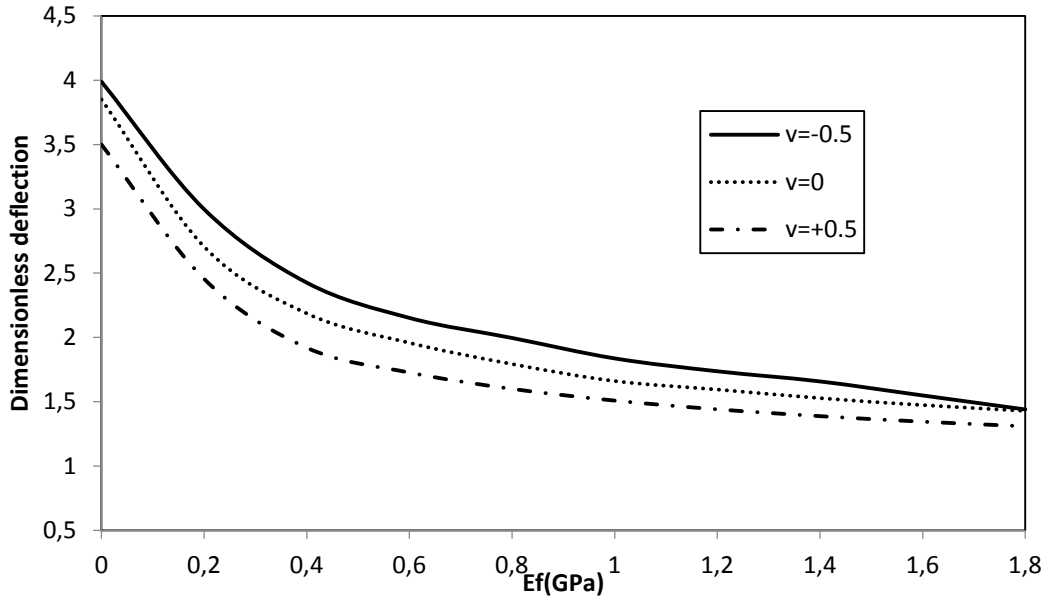

Fig. 10. Effect of Young's modulus of silica aerogel foundation versus dimensionless deflection $\Omega = 0.5$ (L/h=10, $\mu = 2, \Delta H = 1.5$)

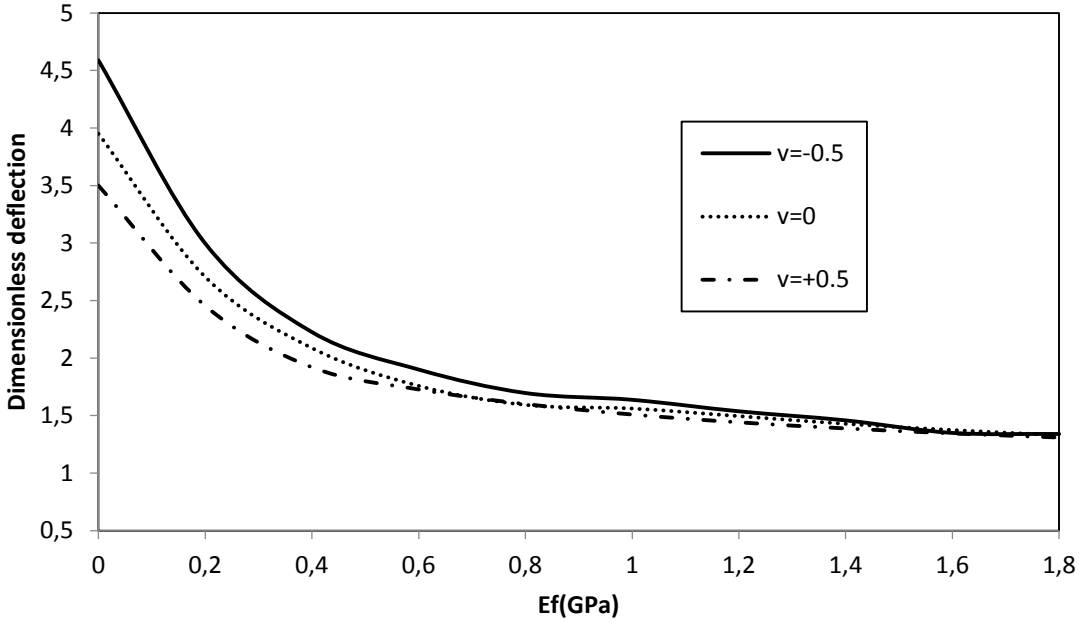

Fig. 11. Effect of Young's modulus of silica aerogel foundation versus dimensionless deflection $\Omega = 1.5$ (L/h=10, $\mu = 2, \Delta H = 1.5$)

The effect of height of the silica aerogel foundation on dimensionless deflection is recorded in Figs. 12 and 13. By raising the height of the silica aerogel foundation the dimensionless deflection is amplified for different applied electric voltages. Again the effect of higher values of magnetic potential is pronounced.

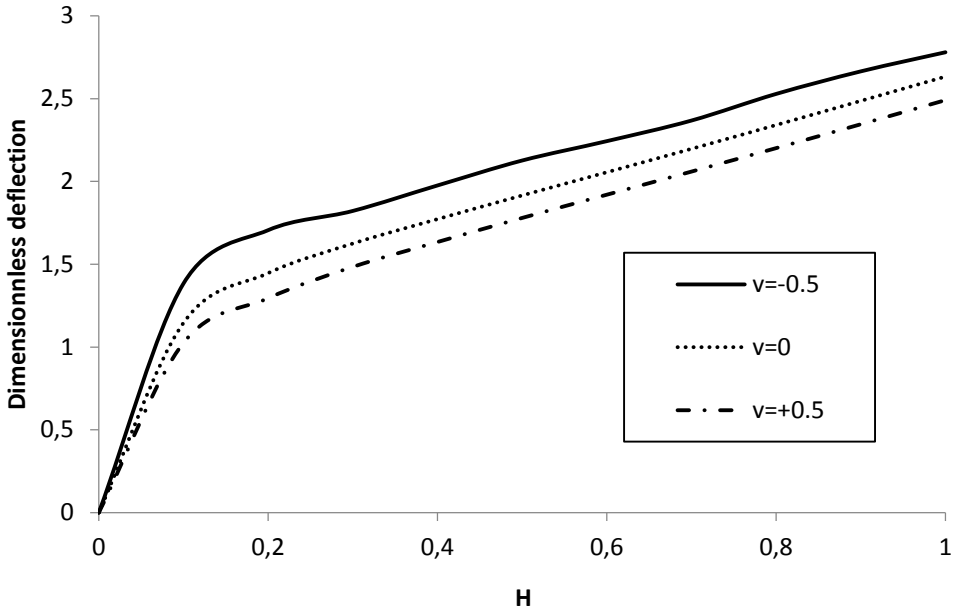

Fig. 12. Effect of Young's modulus of silica aerogel foundation versus dimensionless deflection $\Omega = 1.5$ (L/h=10, $\mu = 2, \Delta H = 1.5$)

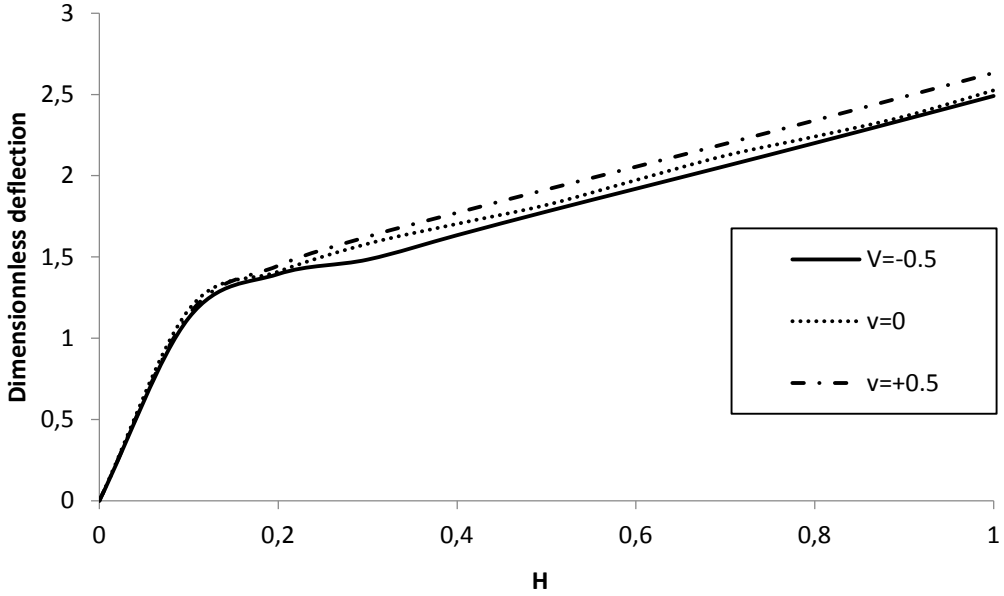

Fig. 13. Effect of Young's modulus of silica aerogel foundation versus dimensionless deflection $\Omega = 1.5$ (L/h=10, $\mu = 2, \Delta H = 1.5$)

6. Conclusions

External electric voltages on the deflection of Hygro-magneto-electro-elastic (HMEE) nanobeams embedded on silica aerogel foundation are studied in this article. The governing equations of nonlocal nanobeams based on higher-order refined beam theory are obtained using Hamilton's principle and solved by analytical solution. A parametric study is presented to observe the effect of the nonlocal parameter, slenderness, moisture constant, critical temperature, and the foundation constants on the deflection characteristics of nanobeam via different applied electric voltages. Some of the bolded highlights of this research are as follows.

- The dimensionless deflection can be amplified using the higher nonlocal parameters.
- The maximum dynamic response can be arrived at by choosing higher magnetic intensity.
- The system's dimensionless deflection can be gradually amplified when the electric voltage is negative.
- The moisture values soften the dimensionless deflection in the presence of magnetic potential.
- The dimensionless deflection may be weakened by bigger values of critical temperature in a humid environment.
- The higher density of foundation (Young's modulus of silica aerogel) reduces the stiffness of the nanobeam. On the other hand, the increase in height of th foundation refers to an amplified deflection
- The compressive and tensile nature is proven in the deflection of nanobeams via positive and negative voltage generation.

References

1. Van den Boomgard J, Terrell DR, Born RAJ. An in situ grown eutectic magnetoelectric composite material. *Journal of Materials Science*. 1974;9: 1705-1709.
2. Zheng H, Wang J, Lofland SE. Multiferroic BaTiO3-CoFe2O4 nanostructures. *Science*. 2004;303(5658): 661-663.
3. Martin LW, Crane SP, Chu YH. Multiferroics and magnetoelectrics: Thin films and nanostructures. *Journal of Condensed Matter Physics*. 2008;20(43): 434220.
4. Wang Y, Hu JM. Lin YH. Multiferroic magnetoelectric composite nanostructures. *NPG Asia Materials*. 2010;2: 61-68.
5. Prashanthi K, Shaibani PM, Sohrabi A. (2012), Nanoscale magnetoelectric coupling in multiferroic BiFeO3 nanowires. *Physica Status Solidi - Rapid Research Letetrs*. 2012;6(6): 244-246.
6. Eringen, A. Nonlocal polar elastic continua. *International Journal of Engineering Science*. 1968;10(1): 1-16.
7. Eringen A. Nonlocal micropolar field theory. In: *Continuum Physics.* Eringen A.C. (Ed.) New York: Academic Press; 1976. p.106.
8. Eringen A. *Nonlocal Continuum Field Theories*. New York: Springer; 2002.
9. Eringen A. Nonlocal continuum mechanics based on distributions. *International Journal of Engineering Science*. 2006;44(3): 141-147.
10. Eringen A, Edelen D. On nonlocal elasticity. *International Journal of Engineering Science*. 1972;10(3): 233-248.
11. Yang J, Ke LL, Kitipornchai S. Nonlinear free vibration of single-walled carbon nanotubes using nonlocal Timoshenko beam theory. *Physica E: Low-Dimensional Systems and Nanostructures*. 2010;42(5): 1727-1735.
12. Ehyaei J. Akbarizadeh MR. Vibration-analysis of micro composite thin beam based on modified couple stress. *Structural Engineering and Mechanics*. 2017;64(4): 793-802.
13. Ebrahimi F, Barati MR. Wave propagation analysis of smart strain gradient piezo-magneto-elastic nonlocal beams. *Structural Engineering and Mechanics*. 2018;66(2): 237-248.
14. Dihaj A, Zidour M, Meradjah M, Rakrak K, Heireche H, Chemi A. Free vibration analysis of chiral double-walled carbon nanotube embedded in an elastic medium using non-local elasticity theory and Euler Bernoulli beam model. *Structural Engineering and Mechanics*. 2018;65(3): 335-342.
15. Ebrahimi F, Barati MR. Dynamic modeling of a thermo–piezo-electrically actuated nanosize beam subjected to a magnetic field. *Applied Physics Research*. 2016;122(4): 1-18.

16. Ebrahimi F, Barati MR. Electromechanical buckling behavior of smart piezoelectrically actuated higher-order size-dependent graded nanoscale beams in thermal environment. *International Journal of Smart and Nano Materials*. 2016;7(2): 69-70.
17. Ebrahimi F, Barati MR. An exact solution for buckling analysis of embedded piezoelectro-magnetically actuated nanoscale beams. *Advances in Nano Research*. 2016c;4(2): 65-84.
18. Ebrahimi F, Barati MR. Vibration analysis of smart piezoelectrically actuated nanobeams subjected to magneto-electrical field in thermal environment. *Journal of Vibration and Control*. 2018;24(3): 549-564.
19. Roque CMC, Ferreira AJM, Reddy JN. Analysis of Timoshenko nanobeams with a nonlocal formulation and meshless method. *International Journal of Engineering Science*. 2011;49(9): 976-984.
20. Peddieson J, Buchanan GR, McNitt RP. Application of nonlocal continuum models to nanotechnology. *International Journal of Engineering Science*. 2003;41(3-5): 305-312.
21. Civalek O, Demir C. Bending analysis of microtubules using nonlocal Euler–Bernoulli beam theory. *Applied Mathematical Modelling*. 2011;35(5): 2053-2067.
22. Wang Q. Wave propagation in carbon nanotubes via nonlocal continuum mechanics. *International Journal of Applied Physics*. 2005;98(12): 124-301.
23. Wang CM, Kitipornchai S, Lim CW, Eisenberger M. Beam bending solutions based on nonlocal Timoshenko beam theory. *Journal of Engineering Mechanics*. 2008;134(6): 475-481.
24. Murmu T, Pradhan SC. Buckling analysis of a single-walled carbon nanotube embedded in an elastic medium based on nonlocal elasticity and Timoshenko beam theory and using DQM. *Physica E: Low-Dimensional Systems and Nanostructures*. 2009;41(7): 1232-1239.
25. Karami B, Janghorban M, Tounsi A. Effects of triaxial magnetic field on the anisotropic nanoplates. Steel. *Composite Structures*. 2017;25(3): 361-374.
26. Ebrahimi F, Rostami P. Propagation of elastic waves in thermally affected embedded carbon-nanotube-reinforced composite beams via various shear deformation plate theories. *Structural Engineering and Mechanics*. 2018;66: 495-504.
27. Ali Hajnayeb AK, Foruzande H. Free vibration analysis of a piezoelectric nanobeam using nonlocal elasticity theory. *Structural Engineering and Mechanics*. 2017;61(5): 617-624.
28. Yazdi AA. Large amplitude forced vibration of functionally graded nano-composite plate with piezoelectric layers resting on nonlinear elastic foundation. *Structural Engineering and Mechanics*. 2018; 68(2): 203-213.
29. Arefi M, Zenkour AM. A simplified shear and normal deformations nonlocal theory for bending of functionally graded piezomagnetic sandwich nanobeams in magneto-thermo-electric environment. *Journal of Sandwich Structures and Materials*. 2016;18(5): 624-651.
30. Ebrahimi F, Barati MR. Buckling analysis of nonlocal third-order shear deformable functionally graded piezoelectric nanobeams embedded in elastic medium. *Journal of the Brazilian Society of Mechanical Sciences and Engineering*. 2016;39: 937-952.
31. Arefi M. Static analysis of laminated piezo-magnetic size-dependent curved beam based on modified couple stress theory. *Structural Engineering and Mechanics*. 2019;69: 145-153.
32. Jiang A, Haojiang D. Analytical solutions to magneto-electro-elastic beams. *Structural Engineering and Mechanics*. 2004;18(2): 195-209.
33. Gayen D, Roy T. Hygro-thermal effects on stress analysis of tapered laminated composite beam. *International Journal of Composite Materials*. 2013;3(3): 46-55.
34. Kurtinaitiene M, Mazeika K, Ramanavicius S, Pakstas V, Jagminas A. Effect of additives on the hydrothermal synthesis of manganese ferrite nanoparticles. *Advances in Nano Research*. 2016;4(1): 1-14.

35. Alzahrani EO, Zenkour AM, Sobhy M. Small scale effect on hygro-thermo-mechanical bending of nanoplates embedded in an elastic medium. *Composite Structures*. 2013;105: 163-172.
36. Sobhy M. Buckling and free vibration of exponentially graded sandwich plates resting on elastic foundations under various boundary conditions. *Composite Structures*. 2013;99: 76-87.
37. Ghorbanpour Arani A, Zamani MH. Investigation of electric field effect on size-dependent bending analysis of functionally graded porous shear and normal deformable sandwich nanoplate on silica Aerogel foundation. *Journal of Sandwich Structures and Materials*. 2017;1099636217721405.
38. Şimşek M, Yurtcu HH. Analytical solutions for bending and buckling of functionally graded nanobeams based on the nonlocal Timoshenko beam theory. *Composite Structures*. 2013;97: 378-386.
39. Ke LL, Wang YS, Yang J, Kitipornchai S. Free vibration of size-dependent magneto-electro-elastic nano plates based on the nonlocal theory. *Acta Mechanica Solida Sinica*. 2014;30(4): 516-525.
40. Selvamani R, Ponnusamy P. Damping of generalized thermoelastic waves in a homogeneous isotropic plate. *Materials Physics and Mechanics*. 2012;14(1): 64-73.
41. Selvamani R.Influence of thermo-piezoelectric field in a circular bar subjected to thermal loading due to laser pulse. *Materials Physics and Mechanics*. 2016;27(1): 1-8.
42. Selvamani R. Free vibration analysis of rotating piezoelectric bar of circular cross section immersed in fluid. *Materials Physics and Mechanics*. 2015;24(1): 24-34.
43. Selvamani R. Dynamic response of a heat conducting solid bar of polygonal cross sections subjected to moving heat source. *Materials Physics and Mechanics*. 2014;21(2): 177-193.
44. SelvamaniR, Ponnusamy P. Elasto Dynamic wave propagation in a transversely isotropic piezoelectric circular plate immersed in Fluid. *Materials Physics and Mechanics.* 2013;17(2): 164-177.
45. Selvamani R, Ponnusamy P. Effect of rotation in an axisymmetric vibration of a transversely isotropic solid bar immersed in an inviscid fluid. *Material Physics and Mechanics*. 2012;15(2): 97-106.
46. Selvamani R, Sujitha G. Effect of non-homogeneity in a magneto electro elastic plate of polygonal cross-sections. *Materials Physics and Mechanics*. 2018;40(1): 84-103.
47. Selvamani R, Flexural wave motion in a heat conducting doubly connected thermo-elastic plate of polygonal cross-sections. *Materials Physics and Mechanics*. 2014;19(1): 51-67
48. Selvamani R, Ponnusamy P. Generalized thermoelastic waves in a rotating ring shaped circular plate immersed in an inviscid fluid. *Materials Physics and Mechanics*. 2013;18(1): 77-92.
49. Selvamani R, Ponnusamy P. Extensional Waves in a Transversely Isotropic Solid Bar Immersed in an Inviscid Fluid Calculated Using Chebyshev Polynomials. *Materials Physics and Mechanics*. 2013;16(1): 82-91.
50. Ramirez F, Heyliger PR, Pan E. Discrete layer solution to free vibrations of functionally graded magneto-electro-elastic plates. *Mechanics of Advanced Materials and Structures*. 2006;13(3): 249-266.
51. Forooghi A, Rezaey S, Haghighi SM, Zenkour AM. Thermal instability analysis of nanoscale FG porous plates embedded on Kerr foundation coupled with fluid flow. *Engineering with Computers*. 2021. Available from: https://doi.org/10.1007/s00366-021-01426-3.
52. Safarpour M, Forooghi A, Dimitri R, Tornabene F. Theoretical and Numerical Solution for the Bending and Frequency Response of Graphene Reinforced Nanocomposite Rectangular Plates. *Applied Sciences*. 2021;11(14): 6331.

53. Forooghi A, Alibeigloo A. Hygro-thermo-magnetically induced vibration of FG-CNTRC small-scale plate incorporating nonlocality and strain gradient size dependency. *Waves in Random and Complex Media*. 2022. Available from: https://doi.org/10.1080/17455030.2022.2037784.
54. Huang W, Ren J, Forooghi A. Vibrational frequencies of FG-GPLRC viscoelastic rectangular plate subjected to different temperature loadings based on higher-order shear deformation theory and utilizing GDQ procedure. *Mechanics Based Design of Structures and Machines*. 2021. Available from: https://doi.org/10.1080/15397734.2021.1878041.

THE AUTHORS

Selvamani R.
e-mail: selvam1729@gmail.com
ORCID: 0000-0001-5166-5449

Rubine L.
e-mail: rubineloganathan5@gmail.com
ORCID:

Rexy J.
e-mail: rexyallan1@gmail.com
ORCID:

Ebrahimi F.
e-mail: febrahimy@gmail.com
ORCID: 0000-0001-9091-4647

Materials Physics and Mechanics. 2022;50(1): 20-36
Research article
http://dx.doi.org/10.18149/MPM.5012022_2

Submitted: January 23, 2021
Approved: August 16, 2022
Accepted: August 16, 2022

Physicochemical and mechanical properties of briquettes prepared from the combination of micrometer-sized areca nutshell, tofu dreg, and citronella: from the literature review to experiments

A.B.D. Nandiyanto✉, S.N. Hofifah, S. Anggraeni, N.Z. Latifah, J.E. Sitanggang, O. Sopian, Z. Saputra

Fakultas Pendidikan Matematika dan Ilmu Pengetahuan Alam, Universitas Pendidikan Indonesia,

Jl. Dr. Setiabudi No. 229, Bandung, Indonesia

✉ nandiyanto@upi.edu

Abstract. Effects of the particle size (i.e. 100, 150, and 500 μm) and composition of biomass on physicochemical and mechanical properties of briquettes were evaluated. This study used biomass from the mixture of tofu dreg (TD), areca nutshell (ANS), and citronella (CN). This study was also completed with a literature review. ANS was carbonized at 250°C for 2 hours. Then, all raw materials (i.e. TD, ANS, and CN) were dried, saw-milled, and mixed with tapioca starch as a binder to form a dough. The particle size and ANS composition gave an impact on the briquettes' performance, including burning rate, specific fuel consumption, and mechanical properties. Particle size influenced the compact component in the briquette. ANS affected carbon and moisture contents in the briquette, improving its compressive strength. This study demonstrates the alternative solution for reducing organic wastes by converting them into briquettes.

Keywords: briquettes, biomass, energy, mechanical properties, tofu dreg, areca nutshell, citronella

Acknowledgements*. This study acknowledged RISTEK BRIN for Grant-in-aid Penelitian Terapan Unggulan Perguruan Tinggi (PTUPT).*

Citation: Nandiyanto ABD, Hofifah SN, Anggraeni S, Latifah NZ, Sitanggang JE, Sopian O, Saputra Z. Physicochemical and mechanical properties of briquettes prepared from the combination of micrometer-sized areca nutshell, tofu dreg, and citronella: from the literature review to experiments. *Materials Physics and Mechanics*. 2022;50(1): 20-36. DOI: 10.18149/MPM.5012022_2.

1. Introduction

Bio briquettes are solid fuels made from a mixture of biomass. Biomass is a term used to describe all types of organic materials that are the results of the photosynthesis process [1]. In Indonesia, biomass is largely abundant, while its usage is not optimal yet [2].

Reports on the use of biomass as alternative energy are well-documented. Many strategies have been reported, and the results were compared to the briquette standard [3].

Detailed current research for the use of briquette from biomass is presented in Table 1. However, studies on the effects of the particle size of raw materials on the briquettes' quality are typically unconcerned.

Table 1. The previous research on the preparation of briquettes from biomass

No	Biomass	Binder	Results	Ref.
1	Water hyacinth (*Eichhornia crassipes*) charcoal	Molasses	The molasses to charcoal ratio had an impact on the briquettes' quality and characteristics. With increasing amounts of binder, ash content decreased while volatile combustible matter and fixed carbon increased. The highest calorific value (16.6 MJ/kg) and compressive strength (19.1 kg/cm^2) were produced by the 30:70 charcoal/molasses ratio. The potential for turning water hyacinth into an alternative fuel source has been demonstrated by the results.	[4]
2	Areca leaves	Wheat flour	According to IS1448-7 standards, the areca leaves' gross calorific value was determined. According to the analysis, compared to briquettes with particle sizes larger than 1700 µm, 600 and 425 µm of areca leaves components are better. Further, briquettes with 85-µm areca leaves have the highest calories at 14.57 MJ/kg. The briquette's physicochemical properties showed low moisture content (8.08%) and low ash content (1.47%). Because they contain less nitrogen (0.61%) and sulfur (0.65%), the briquettes are environmentally friendly. As a result, producing briquettes from 850-µm areca leaves with sawdust as an additive can result in high-quality biomass fuel for use in both homes and businesses.	[5]
3	Carbonized rice husk and jatropha seed waste	Newspaper waste pulp	The briquettes with the highest heat energy content (5,650 cal/g) are those with 8% of newspaper waste pulp adhesives. The best-mixed charcoal briquettes are made from rice husk charcoal and jatropha seed at a 50:50 ratio with 8% newspaper waste pulp added as an adhesive agent. Adding more adhesive will reduce the calorific value. The best properties of mixed charcoal briquette (made from rice husk and jatropha seed waste) are moisture content of 3.85%, volatile matter of 43.87%, ash of 23.78%, fixed carbon of 28.50%, and calorific value of 5,650 cal/g. The calorific value of rice husk can be increased by the addition of jatropha seed charcoal from 3,350 to 5,650 cal/g.	[6]
4	Orange peels and corn cobs	Pasty starch	According to the results, the sample can reach the highest calorific value per kilogram of	[7]

			31,886 kcal. The mixtures made up of 20% of orange peels and 80% of corn cobs have the highest calorific values and carbon contents, which are the most desirable qualities of good solid fuel. In the meantime, a briquette made of 80% orange peels and 20% corn cobs has shown some promise.	
5	Cocoa Shells and Sea Mango	Tapioca flour	Small-particle briquettes have high values for relaxed density, relaxation ratio, and percentage of durability index. However, the high density of briquettes on smaller particles made the compressed density and the percentage of moisture content low.	[8]
6	Sugarcane bagasse	-	Analysis of the fuel's parameters revealed high-quality levels of low ash content (0.97 percent) and high calorific values (18.35 MJ kg-1 for gross calorific value and 17.06 MJ kg-1 for net calorific value), which suggested the fuel was well suited for direct combustion processes. The following observations were supported by indicators of mechanical quality: bulk density of 1022 kg/m^3, compressive strength of 150 N/mm^1, and mechanical durability of 99.29%.	[9]
7	Coconut (*Cocos Nucifera*) Coir and Banana (*Musa Paradisica*) Peels	Tapioca starch	The best performance of briquettes is with 310 µm of particles with a mixture content of banana peels as much as 20% of the total weight. It has good specific fuel consumption (5.42 g/mL) and a burning rate (5.10 g/min). The briquette has a compressed density of 0.39 g/cm^3, relaxation ratio of 1.70, a relaxed density of 0.23 g/cm^3, a water resistance index of 80.14%, a moisture content of 58.55%, and a durability index of 98.92%.	[10]
8	Melinjo (*Gnetum gnemon*) Shell	Tapioca	Briquettes with 10% of tapioca (sizes of 465-1000 µm) have the best relaxation ratio values, percentage moisture content, burning rates, and specific fuel consumption. Briquettes with 50% of tapioca (sizes of 74-105 µm) have the highest compressed density, relaxed density value, durability index percentage, and water resistance index percentage.	[11]
9	Banana peels, sugarcane bagasse, coconut shells, and rattan waste	Cassava starch	Banana peels (97.98%) and sugarcane bagasse (97.98%) losses are more significant in the mass reduction (96%). High calorific values of the briquettes produced are 16.98, 30.07, 32.16, and 25.93 MJ/kg for banana peels, rattan waste, coconut shells, and sugarcane bagasse, respectively. Volatile matters are gradually lower. Ash content was 7.44-11.95%, and	[12]

			moisture content is relatively low.	
10	Rice husk and red bean skin	Tapioca starch	Small particles (74-100 µm) with a binder concentration of 50% produce briquettes of good quality. Due to the small size and large surface area of the particles, as well as the high binding agent concentration, the bonds between the particles are very strong. A 20% binder concentration produced good quality briquettes for the briquettes with large particles (500-2000 µm).	[13]
11	Durian eel (*Durio kutejensis Becc*) charcoal	Starch	The briquettes were made from durian peel charcoal by adding starch as a binder at different concentrations of 3, 4, 5, and 6% to obtain moisture content, volatile matter, ash content, and calorific value. The 3% of starch binder in the durian peel briquettes had the highest quality.	[14]
12	Cassava peels and rice husks	Tapioca starch	The small particle of biomass shows good performance in the compressed and relaxed density. The 90:10 briquette with small particles has an excellent calorific value, according to the water boiling test, burning rate, and specific fuel consumption. For briquettes with medium particles and a 50:50 ratio, a good water-resistant index was obtained. For all briquettes, the average durability index values were 98%.	[15]
13	Sawdust, rice, and coconut husks	Cassava starch	The charred briquettes' calorific value was discovered to be 24.69 MJ/kg. The use of a multi-feed gasifier stove (MFGS) resulted in briquettes burning with the highest combustion efficiency (34.7%). When briquettes were used in the MFGS in place of charcoal, there were reductions in particulate matter and carbon monoxide emissions of 14 and 80%, respectively.	[16]
14	Carbon particles from potato and yam skins	Rice waste	The best quality of the prepared briquettes was for the sample with 10% adhesive. The briquettes with 30% adhesive had the highest durability index. When using 40% adhesive, excellent compressed density and water resistance index were obtained. Briquettes with less adhesive typically have a high density, little moisture content, and long flammability.	[17]
15	Onion peels and tamarind shells	Cassava Starch	Comparatively to pine, cotton stalk, wood sawdust, municipal solid waste (MSW), and cotton straw biomass briquettes, onion peels and tamarind shells (OP-TS) have better fuel properties. Onion peels and tamarind shells were used to create briquettes with a higher	[18]

			heating value. They, therefore, made a great choice for an energy source. The briquettes' carbon content has decreased while their oxygen and hydrogen contents have increased when using OP-TS.	
16	Sawdust and rice husk carbon	Starch paste	High density (bulk, compressed, and relaxed) was produced by the high concentration of carbon rice husks (CRH) in briquettes. The compaction ratio, water resistance, durability, and relative suitability decreased with a high CRH. Sawdust and CRH can be burned cooperatively inside the briquette.	[19]
17	Bamboo Fiber and Dried Clove Leaves	Dextrin	Briquettes made of dried clove leaves and bamboo fibers with 60% have good solidity, durability, fuel consumption, and moisture content, while those at 20% have good combustion performance.	[20]
18	Coffee grounds and soybean peels	Tapioca flour	Briquettes with a ratio of (60:40) and a particle size of 250 μm have good compressed density, burning rate, and specific fuel consumption characteristics.	[21]
19	Durian peels and banana midrib	Tapioca flour	The best briquette results were when using a 70:30 ratio of durian peels and banana midrib with a carbon particle size of 250 μm, according to compressed density, relaxed density, relaxation ratio, percentage moisture content, percentage of water resistance index, water boiling test, burning rate, specific fuel consumption, and durability index.	[22]
20	Peanut shells	Tapioca flour	310-μm particles gave a good performance in the compressed density and relaxed ratio. The 582-μm particle had less moisture content and high specific fuel consumption.	[23]

Our previous studies reported the mechanical properties of materials, such as iron oxide [24], tungsten trioxide [25,26], brake pad[27], bioplastic material [28-30], and food materials [31]. We also reported several characterizations and analyses for supporting the studies [32-36]. Here, this study aims to determine the quality of the briquettes as a function of the particle size and composition of several raw materials. As models of raw materials, we used a combination of tofu dreg (TD), areca nutshell (ANS), and citronella (CN). The main reasons for the use of these raw materials are:

(i) TD as the bioproduct of the tofu industry – one of the important agro-industry in Indonesia that brings great economic impacts – is not carefully handled and treated, creating problems in the environment. Direct disposing of TD causes a bad smell since TD contains high protein content (100 g of TD contains 27 g of protein) [37].

(ii) Areca nut (*Areca catechu*) is a type of palm plant that is widely cultivated in Indonesia. Areca nuts are scattered in all regions of Indonesia. Areca nut is found in various regions of Indonesia, especially in Sumatra, Kalimantan, and Sulawesi [38]. In general, areca farmers only use areca seeds. ANS is not used and becomes waste that can pollute the environment. Areca farmers usually burn ANS to reduce buildup. Combustion that

is carried out can cause air pollution. In fact, ANS and other biomass such as tofu dreg have considerable energy potential and can be used as bio briquettes.

(iii) Citronella (*Cymbopogon nardus L.*) is one of the plants that produce essential oils. Citronella is widely cultivated in Indonesia, and Indonesian land has a climate suitable for its growth[39]. The essential oil from Citronella has a bitter taste, smells good, and evaporates at room temperature without decomposition [40]. The good smell of the essential oil in citronella can be added to bio briquettes, so the briquettes can emit a good smell when baked.

In addition, ANS was used as the main carbon material, where this material was carbonized before use. The carbonization process can increase the carbon content and heating value of the prepared briquette [41,42]. Our research is important to demonstrate the alternative solution for reducing waste management since such TD, ANS, and CN were typically disposed of directly to the environment.

2. Material and method

Material preparation. Briquettes were made from a mixture of TD, ANS, and CN. All materials were obtained from Pangandaran Regency, Indonesia. The tapioca flour as the binder was obtained from Cimahi, Indonesia. The TD/ANS/CN compositions were varied in the ratio of 10/90/30, 40/60/30, 50/50/30, 60/40/30, and 90/10/30.

Briquettes making process. Prior to use, all materials were cut into pieces and dried naturally for about 5 days to remove physical moisture content. The ANS was then carbonized using an electrical furnace at the temperature of 250°C for 1-2 hours. All materials were saw-milled and sieved to obtain the required sizes (i.e. 100, 150, and 500µm), using the similar procedure in our previous report[43]. The particle size was classified as small (100 µm), medium (150 µm), and large sizes (500 µm). All materials were then mixed according to the predetermined variations. The binder of tapioca starch was made by the ratio of tapioca/water of 2/25. The tapioca starch was then mixed with the mixed material and stirred to form a dough. The dough was molded (round shape, 3.80 cm in diameter, and 0.70 cm in height) and pressed with a pressure of 8.74 N/cm^2. The briquettes were dried naturally to remove outer moisture. Then, they were dried at 150ºC in the electrical furnace until their mass is constant.

Briquette performance analysis. The prepared briquettes were tested by several characterizations: density, moisture content, water boiling test, burning rate, specific fuel consumption, water-resistance index, and durability index [44].

(1) Density includes compressed density (*CD*), relaxed density (*RD*), and relaxation ratio (*RR*). *CD*, *RD*, and *RR* were calculated using Eqs**.** (1), (2), and (3), respectively.

$$CD = W_c/V_c, \quad (1)$$

$$RD = W_r/V_r, \quad (2)$$

$$RR = CD/RD, \quad (3)$$

where *Wc* is the weight of the briquette immediately after molding, and *Vc* is the volume of the briquette after molding. *Wr* is the weight of briquettes after drying, and *Vr* is the volume of briquettes.

(2) Percentage moisture content (*PMC*) was determined by calculating the initial mass of briquettes immediately after molding (W_1), and the mass of briquettes after complete drying (W_2)[45]. *PMC* is calculated with Eq. (4).

$$PMC = [(W_1-W_2)/W_2] \text{ X } 100\%. \quad (4)$$

(3) Water boiling test (*WBT*) **i**s a test used to determine the efficiency of briquette combustion. It was carried out by burning the briquette sample, the heat from the combustion was used to boil 100 mL of water in a beaker. The increase in water temperature was recorded during the combustion process.

(4) Burning rate (*BR)* is the combustion rate which was calculated by the ratio of the mass lost when combustion with the total time used [46], calculated using Eq. (5).

$$BR = Q/T, \quad (5)$$

where Q is the mass of briquette burnt out (g) and T is the total burning time (min).

(5) Specific fuel consumption (*SFC*) shows the ratio of the mass of the briquettes burned to the amount of water to boil [46] and it is determined using Eq. (6).

$$SFC = Q/V, \quad (6)$$

where Q is the mass of burning briquettes (g) and V is the volume of boiling water (mL).

(6) Percentage of water resistance index (*PWRI*) test was conducted by immersing the briquettes in water with a temperature of 27ºC for 30 seconds[47]. *PWRI* is calculated using Eq. (7) and (8).

$$PWA = [(Q_2-Q_1)/Q_1] \text{ X } 100, \quad (7)$$

$$PWRI = 100\% - PWA, \quad (8)$$

where *PWA* is the percentage of water absorbed, Q_1 is the initial mass of briquettes (g), and Q_2 is the final mass of briquettes (g).

(7) Percentage of durability index (*DI*). To analyze *DI,* the mass of the briquettes was measured. The briquettes were put into a plastic bag, while the air in the plastic was removed. The briquettes were dropped from a height of 2 m onto a solid surface. The mass of the briquettes that were not crushed was then measured again [47]. The *DI* is determined by Eq. (9).

$$DI = Q_2/Q_1 \text{X} 100, \quad (9)$$

where Q_1 is the mass before being put together (g), and Q_2 is the mass after being dropped (g).

(8) Mechanical test. To analyze the mechanical characteristics of the briquettes, we carried out a compressive test and a puncture test [29,28]. The compressive test was performed using a screw stand test instrument (Mode I ALX-J, China) equipped with a measuring instrument (a Digital Force gauge (Model HP-500, Serial No. H5001909262). The puncture test was done using the Shore Durometer instrument (Shore A Hardness, In size, China). The compressive test was carried out by pressing the briquettes. The pressure given by the instrument to measure the hardness of the briquette, the measurement results are represented as a curve. The puncture test was done by inserting a needle into the surface of the briquette. The measured number was obtained from the depth of the needle puncture

3. Results and discussion

Effect of particle size

Density. Figure 1(a) shows the density in terms of *CD, RD,* and *RR* of the briquettes under varying particle sizes. The *CD* value varied from 1.10 to 1.38 g/cm^3. The highest *CD* value was obtained at the medium particle size of medium sizes. The lowest *CD* values were found in the large particles. The particle size affects the *CD* value, the larger particles resulted in a higher *CD* value [48]. However, anomalies were found in the sample with large particles. This can be due to the incomplete drying of the briquettes, the difference in the pressure exerted on the briquettes with large particles, or the effect of the binders used [41].

The *RD* value ranged from 0.60-0.90 g/cm^3. Briquettes with small particles showed the highest *RD* value, while briquettes with large particles showed the lowest *RD* value. Based on Fig. 1, the smaller particles allowed the obtainment of higher RD. The smaller particles made the larger binding surface area among the particle; Thus, the density was getting higher [49].

The *RR* of samples ranged from 1.3 to 1.7. The density changed from wet to dry, but briquettes were relatively stable. Variations in particle size had a different effect on the *RR*. The highest *RR* was obtained from briquettes with medium and large particles, while the

lowest *RR* was obtained from small particles. This *RR* test showed that the most stable briquettes were the briquettes made with small particles. Small particles caused high briquette density [49].

Percentage moisture content (PMC). Figure 1(b) shows the results of *PMC* analysis on briquettes with different particle sizes. The *PMC* values ranged from 48 to 56%. Results showed that the relative moisture of the briquettes increased with the smaller particles. The highest *PMC* was obtained from briquettes with small particles, while the lowest *PMC* was obtained from large particles. Small particles allowed the briquette to have smaller pores. Small pores hold the transport of moisture and oxygen into the briquette [50].

Percentage of water resistance index (PWRI). PWRI is an analysis that shows the percentage of water content absorbed by the briquette with the effect of particle size (Fig. 1(b)). The highest *PWRI* was obtained for briquettes with large particles, while the lowest *PWRI* was obtained for the medium particles. The large particles make briquettes have many pores. The pores make the cavity on the briquettes and cause infiltration water to the briquette to become higher [51]. However, anomalies were found in samples with medium particle sizes which had a smaller PWRI value than small particles. It can be caused by differences in drying temperature and briquetting pressure when the medium particle size briquettes were made.

Percentage of durability index (DI). The sample showed good *DI* values ranging between 96.5 and 97.9% (Fig. 1(b)). The highest *DI* was obtained when using briquettes from small particles, while the lowest *DI* was obtained from large particles. The smaller particles allowed the obtainment of high density, indeed causing the briquettes to get stronger [52].

Burning rate (BR). Figure 1 (c) shows the effect of particle size on the *BR* of combustion. The *BR* value obtained ranged from 0.55 to 0.78 g/min. The largest *BR* was shown by the briquettes with large particles, and the smallest *BR* was indicated by the briquettes with medium particle size. The smaller particles caused lower porosity, so that mass transfer (i.e. water vapor, volatile matter, and oxygen infiltration) was inhibited. The inhibited mass transfer resulted in a higher *BR* [53]. Large particle shows that are not linear with the theory, this can occur due to the effect of differences in humidity, errors during briquette drying, or errors in the combustion treatment.

Specific fuel consumption (SFC). The results of *SFC* were presented, ranging from 0.066 to 0.1 g/mL (Fig. 1(c)). The lowest *SFC* value was obtained by the medium size, while the highest *SFC* was obtained in the sample with large particles. Briquettes made from large particles produced a large calorific value when they are burned. The high calorific value caused a high *SFC* value. The higher calorific value of the briquette combustion resulted in a better quality of briquettes [54].

Water boiling test (WBT). The water boiling test evaluates the thermal efficiency of briquettes [55]. Table 2 shows the results of the water boiling test (*WBT*) on variations in particle size. The data explains that the smaller particles of TD, ANS, and CN caused the water temperature to increase quickly. The best briquettes from the *WBT* test results are briquettes with small particles. Small particles in the briquettes have a low cavity, even almost non-porous. The less porous causes a higher calorific value so that the burning of the briquettes can increase the water temperature quickly.

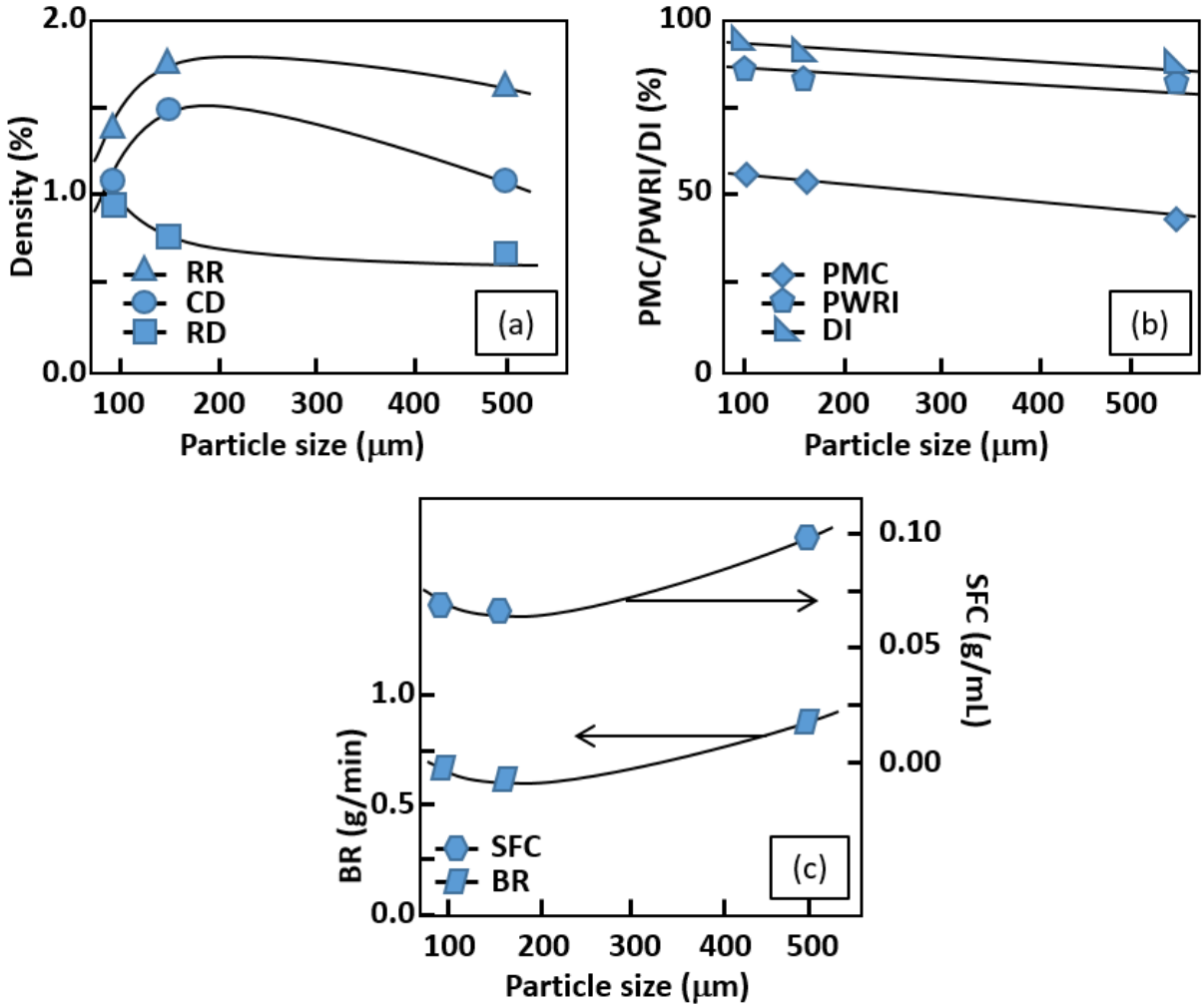

Fig. 1. Effect of particle size on briquettes' performance: (a) *CD, RD, RR,* (b) *PMC, PWRI, DI* (c) *BR* and *SFC*

Table 2. Water boiling test (*WBT*) as a function of particle size of

Particle size (μm)	Burning time (min)	Initial temperature (°C)	Final temperature (°C)
500	6.10	27	84
150	6.01		88
100	5.50		90

Variations of composition

Density. Figure 2 (a) shows the *CD, RD,* and *RR* of the briquettes with varying particle sizes. The density is an important parameter that can affect the quality of briquettes. In general, higher densities result in better briquette quality [56]. The highest *CD* was obtained at the raw material composition ratio of 50/50/30. The lowest *CD* was obtained at the ratio with the raw material composition of 90/10/30. The same ratio between TD and ANS resulted in high *CD* values. The more TD results in the smaller *CD* value. This can be caused by the characteristics of the TD material which cause many pores in the briquette, causing the briquette density to decrease. The density was affected by the size and homogeneity of the briquette constituents.

The *RD* value of briquettes ranged from 0.7 to 0.8 g/cm^3. The highest *RD* value was obtained in the material ratio of 40/60/30 and 50/50/30, while the lowest value was shown by briquettes with a ratio of 10/90/30, 60/40/30, and 90/10/30. From these results, it can be

analyzed that the high carbon content of ANS causes a high *RD* value. However, briquettes with a ratio of 10/90/30 show anomalies. This anomaly could be caused by various possibilities such as the error of the researcher in making measurements, the inaccuracy of measuring instruments, errors in drying briquettes, and so on.

ANS carbon could create high RD values because of lower moisture content. The lower moisture content resulted in a greater RD value [48]. However, our results show an anomaly in the results of TD/ANS/CN were 10/90/30. This can be caused by errors in the production process (pressure, temperature, etc.) [57].

The *RR* value of samples with composition ratios of 10/90/30 and 60/40/30 was the highest. Meanwhile, briquettes with the ratios of 40/60/30, 50/50/30, and 90/10/30 show a low *RR* value. The results are almost inversely proportional to the *RD* value. The greater *RD* value resulted in the *RR* value. The anomaly was shown by briquettes with a ratio of 90/10/30, which still had a low *RR* value even though it had a low *RD* value. This anomaly might be caused by briquettes with a ratio of 90/10/30, which had not dried completely during the drying process. But in general, the *RR* value indicated that the change in briquette density from wet to dry, and is relatively stable. The mean *RR* values ranged from 1.7 to 1.8. The range of these values is quite good. Other reports showed the *RR* values ranging from 1.8 to 2.25 using coconut coir, and the other is from 1.65 to 1.80 using rice straw [58].

Percentage moisture content (PMC). The *PMC* values ranging from 50 to 56% are shown in Figure 3 (b). The highest *PMC* value was obtained from briquettes with compositions of 50/50/30 and 60/40/30 and the lowest *PMC* values were obtained from briquettes with a composition of 10/90/30. A high *PMC* value indicates the high humidity of the briquette. High humidity will make the briquettes produce a lot of smoke when they are burned [59]. The higher content of ANS resulted in a lower *PMC*. The carbonization process on the ANS reduces the moisture of ANS [60].

Percentage of water resistance index (PWRI). The results of *PWRI* varied between 82 and 91% are shown in Fig. 3(b). The *PWRI* indicates the resistance of the briquette to the water. The good have high *PWRI*. Thus, they are not easily destroyed when absorbing water [61]. The lowest *PWRI* value was obtained at the raw material composition ratio of 60/40/30. The highest *PWRI* value was obtained at the raw material composition ratio of 90/10/30. The TD material caused the briquettes to have a high *PWRI*. The briquettes from TD have a low moisture content [3]. Low moisture content increases the resistance of briquettes to water [62]; therefore, the briquettes with a high TD concentration are more resistant to water.

Burning rate (BR). The results of *BR* shown in Fig. 3(c) ranged from 0.55 to 0.84 g/min. The highest value was indicated by the material ratio of 10/90/30 and the lowest value was indicated by the material ratio of 50/50/30. The *BR* value is affected by the density of the briquette. The denser briquette resulted in the longer briquettes running out when it is burned. This is due to the higher the briquette's compacting pressure and processing temperature caused to higher density and energy content per unit volume of briquettes [63].

Percentage of durability index (DI). Figure 3 (b) shows the *DI* value. The results of the study showed a good *DI* value, where the average was between 94.9 and 96.2%. The highest *DI* value was obtained from briquettes with TD/ANS/CN at the ratio of 40/60/30, while the lowest *DI* value was obtained at a ratio of 60/40/30. The briquettes with a higher ANS ratio showed a higher *DI* value than other briquettes because the ANS particle had a smaller surface area. This can be seen from the smaller ANS particles that make the higher density. The high density makes the briquettes not easily crushed. The high density of briquettes improves the handling properties and compressive strength of the briquettes [64].

Specific fuel consumption (SFC). Based on Figure 2 (d), the *SFC* value varied between 0.066 and 0.097 g/mL. Briquettes with a larger ANS composition showed a higher *SFC*. The lowest *SFC* value was obtained at the variation of the raw material composition ratio of

50/50/30. The best briquettes were found at a TD/ANS/CN ratio of 40/60/30. The *SFC* value shows the quantity of fuel needed to boil water. Therefore, the greater the *SFC* value resulted in the better quality of the briquettes.

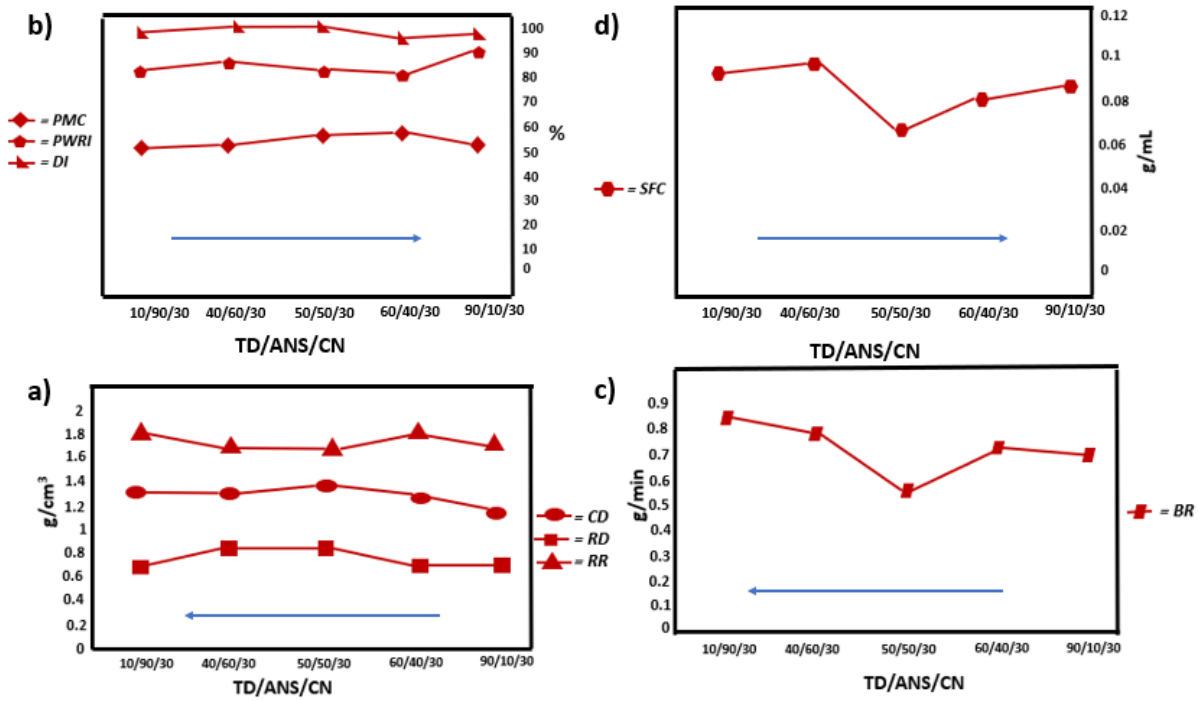

Fig. 2. Analysis composition variations on several parameters: (a) *CD, RD, RR*, (b) *PMC, PWRI, DI (c) BR*, and (d) *SFC*

Water boiling test (WBT). Table 3 shows the results of the water boiling test (*WBT*) on variations in the raw material composition of TD/ANS/CN. The water boiling test evaluates the efficiency of briquettes to increase the temperature [55]. The data obtained explains that the mix of TD/ANS/CN ingredients with a ratio of 50/50/30 maximizes the quality of the briquettes. The high ANS carbon content reduces the humidity of the briquettes so that moisture does not hinder the combustion process.

Table 3. Water boiling test (*WBT*) as a function of TD/ANS/CN ratio

TD/ANS/CN ratio	Burning time (min)	Initial temperature (°C)	Final temperature (°C)
10/90/30	5.57	27	86
40/60/30	6.29		85
50/50/30	6.01		88
60/40/30	5.52		84
90/10/30	6.15		85

Mechanical test. Figure 3 shows the results of the compressive test. The level of briquette hardness was expressed by the height of the curve peak (maximum force). The briquettes with varying particle sizes show the peak from low to high respectively indicated by the large, medium, and small size particles. The smaller the particle size made the briquettes harder. Briquettes with a small particle size have a high density because the bonds between the particles are tighter [65]. The addition of a tapioca starch binder also makes each particle of the material bind more strongly [66].

The curve peaks of the briquettes with variations in material composition (medium particle size) were scattered between the peaks of the large and small particles. However, the peak of the briquette curve with a composition of 10/90/30 looks higher than the peak of the briquette curve with medium size. This result is due to the effect of the high ANS content. ANS carbon could increase the hardness of the briquettes, making the briquettes stronger from collisions.

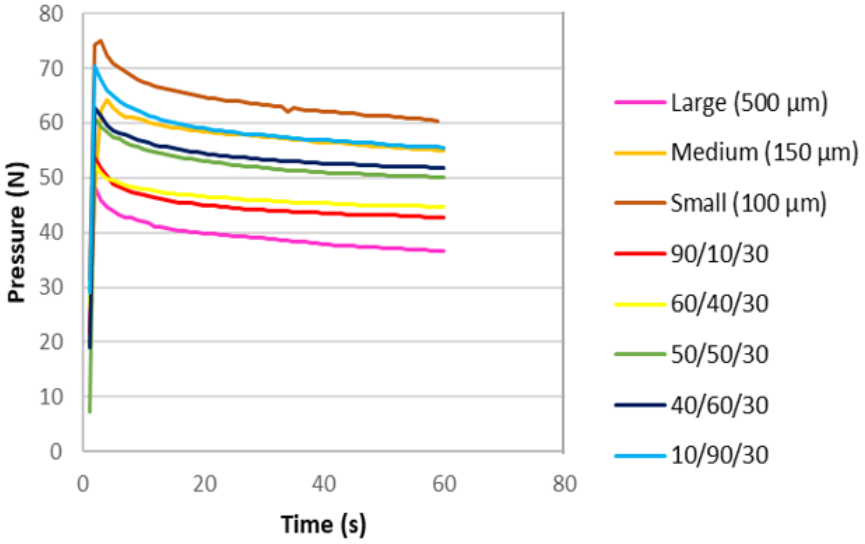

Fig. 3. Compressive test of all sample's briquettes

Table 4. Puncture test analysis results as a function of particle size and TD/ANS/CN ratio

No	Particle size (µm)			TD/ANS/CN ratio				
	500	150	100	90/10/30	60/40/30	50/50/30	40/60/30	10/90/30
1	95	65	30	70	73	60	57	45
2	92	73	34	78	69	67	53	45
3	95	64	45	74	74	66	61	40
4	92	70	43	72	73	72	56	42
5	92	66	35	78	74	69	61	45
average	93.20	67.60	37.40	74.40	72.60	66.80	57.60	43.40

Table 4 shows the results of the puncture test. The hard and compact briquettes make the needle more difficult to puncture so that the average puncture test result will be small. Conversely, briquettes that are not hard and porous make it easier for the needle to puncture the briquette so that the average puncture test result will be large. In line with the results of the compressive test, briquettes with large particles showed a large puncture test result, while the smaller the particle size indicated a smaller puncture test result. The results of the briquette puncture test with variations in the composition were spread between 37.40 and 93.20. This result was greater than the average result of briquettes with small particles' puncture test. It is smaller than the average result of briquettes with large particles' puncture test. This can occur because the briquettes with various material compositions were made with medium particle size. The level of hardness of briquettes was influenced by particle size, characteristics of the material, and compressive strength.

4. Conclusion

The effect of particle size and biomass ratio on the quality of briquettes obtained from TD, ANS, and CN has been investigated. The study has several novelties, which relate to the

improvement of briquettes' quality: (i) the evaluation of particle size of raw materials; (ii) effects of the composition of raw materials; (iii) combination of carbon and dried biomass; and (iv) the use of raw materials that are almost unused and typically disposed directly to the environment. The best briquettes are briquettes with small particles (100 μm) and TD/ANS/CN biomass ratios of 40/60/30 and 10/90/30. The briquettes will be better if the smaller the particle size and the more ANS ratio is used. The high ANS ratio makes the compressive strength high because the ANS particle has a smaller surface area. ANS which is smaller makes the resulting particle denser when compared to TD. This research is important because it utilizes biomass as an alternative fuel to reduce environmental pollution. The good quality briquettes were dense, having low moisture, good strength, and waterproof, as well as high heating value and low burning times.

References

1. Nizamuddin S, Baloch HA, Griffin GJ, Mubarak NM, Bhutto AW, Abro R, Mazari SA, Ali BS. An overview of effect of process parameters on hydrothermal carbonization of biomass. *Renewable and Sustainable Energy Reviews*. 2017;73: 1289-1299.
2. Dani S, Wibawa A. Challenges and policy for biomass energy in Indonesia. *International Journal of Business, Economics, and Law*. 2018;15(5): 41-47.
3. Indrawijaya B, Fathurrohman A, Nisa H. Pembuatan dan karakterisasi briket bahan bakar dari ampas tahu sebagai energi alternatif synthesis and characterization fuel briquettes from tofu dregs as alternative energy. *Jurnal Ilmiah Teknik Kimia*. 2018;2(1): 38-44.
4. Carnaje NP, Talagon RB, Peralta JP, Shah K, Paz-Ferreiro J. Development and characterisation of charcoal briquettes from water hyacinth (Eichhornia crassipes)-molasses blend. *PloS one*. 2018;13(11): e0207135.
5. Deepak K, Manujesh B, Vivek, Yashas B. Development and study of fuel briquettes from areca leaves: A potential renewable energy source. *AIP Conference Proceedings*. 2019;2080(1): 030004.
6. Suryaningsih S, Resitasari R, Nurhilal O Analysis of biomass briquettes based on carbonized rice husk and jatropha seed waste by using newspaper waste pulp as an adhesive material. *Journal of Physics: Conference Series*. 2019;1280(2): 022072
7. Aliyu M, Mohammed IS, Usman M, Dauda SM, Igbetua JI. Production of composite briquettes (orange peels and corn cobs) and determination of its fuel properties. *Agricultural Engineering International: CIGR Journal*. 2020;22(2): 133-144.
8. Nandiyanto ABD, Bustomi ATA, Sugiarti Y, Santiuly GC. The effect of electronic module utilization for biomass briquettes experiment using cocoa shells and sea mango to vocational school students. *Journal of Engineering Education Transformations*. 2020;34: 115-123.
9. Brunerová A, Roubík H, Brožek M, Van Dung D, Phung LD, Hasanudin U, Iryani DA, Herak D. Briquetting of sugarcane bagasse as a proper waste management technology in Vietnam. *Waste Management and Research*. 2020;38(11): 1239-1250.
10. Nandiyanto ABD, Rachmat LA, Rahayu DL, Azizah NN, Al Husaeni DF. Development of job sheet application in making biobriquette based on coconut (cocos nucifera) coir with variation of particle size and banana (musa paradisica) peels for vocational students. *Journal of Engineering Education Transformations*. 2020;34: 132-138.
11. Nandiyanto ABD, Rohman E, Handayani MN, Putri SR. E-Module in producing briquettes from melinjo (gnetum gnemon) shell with various particle sizes and binder concentrations for vocational school students. *Journal of Engineering Education Transformations*. 2020;34: 57-64.
12. Bot BV, Sosso OT, Tamba JG, Lekane E, Bikai J, Ndame MK. Preparation and characterization of biomass briquettes made from banana peels, sugarcane bagasse, coconut

shells and rattan waste. *Biomass Conversion and Biorefinery*. 2021. Available from: https://doi.org/10.1007/s13399-021-01762-w.
13. Anggraeni S, Putri SR, Nandiyanto ABD, Bilad MR. Effect of particle size and tapioca starch content on performance of the rice husk and red bean skin briquettes. *Journal of Engineering Science and Technology*. 2021;16(2): 1733-1745.
14. Wirabuana AD, Alwi RS. Influence of starch binders composition on properties of biomomass briquettes from durian peel (durio kutejensis becc). *AIP Conference Proceedings*. 2021;2349(1): 020020.
15. Anggraeni S, Hofifah S, Nandiyanto ABD, Bilad MR. Effects of particle size and composition of cassava peels and rice husk on the briquette performance. *Journal of Engineering Science and Technology*. 2021;16(1): 527-542.
16. Akolgo GA, Awafo EA, Essandoh EO, Owusu PA, Uba F, Adu-Poku KA. Assessment of the potential of charred briquettes of sawdust, rice and coconut husks: Using water boiling and user acceptability tests. *Scientific African*. 2021;12: e00789.
17. Anggraeni S, Nandiyanto ABD, Putri SR, Anshar AN, Maulana A, Nurazizah S, Nurjihan Z, Al-Obaidi ASM. Mechanical Properties of briquette by mixing rice and micrometer-sized carbon particles from potato and yam skins. *Journal of Engineering Research*. 2021;9(ASSEEE special issue): 1-15.
18. Velusamy S, Subbaiyan A, Kandasamy S, Shanmugamoorthi M, Thirumoorthy P. Combustion characteristics of biomass fuel briquettes from onion peels and tamarind shells. *Archives of Environmental & Occupational Health*. 2022;77(3): 251-262.
19. Anggraeni S, Girsang GCS, Nandiyanto ABD, Bilad MR. Effects of particle size and composition of sawdust/carbon from rice husk on the briquette performance. *J. Eng. Sci. Technol*. 2021;16(3): 2298-2311.
20. Nandiyanto ABD, Tahira AC, Anwar B, Maryanti R. The impact of teaching the effects of dextrin binder composition on bamboo fiber and dried clove leaves briquettes to high school students. *Journal of Engineering Education Transformations*. 2020;34: 65-74.
21. Nandiyanto ABD, Widiaputri SI, Maharani S, Ragadhita R. Job sheet learning media on briquette production from coffee grounds and soybean peel with various compositions and particle sizes for vocational high school students. *Journal of Engineering Education Transformations*. 2020;34: 139-146.
22. Nandiyanto ABD, Simbara AT, Mudzakir A, Maryanti R. Improving the learning process in producing bio-charcoal briquettes from durian peels/banana midrib with various particle sizes and composition to high school students. *Journal of Engineering Education Transformations*. 2020;34: 32-42.
23. Nandiyanto ABD, Tiyana R, Azizah DN, Hofifah SN. Demonstrating the biobriquettes production using variations in particle size and binder concentration using audio-visual to vocational students. *Journal of Engineering Education Transformations*. 2020;34: 87-94.
24. Triawan F, Nandiyanto ABD, Abdullah AG, Aziz M. Plasma nitriding time on the hardness and crystal structure/phase of SUS403 and SCS6 martensitic stainless steels: an analytical study. *Journal of Engineering Science and Technology*. 2018;13(8): 2369-2378.
25. Nandiyanto ABD, Triawan F, Firly R, Abdullah AG, Aono Y, Inaba K, Kishimoto K. Identification of micro-mechanical characteristics of monoclinic tungsten trioxide microparticles by nanoindentation technique. *Materials Physics and Mechanics*. 2019;42(3): 323-329.
26. Nandiyanto ABD. Crystallite Size on Micromechanical Characteristics of WO3 Microparticles. *Journal of Engineering Research*. 2021;9(3A): 268-277.
27. Nandiyanto ABD, Hofifah SN, Girsang GCS, Putri SR, Budiman BA, Triawan F, Al-Obaidi ASM. The effects of rice husk particles size as a reinforcement component on resin-based brake pad performance: From literature review on the use of agricultural waste as a

reinforcement material, chemical polymerization reaction of epoxy resin, to experiments. *Automotive Experiences*. 2021;4(2): 68-82.
28. Triawan F, Nandiyanto ABD, Suryani IO, Fiandini M, Budiman BA. The influence of turmeric microparticles amount on the mechanical and biodegradation properties of cornstarch-based bioplastic material: From bioplastic literature review to experiments. *Materials Physics and Mechanics*. 2020;46(1): 99-114.
29. Nandiyanto ABD, Fiandini M, Ragadhita R, Sukmafitri A, Salam H, Triawan F. Mechanical and biodegradation properties of cornstarch-based bioplastic material. *Materials Physics and Mechanics*. 2020;44(3): 380-391.
30. Anggraeni S, Nandiyanto ABD, Nurjami A, Hofifah SN, Putri SR, Girsang GC, Fiandini M. Palm oil and cinnamon (anti-microbial agent) on the physicochemical, mechanical, and biodegradation properties of micrometer-sized cornstarch-based bioplastic. *Moroccan Journal of Chemistry*. 2021;9(3): 2446-2453.
31. Anggraeni S, Hotimah AP, Girsang GCS, Ragadhita R, Hofifah SN, Nandiyanto ABD. Teaching the Effect of Flour on Mechanical Properties of Shrimp Shell Crackers 'Kerupuk'to High School Students. *Journal of Engineering Education Transformations*. 2020;34: 75-80.
32. Ragadhita R, Nandiyanto ABD. How to calculate adsorption isotherms of particles using two-parameter monolayer adsorption models and equations. *Indonesian Journal of Science and Technology*. 2021;6(1): 205-234.
33. Yolanda YD, Nandiyanto ABD. How to read and calculate diameter size from electron microscopy images. *ASEAN Journal of Science and Engineering Education*. 2022;2(1): 11-36.
34. Nandiyanto ABD, Oktiani R, Ragadhita R. How to read and interpret FTIR spectroscope of organic material. *Indonesian Journal of Science and Technology*. 2019;4(1): 97-118.
35. Fatimah S, Ragadhita R, Al Husaeni DF, Nandiyanto ABD. How to calculate crystallite size from x-ray diffraction (XRD) using Scherrer method. *ASEAN Journal of Science and Engineering*. 2022;2(1): 65-76.
36. Al Husaeni DF, Nandiyanto ABD. Bibliometric using Vosviewer with Publish or Perish (using google scholar data): From step-by-step processing for users to the practical examples in the analysis of digital learning articles in pre and post Covid-19 pandemic. *ASEAN Journal of Science and Engineering*. 2022;2(1): 19-46.
37. Ismanto SD, Murtius WS. Characteristics of chicken sausage treated with using tofu dregs waste. *International Journal on Advanced Science, Engineering and Information Technology*. 2013;3(4): 318-321.
38. Sari LM, Hakim RF, Mubarak Z, Andriyanto A. Analysis of phenolic compounds and immunomodulatory activity of areca nut extract from Aceh, Indonesia, against Staphylococcus aureus infection in Sprague-Dawley rats. *Veterinary World*. 2020;13(1): 134.
39. Kusumaningrum HP, Zainuri M, Endrawati H, Purbajanti ED. Characterization of citronella grass essential oil of Cymbopogon winterianus from Batang region, Indonesia. *Journal of Physics: Conference Series*. 2020;1524(1): 012057.
40. Murni S, Pujiastuti SS, Octoria D. Improving the production quality of atsiri oil industry through the introduction of equipment and diversification of raw materials. *Review of Integrative Business and Economics Research*. 2017;6: 32.
41. Helwani Z, Ramli M, Rusyana A, Marlina M, Fatra W, Idroes GM, Suhendra R, Ashwie V, Mahlia TMI, Idroes R. Alternative briquette material made from palm stem biomass mediated by glycerol crude of biodiesel byproducts as a natural adhesive. *Processes*. 2020;8(7): 777.
42. Seo MW, Jeong HM, Lee WJ, Yoon SJ, Ra HW, Kim YK, Lee D, Han SW, Kim SD, Lee JG. Carbonization characteristics of biomass/coking coal blends for the application of bio-coke. *Chemical Engineering Journal*. 2020;394: 124943.

43. Nandiyanto ABD, Andika R, Aziz M, Riza LS. Working volume and milling time on the product size/morphology, product yield, and electricity consumption in the ball-milling process of organic material. *Indonesian Journal of Science and Technology*. 2018;3(2): 82-94.
44. Sotannde OA, Oluyege AO, Abah GB. Physical and combustion properties of charcoal briquettes from neem wood residues. *International Agrophysics*. 2010;24(2): 189-194.
45. Singh RN. Equilibrium moisture content of biomass briquettes. *Biomass and Bioenergy*. 2004;26(3): 251-253.
46. Onuegbu TU, Ekpunobi UE, Ogbu IM, Ekeoma MO, Obumselu FO. Comparative studies of ignition time and water boiling test of coal and biomass briquettes blend. *IJRRAS*. 2011;7(2): 153-159.
47. Rajaseenivasan T, Srinivasan V, Qadir GSM, Srithar K. An investigation on the performance of sawdust briquette blending with neem powder. *Alexandria Engineering Journal*. 2016;55(3): 2833-2838.
48. Bello RS, Onilude MA. Physico-mechanical characteristics of high density briquettes produced from composite sawdust. *Journal of Applied Sciences and Environmental Management*. 2020;24(5): 779-787.
49. Mitchual SJ, Frimpong-Mensah K, Darkwa NA. Effect of species, particle size and compacting pressure on relaxed density and compressive strength of fuel briquettes. *International Journal of Energy and Environmental Engineering*. 2013;4(1): 1-6.
50. Zhang G, Sun Y, Xu Y. Review of briquette binders and briquetting mechanism. *Renewable and Sustainable Energy Reviews*. 2018;82: 477-487.
51. Fiandini M, Ragadhita R, Nandiyanto ABD, Nugraha WC. Adsorption characteristics of submicron porous carbon particles prepared from rice husk. *Journal of Engineering, Science and Technology*. 2020;15: 022-031.
52. Zhang J, Guo Y. Physical properties of solid fuel briquettes made from Caragana korshinskii Kom. *Powder Technology*. 2014;256: 293-299.
53. Davies RM, Abolude DS. Ignition and burning rate of water hyacinth briquettes. *Journal of Scientific Research and Reports*. 2013;2(1): 111-120.
54. Kongprasert N, Wangphanich P, Jutilarptavorn A. Charcoal briquettes from madan wood waste as an alternative energy in Thailand. *Procedia Manufacturing*. 2019;30: 128-135.
55. Sawadogo M, Tanoh ST, Sidibé S, Kpai N, Tankoano I. Cleaner production in Burkina Faso: Case study of fuel briquettes made from cashew industry waste. *Journal of Cleaner Production*. 2018;195: 1047-1056.
56. Rahmawati S, Sakung J, Fudholi A, Sushmita L. The utilization of corncob for the manufacture of charcoal briquette as an alternative fuel. *Journal of Physics: Conference Series*. 2020;1563(1): 012022.
57. Nakashima GT, Martins MP, Hansted ALS, Yamamoto H, Yamaji FM. Sugarcane trash for energy purposes: Storage time and particle size can improve the quality of biomass for fuel? *Industrial Crops and Products*. 2017;108: 641-648.
58. Oladeji JT, Enweremadu CC. The effects of some processing parameters on physical and densification characteristics of corncob briquettes. *International Journal of Energy Engineering*. 2012;2(1): 22-27.
59. Aransiola EF, Oyewusi TF, Osunbitan JA, Ogunjimi LAO. Effect of binder type, binder concentration and compacting pressure on some physical properties of carbonized corncob briquette. *Energy Reports*. 2019;5: 909-918.
60. Nazari MM, Idroas MY, Ayuni FA. Carbonization effect on EFB briquettes prepared with different type of binders. *IOP Conference Series: Earth and Environmental Science*. 2020;476(1): 012072.
61. Zanjani NG, Moghaddam AZ, Dorosti S. Physical and chemical properties of coal briquettes from biomass-bituminous blends. *Petroleum and Coal*. 2014;56(2): 188-195.

62. Yaman S, SahanŞahan M, Haykiri-Acma H, Şeşen K, Küçükbayrak S. Fuel briquettes from biomass–lignite blends. *Fuel Processing Technology*. 2001;72(1): 1-8.
63. Olugbade T, Ojo O, Mohammed T. Influence of binders on combustion properties of biomass briquettes: a recent review. *BioEnergy Research*. 2019;12(2): 241-259.
64. Hamid MF, Idroas MY, Ishak MZ, Zainal Alauddin ZA, Miskam MA, Abdullah MK. An experimental study of briquetting process of torrefied rubber seed kernel and palm oil shell. *BioMed Research International*. 2016;2016(1): 1-11.
65. Igbo KP. Physico-mechanical characteristics of rice husk briquettes using different binders. *Agricultural Engineering International: CIGR Journal*. 2016;18(1): 70-81.
66. Akogun OA, Waheed MA, Ismaila SO, Dairo OU. Co-briquetting characteristics of cassava peel with sawdust at different torrefaction pretreatment conditions. *Energy Sources, Part A: Recovery, Utilization, and Environmental Effects*. 2020;10: 1-19.

THE AUTHORS

A.B.D. Nandiyanto
e-mail: nandiyanto@upi.edu
ORCID: 0000-0002-9753-1267

S.N. Hofifah
e-mail: sitinurhofifah@upi.edu
ORCID: -

S. Anggraeni
e-mail: anggraeni_said@upi.edu
ORCID: -

N.Z. Latifah
e-mail: nurzahralatifah@upi.edu
ORCID: -

J.E. Sitanggang
e-mail: juliaelisabeth@upi.edu
ORCID: -

O. Sopian
e-mail: opisopian@upi.edu
ORCID: -

Z. Saputra
e-mail: ziyansaputra@upi.edu
ORCID: -

Materials Physics and Mechanics. 2022;50(1): 37-55
Research article
http://dx.doi.org/10.18149/MPM.5012022_3

Submitted: March 10, 2022
Approved: May 18, 2022
Accepted: August 4, 2022

The effect of mangosteen peel compositions as reinforcement components on resin-based brake pad performance with computational bibliometric mapping analysis

Asep Bayu Dani Nandiyanto[1]✉, Dwi Fitria Al Husaeni[2], Risti Ragadhita[1], Meli Fiandini[3], Karina Mulya Rizky[1], Dwi Novia Al Husaeni[2]

[1]Departemen Kimia, Universitas Pendidikan Indonesia, Indonesia

[2]Departemen Pendidikan Ilmu Komputer, Universitas Pendidikan Indonesia, Indonesia

[3]Departemen Pendidikan Kimia, Universitas Pendidikan Indonesia, Indonesia

✉ nandiyanto@upi.edu

Abstract. This study aims to determine the effect of differences in the composition of mangosteen peels mangosteen peel particles as a reinforcing component in resin-based brake pads. The manufacture of a brake pad is done by mixing mangosteen peel particles with resin (bisphenol A-epichlorohydrin, and cyclo aliphatic amine (1:1 ratio). Mangosteen rind has a high carbon fiber content as a reinforcing material. Mangosteen rind particles, liquid resin, and hardener were mixed in various ratios of 10:5:5 (MA), 8:5:5 (MB), 6:5:5 (MC), and 4:5:5 (MD). The physical properties and mechanical properties were investigated. The results showed that the friction coefficient of the brake pads made from MA, MB, and MC were 0.69×10^{-5}, 0.68×10^{-5}, and 0.67×10^{-5}, respectively. MD specimens do not allow friction tests due to their highly elastic properties. MA has the lowest wear rate of 0.64, the maximum friction coefficient of 0.69, and the highest hardness level based on mechanical tests. MA specimens have the best ratio of resin to mangosteen peel mixture. This is because, the more the number of mangosteen rind particles used, the harder the brake pads will be. Materials with higher hardness have less mass loss and a higher coefficient of friction. The completion of the research shows that mangosteen peel has a high enough effect as an environmentally friendly brake pads reinforcement material.

Keywords: agricultural waste, brake pad, mangosteen peel, resin-based brake pad

Acknowledgements*. This study acknowledged RISTEK DIKTI for Grant-in-aid Penelitian Terapan Unggulan Perguruan Tinggi (PTUPT), and Bangdos Universitas Pendidikan Indonesia.*

Citation: Nandiyanto ABD, Al Husaeni DF, Ragadhita R, Fiandini M, Rizky KM, Al Husaeni DN. The effect of mangosteen peel compositions as reinforcement components on resin-based brake pad performance with computational bibliometric mapping analysis. *Materials Physics and Mechanics*. 2022;50(1): 37-55. DOI: 10.18149/MPM.5012022_3.

1. Introduction

The brake system is a mechanism to slow down the speed of a vehicle so that the speed of the vehicle can be controlled [1]. One of the brake systems used is brake pads. Brake pads are one of the most important parts of a vehicle. The working principle of brake pads is to convert kinetic energy into heat by rubbing the disc with the brake pads when the two components are in contact [2] When the vehicle is traveling at high speed, brake pads play a very important role because it supports the safety of the driver and passengers.

The friction material is an important component of brake pads in addition to fasteners, fillers, and reinforcing elements. Friction materials play an important role in brake-bearing properties such as fade resistance, friction coefficient management, and porosity reduction. The composition of brake pad material generally consists of 60% asbestos, causing environmental pollution problems and health problems [3]. Asbestos-based brake pads are widely sold commercially at low prices and guarantee the durability of the brake pads. However, the friction of the powder in the form of small particles is very dangerous for human health because of the asbestos content. The use of asbestos is avoided because of its carcinogenic properties [4]. Therefore, brake pads supported by asbestos-free materials should be avoided.

One way to replace the asbestos material is to make brake pads from organic materials. There have been many studies on resin-based brake pads by mixing them with organic materials, including resin-based brake pads from rice husks [5], corn husks [6], snail shell and rubber seed husks [7], banana fiber [8], cocoa beans shells [3], palm kernels [9], and banana peels [4,8]. However, there are no studies on resin-based brake pads that discuss the manufacture of resin-based brake pads from mangosteen peel.

Table 1 shows previous studies in more detail regarding the manufacture of brake pads using organic materials, especially agricultural waste as reinforcement components. Table 1 presents some data including the types of agricultural waste, supporting components, and the results obtained from the research. These studies show significant results which means that agricultural waste has great potential to replace inorganic materials for brake pads.

Table 1. Previous research in the preparation of brake pads used agricultural waste as a reinforcement component

No.	Type of Agricultural Waste	Supporting Component	Results	Refs
1.	Palm kernel shell (PKS)	Cow bone, Expoxy Resin, and Hardener	PKS has a hardness value of 55.7 HRB each. PKS has a water absorption rate of 5.05%. PKS oil absorption is 2.23%. The VFD has a friction coefficient of 0.735. VFD has a crushing strength of 23 N/mm^2. Low density, strong impact strength, low hardness value, low water resistance, and low oil resistance all contribute to the increase in the PKS particle size.	[10]
2.	Coconut shell	Coconut shell powder, cast	The higher the percentage of grounded coconut powder the lower	[11]

No.	Type of Agricultural Waste	Supporting Component	Results	Refs
		iron filings, silica, and epoxy (liquid resin).	the breaking strength, impact, hardness, compressive strength, and vice-versa respectively. Thus, a high percentage of grounded coconut powder induces brittleness.	
3.	Banana peels	phenolic resin (phenol-formaldehyde)	In the production of brake pads, banana peel particles can efficiently substitute asbestos.	[4]
4.	Lemon peels	Calcium hydroxide, epoxies, aluminum oxides, graphite, iron oxides, and calcium hydroxide	Brake Pads lemon peels have 1.55–2.00 g/cm^3, hardness 26–32 (Barcol hardness), percentage wear loss of 13.45–19.14%, percentage water loss of 0.96–1.38%, and an oil absorption of 0.01-0.02% are obtained, which is superior to commercial brake pads.	[12]
5.	Risk Husk	Bisphenol A-epichlorohydrin and cyclo aliphatic amine	The inter-packing distance, interfacial bonding, and thermal softening of the rice husk resin-particle matrix are all affected by particle size. The brake pads' compressive strength is increased by small particles. Reduced pore formation, less mass loss, improved wear rates, a greater coefficient of friction, and a rougher brake pad surface are all benefits of reducing particle size.	[5]
6.	Durian Peels	Banana midribs	The findings of the comparison between commercially available brake pads show that agricultural waste has the potential to replace friction components in brake pads. The hardness, wear, and friction coefficient of a brake pad using durian peels are the highest.	[13]
7.	Palm Ash	PCB waste, phenolic resin, and aluminum.	The higher the palm ash content, the better the wear and mechanical qualities. The wear qualities of palm ash brake pads are equivalent to	[14]

No.	Type of Agricultural Waste	Supporting Component	Results	Refs
			those of conventional brake pads.	
8.	Groundnut shell	Phenolic resin	Increases in groundnut shell density, compressive strength, and oil absorption are all attributed to increased oil absorption, water absorption, and density. The compressive strength was increased by using large groundnut shell particles.	[15]
9.	Corn Husks	Phenolic Resin (Phenol-Formaldehyde), Silicon Carbide, Steel Dust, Graphite, and Corn Husk	Brake pads with corn husks provide better compressive strength, higher hardness, lower porosity, and lower wear rates. Corn husks can be used in the production of asbestos-free brake pads according to the ratio of commercial brake pad yields	[16]
10.	Sawdust	Slag waste, resin, epoxy, graphite, and silicon carbide.	The addition of sawdust has an impact on the level of wear and degradability of the brake pad. Sawdust brake pads have high ash content, low density, low compressive strength, and high levels of degradability/wear.	[17]

Mangosteen peel has a fairly high carbon content, as do coconut shell and corn cob, which is around 48.81%. In addition, mangosteen peel has a higher carbon fiber content than coconut shell and corn cob. This carbon fiber content indicates the maximum amount of carbon that can be produced from biomass after the pyrolysis process. The high amount of carbon fiber is due to the fact that biomass has a fairly high lignin content. As is well known, one of the materials for making brake pads is carbon fiber [18]. Carbon fiber was chosen because it is very strong and heat resistant, considering the friction that occurs in commercial motorcycle brake pads, which is 150˚C-250°C [19]. Mangosteen peel has a fixed carbon content of 26.60% and carbon of 48.81% [20], which is considered suitable to be used as a material for making brake pads.

Therefore, this study was conducted to analyze the use of mangosteen peel as a material for making brake pads. This study aims to determine the effect of differences in the composition of mangosteen peels as a fiber reinforcement component on the performance of resin-based brake pads. The novelty of this research is the use of mangosteen peels as reinforcement for the manufacture of resin-based brake pads. The completion of this research is expected to reduce the use of brake pads made of asbestos which is dangerous and the increasing use of brake pads made of organic materials.

2. Method

The research was carried out in several stages, each stage of the research carried out is shown in Fig. 1. The research was conducted in 3 core stages, namely brake pad production, computational bibliometric mapping analysis, and test of brake pads. The brake pads that have been made are tested in several types of tests, namely physical, mechanical, and chemical properties tests.

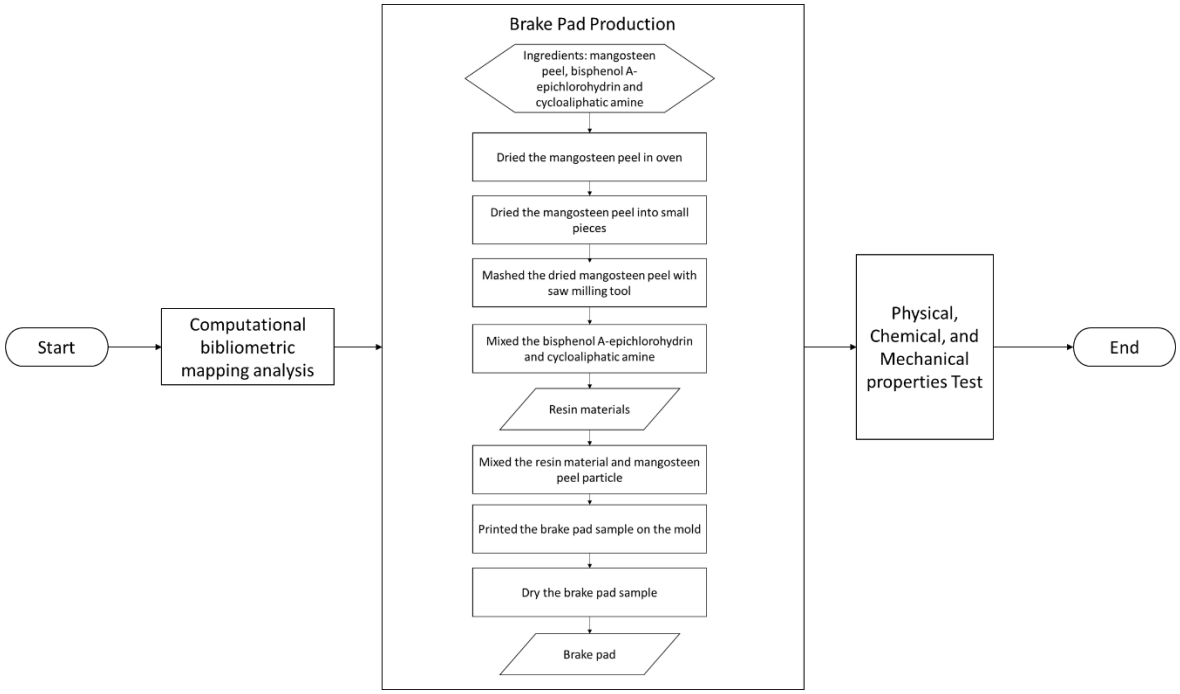

Fig. 1. Flow chart of research stages

Brake pad production. The brake pads are made from mangosteen peel from Subang, Indonesia. The mangosteen peel that had been collected was then dried in an oven (Kirin Griya Indotama, Indonesia) at a temperature of 150°C. The time needed to dry the mangosteen peel was 2 hours. The dried mangosteen peel is then cut into small pieces and mashed using a sawmilling tool. Therefore, the specific particle size required is obtained. After being mashed, the mangosteen peel powder was added to a sieve shaker (Niaga Kusuma Lestari, Indonesia). After the mangosteen peel particle has been prepared, the next step is to make a brake pad.

The brake pad is made from a mixture of mangosteen peel particles and resin material. The resin materials used are bisphenol A-epichlorohydrin (as a binder) and cyclo aliphatic amine (as a hardener). The two resin materials were mixed evenly in a ratio of 1:1. Particles of mangosteen peel, Bisphenol A-epichlorohydrin, and cyclo aliphatic amine were then mixed in various ratios, namely 10:5:5 (MA), 8:5:5 (MB), 6:5:5 (MC), and 4:5: 5 (MD). The choice of composition ratio was due to referring to our previous study [13]. After that, the brake pad samples went through a printing process and drying process for 5 days at room temperature and pressure. The brake pad as a model object has a size of 1×1×1 cm based on the size of the silicone mold used.

Physical, chemical, and mechanical properties test. The particle size and shape of the raw material (BPP and ES particles), as well as the outer surface and inner surface of the brake pad samples, were investigated using a digital microscope. Fourier transform infrared is used for chemical characterization to assess elemental structure products (FTIR, FTIR-6600, Jasco Corp., Japan). Meanwhile, the mechanical characterization consists of the following:

Compressive and puncture strength. A Screw Mount Test equipment (Model I ALX-J, China) with a digital force measurement instrument was used to perform the compression test (Model HP-500, Serial Number H5001909262). The brake pads were subjected to a constant displacement rate of 2.6 mm/min during the test. At the same time, the compressive force is recorded, resulting in a curve that depicts the texture profile. The compressive strength is then calculated using the maximum point of the compressive stress-strain curve. Furthermore, the highest applied force (in Newtons (N)) is utilized to determine the sample's hardness during the test. The Shore Durometer instrument (Shore A Hardness, in size, China) was used in the puncture strength test process. The hardness scale used in the tool is 0 to 100. Density can be calculated using Equation (1):

$$\rho = \frac{m}{v}. \quad (1)$$

In the process of recording, the results of the puncture test are stored in a C language program with the algorithm (see Fig. 2), and an example of the program output is shown in Fig. 3 (a, b).

```c
#include <stdio.h>
#include <string.h>
#include <math.h>

typedef struct punctureStrength {
    char sampel[255];
    int resulOfPuctureStrength[40];
    double averange;
} punctureStrength;

int main() {
    int totalVarious, i, j, totalTestPunctureStrength, count = 0;
    double average;

    printf("Input total various composition of sample : ");scanf("%d", &totalVarious);
    punctureStrength variousComposition[totalVarious];

    printf("Input total test puncture strength : ");scanf("%d", &totalTestPunctureStrength);

    for (i = 0; i < totalVarious; i++) {
        printf("Input name of sample : ");
        fflush(stdin);
        gets(variousComposition[i].sampel);
        for (j = 0; j < totalTestPunctureStrength; j++) {
            printf("Input result %d: ", j+1);
            scanf("%d", &variousComposition[i].resulOfPuctureStrength[j]);
            printf("\n");
        }
        printf("\n");
    }
    //count of average
    for (i = 0; i < totalVarious; i++) {
        for (j = 0; j < totalTestPunctureStrength; j++) {
            count = count+variousComposition[i].resulOfPuctureStrength[j];
        }
        average = (double) count/totalTestPunctureStrength;
        variousComposition[i].averange = average;
        count = 0;
    }

    //result of average

    for (i=0; i < totalVarious; i++) {
        printf("Sampel name : %s\n", variousComposition[i].sampel);
        printf("Averange pucture strength %s: %lf\n", variousComposition[i].sampel, variousComposition[i].averange);
    }

    return 0;
}
```

Fig. 2. Puncture strength test calculation algorithm

```
Input name of sample : MD
Input result 1: 95

Input result 2: 95

Input result 3: 95

Input result 4: 99

Input result 5: 96

Input result 6: 98

Input result 7: 98

Input result 8: 95

Input result 9: 98

Input result 10: 99
```

(a) Input program

```
Sampel name : MA
Averange pucture strength MA: 92.600000
Sampel name : MB
Averange pucture strength MB: 93.100000
Sampel name : MC
Averange pucture strength MC: 96.500000
Sampel name : MD
Averange pucture strength MD: 96.800000
```

(b) Output program

Fig. 3. The results of the calculation of the puncture strength test with the C program

Specific gravity. The Archimedes principle was used to conduct the density test. The sample's weight is first determined in the open air. Weighing took place after the test object had been submerged in water for 48 hours. The difference in weight determines the density of the sample. The formula for calculating density is Equation (2).

$$Density = \frac{W_o}{W_o - W_1} \times 1000 \ (\frac{kg}{m^3}), \quad (2)$$

where W_o is weight in the air (g) and W_t is weight in water (g).

Water absorption rate. A 24-hour water test was used to examine the specimens' water adsorption behavior. The dried sample weights were measured after a 24-hour soaking at room temperature. The specimens were weighed after the extra tear was drained. Equation (3) was used to obtain the absorption percentage.

$$Absorption\ (\%) = \frac{M_1 - M_0}{M_0} \times 100, \quad (3)$$

where M_1 is mass after immersion and M_0 is mass before immersion.

Friction test. Before friction testing, the brake pad was polished to eliminate the resin layers on the surface. The friction of the brake pad was tested by sliding it against sandpaper (80 grit; Dae Sung CC-80Cw) with a mass load of 9 kg at a speed of 25 cm/s for 20 minutes. Every two minutes, the weight of the brake pads was measured. The wear rate was calculated using Equation (4).

$$Wear\ Rate\ (M) = \frac{(M_a - M_b)}{t \times a}, \quad (4)$$

where M_a is the initial weight of the brake pad (g), M_b is the final weight of the brake pad (g), t is time (s), and a is the friction cross-section area (mm^2).

The friction coefficient (μ) was the ratio of friction force (f; Newton) to applied force (N; Newton) that is shown in Equation (5).

$$\mu = \frac{f}{N}. \quad (5)$$

3. Result and discussion

Computational literature with mapping analysis on mangosteen peel research. Before this research, we conducted a literature study on related research. We analyzed research on the use of mangosteen peel. Research data was collected through publishing or perish 7 which was taken from the google scholar database. All articles taken were articles published in google scholar indexed journals from 2012 to 2021 by specifying the keyword "Mangosteen Peel". This literature study was conducted to seek new research on mangosteen peel.

Research on the use of mangosteen peel is still relatively small, namely over 10 years (2012-2021), and there are a total of 91 publications. Figure 4 shows the development of mangosteen peel research from 2012 to 2021. The highest number of mangosteen peel studies occurred in 2019 and 2021 with a total of 14 publications. In 2012 there were only 7 studies and it decreased drastically in 2013 when there were 2 publications in one year. In 2014 there was an increase in publications, namely 8 publications. In 2015-2018 research on mangosteen peel experienced a high enough increase to reach 14 publications. However, in 2019-2020, it decreased again, namely 11 publications and in 2021 it increased to 14 publications.

In previous studies on mangosteen peel, it is known that research on mangosteen peel has several interrelated terms, namely peel powder, mangosteen extract, antioxidant activity, gel, adsorbent, removal, and carbon, as shown in Fig. 5 regarding network visualization [21]. These interrelated terms indicate with what terms the mangosteen peel research is carried out so that we can look for other terms that can be related to the mangosteen peel research [22].

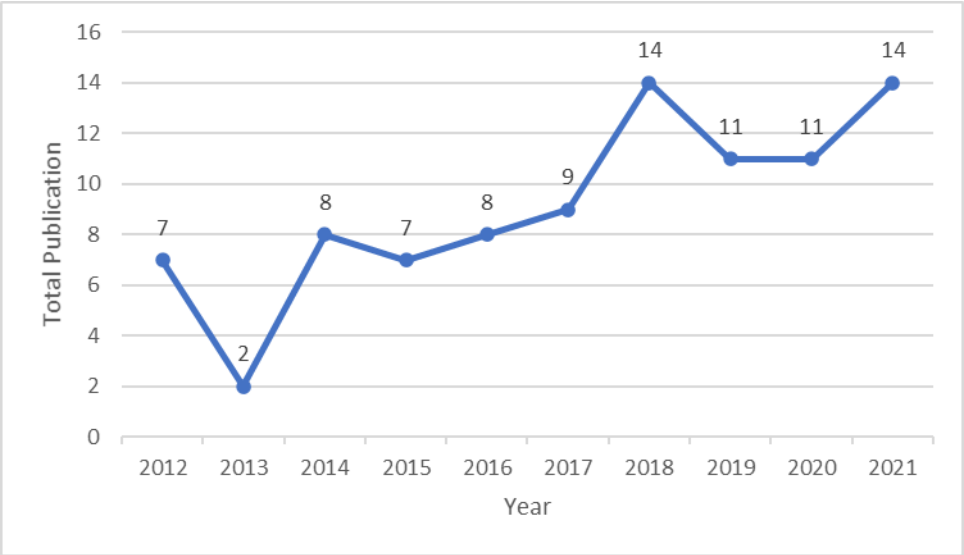

Fig. 4. The development of research on the use of mangosteen peel in the last 10 years (2012-2021)

Figure 6 shows the density visualization in a study on mangosteen peel. The brighter the yellow color in the term circle, the more research on that term is carried out [23]. Figure 6 shows that mangosteen peel is the most widely used as mangosteen peel extract, followed by research on mangosteen peel as carbon. Figure 7 clarifies the number of terms found when the computational mapping analysis is carried out. Based on Fig. 7, it is known that 11 types of mangosteen peel utilization have been carried out in previous studies, namely peel powder, adsorbent, antioxidant activity, mangosteen peel powder, gel, antioxidant, removal, activated carbon, carbon, extract, and mangosteen peel extract. The use of mangosteen peel as mangosteen peel extract was found the most, namely 13 times, followed by carbon base material, which was 6 times, and the least research that discussed the use of mangosteen peel as peel powder was only 3 times.

From the results of computational literature analysis using the mapping visualization technique of research data from 2012-2021 published in google scholar indexed journals, it is known that research on the use of mangosteen peel as a reinforcing fiber material for the manufacture of resin-based brake pads has not been carried out. Therefore, this study has a fairly large novelty value. This is because one of the benefits of mapping analysis research is to find out the novelty of a study [24].

Fig. 5. Network visualization of mangosteen peel research

Fig. 6. Density visualization research on mangosteen peel

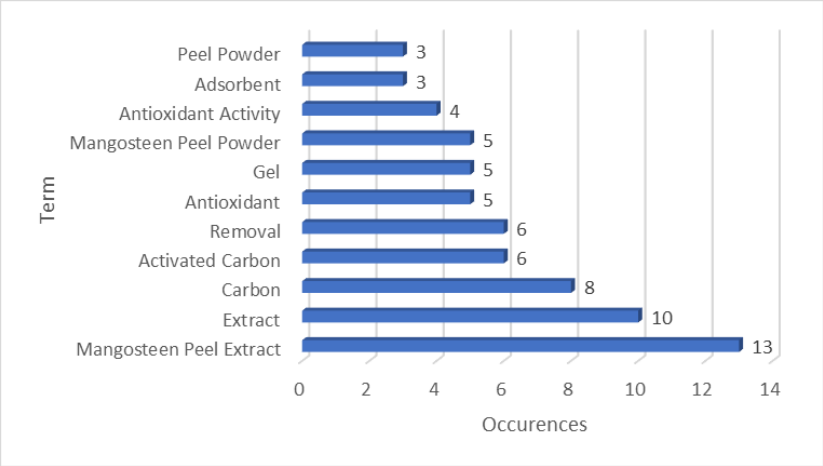

Fig. 7. Utilization of mangosteen peel in the previous studies

Figure 8 depicts a resin-based brake pad research visualization network. According to Fig. 8, resin-based brake pad research is often associated with terminology like bearing materials, bearing development, and epoxy resin as the most extensively used material in the fabrication of resin-based brake pads [25]. These terms explain the process of researching resin-based brake pads. This enabled us to explore more terms relating to resin-based brake pad research. Figure 9 shows the phrases epoxy resin and pad material, which are related to research on resin-based brake pads with the greatest number of densities [25].

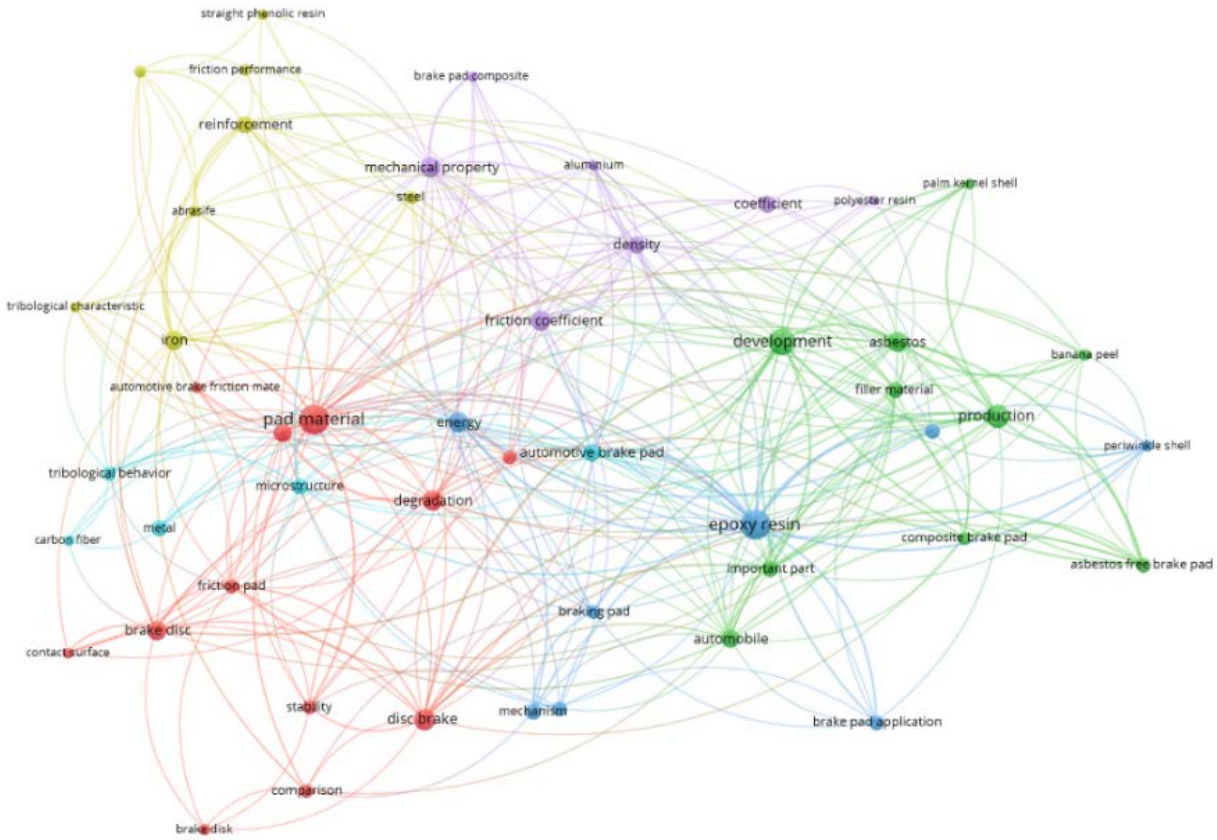

Fig. 8. Network visualization of resin-based brake pad (adopted from Nandiyanto et al. [25])

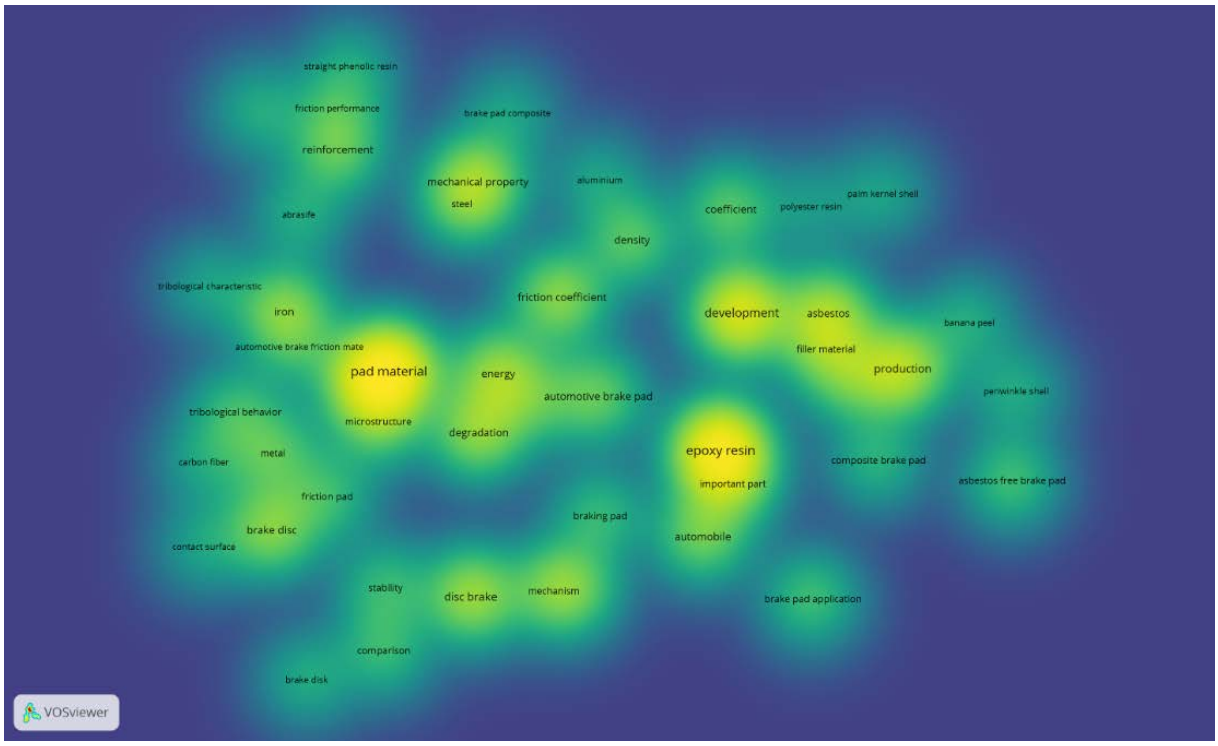

Fig. 9. Density visualization of resin-based brake pad (adopted from Nandiyanto et al. [25])

Figure 10 shows the FTIR analysis. The FTIR was then compared to the literature regarding FTIR spectrum data for organic component [26] and the application of resin as brake pad [27]. The presence of an absorption band in the wavelength of 2871 cm^{-1} is symmetric stretching vibrations of methyl (CH_3). The absorption band in the wavelength range of 1760 – 1741 cm^{-1} is a stretching vibration of the unconjugated carbonyl (C=O) group. The absorption band at 1690 cm^{-1} is the stretching vibration of conjugated carbonyl (C=O). Absorption band in the wavenumber's range of 1654 – 1523 cm^{-1} that is C=C. CH_2-bending is shown in wavenumbers 1409 cm^{-1} dan CH_3- bending is presented on wavenumbers 1367-1322 cm^{-1}. In the range, 1278 – 1046 cm^{-1} of the absorption band is stretching vibration of C-O. Wavenumber 1011 cm^{-1} is C-OH stretching. The absorption band of the component at 908 cm^{-1} is functional groups -HC=CH-(*trans)* out of the plane, 772 cm^{-1} is -HC=CH-(*cis*) out of the plane, and wavenumbers at 677 cm^{-1} is $–(CH_2)_n$; -HC=CH- bending [28]. The presence of an epoxy group is indicated by a peak in the 950 to 860 cm^{-1} range [30]. Spectrum mangosteen peel in Fig. 10a had no absorption at 950-860 cm^{-1} because it was not prepared using resin.

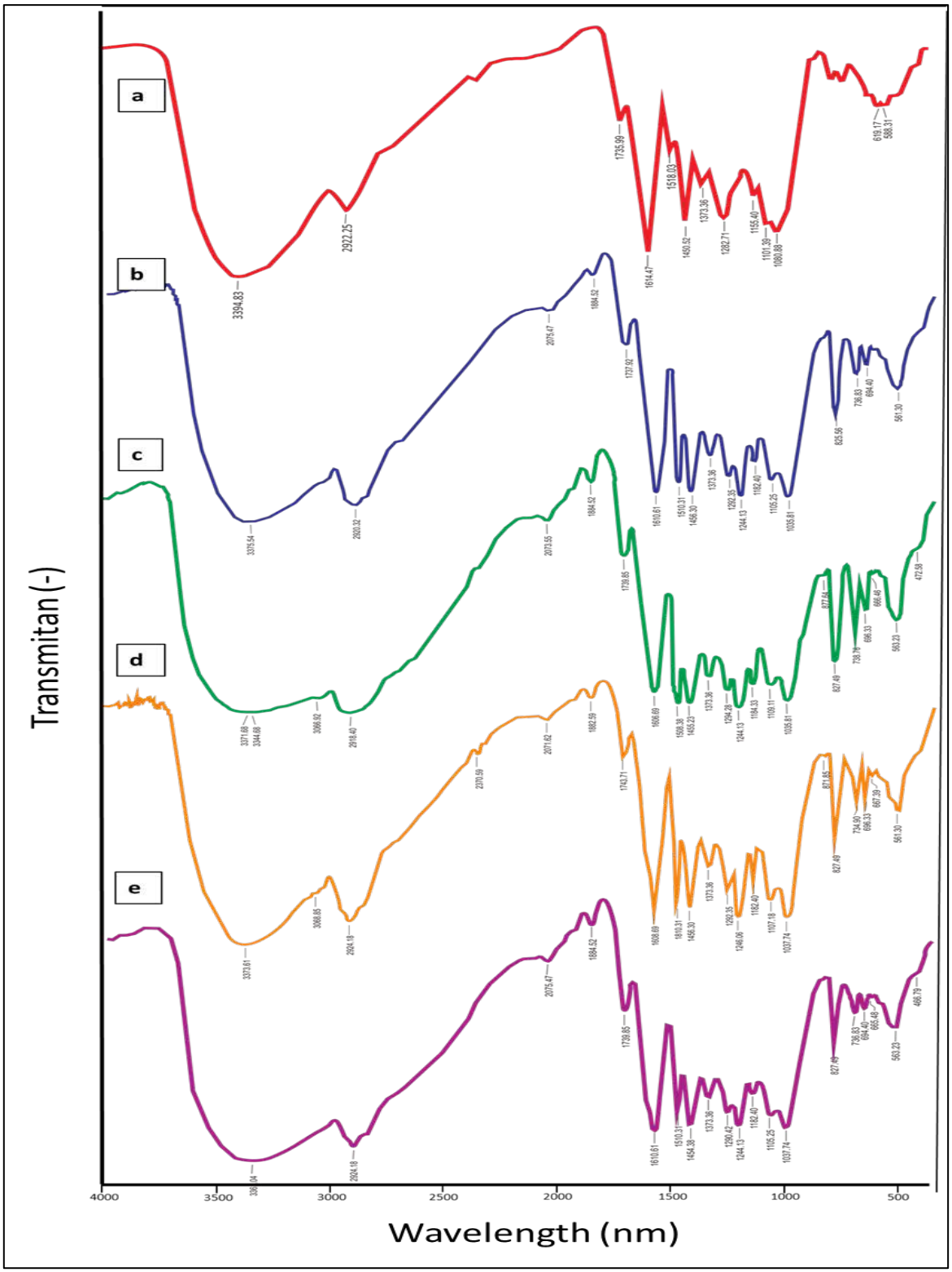

Fig. 10. FTIR spectrum of fabricated brake pad from a) mangosteen peels; b)MA; c)MB; d) MC; and e) MD

Figure 11a shows a microscopic image of mangosteen peel particles. The mangosteen peel particles show an inhomogeneous particle size (see Fig. 11a). Ferret analysis was used to perform the particle size analysis of mangosteen peel as shown in Fig. 11b. Figure 11b shows the results of Feret's analysis, where the mangosteen peel particle size is in the range of 100-500 μm with an average size of 281.5192 μm.

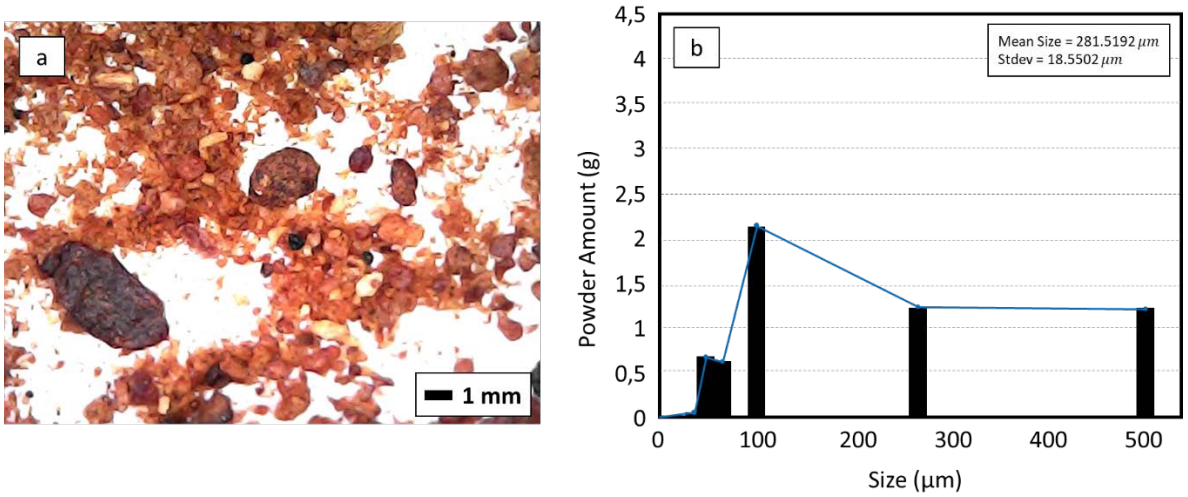

Fig. 11. Photographic image and particle size distribution of mangosteen peel particles (a-b)

Figures 12 (a-d) show the fabricated brake pads based on MA, MB, MC, and MD, respectively. Brake pads that have been fabricated have color differences that are not too noticeable. All brake pads with different compositions of mangosteen peel particles have a color close to black with a little part of brownish powder. From the microscope image, there are yellow and black areas that show mangosteen peel particles and the shiny areas are resinous. Figures 12 (e-l) shows the surface view (outside and inside) of the brake pads. Based on Figs. 12 (e-l) all fabricated brake pads have an uneven surface and have pores. The results of the observations that have been made, brake pads made from MA or brake pads that have a high content of mangosteen peel particles have smoother inner and outer surfaces when compared to other specimens. Therefore, the use of mangosteen peel particles in the manufacture of brake pads results in a smoother brake pad structure in the final product.

The characteristics of the specific gravity of the brake pads to support the analysis of the texture profile on the brake pads are shown in Fig. 13. Based on the specific gravity plots of various brake pad specimens, the MB base brake pads have the highest specific gravity value of 1.16 g/cm^3. The specific gravity of the MC-based brake pads is 1.15 g/cm^3, the MA-based brake pads are 1.01 g/cm^3. Meanwhile, the MD-based brake pads have the smallest specific gravity value of 0.99 g/cm^3.

The high specific gravity values in the brake pad composite matrix phase correlated with the density level of the filler particles whose distribution properties became more homogeneous [31]. Thus, this can be attributed to the most acceptable impact of brake pad reception on brake pad characteristics. However, apart from this, the specific gravity of other specimens could be better because the weight of the brake pad is lighter, so it can meet the standard as well. In this case, all specimens have lower specific gravity than commercial brake pads of 1.890 g/cm^3 but still exceed the requirements [6].

Smaller particle sizes result in fewer pores and a finer structure in brake pads. The pores of the brake lining are also influenced by particle size [5]. Because less connection between materials generates more room, brake pads with a large particle size also have larger pores. The performance of the brake pad degrades as the pores grow larger, and vice versa. This occurs because the outer bond between materials is stronger, resulting in improved brake pad performance [5].

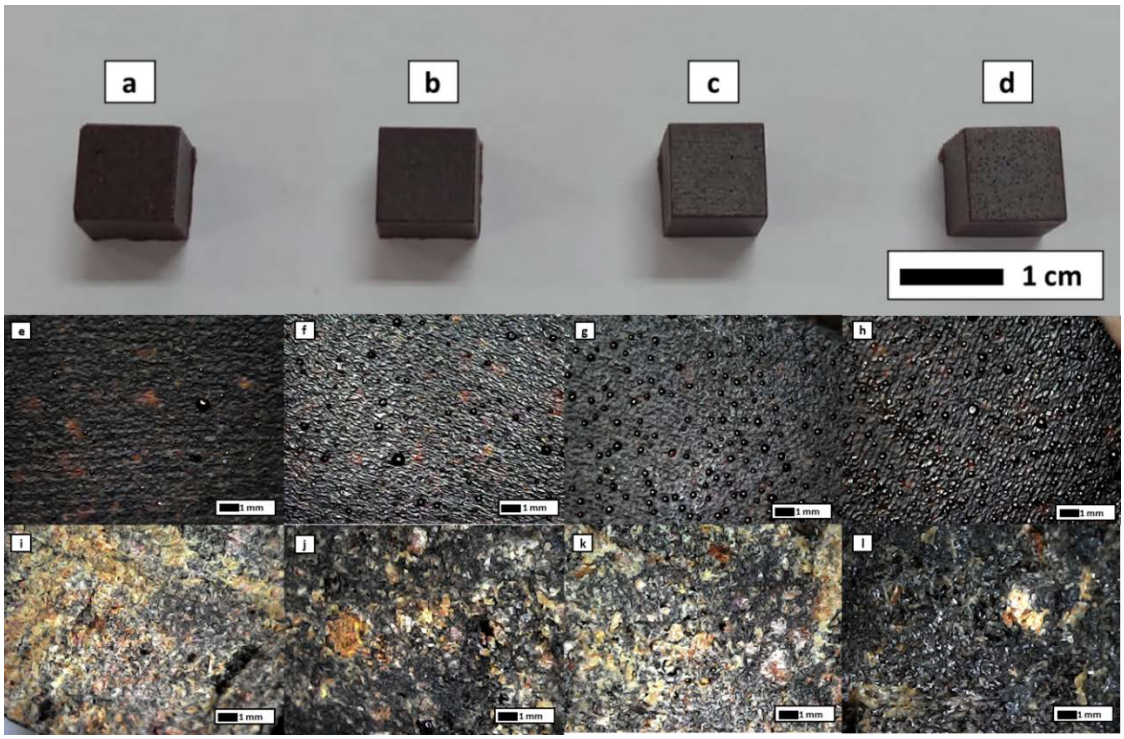

Fig. 12. A photo of the brake pad that was successfully made. Figures (a-d) are MA, MB, MC, and MD-based brake pads, respectively. Figures (e-h) are the outer surfaces of the brake pads and (i-l) are the inner surfaces of the brake pads of MA, MB, MC, and MD, respectively

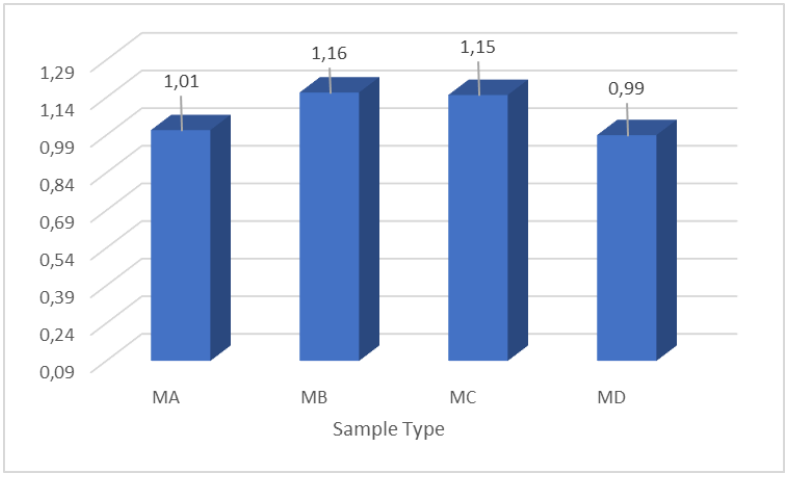

Fig. 13. The plot of specific gravity of various brake pad specimens

Mechanical characteristics. Figures 14(a-b) shows the results of the compression test for each sample brake pad (MA, MB, MC, and MD). Based on Fig. 14 shows that the greater the compressive resistance of the material, the higher the compressive stress obtained from the compression test. Figure 14(a) shows the highest average compressive stress-strain is MA and the lowest is MD. Figure 14(b) shows in more detail each value of the various MA, MB, MC, and MD specimens respectively, namely 0.101, 0.099, 0.095, and 0.094 N/cm^2. Therefore, based on the compression test, the hardest specimen is MA.

The effect of the heating temperature is unavoidable during the operation of the brake pads [32]. Although, initially attention was paid to the material requirements of the brake pads and the importance of meeting the required aspects.

Table 2 shows the results of the puncture test for each sample of brake pads mangosteen peels. A puncture test was performed to confirm the results of the compressive test results.

The puncture test shows that the smaller the average puncture test value that has been obtained, the higher the hardness [5]. In the puncture test, the hardness value of the sample obtained shows the depth of the needle that has been inserted into the sample. A deeper puncture indicates a more brittle specimen [5].

Table 2 shows the results of the puncture test following the results of the compressive test that has been carried out. The combination of components that has the highest level of hardness is MA. Based on the pressure and puncture test data, a brake pad with MD particle composition has the lowest level of hardness. The composition of MB particles is in second place with a prick test value of 93.1 and MC is in third place with a puncture test value of 96.5. This shows that the more mangosteen peel as a reinforcement component is used, the higher the hardness of the brake pads. Mangosteen peel has a high carbon content of about 48.81 percent. Carbon fiber is one of the reinforcing materials that has proven to be good for use in the manufacture of brake pads [18].

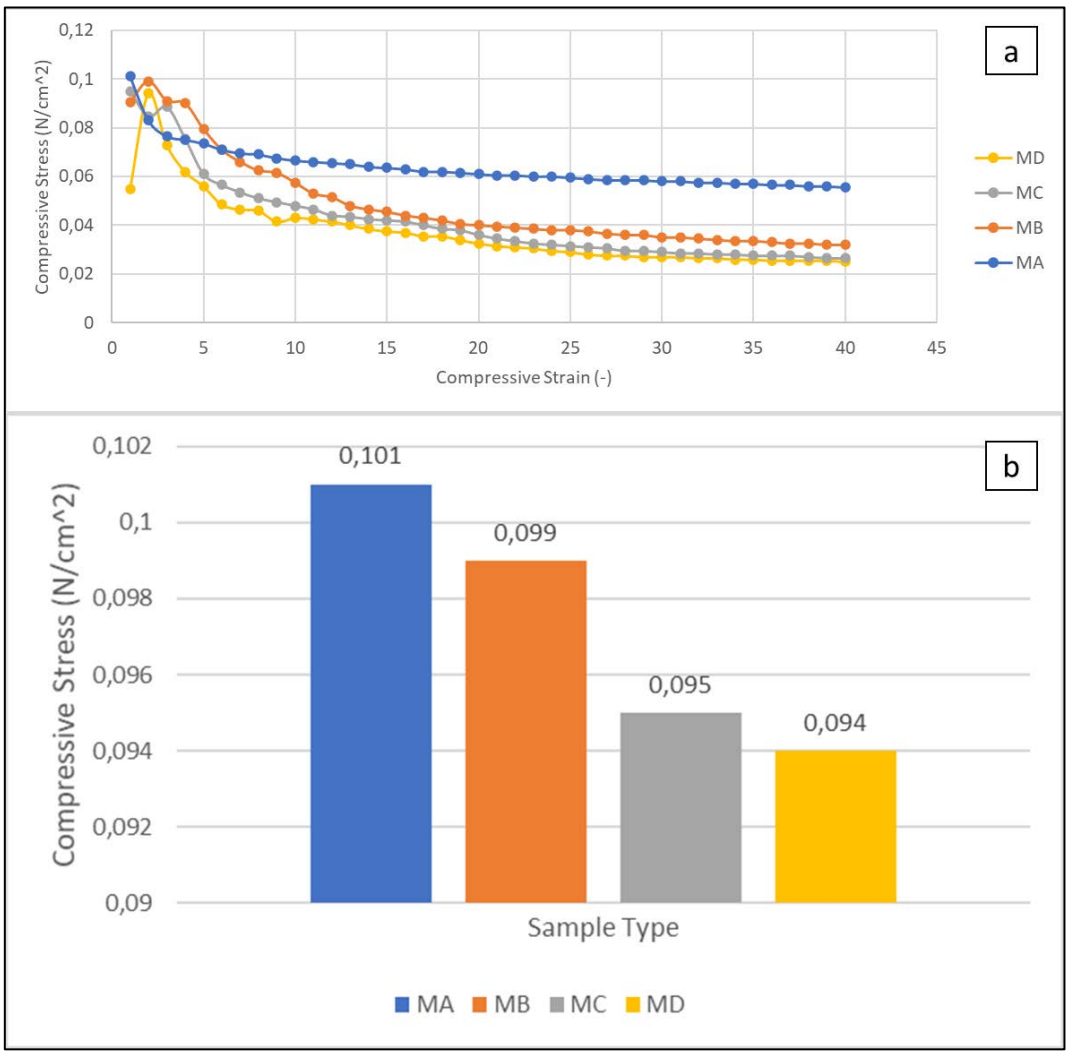

Fig. 14. The results of the compression test are as follows: (a) compressive stress-strain curve and (b) compressive strength

Table 2. Brake pad specimen puncture strength test results

Sample	Durometer shore a hardness scale of brake pad
MA	92.6
MB	93.1
MC	96.5
MD	96.8

The change in mass of each brake pad sample (MA, MB, MC) during the friction test is depicted in Fig. 15. Only three specimens, MA, MB, and MC, were subjected to the friction test. The MD specimen does not allow for a friction test due to its extremely elastic nature, which means it may readily bend from one shape to another, making it impossible to conduct a friction test [33]. During friction testing, the brake pads (as in the braking drum/disc model) are forced to make contact with the sandpaper, converting kinetic energy into heat energy and generating heat and friction [34]. During this process, debris is also produced. A drop in the mangosteen peel particle ratio in double reinforcement induced a decrease in the hardness properties, which resulted in an increase in mass loss.

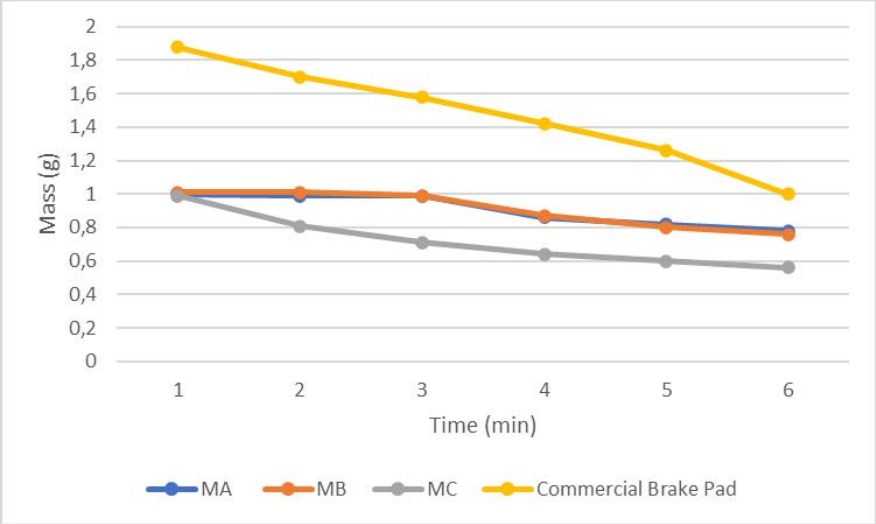

Fig. 15. Graph of change in brake pad loss mass during friction test

The findings of the mass loss rate, friction coefficient, and brake pad wear are summarized in Table 3. Lower mass-loss rates are linked to lower wear rates and greater friction coefficients in friction testing. The lower the wear value of a brake pad specimen, the higher the friction coefficient value [35]. The MA ratio composition brake pad has the lowest wear rate of 0.64 and the maximum friction coefficient of 0.69 (see Table 3). The friction coefficients of brake pads constructed of MA, MB, and MC, respectively, are 0.69×10^{-5}, 0.68×10^{-5}, and 0.67×10^{-5}. Commercial brake pads have a coefficient of friction of 0.61×10^{-5}. Among all commercial brake pad and brake pad specimens, the MA specimen had the best mix of resin and mangosteen peel ratio. All samples exhibit better characteristics than commercial brake pads based on mass loss, friction rate, and coefficient of friction test findings. The results have been compared with commercial standards although with mass production further research is needed.

Brake pads with a lower mass-loss rate and greater friction coefficient characteristics are brake pads with hardness characteristics, according to the findings of the research.

According to research conducted by Dhanasekaran and Gnanamoorthy [36], materials with a higher hardness have a smaller mass loss and a higher coefficient of friction.

In addition, that is true that it is important to analyze or regulate the shape and size of reinforcing particles as we documented in our previous study [5]. Further analysis of the effect of the shape and sizes of the mangosteen peel particles will be done in our future work.

Table 3. The mass-loss rate, wear rate, and friction coefficient of specimens of various compositions

Sample	Initial Mass (g)	Final Mass (g)	Mass loss rate (%)	t (s)	A (mm^2)	Wear Rate ($g/s.mm^2$) ($\times 10^{-5}$)	Friction Coefficient ($\times 10^{-5}$)
MA	1.01	0.78	3.8	360	100	0.64	0.69
MB	1.10	0.76	5,2	360	100	0.94	0.68
MC	1.01	0.56	7.4	360	100	1.25	0.67
Commercial	1.88	1.00	7.8	360	100	2.44	0.61

4. Conclusion

This study was conducted to analyze the effect of differences in the composition of the mangosteen peel as an environmentally friendly reinforcement component in resin-based brake pads. The brake pad was made by mixing mangosteen peel particles, bisphenol A-epichlorohydrin, and cyclo aliphatic amine in various ratios of 10:5:5 (MA), 8:5:5 (MB), 6:5:5 (MC), and 4:5:5 (MD). The physical properties and mechanical properties of each brake pad specimen were investigated. The results showed that MA specimens had the highest hardness, followed by MB, MC, and MD respectively. This research shows that the number of mangosteen peel particles affects the hardness of the brake pad. The higher the ratio of using mangosteen peel, the harder the brake pad was obtained. The mangosteen peel contains carbon fiber, which is one of the effective reinforcing materials in the manufacture of brake pads because it is very strong and heat resistant.

References

1. Wang M, Daamen W, Hoogendoorn SP, van Arem B. Connected variable speed limits control and car-following control with vehicle-infrastructure communication to resolve stop-and-go waves. *Journal of Intelligent Transportation Systems.* 2016;20(6): 559-572.
2. Belhocine A, Abdullah OI. Thermomechanical model for the analysis of disc brake using the finite element method in frictional contact. *Multiscale Science and Engineering.* 2020;2(1): 27-41.
3. Olabisi AI, Adam AN, Okechukwu OM. Development and assessment of composite brake pad using pulverized cocoa beans shells filler. *International Journal of Materials Science and Applications.* 2016;5(2): 66-78.
4. Idris UD, Aigbodion VS, Abubakar IJ, Nwoye CI. Eco-friendly asbestos free brake-pad: Using banana peels. *Journal of King Saud University-Engineering Sciences.* 2015;27(2): 185-192.
5. Nandiyanto AB, Hofifah SN, Girsang GC, Putri SR, Budiman BA, Triawan F, Al-Obaidi AS. The effects of rice husk particles size as a reinforcement component on resin-based brake pad performance: From literature review on the use of agricultural waste as a reinforcement material, chemical polymerization reaction of epoxy resin, to experiments. *Automotive Experiences.* 2021;4(2): 68-82.
6. Ademoh NA, Olabisi AI. Development and evaluation of maize husks (asbestos-free) based brake pad. *Development.* 2015;5(2): 67-80.

7. Abhulimen E, Orumwense F. Characterization and development of asbestos-free brake pad, using snail shell and rubber seed husk. *African Journal of Engineering Research.* 2017;5(2): 24-34.
8. Bashir M, Qayoum A, Saleem SS. Influence of lignocellulosic banana fiber on the thermal stability of brake pad material. *Materials Research Express.* 2019;6(11): 115551.
9. Pujari S, Srikiran S. Experimental investigations on wear properties of Palm kernel reinforced composites for brake pad applications. *Defence Technology.* 2019;15(3): 295-299.
10. Afolabi M, Abubakre OK, Lawal SA, Raji A. Experimental investigation of palm kernel shell and cow bone reinforced polymer composites for brake pad production. International *Journal of Chemistry and Materials Research.* 2015;3(2): 27-40.
11. Bashar DA, Madakson PB, Manji J. Material selection and production of a cold-worked composite brake pad. *World Journal of Engineering and Pure & Applied Sciences.* 20121;2(3): 92.
12. Ramanathan K, Saravanakumar P, Ramkumar S, Pravin KP, Surender SR. Development of Asbestos–Free Brake Pads using Lemon Peel Powder. *International Journal of Innovative Research in Science, Engineering and Technology.* 2017;6(3): 4449-4455.
13. Nandiyanto AB, Simbara AT, Girsang GC. Effects of Particle Size and Composite Composition of Durian Peels and Banana Midribs' as Reinforcement Components on Resin-Based Brake Pad Performance. *Journal of Engineering Research.* 2021;9: 1-15.
14. Ruzaidi CM, Kamarudin H, Shamsul JB, Al Bakri AM, Alida A. Morphology and wear properties of palm ash and PCB waste brake pad. *International Conference on Asia Agriculture and Animal.* 2011;13: 145-149.
15. Solomon WC, Lilly MT, Sodiki JI. Production of asbestos-free brake pad using groundnut shell as filler material. *International Journal of Science and Engineering Invention.* 2018;4(12): 21-27.
16. Asotah W, Adeleke A. Development of asbestos free brake pads using corn husks. *Leonardo Electronic Journal of Practices and Technologies.* 2017;31: 129-144.
17. Mohammed TI, Ojo OO, Olufemi OE. Laboratory Study of a Lignocellulosic Biomass as an Alternative Base Material for Brake Pads. *Current Journal of Applied Science and Technology.* 2018: 1-4.
18. Mukti NI, Prasetyo I, Mindaryani A. Preparasi karbon teremban oksida cobalt dari limbah kulit manggis sebagai adsorben penjerap etilen untuk pengawetan buah. *Reaktor*. 2015;15(3): 165-174.
19. Soehardjo KA, Basuki A, Rahardi SS. The Influences of Carbon Fiber and Nano-Silica in the Making of an Asbestos-Free Composite for a Train Brake Lining. *Polymer-Plastics Technology and Engineering.* 2015;54(3): 246-252.
20. Yudhanto F, Dhewanto SA, Yakti SW. Karakterisasi Bahan Kampas Rem Sepeda Motor Dari Komposit Serbuk Kayu Jati. *Jurnal Quantum Teknika.* 2019;1(1): 19-27.
21. Nandiyanto AB, Al Husaeni DF. A bibliometric analysis of materials research in Indonesian journal using VOSviewer. *Journal of Engineering Research.* 2021;9: 1-16.
22. Hamidah I, Sriyono S, Hudha MN. A Bibliometric analysis of Covid-19 research using VOSviewer. *Indonesian Journal of Science and Technology.* 2020;5(2): 34-41.
23. Nandiyanto AB, Al Husaeni DN, Al Husaeni DF. A bibliometric analysis of chemical engineering research using vosviewer and its correlation with covid-19 pandemic condition. *Journal of Engineering Science and Technology.* 2021;16(6): 4414-4422.
24. Al Husaeni DF, Nandiyanto AB. Bibliometric using Vosviewer with Publish or Perish (using google scholar data): From step-by-step processing for users to the practical examples in the analysis of digital learning articles in pre and post Covid-19 pandemic. *ASEAN Journal of Science and Engineering.* 2022;2(1): 19-46.

25. Nandiyanto ABD, Al Husaeni DF, Ragadhita R. Bibliometric data analysis of research on resin-based brake-pads from 2012 to 2021 using VOSviewer mapping analysis computations, *ASEAN Journal for Science and Engineering in Materials*. 2023;2(1):35-44.
26. Nandiyanto ABD, Oktiani R, Ragadhita R. How to read and interpret FTIR spectroscope of organic material. *Indonesian Journal of Science and Technology.* 2019;4(1): 97-118.
27. Nandiyanto ABD, Fiandini M, Hofifah SN, Al Husaeni DN, Ragadhita R. Production of brake pad from epoxy resin: From polymerization concept to the experiment with analysis of mechanical properties. *Jurnal Penelitian Enjiniring.* 2021;25(2): 110-115.
28. Wathoni N, Shan CY, Shan WY, Rostinawati T, Indradi RB, Pratiwi R, Muchtaridi M. Characterization and antioxidant activity of pectin from Indonesian mangosteen (Garcinia mangostana L.) rind. *Heliyon.* 2019;5(8): e02299.
29. Rohman A, Arifah FH, Irnawati GA, Muchtaridi M. The application of FTIR spectroscopy and chemometrics for classification of mangosteen extract and its correlation with alpha-mangostin. *Journal of Applied Pharmaceutical Science.* 2020;10(4): 149-54.
30. Fernandes IJ, Santos RV, Santos EC, Rocha TL, Domingues Junior NS, Moraes CA. Replacement of commercial silica by rice husk ash in epoxy composites: a comparative analysis. *Materials Research.* 2018;21: e20160562.
31. Colombo P, Mera G, Riedel R, Soraru GD. Polymer-derived ceramics: 40 years of research and innovation in advanced ceramics. *Journal of the American Ceramic Society.* 2010;93(7): 1805-37.
32. Brake DJ, Bates GP. Fluid losses and hydration status of industrial workers under thermal stress working extended shifts. *Occupational and Environmental Medicine*. 2003;60(2): 90-96.
33. Ghosh S, Reddy CM. Elastic and bendable caffeine cocrystals: implications for the design of flexible organic materials. *Angewandte Chemie International Edition.* 2012;51(41): 10319-10323.
34. Uday MB, Ahmad Fauzi MN, Zuhailawati H, Ismail AB. Advances in friction welding process: a review. *Science and technology of Welding and Joining.* 2010;15(7): 534-58.
35. Gai PF. Wear Rate Characteristics of Basalt-Based Composites as Material for Brake Pad. *Saudi Journal of Engineering and Technology.* 2021;6(11): 414-25.
36. Dhanasekaran S, Gnanamoorthy R. Abrasive wear behavior of sintered steels prepared with MoS2 addition. *Wear.* 2007;262(5-6): 617-23.

THE AUTHORS

Nandiyanto A.B.D.
e-mail: nandiyanto@upi.edu
ORCID: -

Al Husaeni D.F.
e-mail: dwifitriaalhusaeni@upi.edu
ORCID: 0000-0002-2640-1086

Ragadhita R.
e-mail: ragadhita@upi.edu
ORCID: 0000-0002-2829-6419

Fiandini M.
e-mail: melifiandini19@upi.edu
ORCID: 0000-0002-8894-6698

Rizky K.M.
e-mail: karinamulya19@gmail.com
ORCID: 0000-0002-9412-5247

Al Husaeni D.N.
e-mail: dwinoviaalhusaeni14@upi.edu
ORCID: -

Materials Physics and Mechanics. 2022;50(1): 56-65
Research article
http://dx.doi.org/10.18149/MPM.5012022_4

Submitted: July 19, 2022
Approved: August 9, 2022
Accepted: August 22, 2022

Analytical and numerical solution to the problem of hydrogen diffusion in rotating cylindrical elastic bodies

A.K. Belyaev, A.R. Galyautdinova✉, S.A. Smirnov, N.M. Bessonov

Institute for Problems in Mechanical Engineering RAS, St. Petersburg, Russia

✉ aliyagalyautdinova@gmail.com

Abstract. The work is devoted to the solution of the problem of hydrogen diffusion in rotating cylindrical elastic bodies compressed by two distributed loads. The study includes the analytical determination of the stress state of the body on the basis of known stresses from the Hertz contact problem, the derivation of the hydrogen diffusion equation in a rotating body in the found field of elastic stresses, and the numerical solution of the obtained hydrogen diffusion equation. The numerical solution of the diffusion equation was carried out by the method of finite differences. According to the numerical solution of the diffusion equation, the effect of hydrogen concentration localization near the outer boundary was detected. This result is consistent with experimental studies of the distribution of hydrogen concentration in roller bearings. This problem is important for diagnostics of failures of rolling bearings due to hydrogen embrittlement.

Keywords: hydrogen diffusion, diffusion equation, rolling bearings, stress state

Acknowledgements*. This paper is based on research carried out with the financial support of the Russian Science Foundation (grant no. 18-19-00160).*

Citation: Belyaev AK, Galyautdinova AR, Smirnov SA, Bessonov NM. Analytical and numerical solution to the problem of hydrogen diffusion in rotating cylindrical elastic bodies. *Materials Physics and Mechanics*. 2022;50(1): 56-65. DOI: 10.18149/MPM.5012022_4.

1. Introduction

The content of hydrogen in metals and alloys leads to a decrease in the strength properties of the material. This problem is present in many machines and mechanisms, including rolling bearings. In particular, 75% of premature failures of wind turbine gearboxes are associated with the destruction of rolling bearings. Near-surface defects called white etching cracks have been found in damaged wind turbine bearings [1]. White etching cracks appear in the material under the combined influence of hydrogen and mechanical stresses. Studies show that increased hydrogen concentrations in bearing steels are a consequence of the diffusion of hydrogen into the metal due to the decomposition of the bearing grease as a result of a tribochemical reaction [2].

After the grease decomposes with the release of hydrogen atoms, the hydrogen begins to interact with the material, causing degradation of its mechanical properties. At the moment, there are several main approaches to describing the effect of hydrogen on the mechanical properties of materials: the HELP model of fracture due to local plasticity [3], the HEDE model of brittle fracture [4,5], the model taking into account the internal pressure of hydrogen

[6], and the bi-continuum model [7,8], which takes into account the influence of hydrogen with different binding energies on the mechanical characteristics of the material.

It is known that even extremely low concentrations of hydrogen lead to a deterioration in the mechanical properties of the material. If the limiting concentrations of hydrogen are not exceeded, the laws of diffusion formulated by Fick [9] are fulfilled. Generalizing Fick's Second Law to the three-dimensional case, we obtain the diffusion equation for material in an elastic body. And the hydrogen diffusion equation in the field of elastic stresses [10] makes it possible to describe the distribution of hydrogen in a metal due to its diffusion under the action of external loads.

In the present work, the hydrogen diffusion equation in a rotating cylindrical elastic body subjected to compression by distributed forces is investigated. This equation includes the hydrostatic component of the stress field, which must be determined at the first step of solving this problem. Its determination is based on the solution of the theory of elasticity problem of loading a body by external forces. This statement simulates the diffusion of hydrogen in the rolling elements of roller bearings during their operation.

This problem has great importance for understanding how the distribution of hydrogen affects the mechanical properties of the material when it leads to premature failure of bearings, and how to prevent it.

2. Determination of the stress state of a cylindrical elastic body

To find the stress state of a considered body, it is reasonable to turn to the solution of the Hertz contact problem of the compression of two cylinders initially touching along the line. The complete solution to this problem is presented in the book by N.M. Belyaev [11]. It is assumed that the cylindrical bodies have an infinite length, along which the compressive load p is distributed perpendicular to the line of contact. When the bodies are compressed, the line of contact, as a result of elastic strains, turns into a pressure area in the form of a strip of width $2b$. During the solution, it was found that the half-width b of the pressure strip for two contacting cylinders of radii R_1 and R_2 is equal to

$$b = \sqrt{4p(\vartheta_1 + \vartheta_1)/(1/R_1 + 1/R_2)}, \tag{1}$$

where ϑ defines the material parameters of both cylinders as

$$\vartheta_{1,2} = \left(1 - {\nu_{1,2}}^2\right)/\pi E_{1,2}, \tag{2}$$

here ν is a Poisson's ratio, and E is Young's modulus.

To calculate stresses, elliptical coordinates α and β are entered

$$\begin{cases} y = b\mathrm{ch}\alpha\cos\beta, \\ z = b\mathrm{sh}\alpha\sin\beta. \end{cases} \tag{3}$$

The reference point of the Cartesian coordinates is associated with the point of initial contact of two cylinders, while the x-axis is directed along the axes of the cylinders, the positive direction of the z-axis for each cylinder is directed inside the considered cylinder.

In the introduced elliptical coordinates, the stresses along the areas perpendicular to the Cartesian coordinate axes in the contacting bodies have the form:

$$\begin{cases} \sigma_x = -\dfrac{2p}{\pi b}\dfrac{\lambda}{\lambda+\mu}e^{-\alpha}\sin\beta, \\ \sigma_y = -\dfrac{2p}{\pi b}e^{-\alpha}\sin\beta + \dfrac{2P}{\pi b}\sin\beta\,\mathrm{sh}\alpha\left(1 - \dfrac{\mathrm{sh}2\alpha}{\mathrm{ch}2\alpha - \cos2\beta}\right), \\ \sigma_z = -\dfrac{2p}{\pi b}e^{-\alpha}\sin\beta - \dfrac{2P}{\pi b}\sin\beta\,\mathrm{sh}\alpha\left(1 - \dfrac{\mathrm{sh}2\alpha}{\mathrm{ch}2\alpha - \cos2\beta}\right), \\ \tau_{yz} = -\dfrac{2p}{\pi b}\sin\beta\,\mathrm{sh}\alpha\dfrac{\sin2\beta}{\mathrm{ch}2\alpha - \cos2\beta}, \\ \tau_{xy} = \tau_{zx} = 0. \end{cases} \quad (4)$$

However, using it in the diffusion equation turns out to be difficult, since explicit analytical expressions that convert elliptic coordinates back to Cartesian or polar ones do not exist.

The next way of solution is an attempt to use the theory of functions of a complex variable to find the stresses in the whole body from the known stress vector on the surface [12]. Since at the contact zone the stresses from the Hertz contact problem have an analytical form in polar coordinates

$$\begin{cases} \sigma_r = -\dfrac{2p}{\pi b}\sqrt{1 - \dfrac{{R_1}^2\sin^2\varphi}{b^2}}, \\ \sigma_\varphi = -\dfrac{2p}{\pi b}\sqrt{1 - \dfrac{{R_1}^2\sin^2\varphi}{b^2}}, \\ \tau_{r\varphi} = 0. \end{cases} \quad (5)$$

In the complex analysis, according to the Goursat formulas, the mean normal stress σ is defined as

$$\sigma = 2Re\Phi(z), \quad (6)$$

where $\Phi(z)$ is a complex potential that is defined by an expression

$$\Phi(\zeta) = \frac{1}{2\pi i}\oint\frac{F(\varphi)ds}{s-\zeta} - \frac{1}{4\pi}\int_0^{2\pi}F(\varphi)d\varphi, \quad (7)$$

where ζ is a variable of coordinates of points of the unit circle on the complex plane, which was entered, when we use a conformal mapping to map the considered area to the inner of the unit circle on the complex plane, s is a boundary of the unit circle. The function $F(\varphi)$ is the stress vector of external loads on the outer surface of the considered body (Fig. 1).

The analytical calculation of the complex potential was considered for three types of external load $F(\varphi)$: in the form of an exact solution of the Hertz contact problem, in the form of an approximate cosine distribution, and in the form of a constant uniform distribution. The considered distributions are illustrated in Fig. 2. Since here we are dealing with the calculation of an improper integral, the solution of the integral could only be found for the case when the stress vector is represented as a constant.

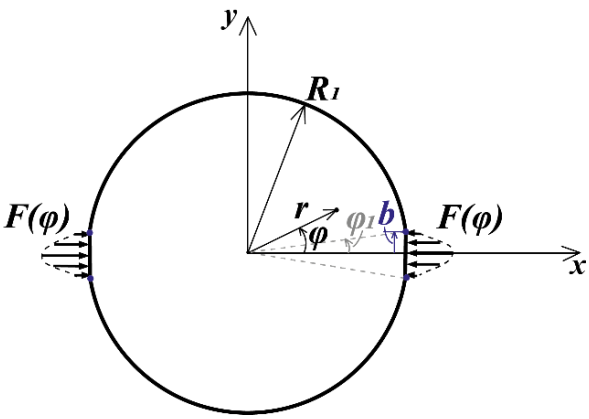

Fig. 1. Action of the stress vector on the outer boundary of the body

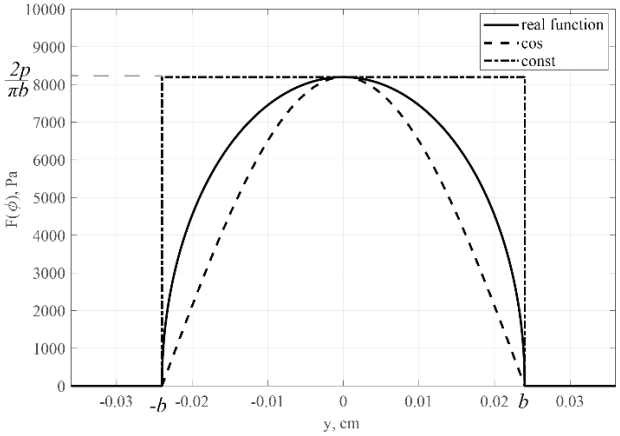

Fig. 2. Three considered options for setting an external load

For the points inside the body, the stresses have such a complicated form

$$\sigma(r,\varphi) = -\frac{p}{\pi R_1} + \frac{p}{\pi b}\operatorname{arctg}\left(\frac{\left(\left(\frac{r}{R_1}\right)^2 + \frac{2r}{R_1}\cos\varphi + 1\right)\operatorname{tg}\frac{b}{2R_1} - \frac{2r}{R_1}\sin\varphi}{\left(\frac{r}{R_1}\right)^2 - 1}\right) -$$

$$-\frac{p}{2\pi b}\operatorname{arctg}\left(\frac{\left(\left(\frac{r}{R_1}\right)^2 + \frac{2r}{R_1}\cos\varphi + 1\right)\operatorname{ctg}\frac{2b}{R_1} + \frac{2r}{R_1}\sin\varphi}{\left(\frac{r}{R_1}\right)^2 - 1}\right) - \tag{8}$$

$$-\frac{p}{2\pi b}\operatorname{arctg}\left(\frac{\left(\left(\frac{r}{R_1}\right)^2 + \frac{2r}{R_1}\cos\varphi + 1\right)\operatorname{ctg}\frac{2b}{R_1} - \frac{2r}{R_1}\sin\varphi}{\left(\frac{r}{R_1}\right)^2 - 1}\right).$$

And at the boundary, where the integrand function tends to infinity, we can use the Sokhotsky-Plemelj formulas [12]. This solution also turns out to be too complicated and cannot be used further in the hydrogen diffusion equation. As a result, the solution of the stress field obtained by the theory of functions of a complex variable also turns out to be too complicated and may not be used in a hydrogen diffusion equation.

To find analytical expressions of the stress state of the loaded cylindrical elastic body it was decided to use a graphical representation of the solution of the Hertz problem in elliptic coordinates (4), reconstructed in polar coordinates using the MATLAB application package [13], shown in Fig. 3. And according to the graphical representation of the dependences of mean stresses on polar coordinates, we can find the approximating functions $f(r)$ and $g(\varphi)$, shown in Fig. 4. The found functions approximate the stress field from the Hertz contact problem with sufficient accuracy

$$f(r) = \frac{\alpha}{\sqrt{1 + \frac{(R_1 - r)^2}{b^2}}}, \qquad g(\varphi) = \frac{\beta}{(\varphi - \pi/2)^2 + \beta^2}, \tag{9}$$

where α and β are the parameters of approximation.

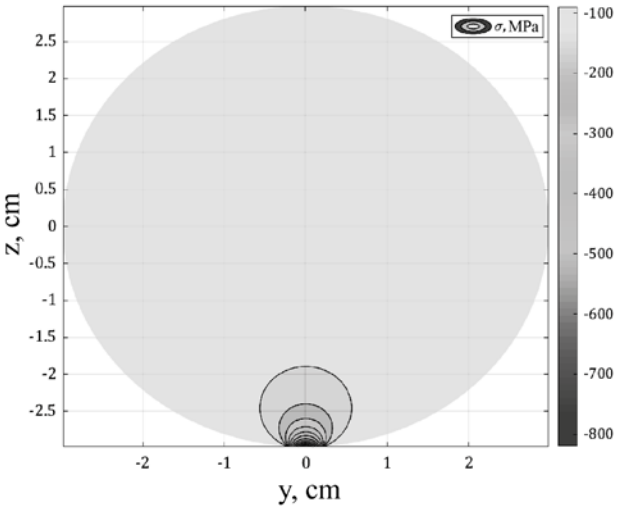

Fig. 3. The mean normal stress field σ from the contact problem

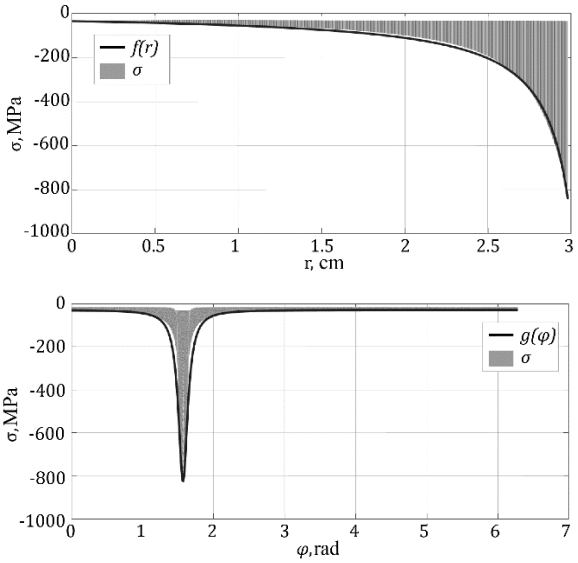

Fig. 4. Dependences of σ and functions $f(r)$ and $g(\varphi)$ on polar coordinates r and φ

Based on the found dependencies (9), we can obtain an analytical expression of the mean normal stresses in a cylindrical body compressed by two symmetrical distributed loads applied at two diametrically opposite points of a cylindrical surface in a horizontal plane

$$\sigma(r,\varphi) = -\frac{2p}{\pi b}\frac{\alpha}{\sqrt{1+\frac{(R_1-r)^2}{b^2}}}\left(\frac{\beta}{\varphi^2+\beta^2}+\frac{\beta}{(\varphi-\pi)^2+\beta^2}\right). \quad (10)$$

The found stress state of a body was graphically represented in Fig. 5.

3. Analytical expression of the hydrogen diffusion equation in the field of elastic stresses

To determine the nature of the distribution of hydrogen concentration in rolling bearings, the equation of hydrogen diffusion in the field of elastic stresses is considered. It was obtained taking into account a number of assumptions: all properties of the metal are isotropic, the contribution from the magnetic and gravitational fields to the process of hydrogen diffusion is negligibly small, the diffusion coefficient of hydrogen and stresses in the body do not depend on the hydrogen concentration. As a result, the equation of hydrogen diffusion in the field of elastic stresses has the following form [10]

$$\frac{\partial C}{\partial t} = D\Delta C - \frac{DV_H}{RT}\nabla C\cdot\nabla\sigma - \frac{DV_H}{RT}C\Delta\sigma, \quad (11)$$

where C − hydrogen concentration, D − hydrogen diffusion coefficient, V_H − partial molar volume of hydrogen, σ − mean normal stress, R − gas constant, T − absolute temperature.

Since considered body rotates with a constant angular velocity ω, the transition to a rotating coordinate system can help to reduce the dynamic problem to a quasi-static one, and the equation turns to the form

$$\Delta C - \frac{V_H}{RT}\left[\frac{\partial C}{\partial r}\frac{\partial\sigma}{\partial r}+\frac{1}{r^2}\frac{\partial C}{\partial\varphi}\frac{\partial\sigma}{\partial\varphi}\right] - \frac{\omega}{D}\frac{\partial C}{\partial\varphi} - \frac{V_H}{RT}C\Delta\sigma = 0. \quad (12)$$

Substituting the found hydrostatic component of the stress state of the body (10) into this hydrogen diffusion equation written in a rotating coordinate system (12), we obtain the analytical form of the hydrogen diffusion equation in the field of elastic stresses found on the basis of approximation of the graphical representation of the Hertz contact problem solution

$$\Delta C + \frac{2p}{\pi b}\frac{V_H}{RT}\left[\frac{\alpha b(R_1 - r)}{(b^2 + (R_1 - r)^2)^{\frac{3}{2}}}\left(\frac{\beta}{\varphi^2 + \beta^2} + \frac{\beta}{(\varphi - \pi)^2 + \beta^2}\right)\frac{\partial C}{\partial r} - \right.$$
$$\left. - \frac{2\beta\alpha}{r^2\sqrt{1 + \frac{(R_1 - r)^2}{b^2}}}\left(\frac{\varphi}{(\varphi^2 + \beta^2)^2} + \frac{\varphi - \pi}{(\varphi^2 + \beta^2)^2}\right)\frac{\partial C}{\partial \varphi}\right] - \frac{\omega}{D}\frac{\partial C}{\partial \varphi} = 0. \quad (13)$$

The resulting equation (13) has a complicated form, so the exact analytical solution of the equation cannot be found. Only approximate analytical or numerical methods may be used. In this paper, we will present the numerical solution to this equation. To implement a numerical solution of the hydrogen diffusion equation the finite difference method is used.

4. Analytical description of the numerical solution realization

For a numerical solution, the hydrogen diffusion equation in rotating cylindrical elastic bodies under compression by distributed forces is rewritten in the following dimensionless form:

$$\frac{1}{\xi}\frac{\partial}{\partial \xi}\left(\xi\frac{\partial C}{\partial \xi}\right) + \frac{1}{\xi^2}\frac{\partial^2 C}{\partial \varphi^2} - V_1\frac{\partial C}{\partial \xi} - V_2\frac{\partial C}{\partial \varphi} = 0, \quad (14)$$

where

$$\xi = \frac{r}{R_1}, \quad V_1 = AK_1, \quad V_2 = AK_2\frac{1}{\xi^2} + W, \quad A = \frac{V_H P}{RT}, \quad W = \frac{\omega {R_1}^2}{D},$$
$$K_1 = \frac{\partial \sigma}{\partial \xi}, \quad K_2 = \frac{\partial \sigma}{\partial \varphi}, \quad 0 \le \xi \le 1, \quad 0 \le \varphi \le 2\pi. \quad (15)$$

A uniform difference mesh along the coordinates ξ and φ of size $N \times M$ ($N = 100, M = 200$) was constructed to solve equation (14). The partial derivatives in equation (14) were replaced by the following approximate difference relations [14], as an approximation of the first derivative with respect to ξ and φ, the right or left difference derivative is used, it depends on the sign of the coefficients in V_1 and V_2:

$$\frac{1}{\xi}\frac{\partial}{\partial \xi}\left(\xi\frac{\partial C}{\partial \xi}\right) = \frac{(\xi_{i+1} + \xi_i)C_{i+1,j} - (\xi_{i+1} + 2\xi_i + \xi_{i-1})C_{i,j} + (\xi_i + \xi_{i-1})C_{i-1,j}}{2\xi\Delta\xi^2},$$
$$\frac{\partial^2 C}{\partial \varphi^2} = \frac{C_{i,j+1} - 2C_{i,j} + C_{i,j-1}}{\Delta\varphi^2}, \quad \frac{\partial C}{\partial \xi} = \begin{cases} \frac{C_{i+1,j} - C_{i,j}}{\Delta\xi}, V_1 > 0 \\ \frac{C_{i-1,j} - C_{i,j}}{\Delta\xi}, V_1 < 0 \end{cases}, \quad (16)$$
$$\frac{\partial C}{\partial \varphi} = \begin{cases} \frac{C_{i,j+1} - C_{i,j}}{\Delta\varphi}, V_2 > 0 \\ \frac{C_{i,j-1} - C_{i,j}}{\Delta\varphi}, V_2 < 0 \end{cases},$$

where $0 \le i \le N - 1,\ 0 \le j \le M - 1$.

Thus, the considered equation can be written in the form:

$$\left(\frac{2\xi_{i+\frac{1}{2}}}{\xi_i\Delta\xi_i(\Delta\xi_i + \Delta\xi_{i-1})} + \frac{|V_1| - V_1}{2\Delta\xi_i}\right)(C_{i+1,j} - C_{i,j}) +$$
$$+ \left(\frac{2\xi_{i-\frac{1}{2}}}{\xi_i\Delta\xi_{i-1}(\Delta\xi_i + \Delta\xi_{i-1})} + \frac{|V_1| + V_1}{2\Delta\xi_{i-1}}\right)(C_{i-1,j} - C_{i,j}) + \quad (17)$$
$$+ \left(\frac{2}{\xi_i^2\Delta\varphi_j(\Delta\varphi_j + \Delta\varphi_{j-1})} + \frac{|V_2| - V_2}{2\Delta\varphi_j}\right)(C_{i,j+1} - C_{i,j}) +$$

$$+\left(\frac{2}{\xi_i^2\Delta\varphi_{j-1}(\Delta\varphi_j+\Delta\varphi_{j-1})}+\frac{|V_2|+V_2}{2\Delta\varphi_{j-1}}\right)(C_{i,j-1}-C_{i,j})=0.$$

where $\xi_{i+\frac{1}{2}}=\frac{\xi_{i+1}+\xi_i}{2}$, $\xi_{i-\frac{1}{2}}=\frac{\xi_i+\xi_{i-1}}{2}$.

Difference scheme can be written as

$$a_{i,j}\,C_{i,j-1}+b_{i,j}\,C_{i,j+1}+d_{i,j}\,C_{i-1,j}+e_{i,j}\,C_{i+1,j}-c_{i,j}\,C_{i,j}=-f_{i,j}, \quad (18)$$

where

$$a_{i,j}=\frac{2}{\xi_i^2\Delta\varphi_{j-1}(\Delta\varphi_j+\Delta\varphi_{j-1})}+\frac{|V_2|+V_2}{2\Delta\varphi_{j-1}}, b_{i,j}=\frac{2}{\xi_i^2\Delta\varphi_j(\Delta\varphi_j+\Delta\varphi_{j-1})}+\frac{|V_2|-V_2}{2\Delta\varphi_j},$$

$$d_{i,j}=\frac{2\xi_{i-\frac{1}{2}}}{\xi_i\Delta\xi_{i-1}(\Delta\xi_i+\Delta\xi_{i-1})}+\frac{|V_1|+V_1}{2\Delta\xi_{i-1}}, \qquad e_{i,j}=\frac{2\xi_{i+\frac{1}{2}}}{\xi_i\Delta\xi_i(\Delta\xi_i+\Delta\xi_{i-1})}+\frac{|V_1|-V_1}{2\Delta\xi_i},$$

$$c_{i,j}=a_{i,j}+b_{i,j}+d_{i,j}+e_{i,j}, \qquad f_{i,j}=0.$$

Next, the difference scheme (18) was rewritten in matrix form

$$\boldsymbol{A}_j\boldsymbol{Y}_{j-1}-\boldsymbol{C}_j\boldsymbol{Y}_j+\boldsymbol{B}_j\boldsymbol{Y}_{j+1}=-\boldsymbol{F}_j, \quad (19)$$

where

$$\boldsymbol{A}_j=\begin{bmatrix} a_{0,j} & 0 & 0 & & & \\ 0 & a_{1,j} & 0 & & 0 & \\ 0 & 0 & \dots & & & \\ & & & a_{i,j} & 0 & 0 \\ & 0 & & 0 & \dots & 0 \\ & & & 0 & 0 & a_{N-1,j} \end{bmatrix}, \quad \boldsymbol{B}_j=\begin{bmatrix} b_{0,j} & 0 & 0 & & & \\ 0 & b_{1,j} & 0 & & 0 & \\ 0 & 0 & \dots & & & \\ & & & b_{i,j} & 0 & 0 \\ & 0 & & 0 & \dots & 0 \\ & & & 0 & 0 & b_{N-1,j} \end{bmatrix},$$

$$\boldsymbol{C}_j=\begin{bmatrix} c_{0,j} & e_{0,j} & & & & \\ d_{1,j} & c_{1,j} & e_{1,j} & & & \\ & d_{i,j} & c_{i,j} & e_{i,j} & & \\ & & \dots & \dots & \dots & \\ & & & \dots & \dots & e_{N-2,j} \\ & & & & d_{N-1,j} & c_{N-1,j} \end{bmatrix}, \qquad \boldsymbol{F}_j=0, \qquad \boldsymbol{Y}_j=\begin{bmatrix} C_{0,j} \\ \dots \\ C_{N-1,j} \end{bmatrix}.$$

To solve the resulting difference scheme (19), the tridiagonal matrix algorithm (or, otherwise, Thomas algorithm) [14] was used.

In our case average normal stresses (10) have the following form

$$\sigma=-Pf(\xi)g(\varphi), \quad (20)$$

where

$$P=\frac{2p}{\pi b}, \qquad f(\xi)=\frac{\alpha}{\sqrt{1+\frac{(1-\xi)^2}{b^2}}},$$

$$g(\varphi)=\left(\frac{\beta}{\varphi^2+\beta^2}+\frac{\beta}{(\varphi-\pi)^2+\beta^2}+\frac{\beta}{(\varphi-2\pi)^2+\beta^2}\right),$$

then

$$A=\frac{V_H P}{RT}=\frac{2V_H p}{\pi RTb}, \qquad W=\frac{\omega R_1^2}{D},$$

$$K_1=\frac{\partial\sigma}{\partial\xi}=-\alpha\beta b\frac{(1-\xi)}{\sqrt{(b^2+(1-\xi)^2)^3}}\left(\frac{1}{\varphi^2+\beta^2}+\frac{1}{(\varphi-\pi)^2+\beta^2}+\right.$$

$$\left.+\frac{1}{(\varphi-2\pi)^2+\beta^2}\right),$$

$$K_2=\frac{\partial\sigma}{\partial\varphi}=2\alpha\beta b\frac{1}{\sqrt{b^2+(1-\xi)^2}}\left(\frac{\varphi}{(\varphi^2+\beta^2)^2}+\frac{\varphi-\pi}{((\varphi-\pi)^2+\beta^2)^2}+\right.$$

$$+\frac{\varphi-2\pi}{((\varphi-2\pi)^2+\beta^2)^2}\Big),$$

$$V_1 = AK_1 = -\frac{2V_H p}{\pi RT}\alpha\beta\frac{(1-\xi)}{\sqrt{(b^2+(1-\xi)^2)^3}}\Big(\frac{1}{\varphi^2+\beta^2}+\frac{1}{(\varphi-\pi)^2+\beta^2}+ \quad (21)$$

$$+\frac{1}{(\varphi-2\pi)^2+\beta^2}\Big),$$

$$V_2 = AK_2\frac{1}{\xi^2}+W = \frac{4V_H p}{\pi RT}\alpha\beta\frac{1}{\xi^2}\frac{1}{\sqrt{b^2+(1-\xi)^2}}\Big(\frac{\varphi}{(\varphi^2+\beta^2)^2}+$$

$$+\frac{\varphi-\pi}{((\varphi-\pi)^2+\beta^2)^2}+\frac{\varphi-2\pi}{((\varphi-2\pi)^2+\beta^2)^2}\Big)+\frac{\omega R_1^2}{D}.$$

5. Numerical results of the solution of the hydrogen diffusion equation

The program code developed to implement the described procedure of the numerical method was written in the C++ programming language. The distribution fields of hydrogen concentration in the body and plots of the dependence of concentration on polar coordinates for the boundary conditions of the first kind and the third kind are represented in Figs. 5- 8. The developed program allows us to set various input parameters for the rotation speed, geometry sizes, finite difference mesh sizes, and various boundary conditions. It is also allowed to construct a non-uniform mesh with thickening near the surface and load application points.

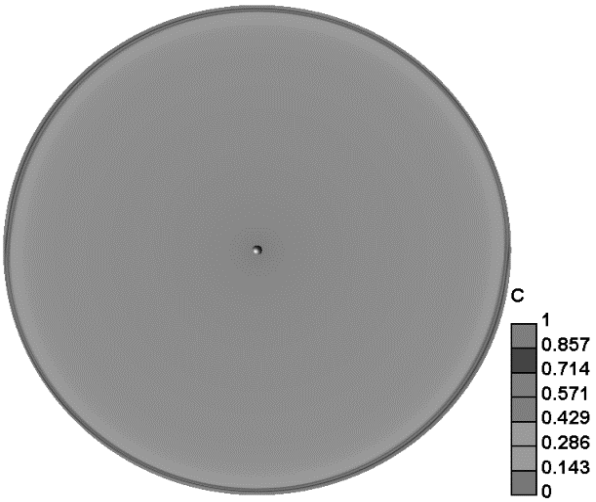

Fig. 5. Concentration field for the boundary conditions of the first kind

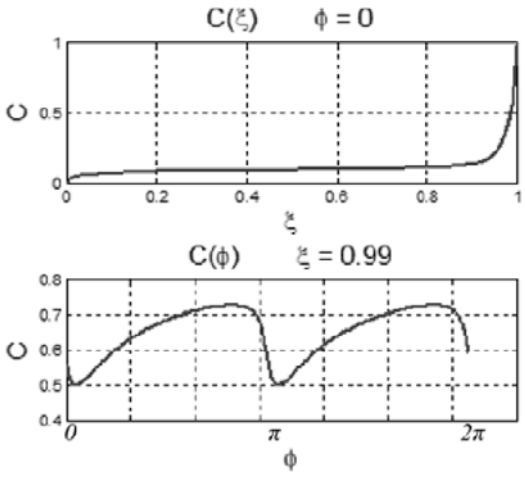

Fig. 6. Concentration plots for the boundary conditions of the first kind

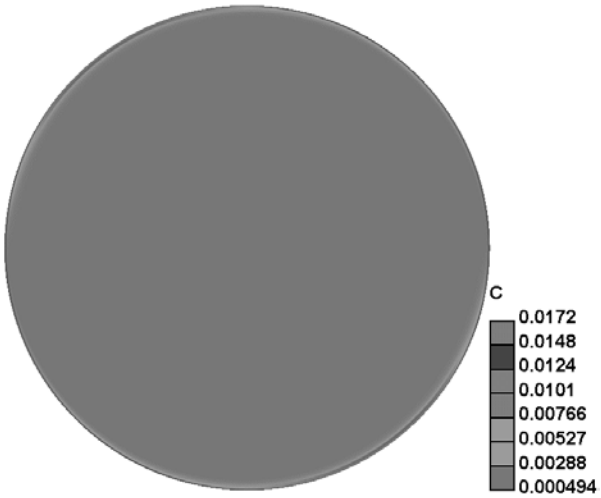

Fig. 7. Concentration field for the boundary conditions of the third kind

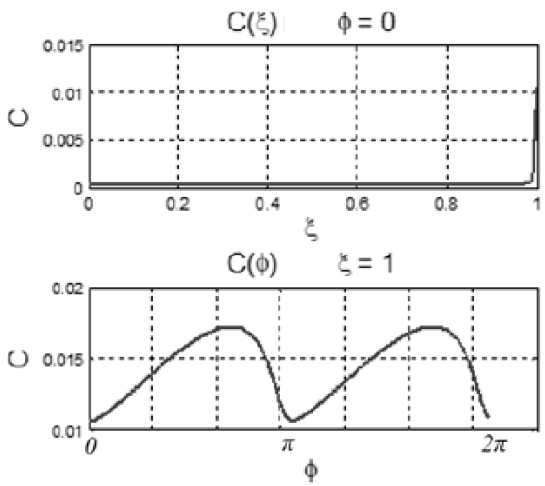

Fig. 8. Concentration plots for the boundary conditions of the third kind

On these plots, a sharp increase in hydrogen concentration in the subsurface layer is observed. This result is consistent with experimental studies of the distribution of hydrogen concentration in roller bearings. In addition, the distribution of hydrogen concentration over the angles φ shows that near the points of load application ($\varphi = 0$ and $\varphi = \pi$), the hydrogen concentration takes the smallest values. This effect is explained by the fact that diffusing hydrogen atoms tend to the region of the material where tensile stresses are distributed.

6. Conclusions

In the framework of this paper, the stress state of the rotating elastic body loaded by two distributed forces was obtained. An analytical form of the equation of the hydrogen diffusion in the rotating body under the field of elastic stresses was written. This equation was solved using numerical methods. A numerical solution of the diffusion equation made it possible to detect the effect of localization of the hydrogen concentration near the outer surface of the body. This result is consistent with experimental research on the hydrogen concentration distribution in roller bearings. The results obtained in this work can help in describing the hydrogen impact on the mechanical properties of rolling bearing materials. This problem requires further research in order to construct the description of the influence of the hydrogen distribution field on the mechanical properties of the material.

References

1. Vegter RH, Slycke JT. The Role of Hydrogen on Rolling Contact Fatigue Response of Rolling Element Bearings. *Journal of Astm International*. 2010;7(2): 1-12.
2. Tamada K, Tanaka H. Occurrence of Brittle Flaking on Bearings Used for Automotive Electrical Instruments and Auxiliary Devices. *Wear*. 1996;199(2): 245-252.
3. Birnbaum HK, Sofronis P. Hydrogen-enhanced localized plasticity – a mechanism for hydrogen-related fracture. *Materials Science and Engineering: A*. 1994;176(1-2): 191-202.
4. Troiano AR. The role of hydrogen and other interstitials in the mechanical behavior of metals. *ASM–Trans*. 1960;52: 54-80.
5. Oriani RA. A mechanistic theory of hydrogen embrittlement of steels. *Berichte der Bunsengesellschaft für physikalische Chemie*. 1972;76(8): 848-857.

6. Carrasco JP, dos Santos NC, Silv AA. Numerical simulation of the hydrogen effect on the deformations of test body models loaded under tensile stress. *International Journal of Modeling and Simulation for the Petroleum Industry*. 2007;1(1): 55-62.
7. Belyaev AK, Polyanskiy AM, Polyanskiy VA, Yakovlev YA. An Approach to Modeling Structural Materials with Low Hydrogen Concentration. In: Altenbach H, Belyaev A, Eremeyev V, Krivtsov A, Porubov A. (eds) *Dynamical Processes in Generalized Continua and Structures*. Springer; 2019. p.63-87.
8. Belyaev AK, Polyanskiy VA, Porubov AV. Nonlinear dynamics of hydrogen concentration in high-strength and high-entropy alloys. *Continuum Mechanics and Thermodynamics*. 2019;31: 1785-1794.
9. Fick A. Ueber diffusion. *Annalen der Physik*. 1855;170(1): 59-86.
10. Kolachev BA. *Hydrogen embrittlement of metals.* Moscow: Metallurgiya; 1985. (In Russian)
11. Belyaev NM. *Proceedings on the theory of elasticity and plasticity.* Moscow: Gostekhizdat; 1957. (In Russian)
12. Lurie AI. *Theory of elasticity*. Berlin: Springer; 2005.
13. Sun C. Explicit Equations to Transform from Cartesian to Elliptic Coordinates. *Mathematical Modelling and Applications*. 2017;2(4): 43-46.
14. Godunov SK, Ryabenky VS. *Difference Schemes: An Introduction to Theory.* Nauka; 1977. (In Russian)

THE AUTHORS

Belyaev A.K.
e-mail: vice.ipme@gmail.com
ORCID: 0000-0002-5934-8138

Galyautdinova A.R.
e-mail: aliyagalyautdinova@gmail.com
ORCID: 0000-0003-2885-4422

Smirnov S.A.
e-mail: serg.a.smir@gmail.com
ORCID: 0000-0002-4098-0344

Bessonov N.M.
e-mail: nickbessonov1@gmail.com
ORCID: 0000-0001-6462-5980

Materials Physics and Mechanics. 2022;50(1): 66-73
Research article
http://dx.doi.org/10.18149/MPM.5012022_5

Submitted: October 5, 2021
Approved: October 11, 2022
Accepted: October 17, 2022

Room-temperature quantum oscillations of static magnetic susceptibility of silicon-carbide epitaxial layers grown on a silicon substrate by the method of the coordinated substitution of atoms

N.T. Bagraev[1,2], S.A. Kukushkin[1]✉, A.V. Osipov[1], V.V. Romanov[3], L.E. Klyachkin[2], A.M. Malyarenko[2], N.I. Rul'[1-3]

[1]Institute of Problems of Mechanical Engineering, Bolshoi pr. 61, Vas. Ostrov, St. Petersburg, 199178, Russia

[2]Ioffe Institute, Politechnicheskaya 26, St. Petersburg 194021, Russia

[3]Peter the Great St. Petersburg Polytechnic University, Politechnicheskaya 29, St. Petersburg 195251, Russia

✉ sergey.a.kukushkin@gmail.com

Abstract. The article presents the results of measurement and analysis of the field dependences of the static magnetic susceptibility of thin epitaxial silicon carbide films grown on the (110) surface of single-crystal silicon by the method of the coordinated substitution of atoms. In weak magnetic fields, the occurrence of two quantum effects at room temperature was experimentally found: the hysteresis of the static magnetic susceptibility and, in the field dependences, quantum Aharonov-Bohm oscillations of the static magnetic susceptibility. The simultaneous occurrence of these effects is a consequence of two- and one-particle interference of charge carriers (two-dimensional holes) on microdefects consisting of dipole centers with negative correlation energy (negative-U dipole centers).

Keywords: silicon carbide on silicon, dilatation dipoles, static magnetic susceptibility, diamagnetism, quantum Aharonov-Bohm oscillations, quantum interference, negative correlation energy, negative-U boron dipoles

Acknowledgements*. The study was supported by the Russian Science Foundation (grant no. 20-12-00193).*

Citation: Bagraev NT, Kukushkin SA, Osipov AV, Romanov VV, Klyachkin LE, Malyarenko AM, Rul' NI. Room-temperature quantum oscillations of static magnetic susceptibility of silicon-carbide epitaxial layers grown on a silicon substrate by the method of the coordinated substitution of atoms. *Materials Physics and Mechanics*. 2022;50(1): 66-73. DOI: 10.18149/MPM.5012022_5.

1. Introduction

The goal of the presented work is to investigate the behavior of the static magnetic susceptibility of the thin silicon carbide epitaxial layers were grown on single-crystal silicon (110) surface by the method of the coordinated substitution of atoms. The method of the coordinated substitution of atoms is based on the special chemical treatment of the Si surface by carbon monoxide (CO). During this treatment, the following chemical reaction occurs on the Si surface:

$$2Si\ (crystal) + CO\ (gas) = SiC\ (layer) + SiO\ (gas)\uparrow. \quad (1)$$

As a result of a reaction (1), the near-surface Si layer transforms into an SiC epitaxial layer. The term "coordinated" means that the new chemical bonds are formed simultaneously and in a coordinated manner with the destruction of the old bonds [1-5]. It was found that the mechanism of the coordinated substitution of atoms preserves the initial silicon cubic lattice, thereby providing the growth of the 3*C*-SiC cubic polytype [4,5]. A detailed description of the processes that occur during the SiC growth by the method of the coordinated substitution of atoms, as well as the synthesis technology, can be found in the reviews [1-5].

The main distinguishing property of SiC films synthesized by this method is the formation of an excess concentration of silicon vacancies in them, while in SiC growth by standard methods, there are mainly carbon vacancies. The interaction of silicon vacancies and carbon atoms leads to the formation of the ordered ensembles of carbon-vacancy structures in the SiC layers grown by the method of the coordinated substitution of atoms. The presence of carbon-vacancy structures in SiC gives rise to the unique properties of such films [6-8]. The quantum chemistry and the experimental methods demonstrated that so-called C_4V centers are formed is SiC on Si at synthesis temperature ~1350ºC. During the SiC growth by this method on the SiC/Si interface an interfacial layer with a thickness of the order of several nanometers, which demonstrates the extraordinary optical and electric features, appears. It is so due to the process of shrinkage of the initial Si lattice with the parameter of 0.543 nm into the SiC cubic lattice with the parameter of 0.435 nm, which appears during the final stage of the silicon transformation into silicon carbide; this process occurs in the plane of the substrate [1-8]. At the same time, silicon carbide separated from the silicon matrix subjects it to anomalously strong compression, the values of which exceed 100 GPa. At such high pressures, obtaining of SiC with such a good structure would be impossible without the high-accuracy coincidence of every fifth silicon carbide crystal cell with every fourth silicon cell. The shrinkage of the material results in the coordinated arrangement of every fifth SiC chemical bond with every fourth Si bond. The remaining bonds either break, which leads to the vacancies and pores formation, or undergo compression, which leads to the change in the structure of the surface zones of silicon carbide transforming it into "semimetal". For the first time, this phenomenon was discovered by spectral ellipsometry in the photon energy range of 0.5-9.3 eV [6,7]. It was shown that the carbon-vacancy structures result in the appearance of other unique optical, electric, and magnetic features [6-8]. Particularly, the possibility of creating field-effect transistor structures on the SiC/Si layers was demonstrated in [9]. On the basis of the macroscopic quantum properties of obtained structures, the emitters and recorders of the terahertz (THz) frequency range of the electromagnetic spectrum with amplitude and frequency modulation in the entire spectrum were implemented. The possibilities of the spectral dependencies control by using the external characteristics of the sample under study (source-drain current and voltage applied to the horizontal gates in the frameworks of the Hall geometry of the transistor structure) were demonstrated, and the basis of the mechanism of the THz radiation appearance was identified as the quantum analogue of the Faraday's electromagnetic induction [9]. Such an approach opens up huge possibilities for creating coupled systems of GHz–THz frequency range emitter-recorder for the radio-photonics and nano-electronics purposes, in particular, for the possible implementation of quantum-computing operations under the conditions of controlled carriers transport in the obtained structures at high temperatures.

In [8] theoretically using the modeling based on the method of the density functional theory the significant effect of C_4V centers in the SiC/Si on the magnetic properties of silicon carbide was predicted. While the ideal 3*C*-SiC grown by the standard methods is a classical semiconductor, 3*C*-SiC grown by the method of the coordinated substitution of atoms demonstrates magnetic properties depending on the C_4V concentration (n_{C_4V}).

In [8] it is shown that n_{C_4V} can be controlled by varying the time and the temperature of the SiC synthesis.

Thus, the experimental research of the extraordinary magnetic features of the SiC/Si interface grown by the method of the coordinated substitution of atoms was the goal of the presented paper.

2. The sample's preparation method

In this study, as the experimental sample, we used the nanoscale SiC layer of ~ (90-100) nm thickness, synthesized on the (100) surface of the single-crystal *n*-type silicon (doped with phosphorus) by the method of the coordinated substitution of atoms [1-5]. After synthesis, the SiC layer was doped with boron under the conditions of non-equilibrium diffusion from the gas phase in the excess flow of the silicon vacancies from the surface of the sample. The synthesis and doping parameters, as well as the sample's characteristics, are presented in Table 1. The formed Hall topology of the transistor structure on the surface of the sample made in the framework of the planar technology has the following parameters: the chip dimensions are 5 × 5 mm with 12 field-transistor structures inside the chip.

Table 1. Technological characteristics of the sample

Substrate	Synthesis conditions	Doping Temperature	Conductivity type, carriers concentration		Transistor structure
			Before Doping	After Doping	
n-Si, $20\ \Omega \cdot cm$, (110)	$T = 1290$℃, $t = 15\ min$, $P = 2.3\ Torr$, $I_{CO} = 12\ sccm$, $\%_{SiH4} = 0.25\%$	900℃	*p*-type, $\sim 6 \cdot 10^{17}\ cm^{-3}$	*p*-type, $> 1 \cdot 10^{19}\ cm^{-3}$	Planar

As the synthesis conditions here presented: T – synthesis temperature, t – synthesis time, P – CO pressure, I_{CO} – CO flow, $\%_{SiH_4}$ – volume percent of silane (SiH_4), which is used during the synthesis [3]. The carriers concentration values were obtained from the capacitive measurements.

3. The experimental method

The realization of the "strong-field" criterion ($\omega_c\tau = eB\tau/m^* = \mu B \gg 1$, where τ – transport time, m^* – carriers effective mass value, μ – mobility, ω_c – cyclotron frequency, B – magnetic field value) in the weak magnetic fields at room temperature became possible due to the low values of the carriers' effective mass with their high mobility [7,8]. Thus, the tasks of the study were to measure and analyze the static magnetic susceptibility of the presented sample.

The static magnetic susceptibility was measured by the Faraday method in the magnetic field range of $H = 0 \div 500\ Oe$ in a step-by-step mode with the 1 *Oe* step using the automated Faraday Balance setup, based on the MGD 312 FG spectrometer, at room temperature in the regime of the thermodynamic equilibrium sample's state realization. The Faraday method is based on measuring the force acting on the sample with the mass *m* in an inhomogeneous external magnetic field. The relationship between the static magnetic susceptibility $\chi\ (T, B)$ and the measured force acting on the sample $F\ (T,\ B)$ is determined by the following expression:

$$\chi\,(T,B) = \frac{F\,(T,B)}{m \cdot BdB/dz}. \quad (2)$$

The external field gradient dB/dz is provided by the special shape of the pole pieces used in the magnet while the value BdB/dz remains constant throughout the volume occupied by the sample. For the measurements, the sample was placed in a quartz cup connected to the scales by a quartz suspension. The force $F\,(T,\ B)$ acting on the sample was defined as the difference between the force of the sample interaction with the field and the force acting on the empty quartz cup, measured under the same external conditions.

The calibration of the experimental setup was carried out using the reference sample – a single-crystal of the magnetically pure indium phosphide with the known value of the static magnetic susceptibility $\chi = -313 \cdot 10^{-9}\ cm^3/g$. The high sensitivity of the MGD 312 FG balance spectrometer in the range of $10^{-10} \div 10^{-9}$ CGS ensures the appropriate calibration stability of BdB/dz values [10].

4. Results and discussion

The sample under study reveals a number of features, the analysis of which makes it possible to interpret the results of the experiment, linking them with the structural features of the material, which are obtained due to the original technology of the thin epitaxial SiC layers growth on the near-surface layer of single-crystal silicon.

At low fields, the measured static magnetic susceptibility of the SiC sample grown on the (110) silicon surface demonstrates a transition from the diamagnetic state to the paramagnetic state – dia-para-hysteresis (Fig. 1(a)). Similar behavior of the static magnetic susceptibility was previously discovered in low-temperature experiments on the boron-doped diamond synthesized at high pressures (~ 100 000 *atm*.) and temperatures above 2500 *K* [11].

As was shown [11, 2], the observed phenomenon is an experimental demonstration of the Meissner-Ochsenfeld effect, which is quite unexpected at room temperature due to the seemingly obvious dominance of the electron-electron interaction in the structure under study. At the same time, the reduction of the electron-electron interaction at room temperature in thin SiC epitaxial layers grown by the method of the coordinated substitution of atoms on the (110) single-crystal silicon surface primarily can arise from the vacancy microdefects presence, which is generated during the synthesis of the SiC layers on the silicon surface, while further boron doping results in the formation of the dipole boron centers with negative correlation energy in the vicinity of the microdefects. The electrostatic field of the negative-U dipole boron centers is exactly responsible for the electron-electron interaction reduction.

As was shown in [9], in the studied structure the "strong-field" criterion at room temperature at an extremely low charge carrier effective mass value is implemented. Moreover, the local phonon mode, which is caused by the dipole boron centers reconstruction, can result in the effective local cooling of the structure at room temperature [13,14].

Within the framework of this approach, apparently, the existence of a superconducting state in the system under study can be accepted, which explains the observed hysteresis of the static magnetic susceptibility of the sample.

Returning to the analysis of the magnetic susceptibility field dependence, it should be noted that the experimental results demonstrate the modulation on the hysteresis curve. The oscillations observed in the weak magnetic field on the background of the hysteresis were interpreted as the macroscopic quantum Aharonov-Bohm effect.

In the presented paper, we only discuss the two mentioned macroscopic quantum magnetic effects, without going into the other features of obtained experimental curve. The Aharonov-Bohm quantum oscillations (A – B) are determined by the change in the value of the magnetic flux passing through the plane of the sample, $\Delta\Phi = \Delta n \Phi_0$, where Φ_0 is the magnetic flux quantum. If the area of an interference circuit S penetrated by the magnetic

field is constant, then the magnetic flux quantum is defined as $\Phi_0 = \Delta BS$, and ΔB is the period of oscillations in the external field. It should be noted, that the experimental observation of the Aharonov-Bohm oscillations on the field dependencies of the static magnetic susceptibility is possible only if the length of the closed carrier trajectory L is less than the phase relaxation length L_φ. Since in this paper we are talking about the superconducting properties of the low-dimensional structure under study, it should be also noted, that the mentioned condition must be satisfied for both one- and two-particles interference.

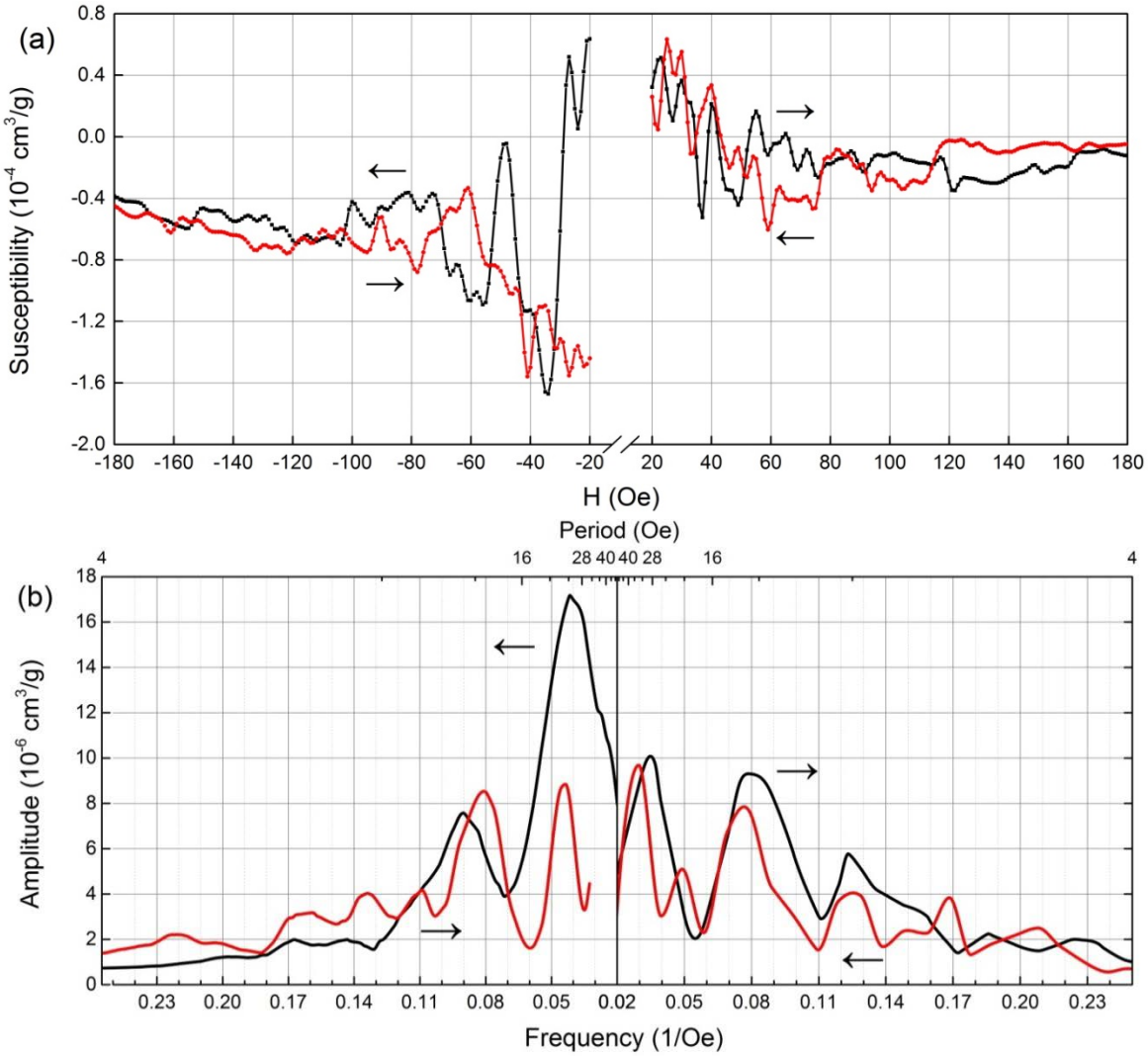

Fig. 1. The magnetic susceptibility (a) of the sample for negative and positive directions of the external magnetic field (arrows indicate the direction of increase/decrease in the magnetic field modulus), as well as the Fourier-analysis results (b) for the presented dependencies, respectively

The observation of the A – B oscillations in the SiC nanolayers grown by the method of the coordinated substitution of atoms on the silicon surface determines the condition for the carriers' interference existence on the microdefect of the structure under study and, thus, provides important information about its electric and magnetic properties.

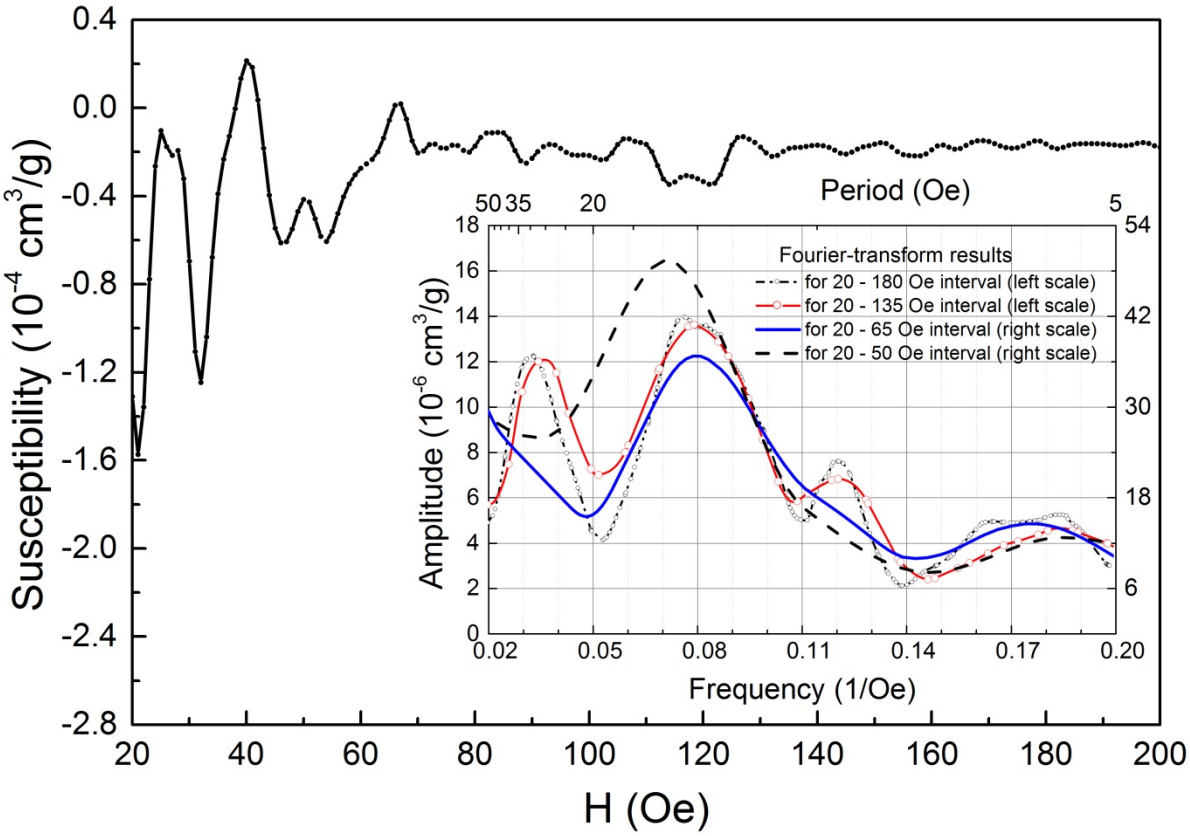

Fig. 2. The magnetic susceptibility and the corresponding Fourier spectrum, which demonstrates the existence of two- and one-particle interference of charge carriers in the range of magnetic fields up to 180 *Oe*, as well as the dominance of the superconducting state in the fields range up to 65 *Oe*

The Fourier analysis of the experimental dependencies of the static magnetic susceptibility carried out in this paper made it possible to determine the periods of the A – B oscillations with good accuracy. The oscillations with the periods of 12.5 and 25 *Oe*, which are in our opinion responsible for the appearance of two-particle ($\Phi_0 = h/2e$) and single-particle ($\Phi_0 = h/e$) interference, respectively, and manifest themselves during the process of the single magnetic flux quanta capture, are the most reliably identified in the obtained spectrum.

The occurrence of the above-mentioned oscillations is attributed to the presence of the vacancy microdefects with the sizes of $\sim 1.65\ \mu m^2$ in the SiC/Si structure under study, which is confirmed both by the corresponding structural research and microdefects similarity to the sizes of the pores formed on the surface of the single-crystal silicon under the SiC layer during the synthesis of SiC.

Here we discuss the effects observed in the range of magnetic fields up to 180 *Oe* (Fig. 2). The analysis of the magnetic susceptibility field dependence of the structure under study demonstrates that in the magnetic field above 50 *Oe* there is a dominance of the A – B oscillation with the period equals to 25 *Oe*, while for the fields below 50 *Oe* the oscillations with the periodicity of 12.5 *Oe* are observed. Thus, it can be assumed that in the vicinity of the magnetic field H = 50 *Oe* there is a critical field value, above which the destruction of the carriers, which is the analogue of the Cooper pair, occurs.

5. Conclusions

The presence of the negative-U dipole centers made it possible to realize such qualities as the low effective mass of the carriers and the strong reduction of the electron-electron interaction in the structure under study, which provided the realization of the "strong-field" criterion and determined the possibility of the observation of macroscopic quantum effects in weak magnetic fields at room temperature.

In the SiC structure grown by the method of the coordinated substitution of atoms on the (100) Si surface in weak magnetic fields both one- and two-particle interference were observed, which is possible only when the superconducting state is realized at room temperature.

At low magnetic fields at room temperature, the measured magnetic susceptibility of the SiC sample the transition from diamagnetic state to paramagnetic state – dia-para-hysteresis – was demonstrated, which confirms the occurrence of the high-temperature superconductivity.

References

1. Kukushkin SA, Osipov AV. A new mechanism of elastic energy relaxation in heteroepitaxy of monocrystalline films: Interaction of point defects and dilatation dipoles. *Mechanics of Solids*. 2013;48(4): 216-227.
2. Kukushkin SA, Osipov AV. New method for growing silicon carbide on silicon by solid-phase epitaxy: model and experiment. *Physics of the Solid State*. 2008;50(7): 1238-1245.
3. Kukushkin SA, Osipov AV. Theory and practice of SiC growth on Si and its applications to wide-gap semiconductor films. *Journal of Physics D: Applied Physics*. 2014;47: 313001.
4. Kukushkin SA, Osipov AV. Nanoscale single-crystal silicon carbide on silicon and unique properties of this material. *Inorganic Materials*. 2021;57(13): 1319-1329.
5. Kukushkin SA, Osipov AV. Epitaxial silicon carbide on silicon. Method of coordinated substitution of atoms (A Review). *Russian Journal of General Chemistry***.** 2022;92(4): 584-610.
6. Kukushkin SA, Osipov AV. The optical properties, energy band structure, and interfacial conductance of a 3*C*-SiC(111)/Si(111) heterostructure grown by method of atomic substitution. *Technical Physics Letters*. 2020;46(11): 1103-1106.
7. Kukushkin SA, Osipov AV. Anomalous properties of the dislocation-free interface between Si(111) substrate and 3*C*-SiC(111) epitaxial layer. *Materials*. 2021;14(1): 78-90.
8. Kukushkin SA, Osipov AV. Spin polarization and magnetic moment in silicon carbide grown by the method of coordinated substitution of atoms. *Materials.* 2021;14(19): 5579-5592.
9. Bagraev NT, Kukushkin SA, Osipov AV, Romanov VV, Klyachkin LE, Malyarenko AM, Khromov VS. Magnetic properties of thin epitaxial SiC layers grown by the atom-substitution method on single-crystal silicon surfaces. *Semiconductors*. 2021;55(2): 137-145.
10. Romanov VV, Kozhevnikov VA, Mashkov VA, Bagraev NT. Description of magnetization oscillations of a silicon nanostructure in weak fields at room temperature. The Lifshitz – Kosevich formula with variable effective carrier mass. *Semiconductors*. 2020;54(12): 1593-1597.
11. Ekimov EA, Sidorov VA, Bauer ED, Mel'nik NN, Curro NJ, Thompson JD, Stishov SM, Superconductivity in diamond. *Nature.* 2004;428: 542-545.
12. Bagraev NT, Klyachkin LE, Koudryavtsev AA, Malyarenko AM, Romanov VV. Superconducting properties of silicon nanostructures. *Semiconductors.* 2009;43(11): 1441-1454.
13. Šimánek E. Superconductivity at disordered interfaces. *Solid State Communications.* 1979;32(9): 731-734.

14. Ting CS, Talwar DN, Ngai KI. Possible mechanism of superconductivity in metal-semiconductor eutectic alloys. *Physical Review Letters.* 1980;45(14): 1213-1216.

THE AUTHORS

Bagraev N.T.
e-mail: Nikolay.Bagraev@gmail.com
ORCID: 0000-0001-8991-6784

Kukushkin S.A.
e-mail: sergey.a.kukushkin@gmail.com
ORCID: 0000-0002-2973-8645

Osipov A.V.
e-mail: andrey.v.osipov@gmail.com
ORCID: 0000-0002-2911-7806

Romanov V.V.
e-mail: romanov@phmf.spbstu.ru
ORCID: 0000-0002-3440-8237

Klyachkin L.E.
e-mail: leonid.klyachkin@gmail.com
ORCID: 0000-0001-7577-1262

Malyarenko A.M.
e-mail: annamalyarenko@mail.ru
ORCID: 0000-0002-4667-7004

Rul' N.I.
e-mail: rul.nickolai@mail.ru
ORCID: 0000-0001-8991-6784

Materials Physics and Mechanics. 2022;50(1): 74-88
Research article
http://dx.doi.org/10.18149/MPM.5012022_6

Submitted: May 28, 2022
Approved: August 2, 2022
Accepted: August 18, 2022

Numerical study of thin UHPC targets response against ballistic impact

M. Bisht[1]✉, M.A. Iqbal[1], K. Kamran[1], V. Bratov[2], N.F. Morozov[2,3]

[1]Department of Civil Engineering, Indian Institute of Technology Roorkee, Roorkee-247667, India

[2]Institute for Problems in Mechanical Engineering, Russian Academy of Sciences, Saint Petersburg, Russia

[3]Department of Theory of Elasticity, Saint Petersburg State University, Saint Petersburg, Russia

✉ bishtm809@gmail.com

Abstract. The modelling of concrete and its dynamic strength analysis has been an interesting field which seeks many researchers' attention for the last few decades. The material behavior of concrete in extreme dynamic events like blast and impact calls for the understanding of its dynamic characterization as well which demand a suitable material model that can depict the behavior of concrete under high strain rate, high pressure, and large deformations. One of the most used constitutive material models for concrete is HJC (Holmquist Johnson Cook). This model covers most of the essential features of concrete pertaining to response against blast and impact loads. The objective of this paper is to provide an in-depth assessment of the HJC model implemented in ABAQUS Explicit finite element code. The assessment involves various tests such as compression, tensile and tri-axial tests on a single element followed by validation of the numerical model with the help of ballistic experimental tests available in the open literature. Finally based on the assessment, the HJC material model utility for the behavior of thin i.e., H/d $\geq$ 5, UHPC (Ultra High-Performance Concrete) targets against impact loading has been discussed.

Keywords: HJC (Holmquist Johnson Cook), UHPC (Ultra High-Performance Concrete), ABAQUS Explicit finite element code, ballistic experimental tests

Acknowledgements. *Authors gratefully acknowledge the financial support provided by the Department of Science and Technology (DST) India and Russian Foundation for Basic Research (RFBR) Russia through research grant nos. INT/RUS/RFBR/DST-1509-CED for successfully carrying out this work.*

Citation: Bisht M, Iqbal MA, Kamran K, Bratov V, Morozov NF. Numerical study of thin UHPC targets response against ballistic impact. *Materials Physics and Mechanics*. 2022;50(1): 74-88. DOI: 10.18149/MPM.5012022_6.

1. Introduction

The wide utility of concrete material in many critical structures such as nuclear, defense, and protective structures demand the study of its behavior exposed to extreme loadings. To meet this demand, many studies had been carried out on the concrete behavior under extreme dynamic events such as blast and ballistic impact events in literature [1]. All of the studies consist of either experimental assessment [2-8] or investigation through any available FEM tools [9,10] or analytical models [11,12] or combination of any of these two or more methods [13,14]. The development of commercial FEM tools in the past two decades now make it

Publisher: Peter the Great St. Petersburg Polytechnic University

possible to develop a more accurate constitutive material model which is able to produce material behavior in a good agreement to a greater extent. Otherwise, the ballistic impact study was restricted to majorly empirical assessment methods only in which targets were divided into two domains i.e., semi-infinite targets and finite thickness targets. Where, semi-infinite targets were used to investigate the deep penetration process into humongous concrete structures by assuming zero lateral boundary effect whereas, finite target thickness was put to use in the study of projectile perforation.

UHPC being a novel material, all its study by the researchers has been majorly done in the last two decades only and are still in progress. Three types of commercially produced concrete having nominal unconfined compressive strength as 35.75 and 110 MPa were cast in order to perform the ballistic impact tests on 50 mm thick targets impacted against by 20 mm diameter ogival nosed steel projectiles. The ballistic impact tests were then examined in terms of the ballistic limit curve and its velocity for each concrete type. Furthermore, various material tests were also conducted to examine the mechanical properties of the concrete. Finally, the Modified HJC material model was calibrated and validated with the experimental ballistic perforation results in good agreement through LS Dyna FEM tool [15].

Ballistic perforation tests had been carried out on thin 129 MPa UHP-SFRC targets. The range of UHP-SFRC (Ultra High-Performance Steel Fibre Reinforced Concrete) targets thickness varied from 40 mm to 100 mm and the diameter of the projectile was 25.3 mm with a 3 CRH (Caliber Radius Head) ogival nose measured 331 grams in weight. The objective of the study was to capture the residual velocities of normally perforated projectiles with the help of high-speed cameras in order to develop a semi-analytical projectile perforation model for thin concrete slabs i.e., H/d is less than or equal to 5. Subsequently, the developed semi-analytical model was validated by the existing available perforation test data on a thin concrete slab. Furthermore, the developed model show results in good agreement when put forward to investigate the ballistic resistance of spaced layered concrete targets [16].

The ballistic impact of UHPCC (Ultra High-Performance Cement-based Composites) developed with steel fibres and basalt coarse aggregates was experimentally evaluated by carrying out very high-velocity projectile penetration tests ranging from 510 m/s to 1320 m/s. It was observed that as the impact velocity go beyond 1000 m/s, the projectile no more behaved like a rigid mass projectile. On the basis of parameters influential analyses, it was observed that the most effective and cost-effective selection for the anti-strike protective structure was UHPCC which was having 90 MPa as compressive strength with 1.5 % of steel fibres in the mix. It was further validated through experimental results that UHPCC performed outstandingly against ballistic impact in terms of reducing the depth of penetration, deviating the terminal ballistic trajectory of the abrasive projectile, and reducing the crater damage dimensions [17].

The study of damage caused by explosion-generated fragments impact had been done through the behavior of several UHPFRC (Ultra High-Performance Fibre Reinforced Concrete) targets against small firearm projectile impact. The range of real ammunition impact velocity was kept between 691 m/s to 720 m/s. Moreover, fibre content in the UHPFRC mix was increased up to 3 % by volume to examine the effect of fibres on the target damage in terms of penetration depth, debris fragment mass, crater diameter, and residual penetration potential of the bullet. On the basis of experimental observations, it was concluded that the optimum fibre amount in the UHPFRC mix came out to be 2 %. Less than 2 % fibres lead to an increased volume of secondary fragments generated from the rear side of the targets and also the residual penetration potential of the small fire ammunition leaving from the rear side of the target was found to be higher. Whereas, more than 2 % fibres showed no significant improvements in all the damage parameters [18].

The experimental impact resistance study of concrete having compressive strength ranging from 45 MPa to 235 MPa was carried out. The concrete targets were impacted by a 12.6 mm ogive nosed projectile with 15 grams in weight at impact velocities ranging from 620 m/s to 700 m/s. it was witnessed that as the compressive strength of the concrete target increased, the penetration depth and crater diameter magnitude decreased with a non-linear trend. Moreover, the presence of steel fibres did not show any substantial influence on penetration depth unlike the presence of coarse granite aggregates. However, both steel fibres, as well as coarse granite aggregates, proved to be advantageous in order to minimize the crater diameter and crack propagation thereby increasing the impact resistance. Finally, it was concluded that the most effective anti-strike protective high-strength fibre reinforced concrete target was the one which was having compressive strength of 100 MPa [19].

The study of novel UHPC behavior under extreme dynamic events like blast and impact loadings is a new field for many researchers across the globe because of its high capacity to absorb energy, greater resistance to impact loadings, being a novel material [20-22] and high utility in major infrastructure susceptible to dynamic loadings are the few reasons out of many. This present paper aims to provide in-depth evaluation of the HJC material model implemented in ABAQUS Explicit finite element code in order to find its utility for the UHPC behavior under impact dynamic loading.

2. Constitutive Material Model: HJC

The HJC [23] material model was developed by Holmquist, Johnson, and Cook in 1993 in order to describe the dynamic behavior of concrete subjected to high pressures, high strain rates, and large deformations. It is an elastic-viscoplastic model and consists of three components as Strength, Damage, and Equation of State model. All three model components are briefly described below one by one:

Strength Model is an illustration of the intact and fractured material's normalized deviatoric strength in the form of normalized pressure-dependent yield surface as shown in Fig. 1. The normalized deviatoric strength can be given as the function of the pressure and strain rate as

$$\sigma^* = [\mathrm{A}\,(1-\mathrm{D}) + \mathrm{B}\,(P^*)^N]\;\;[1+\mathrm{C}\ln(\dot{\varepsilon}^*)] \le S_{max}\,, \tag{1}$$

where σ^* is the normalized deviatoric strength.

Further, ABAQUS Explicit finite element code assumes plastic flow to be isochoric i.e., volume-preserving using a Mises flow surface.

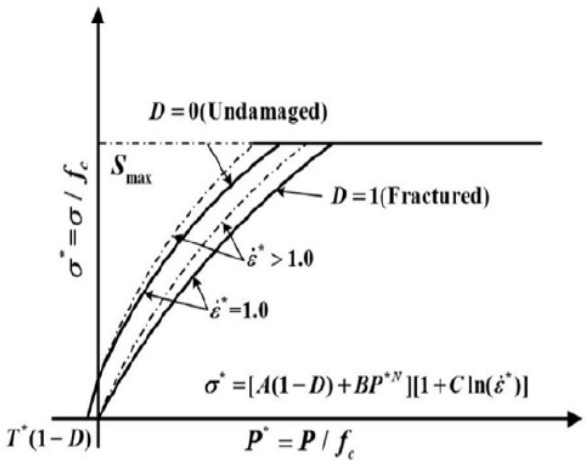

Fig. 1. Strength of HJC model [24]

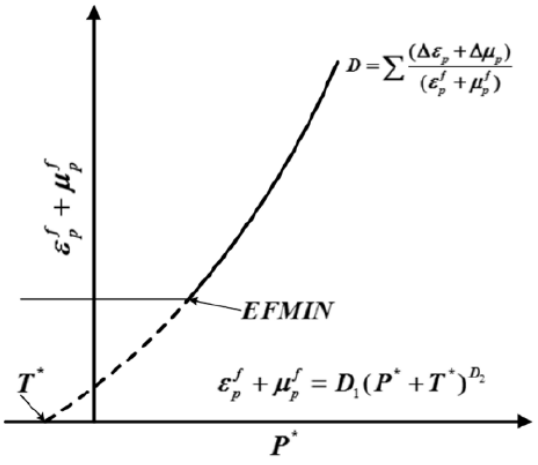

Fig. 2. Damage of HJC model [24]

Damage Model explains how the damage variable accumulates with the equivalent plastic strain and volumetric plastic strain as shown in Fig. 2. Moreover, the concrete material can not undergo any plastic strain at P^* equals to T^*, and plastic strain to fracture increases as P^* increases. Whereas, in order to suppress fracture from low magnitude tensile waves, EFMIN is introduced which allows for a finite amount of plastic strain to fracture the material. Although, under most conditions, the majority of the damage would occur only from equivalent plastic strain damage due to plastic volumetric strain is also included in this model to take into account the loss of cohesive strength during air void collapse.

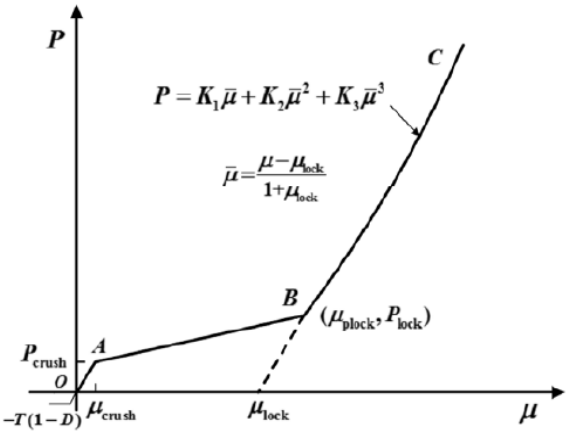

Fig. 3. EOS of HJC model [24]

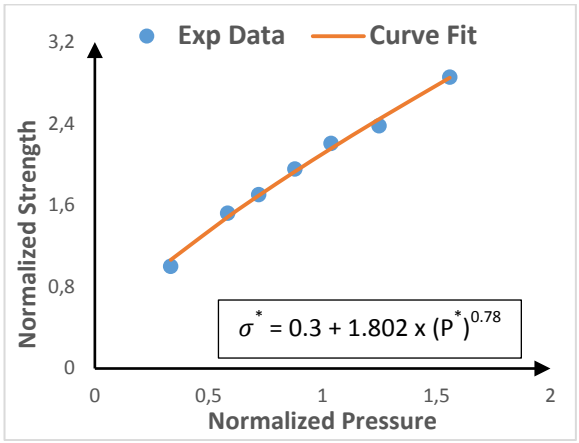

Fig. 4. HJC-Strength Model Curve fit

Table 1. HJC material model parameters used in the present study

Material Parameters	**Numerical Value**
Density (kg/m^3)	2600
Shear Modulus (GPa)	22
Strength Model	**HJC**
Normalized Cohesive strength, A	0.3
Normalized pressure hardening coefficient, B	1.802
Pressure hardening exponent, N	0.78
Strain rate coefficient, C	0.005
Quasi-static uniaxial compression strength, f_{ck} (GPa)	0.129
Normalized maximum strength, S_{max}	3.5
Damage Model	**HJC**
Parameter for plastic strain to fracture, D_1	0.04
Parameter for plastic strain to fracture (exponent), D_2	1
Equation of State	**Polynomial**
Pressure at crushing, P_{crush} (GPa)	0.043
Volumetric strain at crushing, μ_{crush}	0.001
Pressure at fully compaction, P_{lock} (GPa)	3.47
Volumetric strain at fully compaction, μ_{lock}	0.11
First pressure coefficient, K_1 (GPa)	116
Second pressure coefficient, K_2 (GPa)	-243
Third pressure coefficient, K_3 (GPa)	506
Maximum tensile hydrostatic pressure, T (GPa)	0.006

Equation of State Model explains the pressure-volume response of the material under compression as shown in Fig. 3. The response is divided into three regions. The first region

depicts the linear elastic behavior. The second region depicts the linear inelastic behavior or also refer as the transition region. In this region, the air voids are progressively expelled out of the concrete resulting in volumetric plastic strain. And the third region represents the fully compacted material behavior through the cubic polynomial equation. In this region, no air voids are left in the concrete matrix.

HJC material model parameters Assuming 'A' as 0.3, HJC strength model parameters *B* and *N* are confirmed as 1.802 and 0.78 respectively through curve fitting of experimental Tri-axial tests data [25] as shown in Fig. 4 by neglecting strain rate effect i.e., 'C' equals to 0. All the other model parameters are taken directly from available literature [24]. Readers are advised to refer [23,24] in order to get more insight into the procedure for determining the material constants. Table 1 shows all the HJC material model parameters used for UHPC material in the present numerical study.

3. Numerical Study

In this section of the paper, numerical study on HJC material model implemented in ABAQUS Explicit FEM code has been carried out. This is done by performing various tests on a single element required to examine the HJC material model. Furthermore, a numerical model is also developed to validate the experimental ballistic test results through HJC material model. Finally, the results obtained from the numerical study are discussed and concluded.

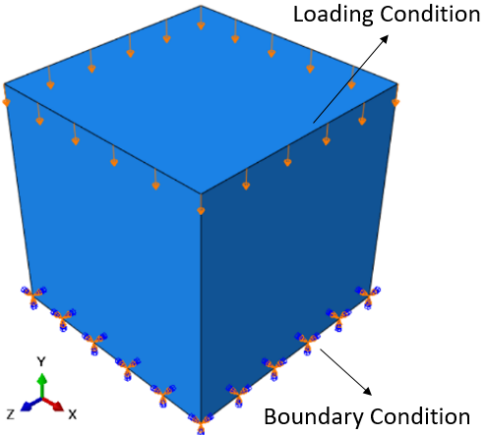

Fig. 5. Boundary conditions for compression test on a single element

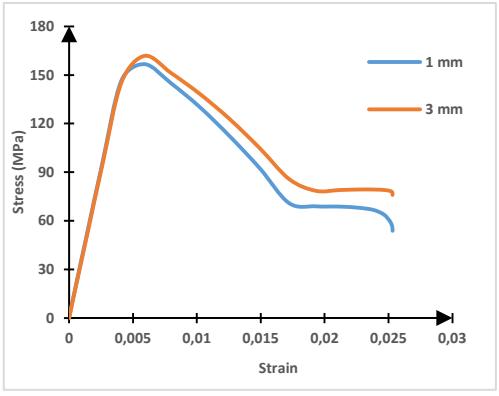

Fig. 6. Compression stress-strain curve

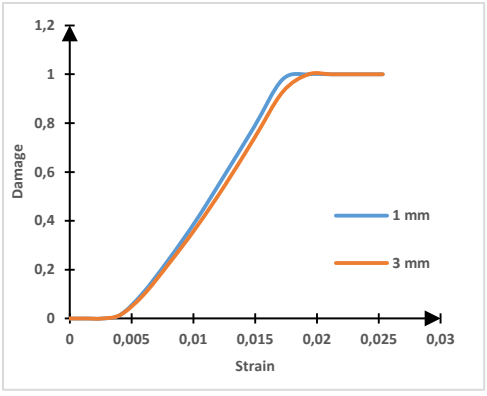

Fig. 7. Evolution of damage

Compression Tests on 1 mm and 3 mm C3D8R (Continuum 3 Dimensional 8 Node Reduced Integrated) single element are carried out separately. The boundary conditions of the single element are shown in Fig. 5 in which translational and rotational motion of the bottom

plane surface is restricted in all directions and the compression loading is provided through the downward displacement of the top surface. The stress-strain curve of a single element under compression is shown in Fig. 6 and the development of damage in the element with respect to strain is shown in Fig. 7. It has been noticed that the developed damage reaches one as the element approaches its critical state or residual stress state. Furthermore, no significant difference is observed in the stress-strain curve of 1 mm and 3 mm C3D8R single element under compression.

Tri-axial Tests on 1 mm C3D8R single element are carried out at various confinement pressure. The boundary conditions of a single element under the Tri-axial test are shown in Fig. 8 in which translational and rotational motion of the bottom plane surface is restricted in all directions, an instantaneous pressure load is provided on all the surfaces followed by the downward displacement loading on the top surface. The stress-strain curves of a single element under the Tri-axial test at four various confinement pressure obtained from numerical study are shown in Fig. 10. Tri-axial numerical test results at four various confinement pressure are found to be in good agreement with Ren et al. [25] experimental test results as shown in Fig. 9. Although a significant difference in the numerical strength result when compared to the experimental strength result is detected at the unconfined i.e., 0 MPa Tri-axial test or simple compression test as shown in Fig. 11.

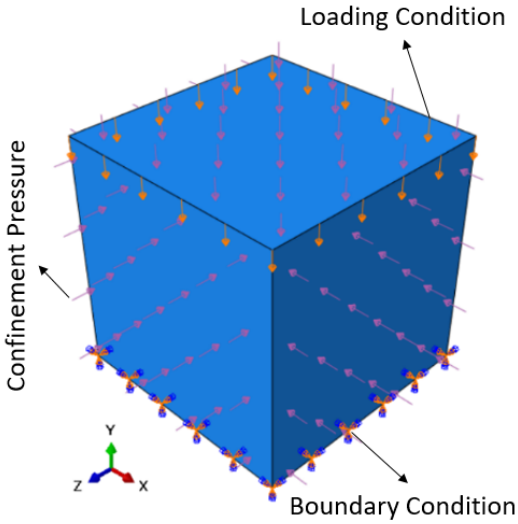

Fig. 8. Boundary conditions for tri-axial test on a single element

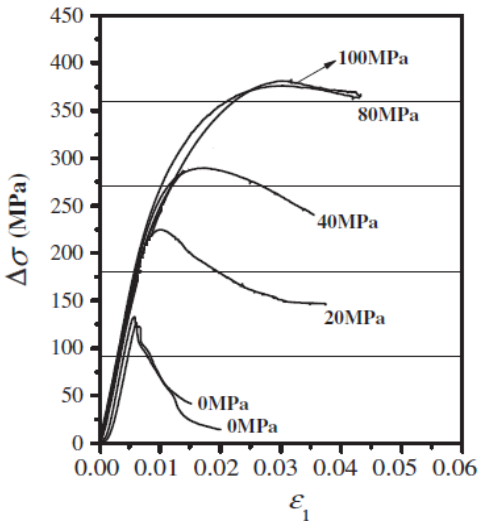

Fig. 9. Exp. Tri-axial stress-strain curve [25]

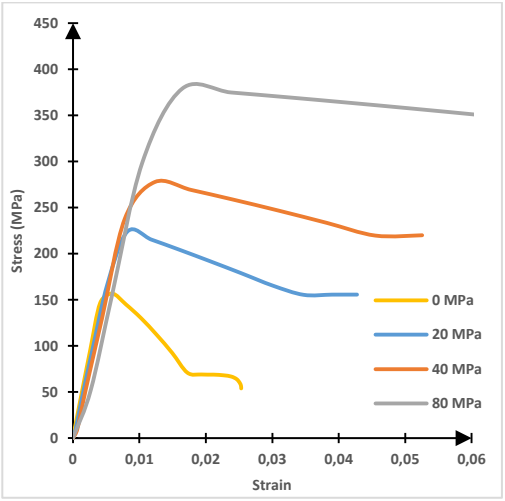

Fig. 10. Num. Tri-axial stress-strain curve

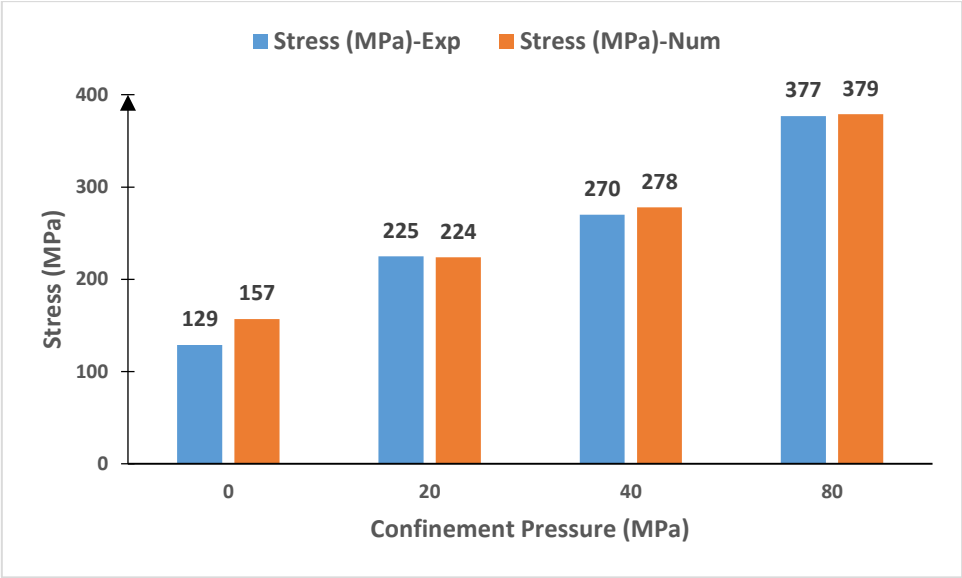

Fig. 11. Comparison of Exp. & Num. Tri-axial test results

Tensile Test on 1 mm C3D8R single element is carried out. The boundary conditions of the single element are shown in Fig. 12 in which translational and rotational motion of the bottom plane surface is restricted in all directions and the tensile loading is provided through the upward displacement of the top surface. The stress-strain curve of a single element under tensile loading is shown in Fig. 13 and the evolution of damage in the element with respect to strain is shown in Fig. 14. Similar to the unconfined compression test results, here also numerical study result overestimates the experimental study result since the tensile strength input in HJC material model is 6 MPa.

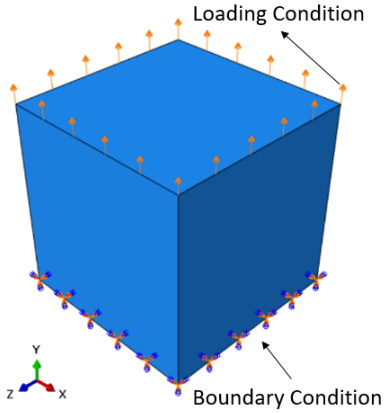

Fig. 12. Boundary conditions for tensile test on a single element

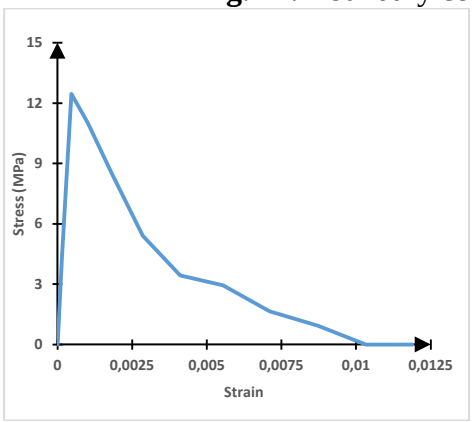

Fig. 13. Tensile stress-strain curve

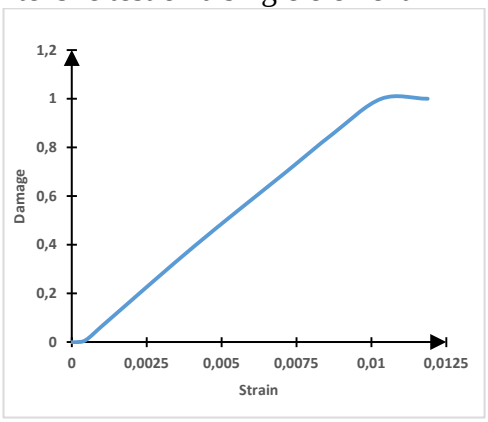

Fig. 14. Evolution of damage

Validation The numerical model validation is done with the help of Peng et al. ballistic study [16]. He had carried out a projectile perforation test on the thin UHP-SFRC slabs, in which the diameter of the projectile was 25.3 mm and the thicknesses of slabs ranged from 40 mm to 70 mm. All the slabs were perforated normally and the projectile residual velocities were captured by a high-speed camera.

In the developed numerical model, HJC constitutive material model is used for UHP-SFRC targets whereas, the analytical rigid material model is assigned to the steel projectile as no deformation was observed in the projectiles after perforation in the ballistic tests. UHP-SFRC targets having a clear arial dimension of 400 × 400 mm with thickness ranging from 40 mm to 70 mm were impacted by 331 grams, 3.0-caliber radius head ogival nose steel projectile with 25.3 mm shank diameter and total length of 152 mm. Surface-to-surface interaction with kinematic contact algorithm has been provided between the steel projectile and UHP-SFRC target. The peripheral surface edges of UHP-SFRC targets are constrained with respect to all translational and rotational movement as shown in Fig. 15. The UHP-SFRC targets are modelled with linear C3D8R elements of size 1.5 × 1.5 × 1.5 mm, as shown in Fig. 16. Whereas, no meshing has been provided to steel projectile due to its analytical rigid material model.

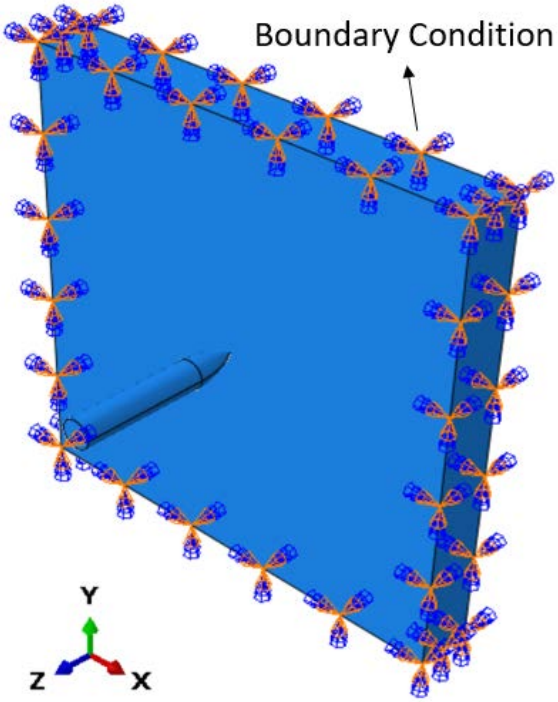

Fig. 15. Numerical model

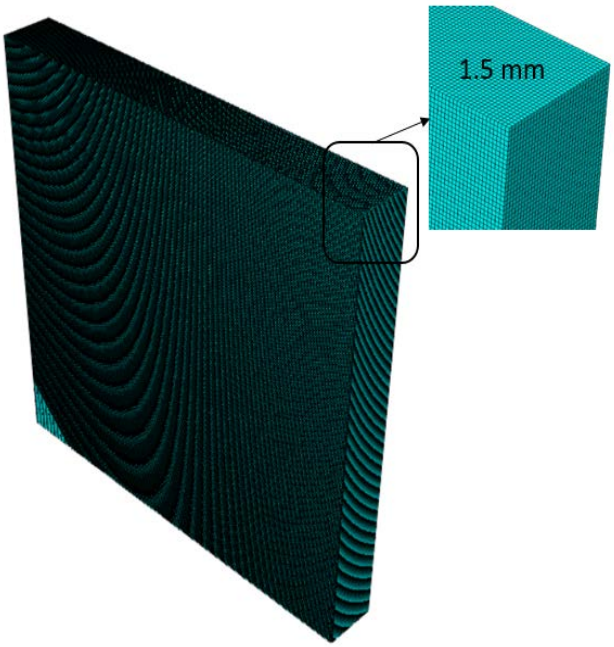

Fig. 16. Mesh on Numerical model

Figures 17 and 18 show the comparison between experimental and numerical model damage on the front and the rear surface of 40 and 70 mm UHP-SFRC targets against steel projectile with 352 and 348 m/s impact velocities respectively. The diameter of the front and the rear damages obtained from experimental ballistic test are found to be 62.3 and 106 mm on 40 mm thick target and 107 and 129 mm on 70 mm thick target respectively. Whereas, the diameter of the front and the rear damages obtained from numerical ballistic test are found to be 85 and 119 mm on 40 mm target and 98 and 150 mm on 70 mm thick target respectively.

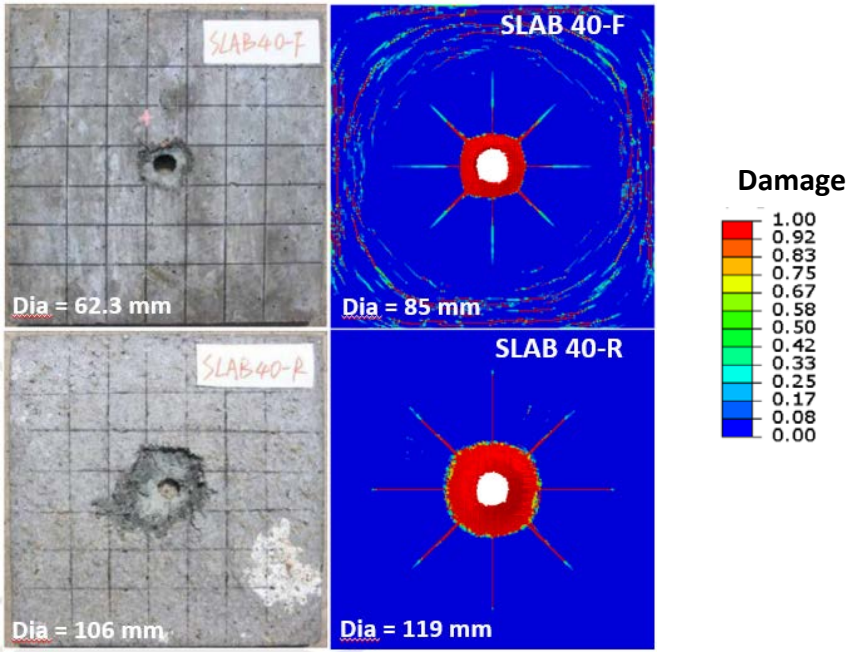

Fig. 17. Experimental and numerical model damage on the front (F) and the rear (R) of 40 mm UHP-SFRC targets @ 352 m/s impact velocity

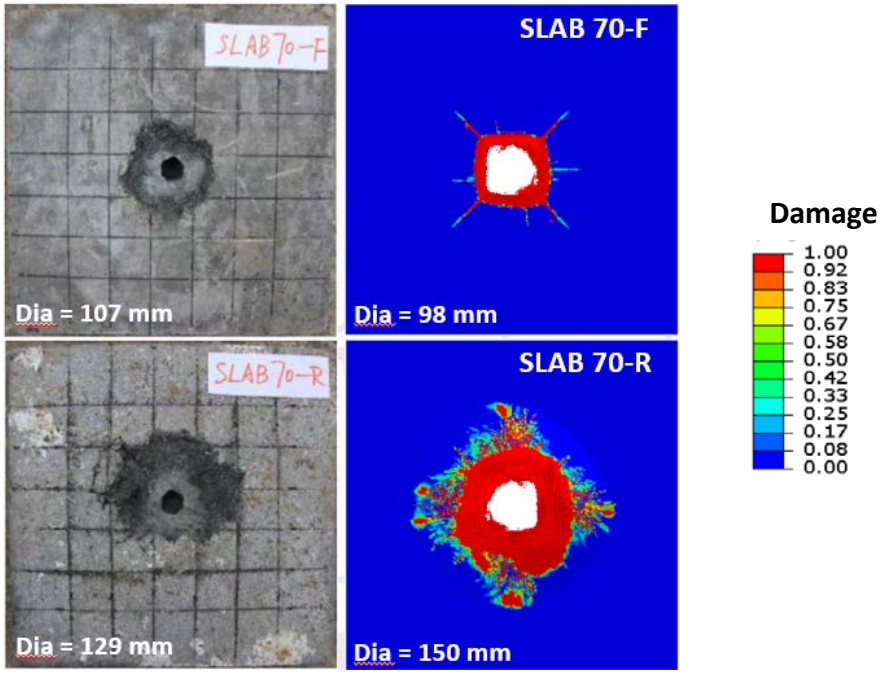

Fig. 18. Experimental and numerical model damage on the front (F) and the rear (R) of 70 mm UHP-SFRC targets @ 348 m/s impact velocity

Table 2 shows the ballistic perforation results obtained from the numerical study which are in very good agreement with respect to the experimental study as the maximum error was found to be 2.92 % for 50 mm thick UHP-SFRC at 250 m/s impact velocity. Moreover, Figure 19 shows the comparison between experimental and numerical ballistic perforation results of 50 mm thick targets against steel projectile impact in terms of residual velocities corresponding to various impact velocities i.e., 250, 347, and 478 m/s through a histogram plot. Similarly, Figure 20 shows the comparison between experimental and numerical ballistic perforation results of 40, 50, 60, and 70 mm thick targets against steel projectile impact in

terms of residual velocities corresponding to 352, 347, 341, and 348 m/s impact velocities respectively through histogram plot.

Table 2. Ballistic Perforation Results of 40, 50, 60, and 70 mm thick UHP-SFRC targets

Thickness	Impact Velocity (m/s)	Residual Velocity (m/s)		
		Exp	Num	Error (%)
50 mm	250	171	176	2.92
	347	283	280	-1.06
	478	425	416	-2.12
40 mm	352	305	303	-0.66
60 mm	341	251	248	-1.20
70 mm	348	232	232	0.00

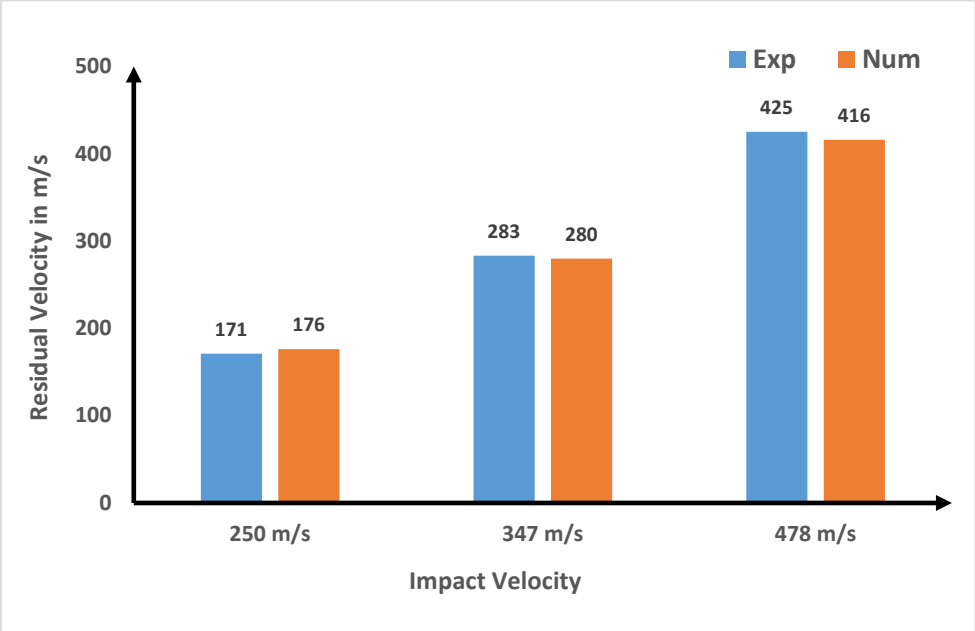

Fig. 19. Ballistic perforation results of 50 mm targets

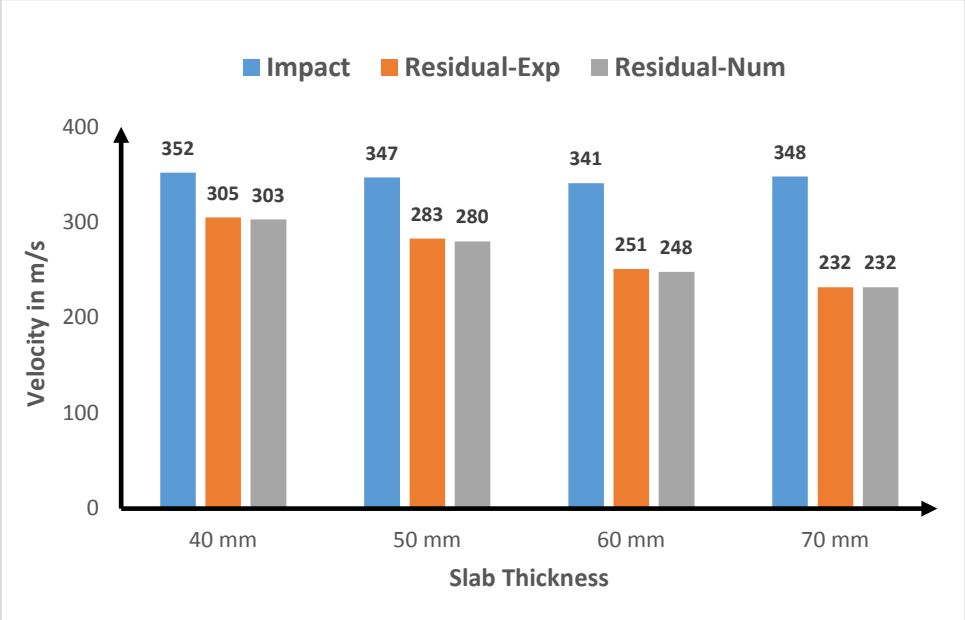

Fig. 20. Ballistic perforation results of 40, 50, 60, and 70 mm targets

Figure 21 shows damage on the front and the rear surface of 50 mm UHP-SFRC targets against steel projectile obtained from the numerical study at 250, 347, and 478 m/s impact velocities. The diameter of the front and the rear surface damages are found to be 97 mm and 173 mm at 250 m/s impact velocity, 95 mm and 141 mm at 347 m/s impact velocity, and 90 mm and 114 mm at 478 m/s impact velocity. It is observed that the nature of the damage gets transformed from global to local as the impact velocity increases from 250 to 478 m/s. This is because of the fact that as the impact velocity increases, the duration of loading decreases, and thus the whole target does not get sufficient time to respond against it. As a result, only the portion which is near in the vicinity of the fast-moving steel projectile responds and gets damaged.

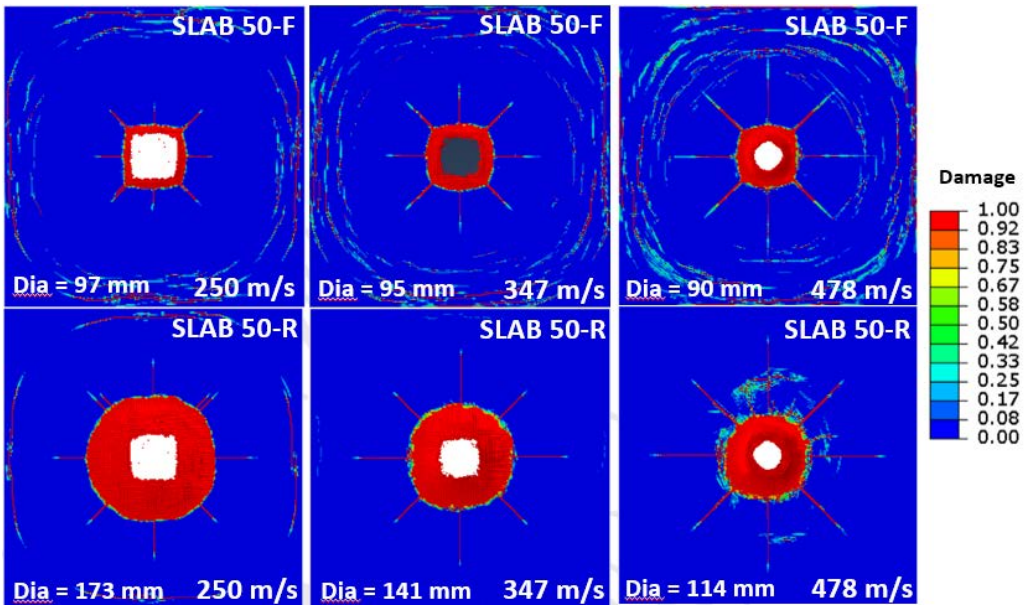

Fig. 21. Numerical model damage on the front (F) and the rear (R) of 50 mm UHP-SFRC targets at 250, 347, and 478 m/s impact velocity

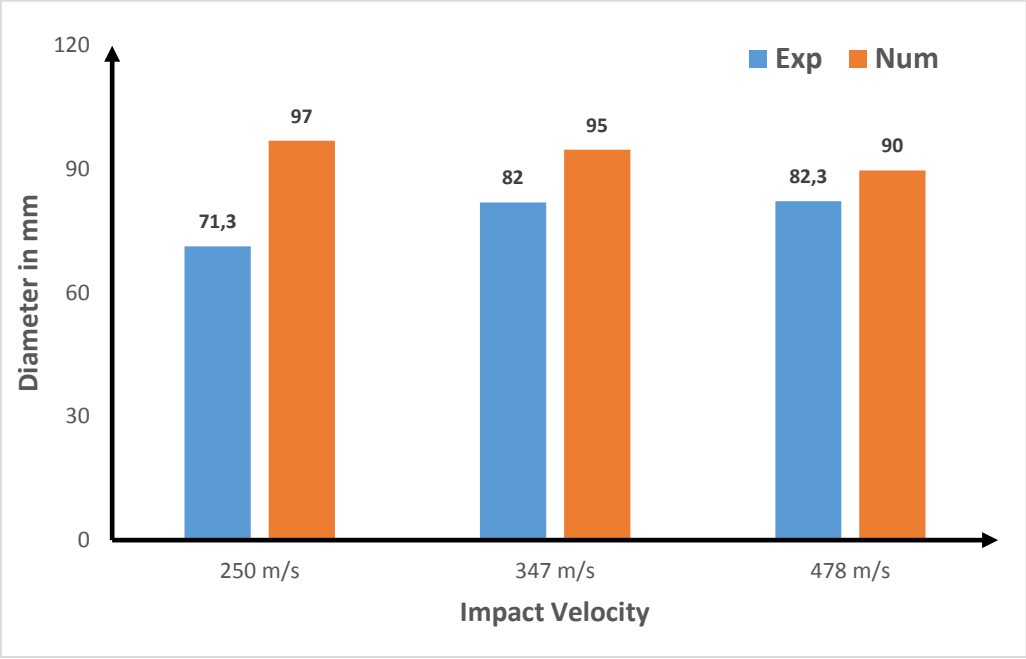

Fig. 22. Front damage crater diameter of 50 mm targets

Figures 22 and 23 show histogram plot comparison between experimental and numerical study's damage on the front and the rear surface of 50 mm thick UHP-SFRC targets at various impact velocities respectively. It has been noticed that as the impact velocity increases the damage results obtained from numerical study converge to damage results obtained from the experimental study. The local damage in the experimental study can be attributed to the steel fibres present in the UHP-SFRC targets, as the steel fibres do not allow cracks to propagate further thus restricting the damage to the near vicinity of the moving steel projectile.

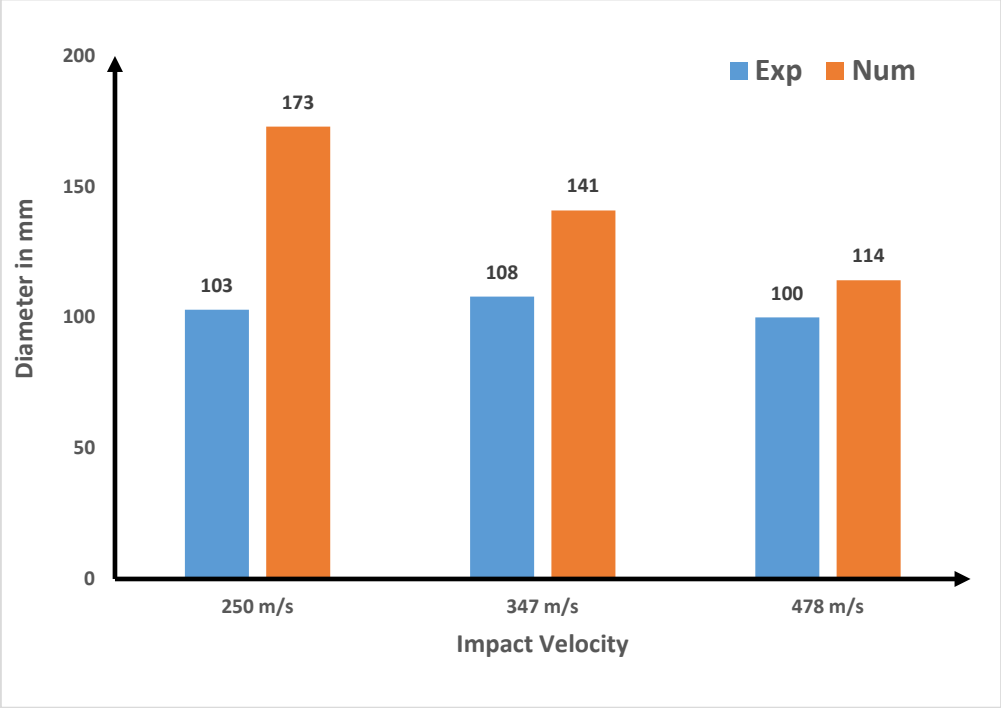

Fig. 23. Rear damage crater diameter of 50 mm targets

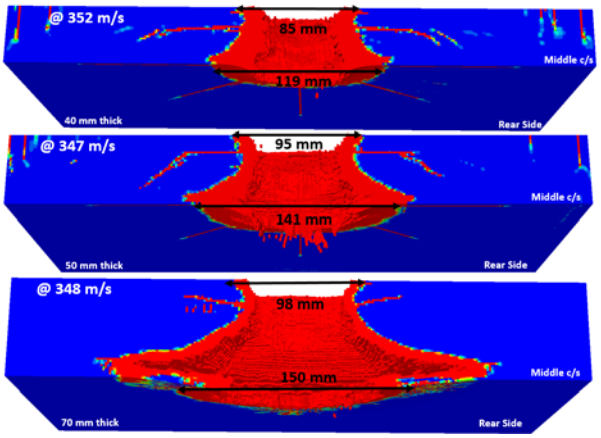

Fig. 24. Damage contour of 40, 50, and 70 mm targets at mid c/s against nearly 350 m/s impact velocity

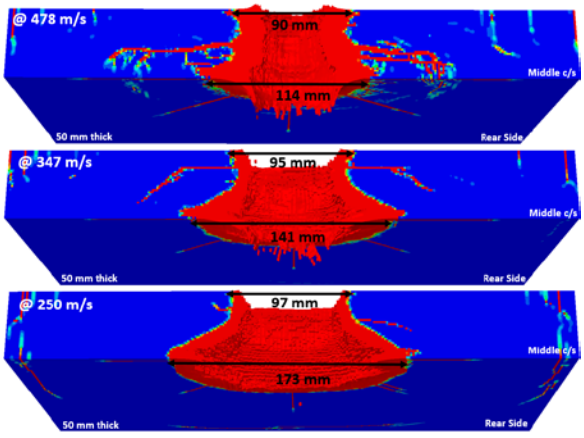

Fig. 25. Damage contour of 50 mm targets at mid c/s against 478, 347, and 250 m/s impact velocity

Figure 24 shows the damage contour variations at the mid-cross-section of the target having 40, 50, and 70 mm thickness at nearly 350 m/s impact velocity respectively. Whereas, Figure 25 shows the damage contour variations at the mid-cross-section of 50 mm targets at

various impact velocities i.e., 478, 347, and 250 m/s respectively. The change in the nature of the damage from local to global appears to be the same as the thickness of the target increases (keeping impact velocity constant) or the impact velocity decreases (keeping the thickness of the target constant).

4. Conclusions

In the present paper, a detailed investigation of HJC material model implemented in ABAQUS software has been carried out. Based on the various tests performed on a single element followed by the ballistic tests, the following conclusions are made:

- The unconfined compression and tensile test results obtained from the numerical study overestimate the test results when compared with the experimental study. It indicates that strength definition in the lower confinement zone is not properly defined in HJC-Strength model.
- However, tri-axial test results at various confinement pressure obtained from the numerical study are found to be in good agreement with the experimental study results.
- Further, ballistic perforation results of 40, 50, 60, and 70 mm thick UHP-SFRC targets obtained from the numerical study in terms of residual velocities and their corresponding impact velocities are found to be in good correspondence with the experimental results with a maximum error of 2.92%.
- Although, the nature of the damage on the front and the rear surface has been found to transform from local to global damage as the impact velocity decreases or the thickness of the target increases. It was so because of two reasons. Firstly, ballistic perforation time duration i.e., as the time duration increases, more area of the target able to involve in the damage mechanism. Secondly, bi-linear strain softening of HJC-Tensile strength model does not incorporate the behavior of strain hardening of UHP-SFRC concrete in tension. The strain hardening behavior of UHP-SFRC concrete in tension is due to the presence of steel fibres which create hindrance in the cracks propagation.

References

1. Das N, Nanthagopalan P. State-of-the-art review on ultra high performance concrete-Ballistic and blast perspective. *Cement and Concrete Composites.* 2022;127: 104383.
2. Máca P, Sovják R, Konvalinka P. Mix design of UHPFRC and its response to projectile impact. *International Journal of Impact Engineering.* 2014;63: 158-163.
3. Dancygier AN, Yankelevsky DZ, Jaegermann C. Response of high performance concrete plates to impact of non-deforming projectiles. *International Journal of Impact Engineering.* 2007;34(11): 1768-1779.
4. Wang S, Le HT, Poh LH, Feng H, Zhang MH. Resistance of high-performance fiber-reinforced cement composites against high-velocity projectile impact. *International Journal of Impact Engineering.* 2016;95: 89-104.
5. Hanchak SJ, Forrestal MJ, Young ER, Ehrgott JQ. Perforation of concrete slabs with 48 MPa (7 ksi) and 140 MPa (20 ksi) unconfined compressive strengths. *International Journal of Impact Engineering.* 1992;12(1): 1-7.
6. O'Neil EF, Neeley BD, Cargile JD. Tensile properties of very-high-strength concrete for penetration-resistant structures. *Shock and Vibration.* 1999;6(5-6): 237-245.
7. Forrestal MJ, Altman BS, Cargile JD, Hanchak SJ. An empirical equation for penetration depth of ogive-nose projectiles into concrete targets. *International Journal of Impact Engineering.* 1994;15(4): 395-405.
8. Almusallam TH, Siddiqui NA, Iqbal RA, Abbas H. Response of hybrid-fiber reinforced concrete slabs to hard projectile impact. *International Journal of Impact Engineering.* 2013;58: 17-30.

9. Murthy A, Palani GS, Iyer NR. Impact Analysis of Concrete Structural Components. *Defence Science Journal.* 2010;60(3): 307-319.
10. Polanco-Loria M, Hopperstad OS, Børvik T, Berstad T. Numerical predictions of ballistic limits for concrete slabs using a modified version of the HJC concrete model. *International Journal of Impact Engineering.* 2008;35(5): 290-303.
11. Forrestal MJ, Altman BS, Cargile JD, Hanchak SJ. An empirical equation for penetration depth of ogive-nose projectiles into concrete targets. *International Journal of Impact Engineering.* 1994;15(4): 395-405.
12. Li QM, Chen XW. Dimensionless formulae for penetration depth of concrete target impacted by a non-deformable projectile. *International Journal of Impact Engineering.* 2003;28(1): 93-116.
13. Shafieifar M, Farzad M, Azizinamini A. Experimental and numerical study on mechanical properties of Ultra High Performance Concrete (UHPC). *Construction and Building Materials.* 2017;156: 402-411.
14. Tai YS. Flat ended projectile penetrating ultra-high strength concrete plate target. *Theoretical and Applied Fracture Mechanics.* 2009;51(2): 117-128.
15. Kristoffersen M, Toreskås OL, Dey S, Børvik T. Ballistic perforation resistance of thin concrete slabs impacted by ogive-nose steel projectiles. *International Journal of Impact Engineering.* 2021;156: 103957.
16. Peng Y, Wu H, Fang Q, Liu JZ, Gong ZM. Residual velocities of projectiles after normally perforating the thin ultra-high performance steel fiber reinforced concrete slabs. *International Journal of Impact Engineering.* 2016;97: 1-9.
17. Wu H, Fang Q, Chen XW, Gong ZM, Liu JZ. Projectile penetration of ultra-high performance cement based composites at 510–1320 m/s. *Construction and Building Materials.* 2015;74: 188-200.
18. Sovjak R, Vavřiník T, Zatloukal J, Maca P, Mičunek T, Frydrýn M. Resistance of slim UHPFRC targets to projectile impact using in-service bullets. *International Journal of Impact Engineering.* 2015;76: 166-177.
19. Zhang MH, Shim VP, Lu G, Chew CW. Resistance of high-strength concrete to projectile impact. *International Journal of Impact Engineering.* 2005;31(7): 825-841.
20. Graybeal B. *Ultra-high performance concrete*. 2011. Available from: https://www.fhwa.dot.gov/publications/research/infrastructure/structures/11038/index.cfm
21. Abdulkareem OM, Fraj AB, Bouasker M, Khelidj A. Mixture design and early age investigations of more sustainable UHPC. *Construction and Building Materials.* 2018;163: 235-246.
22. Abbas SM, Nehdi ML, Saleem MA. Ultra-high performance concrete: Mechanical performance, durability, sustainability and implementation challenges. *International Journal of Concrete Structures and Materials.* 2016;10(3): 271-295.
23. Holmquist TJ, Johnson GR, Cook WH. A computational constitutive model for concrete subjected to large strains, high strain rates, and high pressures. In: *Proceedings of the 14th International Symposium on Ballistics*. 1993.
24. Ren GM, Wu H, Fang Q, Kong XZ. Parameters of Holmquist–Johnson–Cook model for high-strength concrete-like materials under projectile impact. *International Journal of Protective Structures.* 2017;8(3): 352-367.
25. Ren GM, Wu H, Fang Q, Liu JZ, Gong ZM. Triaxial compressive behavior of UHPCC and applications in the projectile impact analyses. *Construction and Building Materials.* 2016;113: 1-4.

THE AUTHORS

Bisht M.
e-mail: bishtm809@gmail.com
ORCID: 0000-0001-7322-947X

Iqbal M.A.
e-mail: ashraf.iqbal@ce.iitr.ac.in
ORCID: 0000-0002-3428-1395

Kamran K.
e-mail: kmrn890@gmail.com
ORCID: 0000-0001-6456-3089

Bratov V.
e-mail: vladimir@bratov.com
ORCID: 0000-0003-0564-0800

Morozov N.F.
e-mail: morozov@NM1016.spb.edu
ORCID: -

Materials Physics and Mechanics. 2022;50(1): 89-106
Research article
http://dx.doi.org/10.18149/MPM.5012022_7

Submitted: March 10, 2022
Approved: May 6, 2022
Accepted: September 15, 2022

Microstructural modeling and prediction of effective elastic properties in 3D reinforced composite material

A.N. Anoshkin, P.V. Pisarev, D.A. Ermakov, K.V. Roman✉

Perm National Research Polytechnic University, Perm, Russia

✉ kvroman@pstu.ru

Abstract: We consider a textile composite material reinforced by carbon fibers with 3D orthogonal braiding and a polymer matrix. Microstructural studies were carried out to find the mean values and variation coefficients for the parameters of the braid unit cell within the reinforcement cage. We have constructed an algorithm along with geometric models for cells and fragments of the composite structure, providing different descriptions for the parameters of the binder yarn. The micromechanics problem was solved by the local approximation method; the fields of structural stresses and strains were determined for different models of composite fragments. The fields were averaged to compute the composite's effective elastic properties compared to the experimental data.

Keywords: spatially reinforced composite material, microstructure, experimental studies, unit cell, mathematical modeling, micromechanics, local approximation method, effective elastic properties

Acknowledgments*. The study was financed by the Ministry of Science and Higher Education of the Russian Federation within the framework of the program of activities of the Scientific and Educational Center Rational Subsoil Use.*

Citation: Anoshkin AN, Pisarev PV, Ermakov DA, Roman KV. Microstructural modeling and prediction of effective elastic properties in 3D reinforced composite material. *Materials Physics and Mechanics*. 2022;50(1): 89-106. DOI: 10.18149/MPM.5012022_7.

1. Introduction

Developing 3D reinforced composites (3DRC) incorporating woven, interlock, or rod reinforcements is a promising direction for advancing structures and technologies of composite materials [1]. 3D composite materials with a diverse range of physical and mechanical properties can be produced by tailoring the braiding pattern or the number and type of fibers along the reinforcement directions. In particular, the tear strength in the transverse direction and the shear resistance can be considerably improved in comparison with layered composite materials.

Modern braiding technologies allow generating complex 3D reinforcement cages that can be further impregnated to manufacture preforms whose shapes closely match the required component, reducing the labor intensity and production costs [2]. Spatially reinforced composite materials are increasingly in demand in aerospace engineering for heavily loaded structures, with an ever-widening range of applications.

As more versatile tools emerge for configuring the braiding patterns, novel approaches are developed for predicting effective mechanical characteristics and selecting the optimal

parameters of 3DRC structures for specific components. This paper is dedicated to constructing geometric structural models and predicting the effective elastic characteristics of the 3D reinforced composite accounting for mechanical tolerances in the braiding pattern of the reinforcement cage.

Specialized software packages are used for constructing geometric models describing the 3DRC structure: the best-known examples include TexGen, WiseTex, and Techtext CAD [3-14]. TexGen is an open-source software package developed by the research team led by Prof. Long at the University of Nottingham in 2006 [3-5]. The software can generate unit cells for the braiding pattern, with the geometric parameters input via the menu interface (these include the number of warp and weft yarns, width, height, and spacing for each set of yarns, etc.). WiseTex is a software package developed by Lomov's research group at KU Leuven in 2000 [6–10], capable of not only modeling the geometric structure of cells and fragments of textile composites like TexGen but also predicting their effective elastic properties. Furthermore, WiseTex incorporates an algorithm coding structural topology, providing additional options for computer simulation of geometric models for complex braiding patterns in 3DRC. The TechText CAD software package was developed at the University of Manchester in 2000-2002. It allows modelling the geometric structure of interlock woven fabrics and their deformation during manufacture [11-14]. In addition, TechText CAD can compile additional modules for controlling the production of interlock preforms with industrial weaving machines based on the simulation results.

It should be borne in mind that the above software packages simulate 'idealized' woven textiles corresponding to a given reinforcement geometry within the materials. They can be used to extract qualitative estimates for the effective elastic characteristics of the material from the given parameters of the structure. However, the operational parameters of 3D reinforcements and composite materials based on them (tensile forces and thicknesses for different yarn sets, pressures and flow rates of the impregnating agent, etc.) can fluctuate wildly during manufacture. This inevitably produces deviations/variations in the geometric parameters of the cage, such as paths of yarns, areas, and shapes of their cross-sections, and spacings between the yarns. These fluctuations in the material structure vary in different areas of the component because the textile reinforcement is deformed unevenly throughout the manufacturing process. The effect of these fluctuations in the parameters of the reinforcement cage on the mechanical characteristics of 3DRC has received scarce attention this far. Therefore, it remains to be elucidated whether the software packages developed for modeling geometric structures are suitable for predicting the effective elastic characteristics of real composite materials. We intend to explore this issue in our study.

Efforts should be made to construct models of the real structure of 3D reinforced composites accounting for random or regular deviations in the operational parameters and to assess the effect of these deviations on the elastic characteristics of the composite material. This paper presents the estimates obtained from the results of tomographic and microstructural studies on the parameters of the geometric structure in 3DRC specimens. The resulting estimates were used to construct computational geometric models of the unit cell and fragments of the 3DRC structure with the help of the TexGen software package and an algorithm we developed, aimed at solving the micromechanics problem for 3DRC in fragments of the structure based on local approximation [15]. The algorithm was applied to numerically solve boundary-value problems and compute the effective elastic properties of 3D reinforced composite. The predicted effective elastic properties are compared with the results of mechanical tests in 3DRC specimens.

We intend to resolve the challenge of improving the prediction accuracy for the effective elastic properties in real 3D reinforced composites accounting for manufacturing tolerances in the structure parameters. Moreover, the newly available models can serve for

analyzing how the spread in geometric parameters of the composite structure affects its mechanical characteristics, predicting nonlinear deformation and strength estimates in 3DRC under complex loading.

2. 3D reinforced composite material

We consider a 3D reinforced textile composite with a repeating orthogonal braiding pattern. The preform of the analysed material is a plate with constant thickness, containing 10×10 to 15×15 repeating unit cells in a plane and one cell in the bulk of the plate. Thus, the spatial structure of the weave in the material can be assumed to be repeating in the plane and having a finite size in the third direction. The composite material is prepared by pressurized impregnation of a textile reinforcement cage with a polymer adhesive in a rigid mold.

The repeating cell of the tested material contains two rows of warp yarns, three rows of weft yarns, and two binder yarns (Fig. 1) [16]. The yarns are complex and contain approximately 12,000-15,000 elementary fibers (filaments) [16]. The filaments in the unit cell are characterized by their paths and can have different thicknesses, densities and cross-sectional shapes. Both single and double yarns can be used for cell braiding. Next, we consider a particular case of a unit cell where the weft centerline is a double yarn, and the remaining yarns are single. The mechanical behavior of the filaments in the 3DRC composite is generally described by models of fiber bundles or unidirectional fiber composites; the latter is adopted in this study. The model used is described in [17,18].

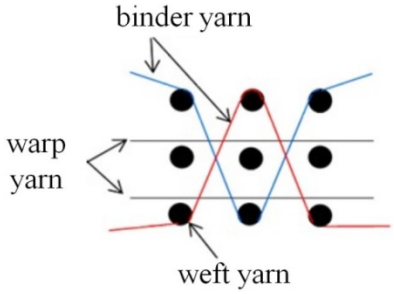

Fig. 1. Reinforcement scheme of repeating unit cell in 3DRC

The racetrack model, first introduced by Kemp [19], was used to describe the unit cell of the material considered in the paper (Fig. 2). The warp and weft yarns are taken to be straight in this model, while the binder yarn is represented by a line segment passing between the warp yarns and connected to two arcs passing around the weft yarns. This description of the binder yarn is simpler than the spline approximation used by other models, for example, in [20]. Kemp's model assumes that all yarns have constant cross-sections, shaped as rectangles with semi-circular corners.

The structure of the unit cell is described by the following main parameters (Fig. 2): w_{1p} and H_{1p} are the width and height of the cross-section for the single warp yarn (Fig. 2b); w_{2p} and H_{2p} are the width and height for the double warp yarn (Fig. 2b); w_{wf} and H_{wf} are the width and height of the cross-section for the single weft yarn (Fig. 2a); H_{wp} is the height of the cross-section for the binder yarn (Fig. 2a); R_{wp} is the width of the binder yarn (Fig. 2a); φ_{wf} is the crimp angle of the weft centerline path undulating around the binder yarn (Fig. 2b); T_{w1} and T_{2p} are the distance (thickness of the adhesive layer) between the warp/weft yarns and between the double warp yarns (Fig. 2b); R_{1p} is the distance between the centerlines of single warp yarns in the top row.

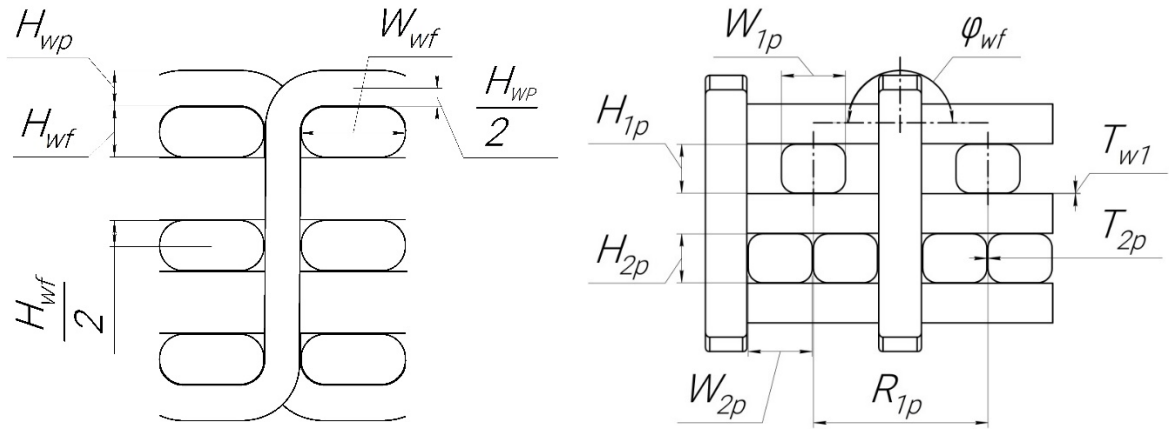

a b

Fig. 2. Kemp's racetrack model for 3DRC unit cell: cross-section of weft yarns (a) and cross-section of warp yarns (b)

The list of parameters used in this paper to describe the unit cell largely corresponds to Kemp's model; the difference is that the paths of the weft yarns are not straight in the model used but are described instead by segments and arcs of the circles around the binder yarns. The problem complexity was increased based on the results of microstructural studies.

The parameter values of the unit cell were found from the results of tomographic and microscopic studies on the composite structure.

3. Tomographic and microscopic studies

Specimens for microstructural studies of 3DRC were cut from a single plate preform together with specimens for subsequent mechanical tests. Four 15×25 mm and 25×25 mm specimens without additional surface treatments were prepared for tomographic studies (Fig. 3). Four 25×25 mm specimen slices with polished surfaces were prepared in accordance with GOST 2789 for optical microscopy studies.

Fig. 3. 3DRC specimens

Tomographic studies were carried out with a prototype microfocus X-ray computer tomograph we constructed at Saint Petersburg Electrotechnical University "LETI" [21–23]. The microfocus source was a sealed tube with an anode voltage of 130 kV, an anode current of 200 μA, and the size of the focal spot ranging from 20 μm to 100 μm. A PRODIS.Mark flat panel detector with a pixel size of 50 μm and an active area of 120x240 mm was used for recording the projection data. Combining this equipment in a laboratory tomography allows obtaining projection data with a magnification up to ×100. Preliminary studies at the laboratory setup were conducted for 25×25 mm specimens of layered and 3D reinforced carbon fibers; we detected pores with the dimensions of 10-12 μm and the parameters of the unit cells in the interlock filler (thickness and crimp angles of the yarns, adhesive layers between the yarns in the cell with the dimensions of about 15 μm).

The tomographic images were reconstructed from the results of multi-angle X-ray imaging of the specimens with the MicroCT Bruker software [24]. Figure 4 shows an example of reconstructed 3D images for structure fragments of the given 3DRC specimens.

We considered a total of 4 3D tomographic images for 4 specimens and 48 planar sections for each specimen.

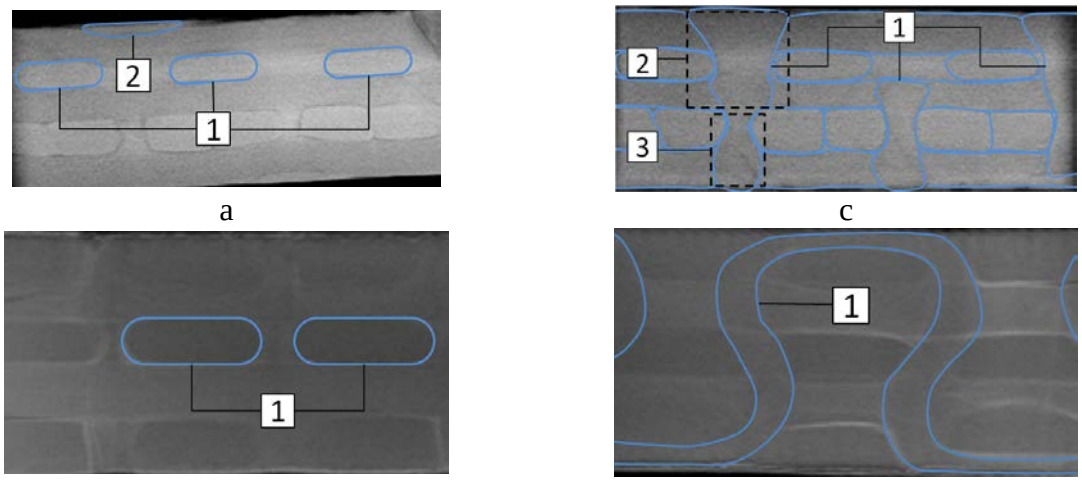

Fig. 4. Plane sections of reconstructed 3D images for structure fragments of the 3DRC specimens: (a) cross-sectional view of warp yarns (along the weft yarns); (b) cross-sectional view of weft yarns (along the warp yarns); (c) cross-sectional view of binder yarns at crossover point, (d) view along the binder yarns

Figure 2 shows an example of plane sections for reconstructed 3D images for single specimens. Analyzing all planar sections of the 3DRC specimens, we found that the paths of the warp yarns can be assumed to be straight, and the weft yarns undulating over the binder yarns deviate slightly from the straight lines described by the angle φ_{wf} (see Fig. 2 and Fig. 6), while the path of the binder yarn is S-shaped (Fig. 2d).

The cross-section of the warp and weft yarns can be described by an ellipse or a rectangle with rounded corners (Fig. 4a-1 and Fig. 4b-1). The cross-sectional shapes and areas of these yarns only vary insignificantly for all the images considered. We decided to describe the section of the warp and weft yarns with a rectangle with rounded corners, which corresponds to Kemp's model, serving as a basis for selecting the parameters of the structure to be determined. The cross-section of the binder yarn between the warp yarns has a shape close to a truncated ellipse with pointed ends (Fig. 4a-2). The cross-sectional area of the binder yarn increases in the area of contact with the warp yarns of the top row (Fig. 4c-2) and decreases in the area of contact with the warp yarns of the bottom row (Fig. 4c-3). An algorithm for modeling the unit cell in 3DRC was developed to account for this phenomenon, allowing to set the variation in the area of the binder yarn along its path.

The results of the tomographic study indicate that Kemp's model with its main assumptions (the warp and weft yarns are straight, the binder yarn is approximated with a truncated ellipse, cross-section of the yarns is described by a rectangle with rounded corners) can be taken as the basis for determining the geometric structure of 3DRC. In this case, the S-shape of the path and the variation in the cross-sectional area of the binder yarns should be additionally taken into account. The numerical values of the parameters for describing and subsequently modeling the given geometric structure of the material were found through microsection analysis.

The computed volumes of geometric objects in tomographic images of the microstructure were used to extract an estimate for the total volume fraction of the reinforcement cage, amounting to 65.51%, and estimates for the volume fractions of the warp,

weft, and binder yarns, amounting to 32.83%, 59.21%, and 7.96%, respectively; all estimates were obtained for a cell in 3DRC (Table 1).

The final stage of tomographic studies consisted of selecting orthogonal planes of the specimen slices to subsequently prepare microsections. This allowed obtaining microsections with planes of characteristic cross-sections: across the weft yarns, across the warp yarns, and across the binder yarn. Several characteristic cross-sections were obtained at different points of the yarn paths perpendicular to the plane of the section, allowing us to estimate the variation in the parameters of the cell along the path of this yarn.

Table 1. The volume fraction of yarns in the reinforcement cage of the 3DRC tested

Estimation method	V_{fo},(%)	V_{fu},(%)	V_{fp},(%)	V_{fk},(%)
Tomography	32.83	59.21	7.96	65.5
TexGen model	38.32	48.07	13.61	52.8
Simplified model of 3DRC cell (model 1)	33.86	52.95	13.19	53.9
Refined model of 3DRC cell (model 2)	33.88	58.06	8.06	68.6

Microscopic studies of 3DRC specimen microsections were carried out with a Carl Zeiss Axiovert 40 MAT microscope. About 90 micrographs with a magnification up to ×10-100 were taken in the course of microscopic studies; Figure 5 shows characteristic micrographs.

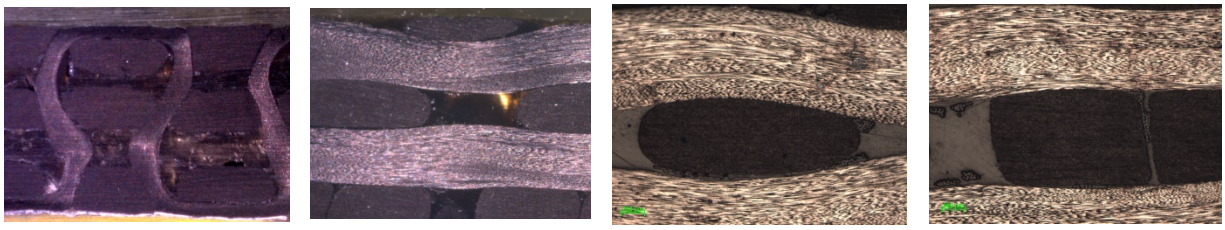

a b c d

Fig. 5. Micrographs of unit cell in 3DRC: along the binder yarns (a); along the weft yarns (b); cross-section of a single warp yarn (c); cross-section of a double warp yarn (d)

The parameter values of the 3DRC unit cell were determined from analysis of the microsections (Fig. 2): W_{1p}, H_{1p}, W_{2p}, H_{2p}, W_{wf}, H_{wf}, R_{wf}, R_{1p}, T_{w1}, T_{2p}, φ_{wf}. The study comprised 5 to 33 measurements of these parameters. The measurement data were statistically processed to obtain the mean value, the standard deviation, and the variation coefficient for each parameter (see Table 2).

Figure 6 shows example schemes for determining these parameters in four microsections of different orthogonal planes for the same specimen. Figure 6a shows the parameters of the cross-sectional areas S_{1f} and S_{wp} for the weft yarn and the stitching yarn (the latter was approximated by a truncated ellipse with pointed ends), the crimp angle φ_{wf} of the weft yarn, the heights H_{1p}, H_{2p} and the widths W_{1p}, W_{2p} for single and double warp yarns. Figure 6b shows the height H_{wf}, the width W_{wf}, the area S_{wf} and the distance R_{wf} between the centerlines of the weft yarns. Notably, the corner radii of the rectangles describing the cross-sections of the warp and weft yarns were taken equal to half the height of the respective cross-sections, and the width was defined as the greatest distance between the centers of the rounded corners. Figure 6c shows the distance R_{1p} between the centers of single warp yarns.

Figure 6d shows the thicknesses T_{w1} of the adhesive layers between the weft and warp yarns and T_{2p} between the double warp yarns.

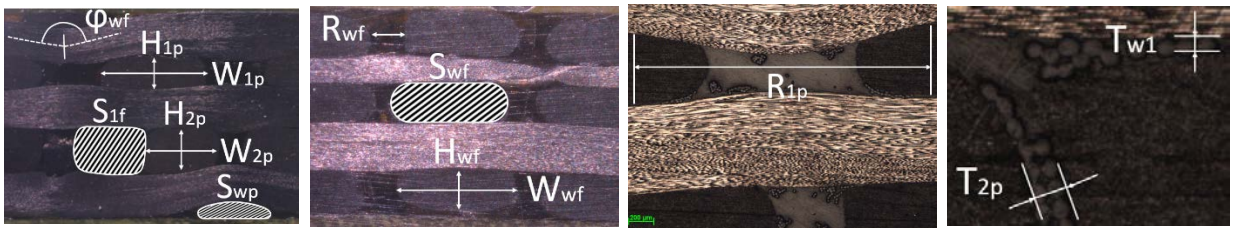

a b c d

Fig. 6. Images of 3DRC microsections with the given parameters of the braided structure: parameters 2-4, 8-12 from Table 2 (a); parameters 1, 5-7 from Table 2 (b); parameter 8 from Table 2 (c); parameters 13, 14 from Table 2 (d)

Table 2. Geometric parameters of 3DRC structure

№	Parameter	Minimum value	Maximum value	Mean value	Variation coefficient, %	Number of measurements
1	Cross-sectional area of weft yarn S_{wf}, mm^2	1.32	1.49	1.415	3.236	15
2	Cross-sectional area of warp yarn S_{1f}, mm^2	0.95	1.07	1.001	3.113	16
3	Cross-sectional area of binder yarn S_{wp}, mm^2	0.32	0.38	0.356	6.256	7
4	Crimp angle of weft yarn φ_{wf}, ^{o}	158.59	163.13	160.438	1.026	8
5	Height of weft yarn H_{wf}, mm	0.62	0.83	0.735	7.436	33
6	Width of weft yarn W_{wf}, mm	1.98	2.36	2.12	5.011	15
7	Distance between weft yarns R_{wf}, mm	0.26	0.65	0.543	10.219	16
8	Distance between centerlines of warp yarns R_{1p}, mm	3.27	3.33	3.3	0.91	5
9	Height of single warp yarn H_{1p}, mm	0.58	0.73	0.651	8.33	7
10	Width of single warp yarn W_{1p}, mm	1.55	2.01	1.825	10.69	5
11	Height of double warp yarn H_{2p}, mm	0.75	0.86	0.791	3.55	19
12	Width of double warp yarn W_{2p}, mm	1.27	1.44	1.345	4.306	12
13	Thickness of adhesive between warp and weft T_{w1}, μm	4.5	18.02	10.51	37.3	12
14	Thickness of adhesive between double warp yarns T_{2p}, μm	12.61	47.75	28.14	48.26	11

Analyzing the microsections, we detected numerous compactions of the binder yarns in the 3DRC structure considered, as illustrated by Fig. 5a. Therefore, in contrast to the assumptions formulated by Kemp [19], we assumed in the simulation that the area and cross-sectional shape of binder yarn were variable along its path. The areas S_{wf} of the binder yarn were determined at seven points along its path; the area here varied in the range from 0.32 mm^2 to 0.38 mm^2.

Considering all of the microsections obtained, we can see that a binding layer (polymer matrix) is found between the yarns of the reinforcement in the composite material considered. Thus, the subsequent statement of the micromechanics problem does not need to account for the contact interaction of reinforcing yarns without a binding layer to compute the structural stress and strain fields or predict the effective elastic characteristics of 3DRC. The parameters of the binding layer between the weft and warp yarns and between the double warp yarns, T_{w1} and T_{2p}, respectively, are given in Table 2.

The parameter values of the 3DRC structure considered were used to construct a geometric model of the unit cell for subsequent prediction of the effective elastic characteristics of the composite.

4. Modeling of the composite material structure

Computer simulation of the composite's unit cell was carried out using TexGen [3-5] and a program written based on the algorithm we developed. Using TexGen with an incomplete set of parameters from Table 1 allows us to quickly construct a geometric model of the unit cell. The unit cell was modeled using the mean values of height, width, and cross-sectional area of the yarns, the distance between the yarn centerlines, and the thickness of the bonding agent between the yarns (Table 1). The geometric model of the 3DRC cell constructed in TexGen is shown in Fig. 7a.

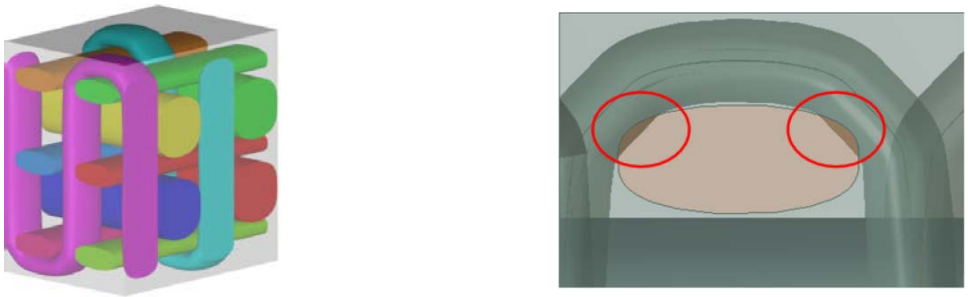

a b

Fig. 7. Model of unit cell in TexGen (a) with intersecting yarns (b)

The volume fractions of warp, weft, and stitching yarns in the 3DRC cell were computed for the model built in TexGen by the formulas from [25] (Table 1). Comparing the estimates obtained from the analysis of the tomographic images (Table 1), we found a difference of 4.44% for volume fractions of warp yarns, 9.99% for weft yarns, and 5.55% for binder yarns. In general, the difference in the volume fractions of the reinforcement cage in the cell, obtained from the results of tomographic analysis and constructed in TexGen, amounted to about 15.8% (Table 1).

The reason for this difference lies in yarn intersection errors generated at crossover points for the unit cell simulated by TexGen with the given parameters of the composite structure (Table 2). Figure 7b shows an example of intersecting weft and warp volumes in the model of the unit cell constructed in TexGen. Intersection correction is done in TexGen by removing crossovers for yarns of the same class, accordingly changing the volume fractions of these yarns in the cell. This circumstance should undoubtedly produce a

difference in the elastic characteristics of the composite predicted using the constructed geometric model of the cell.

The steps necessary for simulating 3D braiding in the cell corresponding to the experimental data include, aside from correctly describing the yarn interlocking, accounting for the variation in their cross-sectional shape along the path. For this purpose, we developed a specialized algorithm for modeling yarns in 3DRC unit cells [26]. We used the boundary-representation method (B-rep) for geometric forms of spatial structures [27-29] so that the yarns were described by surfaces and characterized by two functions, their centerline path and the cross-sectional area of the yarn along the path.

The centerline paths were simulated by straight lines for warp yarns, by line segments connected by arcs at points of crossover with binder yarns for weft yarns, and by S-shaped curves described by a segment with two arcs for binder yarns. The cross-sections of the warp and weft yarns were assumed to be constant and described by rectangles with rounded corners (the parameters are given in Table 2). The cross-section of the binder yarn was generally assumed to be variable and approximated by an ellipse with variable parameters of the semi-axes x_a, x_b.

We constructed two models of the 3DRC cell with different descriptions of the variation in the cross-section of the binder yarn. According to the first, simplified model, the cross-section was assumed to be constant, described by a rectangle with rounded corners, 0.45 mm high, 0.7 mm wide, with a corner radius of 0.1 mm and an area of 0.312 mm^2.

According to the second, refined model, the cross-sectional shape of the binder yarn varied along the trajectory, while the area remained constant, equal to S_{wp} = 0.356 mm^2, corresponding to the mean value measured in the microsections. The cross-section of the binder yarn was described by an ellipse with the parameters of the semi-axes x_a, x_b, whose values were given at seven characteristic points of the path (see Fig. 8). Point 1 corresponds to the region where the binder yarn contacts the weft yarn from the top row, points 2-6 are located in its S-shaped segment of the path with different cross-sectional values, point 7 corresponds to the region where the binder yarn contacts the weft yarn from the bottom row. The value of the semi-axis x_a of the elliptical yarn cross-section varied in the range from 0.31 mm to 0.38 mm, and the values of the semi-axis x_b from 0.28 mm to 0.62 mm. Notably, varying the cross-sectional shape along the path can lead to some variations in the anisotropy parameters for this model of the material, which was established by producing predictions for its effective elastic properties.

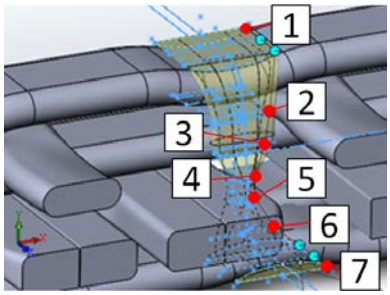

Fig. 8. Scheme for simulating the binder yarn in the 3DRC cell (model 2) with characteristic points along its path

A nonlinear approximation was adopted between the points with the given parameter values of the elliptical semi-axes characterizing the yarn cross-section, making it possible to generate smooth surfaces describing the binder yarns in the simulated cell. The parameter values of the warp and weft yarns used to construct the model of the unit cell are given in Table 2.

The developed algorithm allows describing the configuration of the binder and weft yarns in the 3DRC cell with better accuracy, accounting for the manufacturing tolerance of the reinforcement cage parameters. The geometric models of the 3DRC cell constructed by the developed algorithm and the shape of the binder yarn in the models are shown in Fig. 9. Comparing the volume fractions of different yarn sets in the constructed models of the 3DRC cell (Table 1) with tomographic estimates, we established that the difference in describing the volume fraction for model 1 amounts to 1.04% for warp yarns, to 6.26% for weft yarns, and to 5.23% for binder yarns. For model 2, these differences amount to 1.04%, 1.15%, and 0.1%, respectively. The overall difference in the volume fraction of the reinforcement cage from the tomographic data is of the order of 11.6% and 3.1% for the simplified and refined models, respectively. Apparently, the refined model of the 3DRC cell, constructed by the developed algorithm, is in agreement with the tomographic model with respect to the volume fractions of yarn sets in the reinforcement cage of the material. We should note that a larger number of finite elements are required to subsequently construct the numerical model of the refined 3DRC cell for describing the paths and shapes of the binder and weft yarns, compared to the model constructed in TexGen.

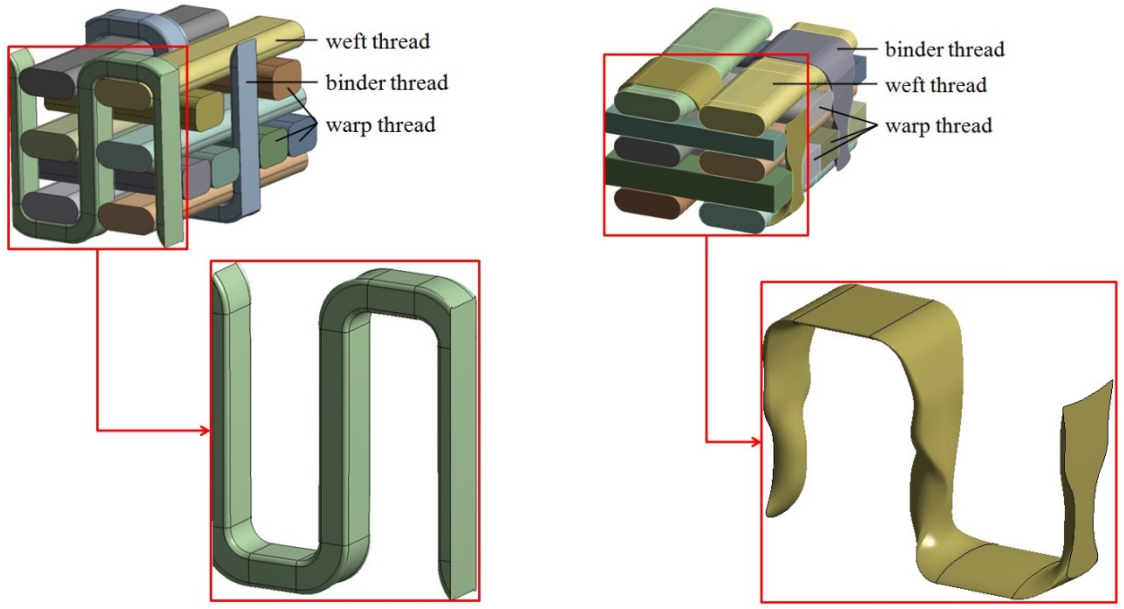

Fig. 9. Model 1 (a) and model 2 (b) of 3DRC unit cells, constructed by the algorithm developed

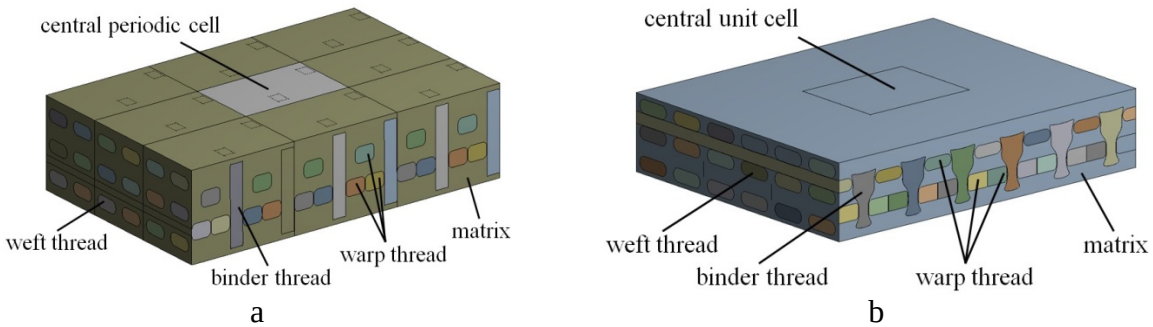

Fig. 10. Simplified model 1 (a) and refined model 2 (b) for a fragment of 3DRC

Fragments of the composite material were constructed based on geometric models of cells using threefold plane translation, including one cell in the center and those adjacent to it

(Fig. 10). A boundary-value problem was formulated below for these fragments to compute the stress and strain fields in the matrix and fibers of the composite material, predicting its mechanical characteristics by the local approximation method.

5. Statement of the micromechanics problem for a structure fragment and an algorithm for predicting the elastic characteristics in composite material

The method of local approximation was proposed by Sokolkin and Tashkinov in [15] and further elaborated in [17,18,30,31]. The method relies on the property of linearity, i.e., rapid attenuation of correlation functions corresponding to non-uniform stress and strain fields (obtained by solving several mechanical problems for composite materials) at a distance of two or three characteristic dimensions [17]. In view of this property, it was proposed to simulate the required stress and strain fields in the structural elements of the composite by its fragments containing one characteristic cell of the structural element in the center and one or two nearby layers of the adjacent cells. As a fragment is deformed, the layers of adjacent cells produce fields of structural stresses and strains in the central cell; these fields are close to those evolving in a composite material with many cells due to the local nature of the interaction between the structural elements. The values of the structural stress and strain fields averaged over the central cell of the fragment corresponding to the macroscopic stresses and strains of equivalent fields evolving in a homogeneous medium with effective mechanical properties. Consequently, solving a number of boundary-value problems for the selected composite fragment, the effective elastic properties of the composite material can be computed from the values found for the averaged (macroscopic) stresses and strains.

The local approximation method was used in [17,18,30,31] for predicting the effective elastic characteristics and solving problems of nonlinear deformation and structural failure in unidirectional fiber composites. Solving these nonlinear problems allows determining the parameters in the constitutive equations of nonlinear deformation and the strength criteria of fiber composites under arbitrary three-dimensional loading.

We considered a structural fragment of the composite including nine unit cells constructed by the developed algorithm with the mean values of the structure parameters given in Table 2. However, the local approximation method also allows solving stochastic micromechanical problems in implementations for samples of composite fragments with an arbitrary arrangement of elements [17]. We intend to explore this topic in our future studies.

Let us formulate a boundary-value problem for the 3DRC fragment. Solving it by the local approximation method, we can obtain microstress and microstrain fields in the structural elements of the composite material (matrix in the fibers) corresponding to the given macroscopic stresses or strains.

The computational scheme of the problem includes the given 3DRC fragment (Fig. 10) containing nine unit cells. According to the local approximation method, such forces $\vec{f}$ or displacements $\vec{u}$ were given at the boundary of the fragment that the strains or stresses averaged over the central cell of the fragment were equal to the given microscopic stresses σ_{ij}^{*} or strains ε_{ij}^{*}.

The system of equations for the boundary-value problem from anisotropic elasticity theory for a fragment of inhomogeneous structure includes the equilibrium equations, the Cauchy geometric relations, and the constitutive equations.

$$\sigma_{ij,j}(\vec{r}) = 0;\ \varepsilon_{ij}(\vec{r}) = \frac{1}{2}\left(u_{i,j}(\vec{r}) + u_{j,i}(\vec{r})\right);\ \sigma_{ij}(\vec{r}) = C_{ijkl}(\vec{r})\varepsilon_{ij}(\vec{r}); \tag{1}$$

$$C_{ijkl} = C_{ijkl}^{(1)}\lambda^{(1)}(\vec{r}) + C_{ijkl}^{(2)}\lambda^{(2)}(\vec{r}); \tag{2}$$

$$\lambda^{(i)}(\vec{r}) = \begin{cases} 1, (\vec{r}) \in V_p^{(i)}, \\ 0, (\vec{r}) \notin V_p^{(i)}. \end{cases}$$

Here $\sigma(\vec{r})$ and $\varepsilon(\vec{r})$ are the stress and strain tensors in the structural elements of the composite material (matrix and fibers), $C_{ijkl}^{(1)}$ and $C_{ijkl}^{(2)}$ are the elastic moduli tensors of fibers and matrix, respectively, $\lambda^{(i)}(\vec{r})$ is the indicator function, where *i* is an index corresponding to the structural element (1 corresponds to the fiber, 2 to the matrix).

System (1) and (2) is closed by boundary conditions and conditions for adjusting them by local approximation [17,18,30,31]. Displacements $\vec{u}$ or forces $\vec{f}$ are given at the fragment boundary Γ; they are computed in terms of auxiliary tensors for adjusting the boundary conditions A_{ijkl} or B_{ijkl} and the given microscopic stresses σ_{ij}^* or strains ε_{ij}^*:

$$\hat{\sigma}_{ij}(\vec{r}) n_j(\vec{r}) = f_i\big|_{r\in\Gamma}, \quad \hat{\varepsilon}_{ij} r_j = u_i^0; \tag{3}$$

$$\hat{\sigma} = A_{ijkl}\sigma_{ij}^*, \; \hat{\varepsilon} = B_{ijkl}\varepsilon_{ij}^*. \tag{4}$$

The boundary conditions (3) and (4) allow obtaining the structural stress and strain fields from the solution of the boundary problem in the central cell of the fragment, corresponding to the given macroscopic stresses or strains. For this purpose, we should first determine the components of the tensors for adjusting the boundary conditions A_{ijkl} or B_{ijkl} from the solution of six test problems on the deformation of the fragment considered. However, conditions (4) do not have to be satisfied precisely to predict the effective elastic properties of the composite. Here it is sufficient to solve six boundary problems for the fragment under arbitrary conditions (3) independent of each other and obtain the stresses σ_{ij}^* and strains ε_{ij}^* by averaging with respect to the central cell:

$$\sigma_{ij}^* = \frac{1}{V_l}\int_{V_l} \sigma_{ij} dV, \; \varepsilon_{ij}^* = \frac{1}{V_l}\int_{V_l} \varepsilon_{ij} dV. \tag{5}$$

We can obtain systems of linear equations by assuming these averaged stresses to be macroscopic, arising in an equivalent homogeneous medium, and substituting them for all k problems (k =1,2,…,6) into Hooke's law for an anisotropic medium in matrix form [32] with the matrix of effective stiffnesses C_{ij}^* or compliances S_{ij}^*.

$$\sigma_i^k = C_{ij}^* \varepsilon_j^k, \; \varepsilon_i^k = S_{ij}^* \sigma_j^k. \tag{6}$$

The corresponding tensor and matrix notations for stresses, strains, and elastic moduli for writing Hooke's law are given, for example, in [33]. Performing a rearrangement, we can divide systems of equations (6) into six systems of linear equations relative to the unknowns C_{ij}^* or S_{ij}^*.

$$\begin{aligned} &\sigma_1^k = C_{1j}^* \varepsilon_j^k, \; \sigma_2^k = C_{2j}^* \varepsilon_j^k, \; \sigma_3^k = C_{3j}^* \varepsilon_j^k, \; \sigma_4^k = C_{4j}^* \varepsilon_j^k, \; \sigma_5^k = C_{5j}^* \varepsilon_j^k, \; \sigma_6^k = C_{6j}^* \varepsilon_j^k; \\ &\varepsilon_1^k = S_{1j}^* \sigma_j^k, \; \varepsilon_2^k = S_{2j}^* \sigma_j^k, \; \varepsilon_3^k = S_{3j}^* \sigma_j^k, \; \varepsilon_4^k = S_{4j}^* \sigma_j^k, \; \varepsilon_5^k = S_{5j}^* \sigma_j^k, \; \varepsilon_6^k = S_{6j}^* \sigma_j^k. \end{aligned} \tag{7}$$

Solving these systems (7) with respect to the unknowns C_{ij}^*, S_{ij}^*, we can determine the effective stiffnesses, compliance, and technical elastic constants for an anisotropic homogeneous medium equivalent to 3DRC.

Considering the boundary-value problems (k =1,2,…,6) mentioned above, it is the most convenient to choose the problems on uniaxial strain in the fragment along each of the coordinate axes and pure shear in three coordinate planes. The corresponding boundary conditions were given by the displacements, and one central point of the fragment was additionally fixed to achieve the stability of numerical simulations performed to solve FEM

problems. Our computations of effective stiffnesses C_{ij}^* and compliances S_{ij}^* from the solution of system (7) assumed that the material was orthotropic and the elastic moduli tensor satisfied the symmetry conditions. For this reason, the diagonal components C_{ij}^*, S_{ij}^*, reflecting the mutual influence of shear strains on each other and on longitudinal stresses, were taken equal to zero, while the components of the effective compliance matrix S_{ij}^* $(i, j = 1,2,3)$, located symmetrically relative to the main diagonal, were averaged for subsequent computations of elastic constants.

The given composite model assumed that the yarns impregnated with a polymer adhesive consisted of a unidirectionally reinforced transversely isotropic composite material whose elastic properties were computed by the Chamis ratios [34]. The elastic properties of impregnated carbon filament and polymer matrix used in the computations are given in Table 3.

Table 3. Properties of structural elements in 3DRC

Material	E_x, GPa	E_y, GPa	E_z, GPa	v_{xy}	v_{yz}	v_{xz}	G_{xy}, GPa	G_{yz}, GPa	G_{xz}, GPa
Impregnated carbon filament	200	9.5	9.5	0.014	0.24	0.014	6.93	12.84	6.93
Polymer matrix	3.7			0.38			1.34		

The boundary-value problem formulated in accordance with the local approximation method for the composite fragment was solved numerically by the finite element method (FEM) using the ANSYS software. Discretization of the fragments was performed using *SOLID*186 solid-state elements. The computational mesh comprised 2.7 million elements and 5.8 million nodes, selected by estimating the convergence of the numerical solution on the predicted values of the elastic moduli (the difference was no more than 1%).

6. Discussion of computational results and comparison with experimental data

We numerically solved six boundary problems on tension along the coordinate axes and with a shift in the coordinate planes of the model fragments constructed for the simplified and refined 3DRC structures, obtaining fields of structural stresses and strains in the central cell of the fragments. Averaging these fields over the volume of the central cell yielded the corresponding values of macrostresses and macrostrains for a homogeneous medium with effective properties; next, the above-described algorithm was applied to produce the effective compliances and elastic constants for 3DRC.

Table 4 and Figure 11 show a complete set of effective elastic characteristics, computed by two 3DRC models, simplified (model 1) and refined (model 2). For comparison, Table 4 presents the experimental estimates of the effective elastic moduli E_x, E_y, G_{xy} (the OX axis is directed along the warp yarns, the OY axis along the weft yarns), obtained by the material's manufacturer. Mechanical tests were performed for the same 3DRC specimens that participated in microstructural studies. Uniaxial tensile tests were performed by the ASTM D3039 standard with a loading rate of 1 mm/min for two sets of strip specimens, the variation coefficient for the mean values of Young's modulus amounted to 2.6%. Shear tests were performed by the ASTM D5379 standard for a set of five V-notched specimens at a loading rate of 2 mm/min, the variation coefficient for the mean values of the shear modulus amounted to 12.3%. For convenience, Table 4 additionally shows experimental and model values for the volume fractions of reinforcing fibers in 3DRC cells: the total value (υ_f) and

the values corresponding to the directions of the OX and OY axes $(\upsilon_{fx}, \upsilon_{fy})$. Furthermore, Table 4 shows the relative differences between δ^1 and δ^2 (%) for the experimental values of elastic characteristics and volume fractions of fibers (x^e) and those computed by the first (x^{m1}) and the second (x^{m2}) model.

$$\delta^i = \frac{(x^e - x^{mi})}{x^e} * 100 . \quad (8)$$

Table 4. Computational and experimental effective elastic properties and volume fractions of reinforcing fibers in 3DRC

Characteristics of 3DRC	Computation		Experiment	δ^1, %	δ^2, %
	Model 1	Model 2			
E_x, GPa	46.18	49.43	52.38	11.84	5.63
E_y, GPa	61.54	76.29	71.35	13.74	-6.93
E_z, GPa	11.59	8.67			
ν_{xy}	0.02	0.02			
ν_{yz}	0.26	0.28			
ν_{xz}	0.29	0.31			
G_{xy}, GPa	6.87	8.33	7.92	13.24	-5.20
G_{yz}, GPa	6.20	7.62			
G_{xz}, GPa	6.56	7.43			
υ_{fx}, %	33.86	33.88	32.83	-3.14	-3.20
υ_{fy}, %	52.95	58.06	59.21	10.57	1.94
υ_f, %	53.90	68.60	65.5	17.71	-4.73

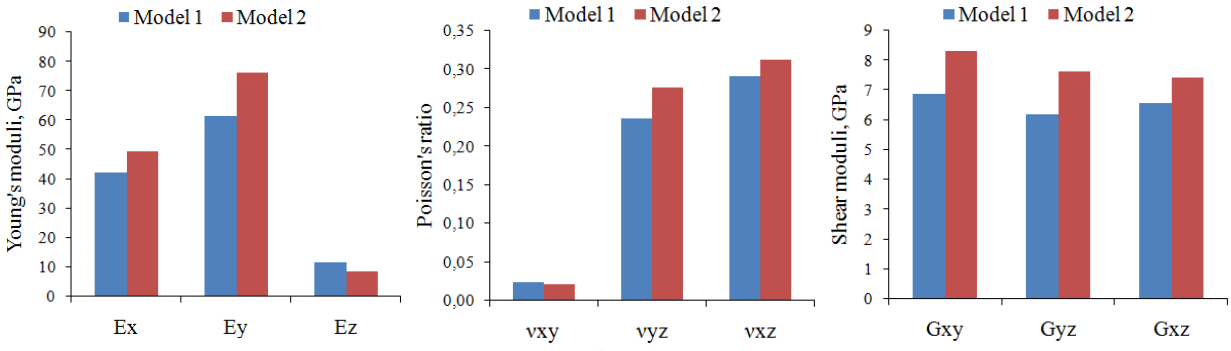

a b c

Fig. 11. Comparison of effective Young's moduli (a), Poisson's ratios (b), and shear moduli (c) computed for the first (simplified) and second (refined) 3DRC models

Analyzing the results obtained (see Table 4), we found that the refined geometric model of the unit cell, along with the technique for solving boundary-value problems for the fragment of the 3DRC structure with subsequent averaging of the obtained stress fields with respect to the central cell of the fragment, allows predicting the effective elastic properties of 3D reinforced composite materials with good accuracy ($\delta \approx$ 5.2-6.5 %). Using a simplified model of the unit cell produces large differences ($\delta \approx$ 11.8-13.7%) in the computational and

experimental data, which is primarily due to the difference in the volume fractions of the weft and binder yarns in the simplified model from the experimental values.

We should note (see Table 4) that the volume fractions of fibers υ_{fx} close to the experimental values ($\delta \approx 3\%$) were obtained for the weft for both 3DRC models. At the same time, the prediction accuracy of effective Young's modulus E_x differs by two times for the two models. Therefore, to achieve good prediction accuracy for effective Young's modulus for the weft ($\delta \approx$ 5-6%), not only good agreement with the experimental volume fractions of fibers in this direction but also agreement with the total volume fraction of fibers for the cell as a whole should be obtained in the geometric model of 3DRC, which is provided by the refined model of the cell (model 2).

Interestingly, the prediction errors of the elastic moduli along the OX and OY axes have different signs in the refined model of the composite. The anisotropy parameter of the material E_x / E_y, equal to 0.648 for this model, differs more from the experimental value $E_x / E_y = 0.73$ than for the simplified model, where $E_x / E_y = 0.75$. The ratio of the volume fractions of fibers in these directions $(\upsilon_{fx} / \upsilon_{fy})$ is closer to the experimental value (0.554) for the refined model $(\upsilon_{fx} / \upsilon_{fy} = 0.583)$ than for the simplified model $(\upsilon_{fx} / \upsilon_{fy} = 0.639)$. The likely reason for this is the variation in the cross-sectional shape of the binder yarn along its path in the refined model of the 3DRC cell. Moreover, we can see that the greatest error in predicting the elastic modulus ($\delta \approx 7\%$) is observed in the refined model for the weft fibers E_y whose volume fraction υ_{fy} is described with good accuracy ($\delta \approx 2\%$).

The difference between the computational and experimental values can also be explained by the difference in the values of the elastic characteristics of complex warp and weft yarns given by the model from the values detected in the composite, as well as by the scatter of the values of the structural parameters in the 3DRC specimen tested. Therefore, we intend to further focus on formulating and solving a stochastic mechanical problem using the developed structural model and the local approximation method to estimate the mean values, variances, and correlation coefficients of the effective elastic characteristics in 3DRC based on the scatter found for the structural parameters of the cell (see Table 2).

7. Conclusions

We have obtained the following key findings:

- microstructural studies were carried out to determine the mean values and variation coefficients for 14 main parameters of the braid unit cell in the given 3D reinforced composite.

- we have constructed an algorithm along with a new model for a braid unit cell of a composite with a modified cross-sectional shape of the binder yarn along the path with the parameters corresponding to the experimental mean values extracted.

- the model allows extracting the volume fractions for different yarn sets in the composite cell, close to experimental estimates (the difference is about 1%), providing accurate predictions for the effective elastic characteristics.

We have developed a new technique based on the local approximation for predicting the effective elastic characteristics of 3D reinforced composite materials. The technique incorporates numerical solutions to spatial boundary-value problems for 3D structural fragments of the composite with subsequent averaging of the stress and strain fields obtained with respect to the central cell of the fragment. We have constructed fragments of the 3DRC structure including nine reference unit cells with mean values of the structure's parameters. The technique presented was used to numerically solve the boundary-value problems for the

constructed structure fragments and compute a full range of effective elastic properties for the given 3DRC.

Comparison with the experimental data showed good accuracy for the proposed new model of the braid unit cell (difference of 5.2-6.5% for the predictions of effective Young's moduli and the shear modulus in the plane of the warp and weft yarns), while the model constructed via the standard TexGen software package yielded predictions with the difference of 11.8-13.7%. We can therefore assume that geometric models of 'ideal' 3DRC cells constructed via standard software without accounting for manufacturing tolerances of the structure parameters cannot provide satisfactory accuracy for the predictions of the effective elastic characteristics in the real composite.

A promising avenue to explore is the further simulation of the stochastic 3DRC structure accounting for both mean values extracted and the variation coefficients of the structural parameters characterizing the geometry of the braid unit cell. Our follow-up studies will formulate and solve a stochastic boundary-value problem for fragments of an arbitrary 3DRC structure by the local approximation method. It would be interesting to develop and implement an algorithm for selecting boundary conditions in boundary-value problems for fragments of the 3DRC structure, subsequently obtaining fields of microstructural stresses and strains in the central cell of the fragment corresponding to predefined macroscopic quantities. This will make it possible to simulate the mechanisms of structural failure (damage accumulation) in the cell, describe nonlinear deformation and assess macroscopic strength under various loading conditions of the composite material.

References

1. Carey JP. *Handbook of Advances in Braided Composite Materials: Theory, Production, Testing and Applications*. Woodhead Publishing; 2016.
2. Bogomolov PI, Kozlov IA, Birulya MA. Review of modern technologies for manufacturing volume-reinforcing preforms for promising composite materials. *Technical and technological problems of the service*. 2017;1(39): 22-27.
3. Brown LP, Long AC, Jones IA. Recent developments in the realistic geometric modelling of textile structures using TexGen. In: *Materials 1st International Conference on Digital Technologies for the Textile Industries*. Manchester; 2013. p.12.
4. Long AC, Brown LP. Modelling the geometry of textile reinforcements for composites: TexGen. In: *Composite Reinforcements for Optimum Performance*. Woodhead Publishing; 2011. p.239-264.
5. Long AC. *Design and manufacture of textile composites*. Woodhead Publishing; 2005.
6. Espadas-Escalante JJ, van Dijk NP, Isaksson P. The effect of free-edges and layer shifting on intralaminar and interlaminar stresses in woven composites. *Compos. Struct.* 2018;185: 212-220.
7. Lomov SV, Gusakov AV, Huysmans G, Prodromou A, Verpoest I. Textile geometry preprocessor for meso-mechanical models of woven composites. *Compos Sci Technol.* 2000;60(11):2083-2095.
8. Verpoest I, Lomov SV. Virtual textile composites software WiseTex: Integration with micro-mechanical, permeability and structural analysis. *Compos Sci Technol.* 2005;65(15-16): 2563-2574.
9. Lomov S, Perie G, Ivanov D, Verpoest I, Marsal D. Modeling three-dimensional fabrics and three-dimensional reinforced composites: Challenges and solutions. *Text Res J.* 2011;81(1): 28-41.
10. Li M, Wang P, Boussu F, Soulat D. Investigation of the Strength Loss of HMWPE Yarns During Manufacturing Process of 3D Warp Interlock Fabrics. *Applied Composite Materials.* 2022;29: 357–371.

11. *Techtext CAD*. URL: https://www.tensiontech.com/software/techtext-cad (access date 10.11.2021).
12. Zeng X, Li Y, Ruan D, Koehl, L. (Eds.). *Computational Textile. Studies in Computational Intelligence*. 2007.
13. Hearle JWS. The challenge of changing from empirical craft to engineering design. *Int J Cloth Sci Technol*. 2004;16(1-2): 141-152.
14. Hobbs RE, Ridge IML. A new estimate of the yarn-on-yarn friction coefficient. *Journal of Strain Analysis for Engineering Design*. 2018;53(4): 191-196.
15. Sokolkin YV, Tashkinov AA. *Mechanics of deformation and destruction of structurally inhomogeneous bodies*. 1984.
16. Evdokimov AA, Gulyaev IN, Nacharkina AV. Investigation of the physicomechanical properties of volume-reinforced carbon fiber reinforced plastic. *Trudy VIAM.* 2020;3(87): 66-73.
17. Anoshkin AN, Sokolkin YV, Tashkinov AA. Microstress fields and the mechanical properties of disordered fiber composites. *Mech Compos Mater.* 1991;26(5): 628-633.
18. Tashkinov AA, Anoshkin AN. Predicting the transverse strength of unidirectional composites under combination loading. *Mech Compos Mater.* 1996;31(4): 346-351.
19. Kemp A. An Extension of Peirce's Cloth Geometry to the Treatment of Non-circular Threads. *Journal of the Textile Institute Transactions.* 1958;49(1): 44-48.
20. Avanaki MJ, Jeddi AAA. Mechanical behavior of regular twill weave structures; part I: 3D meso-scale geometrical modelling. *J. Eng. Fibers Fabr.* 2015;10(1): 115-127.
21. Bessonov VB, Larionov IA, Obodovsky AV. Features of the development of software and hardware systems for microct. *Physical bases of instrumentation* 2019;8(4): 23-33. (In Russian)
22. Bessonov VB, Gryaznov AY, Larionov IA, Osokin VM, Staroverov NE, Kholopowa ED. Development of an algorithm for finding defects on tomographic slices for studying composite materials by microfocus tomography. *Physical bases of instrumentation*. 2020;9(4): 60-63. (In Russian)
23. Bessonov VB, Obodovskiy AV, Gryaznov AY, Klonov VV, Larionov IA, Osokin VM. About possibility of detecting micron-size defects in layered structures using the method of microfocus tomography. *Journal of Physics: Conference Series.* 2017;872(1): 128976.
24. *Bruker Corporation*. URL: https://www.bruker.com/ (access date 10.11.2021).
25. Ansar M, Xinwei W, Chouwei Z. Modeling strategies of 3D woven composites: A review. *Compos Struct.* 2011;93(8): 1947-1963.
26. Anoshkin AN, Pisarev PV, Ermakov DA, Merzlyakova NA. Prediction of elastic characteristics of spatially reinforced composite materials. *IOP Conference Series: Materials Science and Engineering*. 2018;406: 012023.
27. Hiemstra RR, Shepherd KM, Johnson MJ, Quan L, Hughes TJR. Towards untrimmed NURBS: CAD embedded reparameterization of trimmed B-rep geometry using frame-field guided global parameterization. *Comput Methods Appl Mech Eng.* 2020;369: 113227.
28. Maquart T, Elguedj T, Gravouil A, Rochette M. 3D B-Rep meshing for real-time data-based geometric parametric analysis. Adv Model Simul Eng Sci 2021;8(1): 8.
29. Sun Y, Lueth TC. SGCL: A B-Rep-Based Geometry Modeling Language in MATLAB for Designing 3D-Printable Medical Robots. In: *IEEE International Conference on Automation Science and Engineering*. IEEE; 2021. p. 21201930.
30. Anoshkin AN. On one approach to solving a nonlinear spatial problem of micromechanics for unidirectional fibrous composites. *Bulletin of the Perm State Technical University. Mathematical modeling of systems and processes.* 1997;5: 4-10.

31. Anoshkin AN. Micromechanical analysis of inelastic deformation of unidirectional fibrous composites under multiaxial loading and shear. Compound materials Mechanics. 2003;39(5): 575-586. (In Russian)
32. Fudzii T, Dzako M. *Fracture mechanics of compound materials.* Moscow: Mir; 1982. (In Russian)
33. Skudra AM, Bulavs FY. *Strength of reinforced plastics*. Moscow: Khimiya; 1982. (In Russian)
34. Chamis C. C. Mechanics of composite materials: past, present, and future. *J. Compos Technol Res ASTM*. 1989;11: 3-14.

THE AUTHORS

Anoshkin A.N.
e-mail: aan-02@yandex.ru
ORCID: 0000-0002-3972-9902

Pisarev P.V.
e-mail: pisarev85@live.ru
ORCID: 0000-0001-5103-4815

Ermakov D.A.
e-mail: den032895@yandex.ru
ORCID: 0000-0002-3584-1286

Roman K.V.
e-mail: kvroman@pstu.ru
ORCID: 0000-0002-4357-8932

Materials Physics and Mechanics. 2022;50(1): 107-117
Research article
http://dx.doi.org/10.18149/MPM.5012022_8

Submitted: May 12, 2021
Approved: May 30, 2022
Accepted: June 15, 2022

Thin films of gallium oxide obtained by spray-pyrolysis: method and properties

D.I. Panov[1], X. Zhang[1], V.A. Spiridonov[1]✉, L.V. Azina[1], R.K. Nuryev[1], N.D. Prasolov[1], L.A. Sokura[2], D.A. Bauman[1], V.E. Bougrov[1], A.E. Romanov[1]

[1]ITMO University, 49, Kronverkskiy Pr., St. Petersburg, Russia

[2]Ioffe Institute, 26, Polytekhnicheskaya St., St. Petersburg, 194021, Russia

✉ vladspiridonov@itmo.ru

Abstract. In this article, we report on fabricating thin solid films of gallium oxide by the spray-pyrolysis method. This method allows obtaining uniform thin films more easily compared with other sol-gel methods like spin-coating or dip-coating. In the experiment, sol concentrations were experimentally selected for further deposition on substrates. Morphology and chemical composition of the deposited films were studied by Scanning Electron Microscopy and Energy-Dispersive X-ray spectroscopy, respectively. The structural properties of the films were analyzed by X-ray diffraction method. The band gap of the Ga2O3 films was estimated by analyzing the optical transmission spectra and was 4.87 eV. The quality and homogeneity of the obtained coatings are evaluated.
Keywords: Keywords: sol-gel, spray-pyrolysis, thin film, gallium oxide, ultrawide bandgap semiconductor

Acknowledgements*. The authors are grateful to Dr. A.M. Smirnov for valuable discussions. This study was done as part of the research program of the scientific school "Theory and practice of advanced materials and devices of optoelectronics and electronics" (scientific school 5082.2022.4)*

Citation: Panov DI, Zhang X, Spiridonov VA, Azina LV, Nuryev RK et al. Thin films of gallium oxide obtained by spray-pyrolysis: method and properties. *Materials Physics and Mechanics*. 2022;50(1): 107-117. DOI: 10.18149/MPM.5012022_8.

1. Introduction

As a typical representative of the third-generation semiconductor materials, β-Ga_2O_3 has attracted much attention because of its wide band gap (~4.8 eV), high breakdown electric field (> 8 MV/cm), and relatively high electron mobility (~150 cm^2/Vs) [1-4]. This material has not only excellent optoelectronic properties but also good thermal and chemical stability. Therefore, β-Ga_2O_3 becomes a candidate material for high-frequency high-power devices, photodetectors, solar cells, and sensors [2,5,6]. For example, it is reported that there is a MOSFET based on Ga_2O_3 with a breakdown voltage above 1000V [7]. The value of β-Ga_2O_3 bandgap corresponds to the solar-blind ultraviolet region, which makes up for the shortcomings of GaN and ZnO due to the performance degradation caused by doping, which is one of the current international research hotspots [8].

High-quality β-Ga_2O_3 films play a significant role in the development of optoelectronic semiconductor devices, and the quality of thin films appreciably depends on the preparation method and process parameters. There are several methods of preparing Ga_2O_3 films: Radio Frequency Magnetron Sputtering (RFMS) [9,10], Metal Organic Chemical Vapor Deposition (MOCVD) [4,11], Molecular-beam epitaxy (MBE) [12,13], Pulsed Laser Deposition (PLD) [14], halide vapor phase epitaxy (HVPE) [15] and sol-gel processing [16-18]. Compared with other methods, the sol-gel method is widely used in the preparation of oxide films and perovskite materials [18-20] because of its simple equipment, easy operation, no vacuum environment, and relatively low price [21,22]. There are three commonly used approaches to sol-gel methods: dip-coating [23], spin-coating [16] and spray-coating (spray-pyrolysis) [24,25]. The solution is usually applied to prepare single-crystal epitaxial films without high temperatures [23,26]. But this method is only suitable for soluble materials or soluble precursors which can be crystallized at low temperatures. Several studies have shown that the spray-pyrolysis method with a post-annealing process provides a formation of the Ga_2O_3 crystal films of good quality [27,28]. This method was used in our work to obtain gallium oxide thin films. It is easier to obtain uniform gallium oxide thin films by the spray-pyrolysis method compared with the spin-coating one.

2. Experimental setup and methodology

In this work, Ga_2O_3 films were prepared on silica glass (SiO_2) substrates by the spray-pyrolysis method. To obtain a solution for preparing gallium oxide film, the gallium nitrate [$Ga(NO_3)_3$*$8H_2O$] (99,9%) was dissolved in ethylene glycol [$C_2H_6O_2$] (99.5%) with addiction of monoethanolamine [C_2H_7NO] (99.5%) as a stabilizer. The solution was mixed at 60°C for 60 minutes. The concentration of gallium nitride varied from 0.125 to 0.5 mol/l. The molarity of gallium nitrate and ethylene glycol was 0.25 mol/l while the molar ratio of gallium nitrate and monoethanolamine was 3:1. Silica glass substrates were ultrasonically cleaned with isopropyl alcohol for 10 minutes.

The experimental setup for the preparation of Ga_2O_3 thin films by spray-pyrolysis is schematically shown in Fig. 1.

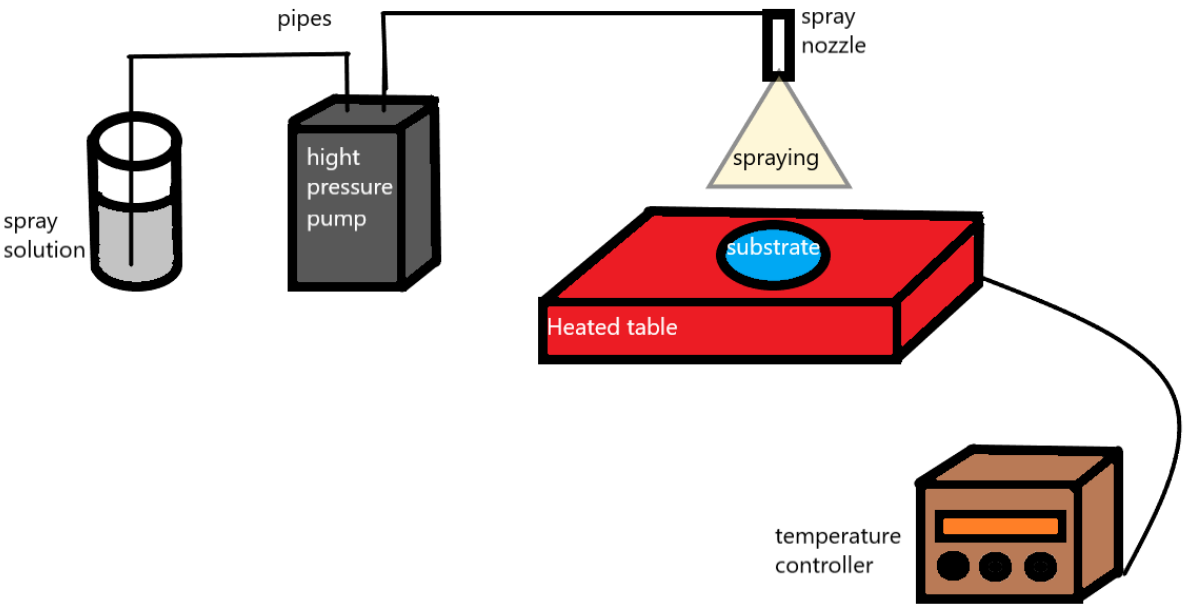

Fig.1. Schematics for spray-pyrolysis gallium oxide application unit

The solution was sprayed onto a substrate with the help of a high-pressure plunger pump and a spray nozzle with an outlet nozzle diameter of 0.1 mm. The substrate was located on a heated table connected to a temperature controller. The distance between the nozzle and the substrate was about 30 cm. Separate parts of the spraying system were connected by silicone pipes. The procedure of spraying is schematically shown in Fig. 2.

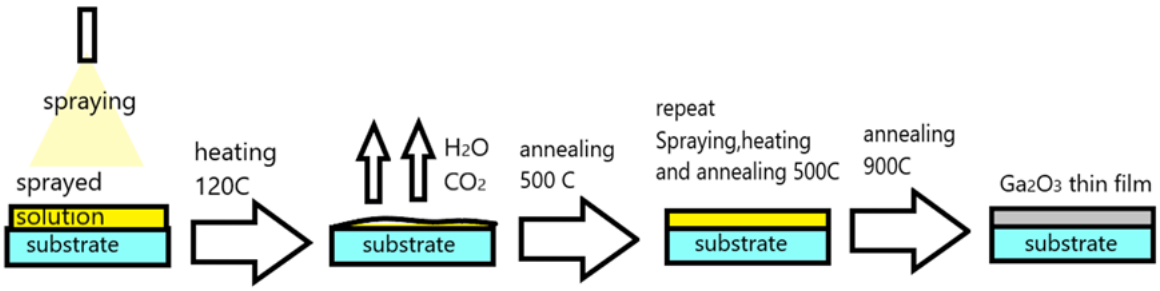

Fig. 2. Schematic representation of the spraying method with pre-annealing at 500°C

Every layer was deposited on the substrate at 120°C for 2 seconds. Then it was dried at 120°C for 120 seconds to get rid of water and carbon dioxide excesses. At this temperature there is a decomposition of gallium nitrate, which can be described by this reaction [29]:
$Ga(NO)_3 \rightarrow GaO(OH) + Ga(OH)_3 + N_2O_5$.

The next step after drying was pre-annealing at 500°C for 5 minutes for each layer, to finally get rid of organic impurities. The process here can be described by the following reaction [29]:
$GaO(OH) + Ga(OH)_3 \rightarrow Ga_2O_3 + H_2O$.

After pre-annealing, the next layer was formed following the same procedure. This method, using pre-annealing at 500°C, was described by Zhu et. al. [17] as the optimal one, allowing to improve the quality of growing gallium oxide films. In our work, the process was repeated until 30 layers were deposited. The last step was the annealing of the sample at 900°C for 30 minutes for obtaining the beta phase of Ga_2O_3. The deposition and annealing processes were carried out in the air.

The morphology of gallium oxide films was characterized by AFM technique, using a Dimension 3100 microscope in dynamic contact mode. SEM images and EDX data of gallium oxide films were obtained by a TESCAN Mira 3 microscope with an Ultima MAX silicon drift detector. The XRD images were obtained using a Rigaku Ultima IV X-ray diffractometer (Japan). The radiation of a copper anode with λ (CuKα) = 1.5418 Å was used. The radius of the goniometer was 285 mm. The X-ray was taken in the range of angles 2θ from 15° to 70° in the geometry of the Bragg-Brentano survey. The measurements were carried out using a CuKß filter. In the experiment, the voltage on the tube was 40 kV, and the current was 40 mA, the output power was 1.6 kW. The diffraction database International Center for Diffraction Data (ICDD) PDF-2 (2008) was used to interpret diffraction reflexes. The optical properties were studied in the range of 200-1000 nm by an optical spectrometer (AvasSpec-ThinFilm).

3. Results and discussion

The main goal of this work was to develop a method of forming a solid film of uniform thickness with a minimum number of defects (cracks, inclusions).

A series of experiments was carried out to figure out the optimal concentration of gallium nitrate, which ensures the formation of a solid film. On the one hand, higher

concentrations of metal ions led to larger numbers of nuclei during crystallization, resulting in smaller average grain sizes. On the other hand, spontaneous island crystallization and the formation of a highly inhomogeneous film are observed at too high concentrations of metal salts. An example of multiple island formations is clearly seen in Fig. 3. In this series of experiments, the concentration of gallium nitride varied from 0.125 to 0.5 mol/l. As a result, it was found that the optimal concentration was 0.25 mol/l.

The results of the studies presented below refer to the samples grown by spray pyrolysis with pre-annealing at 500°C and at the optimal concentration of gallium nitrate.

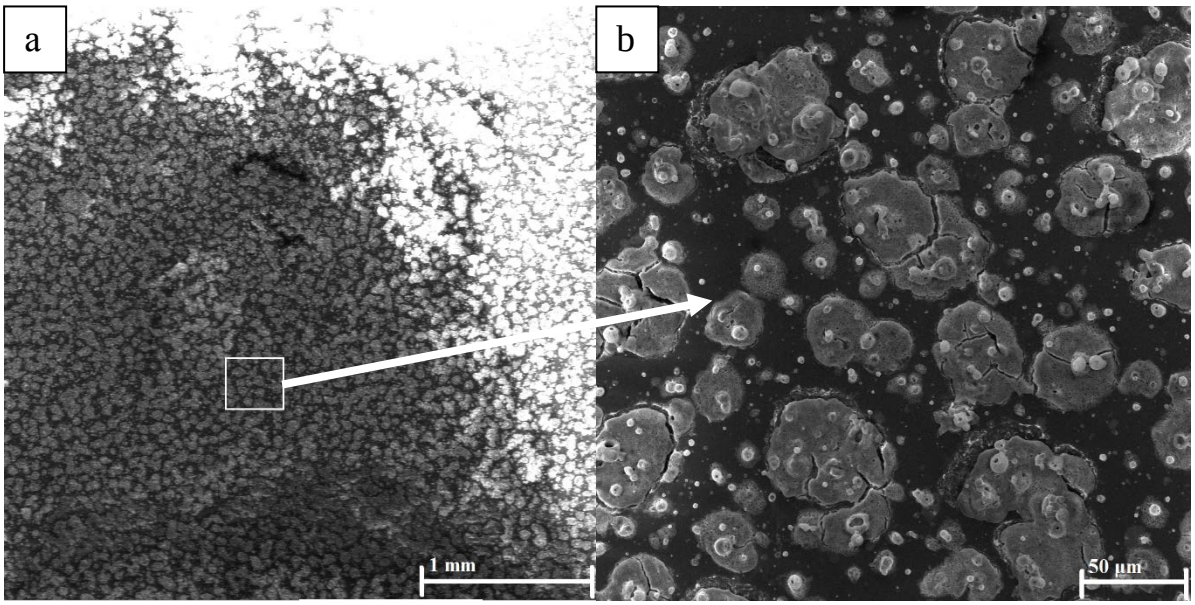

Fig. 3. Top-view SEM images gallium oxide film under varying magnification sample with 0.5 mol/l of gallium nitrate: a) scale 1 mm, b) scale 50µm

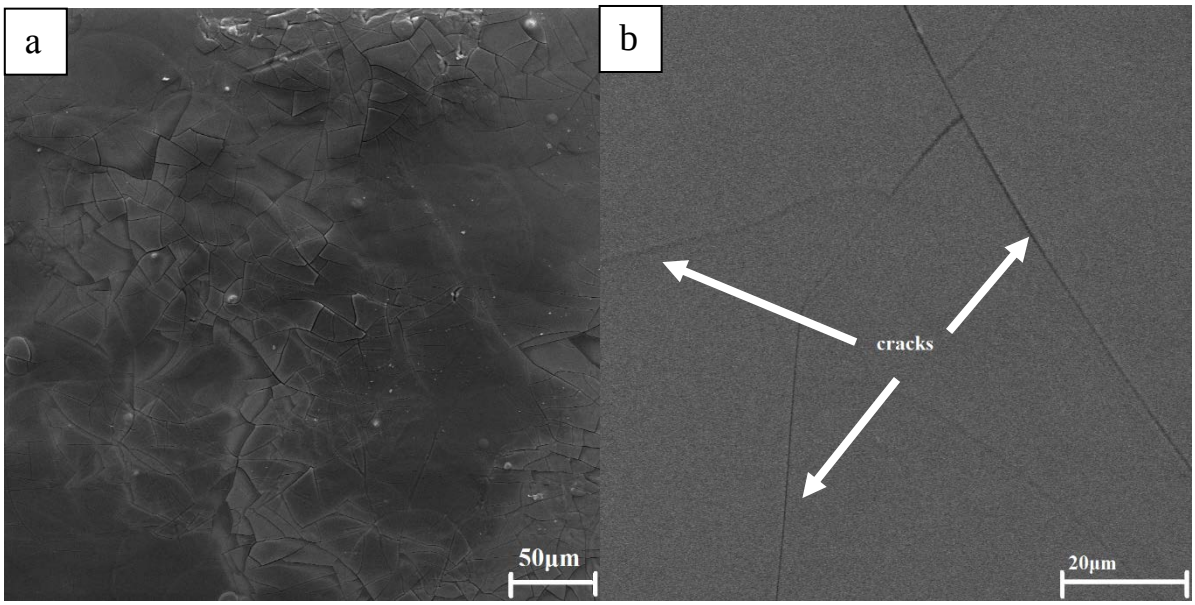

Fig. 4. Top view SEM images of the films with (0.25 mol/l) concentration of gallium nitrate: a) before heat treatment at 900°C, b) after heat treatment at 900°C

Figure 4 shows the surface morphology of the gallium oxide film before and after heat treatment at 900°C. As can be seen from the figure there are cracks on the film, which may be due to the different thermal expansion coefficients of the film (for Ga_2O_3 – $1.8\times10^{-6}\,K^{-1}$ for

the *a* axis and $4.2\times10^{-6}\,K^{-1}$ for the *b* and *c* axes) [30] and the substrate (for fused silica is $0.4\times10^{-6}\,K^{-1}$) [31].

Figure 5 shows the AFM surface images of the same film. As can be seen from the surface scanning data, this Ga_2O_3 film has average roughness Ra=0,954 nm and square roughness Rq=1.21nm for a space of 10 μm × 10 μm.

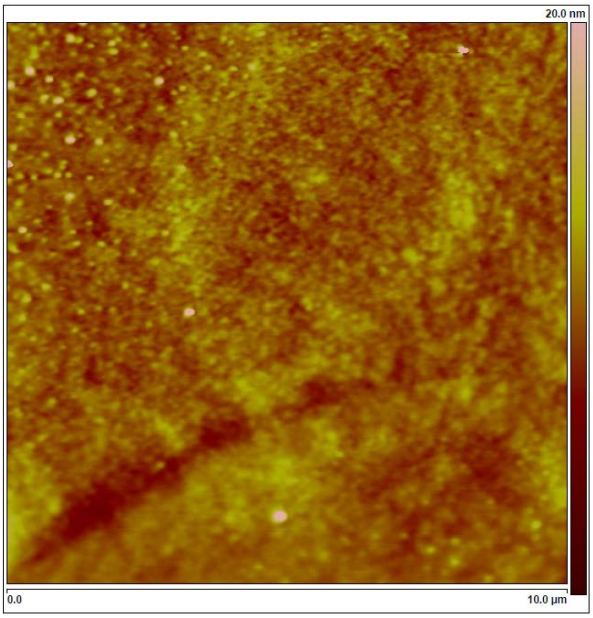

Fig. 5. AFM images (10 μm × 10 μm) of β-Ga2O3 thin films annealed at 900°C (Ra=0.954nm, Rq=1.21nm)

Figure 6 shows a cross-sectional SEM image of the substrate with a gallium oxide film deposited on it after a 900°C heat treatment. The film thickness at the middle area was about 1 μm. A study across the entire width of the sample showed that the film thickness decreased near the edges to 0.75 μm. This is most likely due to the conic shape of the spraying.

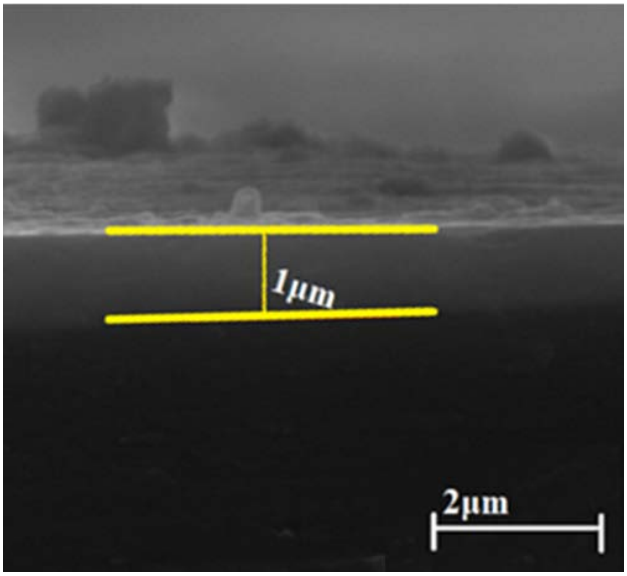

Fig. 6. The side view SEM image of the film: sample with optimal (0.25 mol/l) concentration of gallium citrate, the thickness of 1 μm

The chemical composition of obtained films was determined by the EDX (Energy Dispersive X-Ray Spectroscopy) method at several points and by EDX mapping over the film area. The results are shown in Fig. 7 and Fig. 8, respectively. The films have the correct stoichiometric composition Ga/O = 40/60 distributed evenly over the entire area. The difference in composition values is less than 1.5% while the nominal accuracy of the method is about 0.5%.

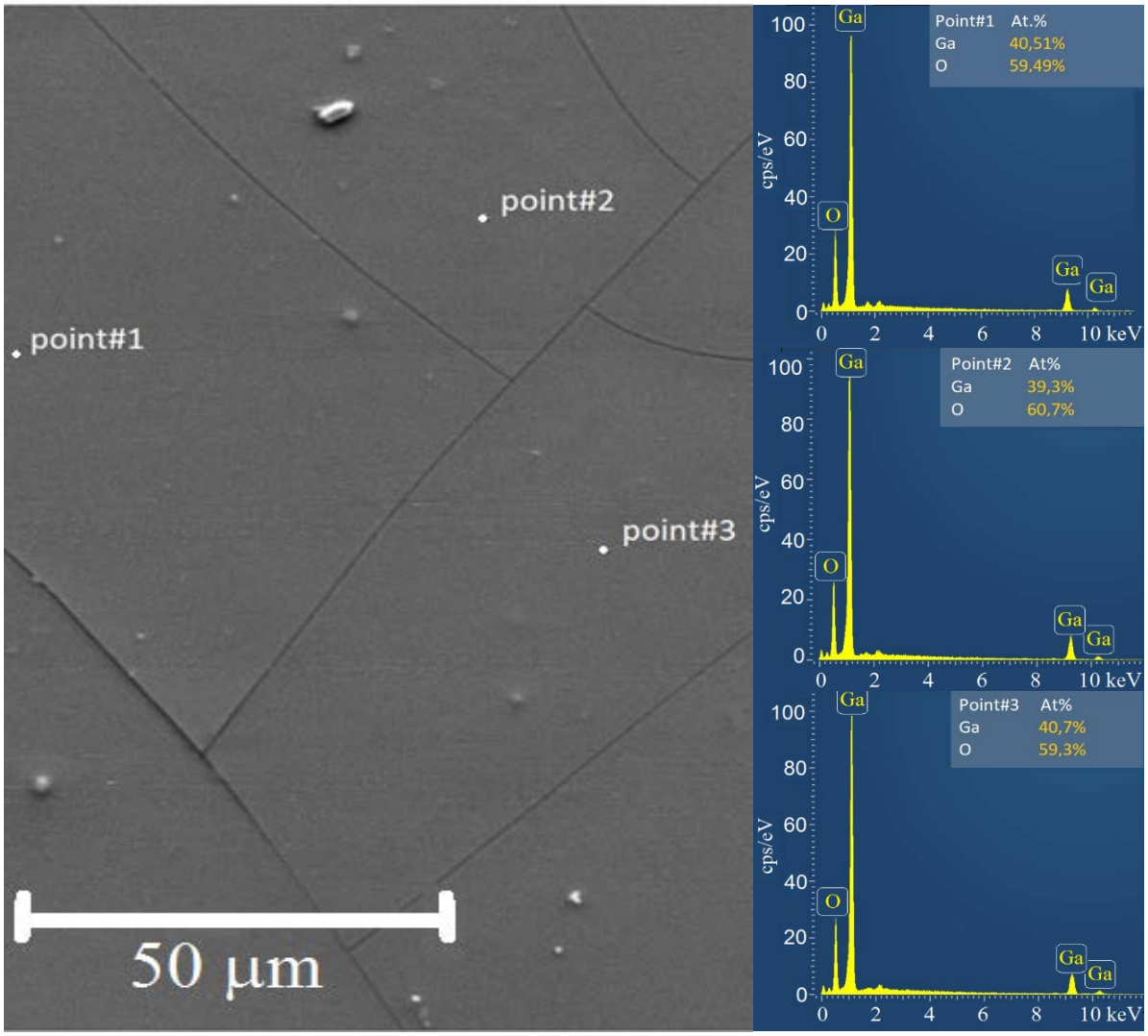

Fig. 7. Results of film composition measurements by the EDX method. Left part of the figure: a top view SEM image of measurement area. Three points of measurements are marked. Right part of the figure: EDX spectra

X-ray diffraction (XRD) spectrum is shown in Fig. 9. In terms of position and integral intensity, the X-ray diffraction peaks of obtained thin films of Ga_2O_3 by spray-pyrolysis method, after annealing at 900°C, correspond to β-Ga_2O_3 ICDD data (PDF 00-041-1103). The size of crystallites reached 10 nm. The size of the crystallites was found by the Scherrer equation:

$$l = K * \lambda/(\beta * \mathrm{Cos}\,\theta), \quad (1)$$

where λ is the X-ray wavelength in nanometer (nm), β is the peak width at half maximum height (rad), and K is a constant related to crystallite shape (0.94).

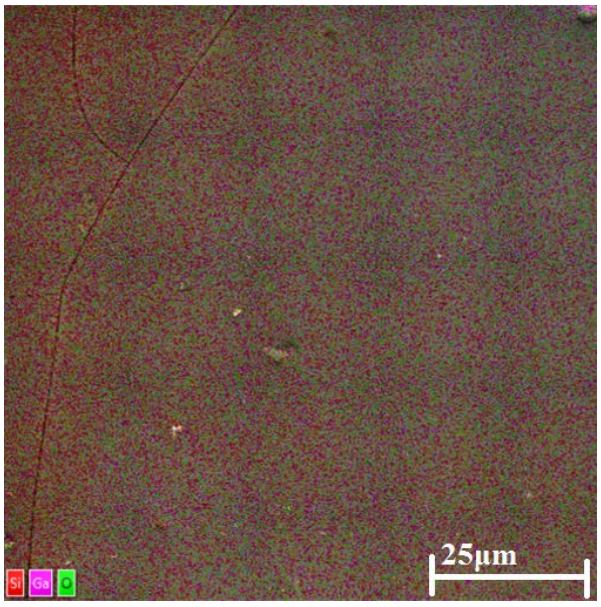

Fig. 8. Results of film composition study by the EDX mapping method: view SEM image of measurements area. The distribution of Ga, Si, and O elements on the resulting sample is shown in different colors

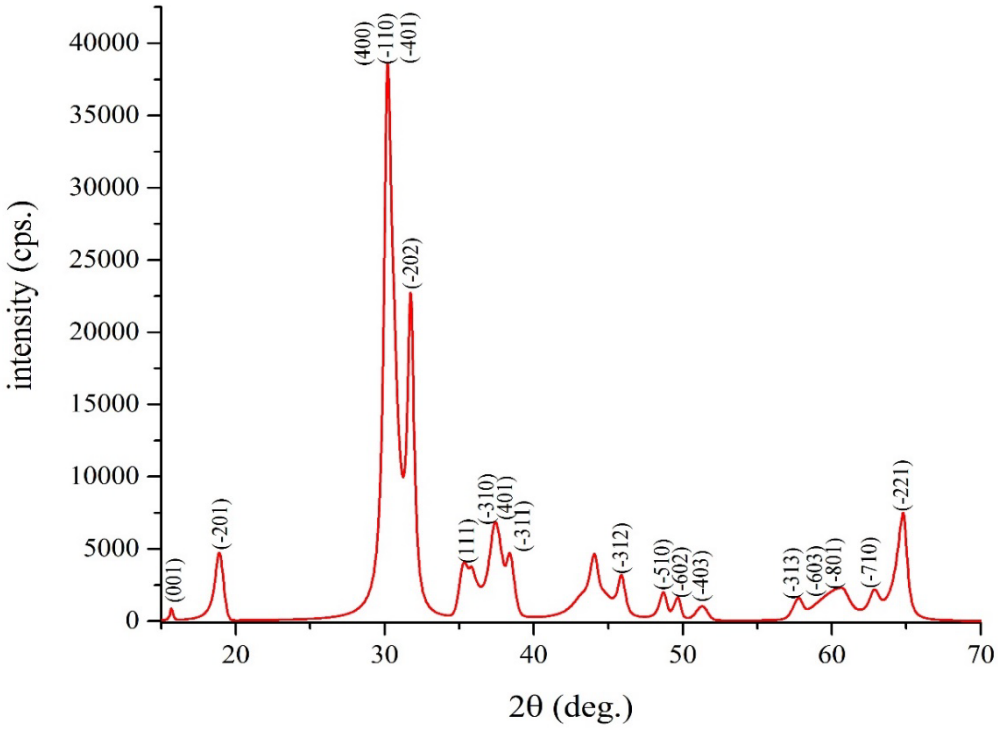

Fig. 9. X-ray diffraction (XRD) pattern of obtained thin films of Ga_2O_3 by spray-pyrolysis method, after annealing at 900°C, indexed in comparison to PDF 00-041-1103

The calculated lattice constants for a thin film of gallium oxide after heat treatment 900°C were *a* = 12.1966(Å), *b* = 3.0313(Å) *c* = 5.7934(Å) (α = 90.0°, β = 103.82°, γ = 90.0°), which corresponds to β-Ga_2O_3 [32].

Transmission spectra of samples and bandgap estimation are shown in Fig. 10. The samples have transmission in the near-ultraviolet (N-UV), visible, and near-infrared (NIR) regions of the spectrum (300-1000 nm), and have an absorption band in the range of 200-250 nm. Also, it should be noted that after heat treatment of samples at 900°C, the

samples have a more intensive absorption in the range of 200-250 nm and more intensive transmission in the range of 300-1000 nm. This can be explained by the transition of the film to a crystalline state and the formation of beta phase of gallium oxide. Based on the optical absorption data, the bandgap value was estimated for the β-Ga_2O_3 film after heat treatment at 900°C by analyzing transmission spectra [32,33]. The estimation gives a value of about 4.87 eV for the band gap which corresponds with the value of β-Ga_2O_3 bandgap in previous works. [8,33,34].

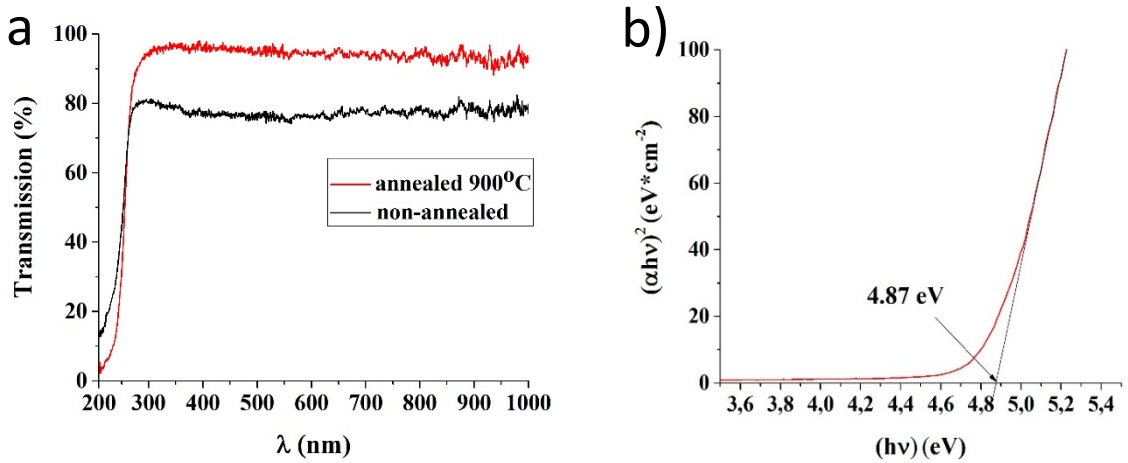

Fig.10. (a) Optical transmission spectra for annealed and non-annealed samples and substrate and (b) bandgap estimation for annealed at 900°C Ga_2O_3 film

4. Conclusions

A modification of the spray-pyrolysis method for the formation of gallium oxide solid films was proposed. The optimal value of the concentration of gallium nitrate was found to be 0.25, which ensures the formation of a solid film. At the optimal concentration of gallium nitrate, the preliminary annealing at 500°C was added to the method after deposition and drying of each layer. It was found that the proposed method ensures the formation of thin (up to 1 μm) solid films of gallium oxide on silica glass substrates. Analysis of the chemical composition by the EDS method showed the correct stoichiometric composition (Ga:O = 2:3) over the entire area of the film. It was proved by X-ray diffraction that the entire film consists of the beta phase of gallium oxide. An analysis of the transmission spectra made it possible to estimate the band gap of the material, which was 4.87 eV.

References

1. Pearton SJ, Yang J, Cary PH, Ren F, Kim J, Tadjer MJ, Mastro MA. A review of Ga_2O_3 materials, processing, and devices. *Applied Physics Reviews*. 2018;5: 011301.
2. Stepanov SI, Nikolaev VI, Bougrov VE, Romanov AE. Gallium oxide: properties and applications – a review. *Reviews On Advanced Materials Science.* 2016;44: 63-86.
3. Galazka Z. β-Ga_2O_3 for wide-bandgap electronics and optoelectronics. *Semiconductor Science and Technology*. 2018;33: 113001.
4. Bauman DA, Borodkin AI, Petrenko AA, Panov DI, Kremleva AV, Spiridonov VA, Zakgeim DA, Silnikov MV, Odnoblyudov MA, Romanov AE, Bougrov VE. On improving the radiation resistance of gallium oxide for space applications. *Acta Astronautica*. 2021;180: 125-129.
5. Yu M, Lv C, Yu J, Shen Y, Yuan L, Hu J, Zhang S, Cheng H, Zhang Y, Jia R. High-performance photodetector based on sol–gel epitaxially grown α/β-Ga_2O_3 thin films. *Materials Today Communications*. 2020;25: 101532.

6. Wenckstern H. Group-III Sesquioxides: Growth, Physical Properties and Devices. *Advanced Electronic Materials*. 2017;3: 1600350.
7. Hu Z, Nomoto K, Li W, Zhang Z, Tanen N, Thieu QT, Sasaki K, Kuramata A, Nakamura T, Jena D, Xing HG. Breakdown mechanism in 1 kA/cm2 and 960 V E-mode β-Ga_2O_3 vertical transistors. *Applied Physics Letters*. 2018;113: 122103.
8. Galazka Z, Irmscher K, Uecker R, Bertram R, Pietsch M, Kwasniewski A, Naumann M, Schulz T, Schewski R, Klimm D, Bickermann M. On the bulk β-Ga_2O_3 single crystals grown by the Czochralski method. *Journal of Crystal Growth*. 2014;404: 184-191.
9. Zhang X, Jiang D, Zhao M, Zhang H, Li M, Xing M, Han J, Romanov AE. The effect of annealing temperature on Ga_2O_3 film properties. *Journal of Physics: Conference Series*. 2021;1965: 012066.
10. Yin-nü. Preparation and Properties of Zn-doped β-Ga_2O_3 Films. *Acta Photonica Sinica.* 2012;41: 1242-1246.
11. Du X, Mi W, Luan C, Li Z, Xia C, Ma J. Characterization of homoepitaxial β-Ga_2O_3 films prepared by metal–organic chemical vapor deposition. *Journal of Crystal Growth.* 2014;404: 75-79.
12. Hassa A, Wouters C, Kneiß M, Splith D, Sturm C, Wenckstern H von, Albrecht M, Lorenz M, Grundmann M. Control of phase formation of $(AlxGa_{1-x})_2O_3$ thin films on c-plane Al_2O_3. *Journal of Physics D: Applied Physics*. 2020;53: 485105.
13. Kaun SW, Wu F, Speck JS. β-$(Al_xGa_{1-x})_2O_3/Ga_2O_3$ (010) heterostructures grown on β-Ga_2O_3 (010) substrates by plasma-assisted molecular beam epitaxy. *Journal of Vacuum Science & Technology A.* 2015;33: 041508.
14. Goyal A, Yadav BS, Thakur OP, Kapoor AK, Muralidharan R. Effect of annealing on β-Ga_2O_3 film grown by pulsed laser deposition technique. *Journal of Alloys and Compounds*. 2014;583: 214-219.
15. Kremleva AV, Sharofidinov ShSh, Smirnov AM, Podlesnov E, Dorogov MV, Odnoblyudov MA, Bougrov VE, Romanov AE. Growth of thick gallium oxide on the various substrates by halide vapor phase epitaxy. *Materials Physics and Mechanics*. 2020;44(2): 164-171
16. Zhu Y, Xiu X, Cheng F, Li Y, Xie Z, Tao T, Chen P, Liu B, Zhang R, Zheng Y-D. Growth and nitridation of β-Ga_2O_3 thin films by Sol-Gel spin-coating epitaxy with post-annealing process. *Journal of Sol-Gel Science and Technology*. 2021;100: 183-191.
17. Cheah LB, Osman RAM, Poopalan P. Ga_2O_3 thin films by sol-gel method its optical properties. *AIP Conference Proceedings.* 2020;2203: 020028.
18. Yu L-Y, Shen H-M, Xu Z-L. PVDF–TiO_2 composite hollow fiber ultrafiltration membranes prepared by TiO_2 sol–gel method and blending method. *Journal of Applied Polymer Science*. 2009;113: 1763-1772.
19. Salles P, Caño I, Guzman R, Dore C, Mihi A, Zhou W, Coll M. Facile Chemical Route to Prepare Water Soluble Epitaxial $Sr_3Al_2O_6$ Sacrificial Layers for Free-Standing Oxides. *Advanced Materials Interfaces.* 2021;8: 2001643.
20. Brunckova H, Medvecky L, Briancin J, Durisin J, Mudra E, Sebek M, Kovalcikova A, Sopcak T. Perovskite lanthanum niobate and tantalate thin films prepared by sol–gel method. *Materials Letters.* 2016;165: 239-242.
21. Corriu RJP, Leclercq D. Recent Developments of Molecular Chemistry for Sol–Gel Processes. *Angewandte Chemie International Edition in English.* 1996;35: 1420-1436.
22. Andronic L, Perniu D, Duta A. Synergistic effect between TiO_2 sol–gel and Degussa P25 in dye photodegradation. *Journal of Sol-Gel Science and Technology*. 2013;66: 472-480.
23. Kelso MV, Mahenderkar NK, Chen Q, Tubbesing JZ, Switzer JA. Spin coating epitaxial films. *Science.* 2019;364: 166-169.

24. Kokubun Y, Miura K, Endo F, Nakagomi S. Sol-gel prepared β-Ga_2O_3 thin films for ultraviolet photodetectors. *Applied Physics Letters.* 2007;90: 031912.
25. Shen H, Yin Y, Tian K, Baskaran K, Duan L, Zhao X, Tiwari A. Growth and characterization of β-Ga_2O_3 thin films by sol-gel method for fast-response solar-blind ultraviolet photodetectors. *Journal of Alloys and Compounds.* 2018;766: 601-608.
26. Ohya Y, Okano J, Kasuya Y, Ban T. Fabrication of Ga_2O_3 thin films by aqueous solution deposition. *Journal of the Ceramic Society of Japan*. 2009;117: 973-977.
27. Winkler N, Wibowo RA, Kautek W, Ligorio G, List-Kratochvil EJW, Dimopoulos T. Nanocrystalline Ga_2O_3 films deposited by spray pyrolysis from water-based solutions on glass and TCO substrates. *Journal of Materials Chemistry C.* 2018;7: 69-77.
28. Kim H, Kim W. Optical properties of β-Ga_2O_3 and α-Ga_2O_3:Co thin films grown by spray pyrolysis. *Journal of Applied Physics.* 1987;62: 2000-2002.
29. Berbenni V, Milanese C, Bruni G, Marini A. Thermal decomposition of gallium nitrate hydrate Ga(NO3)3×xH2O. *Journal of Thermal Analysis and Calorimetry*. 2005; 82: 401-407.
30. Víllora EG, Shimamura K, Ujiie T, Aoki K. Electrical conductivity and lattice expansion of β-Ga2O3 below room temperature. *Applied Physics Letters.* 2008;92: 202118.
31. Oishi J, Kimura T. Thermal Expansion of Fused Quartz. *Metrologia*. 1969;5: 50-55.
32. Dohy D, Gavarri JR. Oxyde β-Ga_2O_3: Champ de force, dilatation thermique, et rigidité anisotropes. *Journal of Solid State Chemistry.* 1983;49: 107-117.
33. Tauc J. Optical properties and electronic structure of amorphous Ge and Si. *Materials Research Bulletin.* 1968;3: 37-46.
34. Zakgeim D, Bauman D, Panov D, Spiridonov V, Kremleva A, Smirnov A, Odnoblyudov M, Romanov A, Bougrov V. Growing of bulk β-$(Al_xGa_{1-x})_2O_3$ crystals from the melt by Czochralski method and investigation of their structural and optical properties. *Applied Physics Express*. 2022;15: 025501.

THE AUTHORS

Panov D.I.
e-mail: Dmitriipnv@gmail.com
ORCID: 0000-0001-8715-9505

Zhang X.
e-mail: 314519083@qq.com
ORCID: 0000-0002-1275-1165

Spiridonov V.A.
e-mail: vladspiridonov@itmo.ru
ORCID: 0000-0001-5751-8597

Azina L.V.
e-mail: lvazina@itmo.ru
ORCID: 0000-0003-3502-1365

Nuryev R.K.
e-mail: nuryev@itmo.ru
ORCID: 0000-0001-9427-1749

Prasolov N. D.
e-mail: ndprasolov@corp.ifmo.ru
ORCID: -

Sokura L.A.
e-mail: sokura@mail.ioffe.ru
ORCID: -

Bauman D.A.
e-mail: dabauman@itmo.ru
ORCID: 0000-0001-5751-8597

Bougrov V.E.
e-mail: Vladislav.bougrov@niuitmo.ru
ORCID: 0000-0001-5751-8597

Romanov A.E.
e-mail: alexey.romanov@niuitmo.ru
ORCID: 0000-0003-3738-408X

Materials Physics and Mechanics. 2022;50(1): 118-125
Research article
http://dx.doi.org/10.18149/MPM.5012022_9

Submitted: April 21, 2022
Approved: June 19, 2022
Accepted: August 17, 2022

Molecular dynamics simulation of severe plastic deformation of nanotwinned Hadfield steel

G.M. Poletaev[1]✉, R.Y. Rakitin[2]

[1]Altai State Technical University, Lenin Str. 46, 656038 Barnaul, Russia

[2]Altai State University, Lenin Str. 61, 656049 Barnaul, Russia

✉ gmpoletaev@mail.ru

Abstract. The features of the plastic deformation at the atomic level and the formation of a dislocation structure in nanotwinned Hadfield steel under severe shear deformation along the direction perpendicular to parallel coherent twins were studied by the method of molecular dynamics. Similar studies for comparison were carried out for austenite. Dislocations in steel propagated and developed more weakly than in austenite, stacking faults between partial dislocations were shorter, and the number of dislocations was smaller, which was a consequence of the interaction of dislocations with impurity carbon atoms in steel. The main plastic shifts inside the computational cells containing parallel twins occurred predominantly along twin boundaries in the form of twinning dislocations. Dislocations from another slip system, not parallel to the twin boundaries, practically did not form. As a result of the passage of twinning dislocations, the twins moved during deformation.
Keywords: molecular dynamics, deformation, nanotwinned metal, Hadfield steel

Acknowledgements*. No external funding was received for this study.*

Citation: Poletaev GM, Rakitin RY. Molecular dynamics simulation of severe plastic deformation of nanotwinned Hadfield steel. *Materials Physics and Mechanics*. 2022;50(1): 118-125. DOI: 10.18149/MPM.5012022_9.

1. Introduction

Hadfield steel, due to its excellent work hardening capacity [1,2], is of great practical importance and has a long history of research into its unique properties. At the same time, to date, there are very few works devoted to modelling its atomic structure and the processes occurring in it under deformation conditions at the atomic level, which is due, in particular, to the complexity of modelling such multicomponent systems. Currently, there are a number of questions related to the mechanisms of plastic deformation at the atomic level in steels and which can be solved mainly by computer simulation methods. Such issues include, for example, the features of the formation and propagation of dislocations depending on various factors, the mechanisms of interaction with each other, grain boundaries, twins, and other defects.

In recent years, it has been found that the introduction of a high density of coherent twin boundaries to grain domains can significantly improve the strength of materials [3,4]. Such phenomenon has been discovered in various materials such as copper, gold, high-entropy alloys, and steels [3-9]. For example, in [5] authors showed that the copper with nanometre-scale twins (in terms of both twin thickness and spacing) exhibits a tensile strength ten times

higher than that of the conventional coarse-grained copper. This excellent strengthening effect of nanotwins is attributed to their role as effective dislocation barriers, which reduce the dislocation mean free path and thereby promote dislocation multiplication, similar to the effect of grain boundaries [10]. In works [11-14], performed using computer simulation, it is shown that a coherent twin is a serious obstacle for a moving edge dislocation. Significant energy and stress are required to overcome a twin by an edge dislocation.

This work is devoted to studying, using molecular dynamics simulation, the features of plastic deformation at the atomic level and the formation of a dislocation structure in nanotwinned Hadfield steel under severe shear deformation along a direction perpendicular to parallel coherent twins. To determine and isolate the role of twins and impurity atoms in steel in the deformation process, studies were carried out in parallel on the example of four samples: Hadfield steel and fcc Fe without twins and containing parallel coherent twins.

2. Description of the model

Hadfield steel, as is known, is a multi-component system and, in addition to classical iron, manganese, and carbon, may contain some other alloying elements [1,2]. In this study, we limited to a system that included three elements: γ-Fe as a matrix, Mn, and C. To describe the Fe-Fe interactions in the austenite matrix, it was used Lau EAM potential [15], which reproduces well the structural, energy, and elastic characteristics of austenite [15,16]. For all other five interatomic interactions in the γ-Fe-Mn-C system, we used the Morse potentials found by us earlier in [17] based on experimental data on the dissolution energy and migration energy of the corresponding impurity atoms in the fcc iron crystal, the atomic radius, their electronegativity, mutual binding energy, and other characteristics.

The standard ratio of components was used: Mn – 13 wt.% and C – 1.2 wt.% (12.63 at.% and 5.33 at.%, respectively) [1,2]. Mn atoms were introduced into fcc iron lattice randomly by replacing Fe atoms. The binding energy of Mn and C atoms in austenite lattice is very high – 0.35 eV, according to [18], which is approximately the same as, for example, the binding energy of carbon atoms with vacancies (0.37–0.41 eV [19]). That is, Mn atoms are a kind of effective "traps" for impurity carbon atoms, not allowing them, in particular, to form clusters on dislocations and grain boundaries. In this connection, carbon atoms were introduced into the octahedral voids closest to Mn atoms. The number of carbon atoms has corresponded to a given concentration. The choice of Mn atoms near which C atoms were introduced, as well as the selection of one of the neighboring octahedral voids, were made randomly.

In pure fcc iron, which was considered in this work for comparison with Hadfield steel, the type of the crystal lattice remained constant over the entire temperature range; the polymorphic transformation was not taken into account in this work. As mentioned above, pure austenite was considered to determine the contribution of Mn and C impurities in the processes under study.

In this work, we considered the computational cells of fcc Fe and Hadfield steels, which initially did not contain defects (except for impurity atoms) (Fig. 1a) and contained four parallel coherent twins $\Sigma3(\bar{1}\bar{1}1)[\bar{1}10]$ (Fig. 1b). A total of four cells were considered. The computational cell of fcc Fe contained approximately 123 thousand atoms, while that of Hadfield steel contained 130 thousand atoms. It was 27.2 nm long, 20.3 nm high, and 2.5 nm thick. Thus, the distance between parallel twins was 6.8 nm, which does not contradict the data on the distance between twins in real materials [20]. Along the *X* and *Y* axes (Fig. 1), an infinite repetition of the structure was simulated, that is periodic boundary conditions were imposed. The shear in the model was initiated by the displacement of atoms in the upper and lower regions highlighted by light grey in Fig. 1 in opposite directions along and against the y-axis (the [111] direction). The areas in the upper and lower parts of the cell in the course of

the computer experiment moved as a whole. In our previous work [17], we selected the optimal shear rate for the molecular dynamics method in this case – 10 m/s.

The time integration step in the molecular dynamics method was 2 fs [21-23]. The simulation of the deformation was carried out at a temperature of 300 K. The temperature in the model was set through the initial velocities of the atoms according to the Maxwell-Boltzmann distribution. When setting the temperature, it was obligatory to take into account the thermal expansion of the crystal lattice. To do this, for the interatomic interaction potentials used in the work, the average thermal expansion coefficients were previously found in the molecular dynamics model: $18 \cdot 10^{-6}$ K^{-1} for γ-Fe and $16 \cdot 10^{-6}$ K^{-1} for Hadfield steel. To keep the temperature constant during the simulation, a Nose-Hoover thermostat was used.

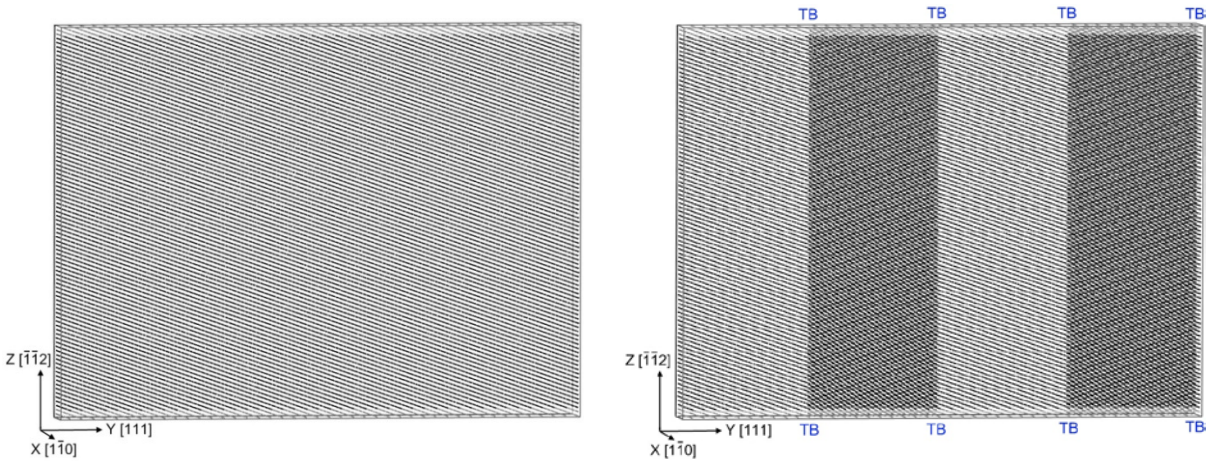

a) b)

Fig. 1. Computational cells for modelling the shear along the [111] direction (y-axis): a) without twins; b) containing four parallel twin boundaries (TB)

3. Results and discussion

To determine the mechanism of plastic deformation and the role of twins and impurity atoms in it, in this work, we studied the transformation of the structure during plastic shear in 15% and 30% of the considered computational cells. As is known, in crystals with an fcc lattice, the slip system {111}<110> is predominant [24,25]. During plastic shear along the <111> direction (y-axis), two slip systems are involved. The joint work of dislocations of two different slip systems is clearly seen, for example, in Fig. 2a, which shows the fcc Fe structure obtained after a 15% shear. In the figure, the computational cell is oriented in such a way that plastic shifts are better seen. Thin dark bands are mainly stacking faults separating partial dislocations. Relatively thick dark bands are the result of twinning. In Figure 2b, which shows the structure after a shear of 30%, this process is more pronounced. With such a large deformation, more complex defects are already formed: grain boundaries and parallel twins. There are fewer simple dislocations. In Figure 2b, near one of the cell borders (in this case, the upper one), along which the shear was performed, a low-angle grain boundary (GB in the figure) was formed, and the plastic shift proceeded mainly due to grain boundary sliding (GBS). Twins actively worked: the twin bands changed their width during deformation, which indicates the frequent passage of twinning dislocations along the twin boundary (TB) (in Fig. 2b one can clearly see such a twinning dislocation in the form of a step on TB in the centre of the computational cell). It is noteworthy that these twins ended at the grain boundary in the upper part of the cell.

The difference between pure austenite and steel, as can be seen in Fig. 3, is quite large and visible visually. Dislocations in steel propagated and developed much more weakly than in pure fcc iron, stacking faults between partial dislocations are noticeably shorter and their

number is smaller. Obviously, in this case, the work of impurity carbon atoms takes place, which, as is known, have positive binding energy both with dislocations and stacking faults [26-28], thereby slowing down the movement of dislocations.

In the case of steel, in contrast to pure austenite, the process of formation of parallel twins was not observed in the model. On the other hand, GBS manifested itself more clearly; it was the main mechanism of plastic deformation at a shear of 30% (Fig. 3b).

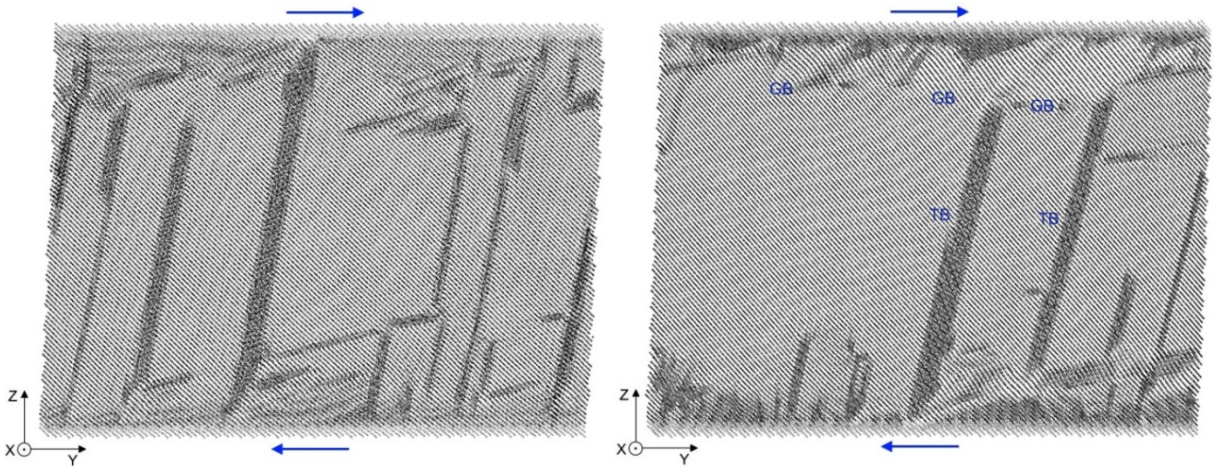

a) b)

Fig. 2. Structure of fcc Fe after a shear along the y-axis [111] by 15% (a) and 30% (b). GB – grain boundary, TB – twin boundary

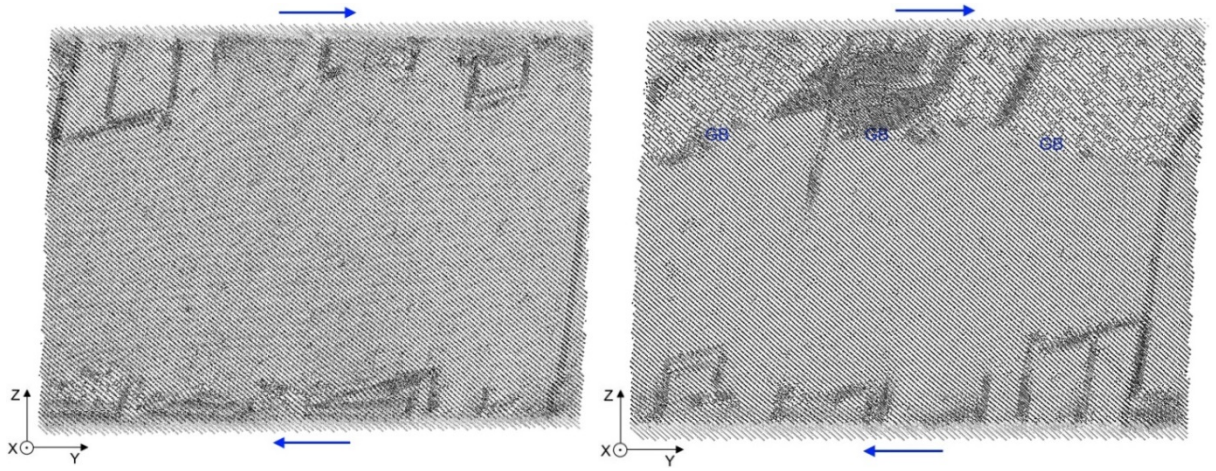

a) b)

Fig. 3. Structure of Hadfield steel after a shear along the y-axis [111] by 15% (a) and 30% (b)

Figure 4 shows the structures of the computational cell of fcc iron, initially containing four parallel twin boundaries at equal distances, deformed by shear along the [111] direction by 15% (Fig. 4a) and 30% (Fig. 4b). When considering the picture obtained with deformation of 15%, the first thing that attracts attention is the almost complete absence of dislocations from the slip system that is not parallel to the twin boundaries. And at the same time, there is a change in the distance between the twins. The displacement or migration of a twin boundary occurs, as is known, as a result of the passage of a twinning dislocation along the twin boundary [24,25]. The change in the distances between twins is the result of the passage of twinning dislocations. They could not go beyond the limits of the computational cell due to the rigid boundary conditions, as a result of which local deformations of the structure were formed in the computational cell near the upper and lower boundaries of the cell. In general,

there are noticeably fewer individual dislocations than in a pure crystal (Fig. 2a), because many of them in this case formed in the form of twinning dislocations, which are visible in the images as steps on twin boundaries. After passing along the twin boundary, they accumulated near the upper and lower boundaries of the computational cell. Intersections of twins by dislocations and shear through twins were not observed; as mentioned earlier, they represent a significant barrier to dislocations.

At a deformation of 30%, the mechanisms described above were supplemented by the formation of a low-angle grain boundary along the upper and lower boundaries of the computational cell and the occurrence of deformation also due to grain boundary sliding (Fig. 4b). It should be noted that the distance between the twins has changed even more, which indicates that the work of twinning dislocations continues.

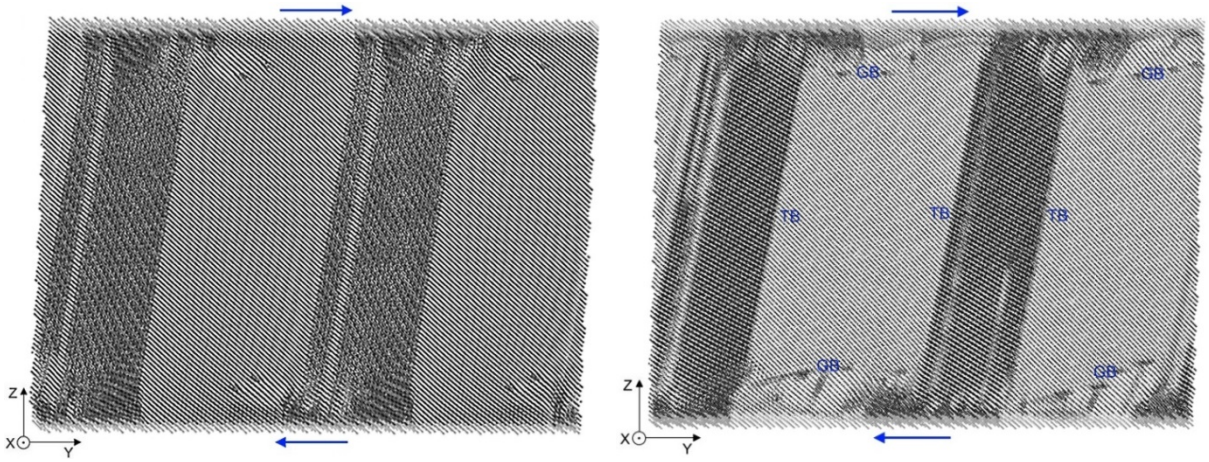

a) b)

Fig. 4. Structure of fcc Fe, which initially contained twins, after a shear along the y-axis [111] by 15% (a) and 30% (b)

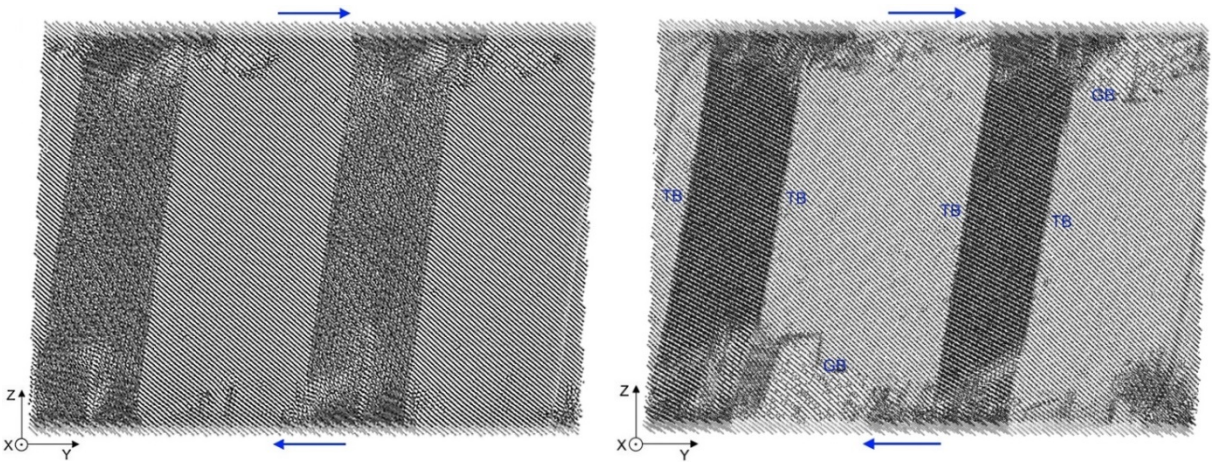

а) б)

Рис. 5. Structure of Hadfield steel, which initially contained twins, after a shear along the y-axis [111] by 15% (a) and 30% (b)

When performing a similar simulation of deformation in steel, all the mechanisms identified above for fcc iron also took place in Hadfield steel, with the difference that there were again much fewer individual dislocations than in iron. The main plastic shifts inside the computational cells occurred along the twin boundaries in the form of twinning dislocations – Fig. 5 shows how the distances between the twins changed as the deformation increased.

Crystalline grains between twins, except for the structure near the upper and lower borders of the cell, remained virtually defect-free.

4. Conclusion

The features of the plastic deformation at the atomic level and the formation of a dislocation structure in nanotwinned Hadfield steel under severe shear deformation along the direction perpendicular to parallel coherent twins were studied by the method of molecular dynamics. Similar studies for comparison were carried out for steel and fcc iron, not containing twins.

In pure fcc iron, which initially does not contain twins, plastic deformation in the considered type of deformation was carried out mainly due to the formation of dislocations in two slip systems. With an increase in deformation up to 30%, more complex defects (twins and grain boundaries) were formed; plastic deformation was carried out by twinning and grain boundary sliding.

Dislocations in steel propagated and developed much more weakly than in pure fcc iron, and stacking faults between partial dislocations were shorter. At a high strain of 30% in steel, in contrast to austenite, the process of formation of parallel twins was not observed in the model. On the other hand, grain boundary sliding manifested itself more clearly; it was the main mechanism of plastic deformation at a shear of 30%.

In the initial presence of twins, both in fcc iron and in steel, the main plastic shears inside the computational cells occurred predominantly along the twin boundaries in the form of twinning dislocations. Dislocations from another slip system, not parallel to the twin boundaries, practically did not form. As a result of the passage of twinning dislocations, the twins moved during deformation.

References

1. Zhang FC, Lv B, Wang TS, Zheng CL, Zhang M, Luo HH, Liu H, Xu AY. Explosion hardening of Hadfield steel crossing. *Materials Science and Technology*. 2010;26(2): 223-229.
2. Chen C, Lv B, Ma H, Sun D, Zhang F. Wear behavior and the corresponding work hardening characteristics of Hadfield steel. *Tribology International.* 2018;121: 389-399.
3. Lu K, Lu L, Suresh S. Strengthening materials by engineering coherent internal boundaries at the nanoscale. *Science*. 2009;324(5925): 349-352.
4. Sun L, He X, Lu J. Nanotwinned and hierarchical nanotwinned metals: a review of experimental, computational and theoretical efforts. *npj Computational Materials*. 2018;4: 6.
5. Lu L, Chen X, Huang X, Lu K. Revealing the maximum strength in nanotwinned copper. *Science*. 2009;323(5914): 607-610.
6. Zhou P, Liang ZY, Huang MX. Microstructural evolution of a nanotwinned steel under extremely high-strain-rate deformation. *Acta Materialia*. 2018;149: 407-415.
7. Li Q, Yan FK, Tao NR, Ponge D, Raabe D, Lu K. Deformation compatibility between nanotwinned and recrystallized grains enhances resistance to interface cracking in cyclic loaded stainless steel. *Acta Materialia*. 2019;165: 87-98.
8. Liu RD, Li YZ, Lin L, Huang CP, Cao ZH, Huang MX. Strain rate sensitivity of a 1.5 GPa nanotwinned steel. *Journal of Iron and Steel Research International.* 2021;28: 1352-1356.
9. Wang HT, Tao NR, Lu K. Strengthening an austenitic Fe-Mn steel using nanotwinned austenitic grains. *Acta Materialia*. 2012;60(9): 4027-4040.
10. Wang G, Li G, Zhao L, Lian J, Jiang Z, Jiang Q. The origin of the ultrahigh strength and good ductility in nanotwinned copper. *Materials Science and Engineering: A.* 2010;527(16-17): 4270-4274.

11. Jin Z-H, Gumbsch P, Albe K, Ma E, Lu K, Gleiter H, Hahn H. Interactions between non-screw lattice dislocations and coherent twin boundaries in face-centered cubic metals. *Acta Materialia.* 2008;56(5): 1126-1135.
12. Malyar NV, Grabowski B, Dehm G, Kirchlechner C. Dislocation slip transmission through a coherent Σ3{111} copper twin boundary: strain rate sensitivity, activation volume and strength distribution function. *Acta Materialia.* 2018;161: 412-419.
13. Liang Y, Yang X, Gong M, Liu G, Liu Q, Wang J. Interactions between dislocations and three-dimensional annealing twins in face centered cubic metals. *Computational Materials Science.* 2019;161: 371-378.
14. Chen C, Zhang F, Xu H, Yang Z, Poletaev GM. Molecular dynamics simulations of dislocation–coherent twin boundary interaction in face-centered cubic metals. *Journal of Materials Science.* 2022;57: 1833-1849.
15. Lau TT, Forst CJ, Lin X, Gale JD, Yip S, Van Vliet KJ. Many-body potential for point defect clusters in Fe-C alloys. *Physical Review Letters.* 2007;98(21): 215501.
16. Oila A, Bull SJ. Atomistic simulation of Fe-C austenite. *Computational Materials Science.* 2009;45(2): 235-239.
17. Poletaev GM, Rakitin RY. Molecular dynamics study of stress-strain curves for γ-Fe and Hadfield steel ideal crystals at shear along the <111> direction. *Materials Physics and Mechanics.* 2021;47(2): 237-244.
18. Massardier V, Le Patezour E, Soler M, Merlin J. Mn-C interaction in Fe-C-Mn steels: study by thermoelectric power and internal friction. *Metallurgical and Materials Transactions A.* 2005;36A: 1745-1755.
19. Slane JA, Wolverton C, Gibala R. Carbon-vacancy interactions in austenitic alloys. *Materials Science and Engineering A.* 2004;370(1-2): 67-72.
20. Zhu T, Gao H. Plastic deformation mechanism in nanotwinned metals: an insight from molecular dynamics and mechanistic modeling. *Scripta Materialia.* 2012;66(11): 843-848.
21. Poletaev GM, Zorya IV, Rakitin RY, Iliina MA. Interatomic potentials for describing impurity atoms of light elements in fcc metals. *Materials Physics and Mechanics.* 2019;42(4): 380-388.
22. Poletaev GM. Self-diffusion in liquid and solid alloys of the Ti-Al system: molecular-dynamics simulation. *Journal of Experimental and Theoretical Physics.* 2021;133(4): 455-460.
23. Poletaev GM, Starostenkov MD. Dynamic collective displacements of atoms in metals and their role in the vacancy mechanism of diffusion. *Physics of the Solid State.* 2009;51(4): 727-732.
24. Friedel J. *Dislocations*. Oxford: Pergamon press; 1964.
25. Hirth JP, Lothe J. *Theory of Dislocations.* 2nd ed. NY: Wiley; 1982.
26. Goldschmidt HJ. *Interstitial Alloys*. London: Butterworths; 1967.
27. Poletaev GM, Zorya IV, Rakitin RY, Glubokova LG. The binding energy of impurity atoms C, N, O with edge dislocations and the energy of their migration along dislocation core in Ni, Ag, Al. *Materials Physics and Mechanics.* 2020;44(3): 404-410.
28. Veiga RGA, Goldenstein H, Perez M, Becquart CS. Monte Carlo and molecular dynamics simulations of screw dislocation locking by Cottrell atmospheres in low carbon Fe-C alloys. *Scripta Materialia.* 2015;108: 19-22.

THE AUTHORS

Poletaev G.M.
e-mail: gmpoletaev@mail.ru
ORCID: 0000-0002-5252-2455

Rakitin R.Y.
e-mail: movehell@gmail.com
ORCID: 0000-0002-6341-2761

Materials Physics and Mechanics. 2022;50(1): 126-140
Research article
http://dx.doi.org/10.18149/MPM.5012022_10

Submitted: May 18, 2021
Approved: August 26, 2022
Accepted: September 2, 2022

Numerical simulation of low-velocity impact test on PALF/Epoxy bio-composite laminates

Raut Pavan[1], Anerao Prashant[1], Topa Ameen[2,3], Munde Yashwant[4]✉, Avinash Shinde[4], Irulappasamy Siva[5]

[1]BRACT's Vishwakarma Institute of Information Technology, Pune 411048, Maharashtra, India

[2]Institute of Transportation Infrastructure, Universiti Teknologi PETRONAS, Perak, 32610, Malaysia

[3]Faculty of Ocean Engineering Technology and Informatics, Universiti Malaysia Terengganu, Kuala Terengganu, 21030, Malaysia

[4]MKSSS's Cummins College of Engineering for Women, Karvenagar, Pune 411052, Maharashtra, India

[5]Center for Composite Materials, Kalasalingam Academy of Research and Education, Krishnankoil 626126, Tamilnadu, India

✉ yashwant.munde@gmail.com

Abstract. Natural fiber-reinforced composites are highly demanded as it reduces the dependency on petroleum-based materials. The present work is focused on investigating the performance of PALF/Epoxy composite laminates under low-velocity impact through finite element analysis. The study presented to understand energy absorption, force-time response, force-displacement response, and damage characteristics of PALF/Epoxy composites. The composites with varying PALF fiber content (30, 40, and 50 % volume fraction) are modeled and simulated using LS-Dyna. Drop weight impact simulations of these composites are performed at different energy levels (3, 5, 10, 15, 20 J). The Impact simulations showed that the peak force of impact and displacement increases as the impact energy level increases. For 20 J of impact energy, a rise in fiber content from 30 to 40% and 40 to 50% volume fraction improved the energy absorption by 30.7 and 10.1 % respectively. PALF/Epoxy (30 % volume fraction) composites exhibited the peak force of 0.7678, 0.8666, and 0.9113 kN with a maximum displacement of 6.09, 14.74, 38.42 mm at 3, 10, and 20 J impact energy levels respectively. The impact study results designate that energy absorption of the specified composites is enhanced with increased loading of PALF content. H and Cross kind-shaped damage were witnessed for the first layer of PALF/Epoxy composites laminates.

Keywords: pineapple leaf fiber (PALF), epoxy, low-velocity impact, LS-Dyna, finite element analysis (FEA)

Acknowledgements*. No external funding was received for this study.*

Citation: Pavan R, Prashant A, Ameen T, Yashwant M, Avinash S, Irulappasamy S. Numerical simulation of low-velocity impact test on PALF/Epoxy bio-composite laminates. *Materials Physics and Mechanics*. 2022;50(1): 126-140. DOI: 10.18149/MPM.5012022_10.

1. Introduction

Natural fibres are widely used as reinforcement in composites. Manufacturers are interested in them because of attributes such as ease of processing, good specific stiffness, non-abrasiveness, biodegradability, and low cost. Synthetic fibres such as glass, carbon, and kevlar are made from petrochemicals-based synthetic materials. Those synthetic fibers are not environment-friendly and harmful to operating human beings. So the petroleum crisis and environmental sustainability make significant importance to natural fiber composite in the automotive, paper, and packaging industry. It has a very wide range of properties to become engineering application materials [1]. Low-velocity impact on the materials is of high concern as they are not visible and can be left undetected [2] With the rise in the practical applications of composite materials considering their lightweight, strength, and stiffness focus is on their properties. As natural fiber-reinforced polymer composites are susceptible to biodegradation at high humidity and temperature, variation in mechanical properties, dimensional instability, and poor impact performance is observed compared to synthetic fibers [3]. Thus Hybrid composites are also highly preferred because of the damage tolerance capability [4].

Mathivanan et al. [2] tested E-glass epoxy composite for low-velocity impact, it is studied that the perforation of the energy absorbed by the material is responsible for the damage. The force-displacement curve shows the absorbed energy with the change in impact velocity. The first threshold is when the material is damaged and the second is when the lamina fails. It has been observed that as the cross-ply fibers have better fiber interlock making them compact the impact energy absorbed is high compared to UD composites [3]. Hybridization has mostly increased energy absorption. Ahmed et al. [4] have studied the low-velocity impact behavior of hybridized fiber with jute. The load–energy-time plot study indicated pure jute composite has better absorption of impact energy compared to the hybrid and the post-impact tests showed that delamination is the major cause of the damage in hybrid. Mahesh et al. [5] numerically investigated the effect of thickness and impactor shape (Hemi, Flat and conical) on the LVI behavior of jute fiber reinforced epoxy bio-composite. The laminate impacted with a conical-shaped impactor absorbs the most energy, but with a flat-shaped impactor, it suffers more severe damage. To investigate the LVI response of Sisal/Epoxy composites, a finite element (FE) technique was used by Mahesh and Nilabh [6]. They discovered that when the impact velocity and laminate thickness rise, so does the energy absorption. Mahesh et al. [7] studied the effect of the stacking sequence of Jute(J)/Rubber(R) composites on LVI behavior at different energy levels using a conical shape impactor. Results depicted JRJ and JRJRJ provide better energy absorption and damage resistance respectively compared to other sequences. Failure pattern is also different in these flexible composites compared to stiff composites.

Militello et al. [8] conducted low-velocity impact tests on various Sisal/green epoxy composites by varying fiber volume fraction and lay-up. The result shows that angle-ply laminates exhibit superior impact performance. Sheikh Md Fadzullah et al. [9] developed pineapple leaf fiber reinforced polylactic acid bio-composites and tested them for drop weight impact test. Severe damage was observed for 3251D PLA-based bio-composites compared to 6100D PLA-based. The impact behavior of jute/methacrylate soybean oil (MSO) composites was studied using different thicknesses, fibre orientations, and weave patterns by Dhakal et al. [10]. Due to its larger areal weight and higher yarn per 10 cm compared to other specimens, the woven W2 sample exhibits the greatest impact resistance among the bio-composites investigated. Mahesh, Harausampath et al. [11] studied the effect of the content of nano-silica on the ballistic impact behavior of jute reinforced polyethylene glycol (PEG) composites. The ballistic results indicate that energy absorption of the proposed composites is enhanced with the increased loading of nano-silica particles. C.S. Hassan et al. [12] simulated the crash performance of Oil Palm Empty Fruit Bunch (OPEFB) fiber reinforced epoxy composite

bumper beam according to Federal Motor Vehicle Safety Standards (FMVSS) 581 regulation. These composites exhibit comparable specific energy absorption with 56 % reduced mass compared to aluminum. Yahaya et al. [13] perform a ballistic test on Kenaf/Kevlar epoxy composites by varying the volume fraction of Kenaf fiber from 5.40 to 14.99 %. Hybrid composites show superior performance compare to dedicated composites.

On Glass, Kenaf, and hybrid Glass/Kenaf reinforced epoxy composites, low-velocity impact tests were performed at three distinct levels of energies (3, 6, and 9 J) by Majid et al. [14]. To improve impact resistance, chopped strand mat of glass fiber should replace with woven glass fiber. Mahesh et al. [15] compared the LVI performance of are Jute-Epoxy (JE) and Jute-Rubber-Jute (JRJ) composites. For impact speeds of 2.5, 5, 7.5, and 10 m/s, JRJ composites absorb about 54, 51.2, 58.1, and 61.78 % more energy than JE laminate. So it is prominent material for structural protective claddings. Flax fiber reinforced PP composite was studied by Dutta et al. [16] and observed that at initiation the energy absorption is low compared to the propagation phase the results indicate that the amount of energy absorption is lower in the initiation phase when compared to the propagation phase. Thus the numerical model proposed is effective to study the low-velocity impact behavior of natural fiber composites. The peak load sustained by the composite indicates the change in orientation and volume fraction can help increase the load capacity.

Panciroli et al. [17] compared the impact resistance of flax/epoxy with glass/epoxy composites. Numerical simulations were performed to get more insights into the mechanism and evolution of damage during the impact. Deng et al. [18] studied the damage behavior of sandwich panels made up of honeycomb core and CFRP factsheets. The effect of the structural factors and impact energy were studied when these panels were loaded with localized low-velocity impact. Patil et al. [19] investigated the effect of impact energy on LVI and Compressive After Impact (CAI) properties of Hemp/epoxy and Jute/epoxy composite. Jute/epoxy composites exhibited higher impact energy absorption and CAI strength compared to Hemp/epoxy. Nayak et al. [20] reviewed the impact characteristics of nanofiller synthetic and natural fiber reinforced polymer nanocomposites.

Most of the research reported in the referred literature is to study the low-velocity drop weight impact performance of bio-composites using different natural fiber as Jute, Kenaf, Oil Palm, and Sisal fiber. In this article, an attempt has been made to investigate the performance of PALF/Epoxy bio-composite laminate under low-velocity impact loading. The effect of PALF fiber content and different energy levels of impact are studied through finite element analysis using LS-Dyna for its performance under LVI.

2. Materials and methods

Materials. The three configurations of PALF reinforced epoxy composites laminates of stacking sequence [0/90, ±45, 0/90, 0/90, ±45, 0/90] with six layers each of 0.5 mm are considered. Each configuration is designated as 30PE, 40PE, and 50PE based on the content of PALF fiber as 30, 40, and 50% of volume fraction respectively. The mechanical elastic and strength properties of the proposed PALF/Epoxy composite laminate are necessary for impact simulation. These properties are evaluated by micromechanical modeling principles through the material designer of ANSYS 19.2. The constituent properties for this are referred from the literature[21,22]. The evaluated mechanical properties of PALF/Epoxy are summarized in Table 1.

Modelling and Simulation. ANSYS LS-Dyna 2020 is used to simulate the low-velocity impact response of the PALF/Epoxy composite laminate of three configurations. LS-Dyna software package contains a huge library of material constitutive models. The composite enhanced damage material model (MAT054) is commonly adopted for modelling composite structures under impact loading owing to its robustness and simplicity [23-26,27].

MAT054 is an orthotropic material model with optional brittle failure for composites following either the suggestions of Chang and Chang [28] or Tsai and Wu[29]. The composite plate of size 150 × 100 mm is modeled with 8-node brick elements with a single integration point. A biased meshing scheme is adopted with a minimum element size of 0.5 mm and the total number of elements is 403,200 elements. The model plate i.e. laminate is made up of six laminae of stacking sequence [0/90, ± 45, 0/90, 0/90, ± 45, 0/90], each lamina possesses a thickness of 0.5 mm. The impact ball is modeled as a rigid hemispherical solid with a diameter of 12.7 mm. The ball is having a mass of 1.3 kg and is defined to move in a perpendicular direction with an initial velocity (2.21, 2.88, 3.87, 4.72, 5.55 m/s) as per the requirement of energy level (3, 5, 10, 15, 20 J). The meshing of PALF/Epoxy laminated composite with impactor is shown in Fig. 1. Fixed boundary conditions on edge of the laminated plate are applied and solved to get impact properties as the energy absorbed, reaction force, and deformation.

Table 1 Elastic and strength properties of PALF/Epoxy used in the impact simulation study

Elastic and Strength Properties	Unit	Configuration		
		30PE	40PE	50PE
Young's Modulus along X direction (E_1)	MPa	16115	18517	20492
Young's Modulus along Y direction (E_2)	MPa	16115	18517	20492
Young's Modulus along Z direction (E_3)	MPa	10323	11968	13473
Shear Modulus in XY (G_{12})	MPa	5663.6	6734.4	7617.6
Shear Modulus in YZ (G_{23})	MPa	2565.8	2947.4	3322.6
Shear Modulus in XZ (G_{31})	MPa	2565.8	2947.4	3322.6
Poisson's Ratio in XY (μ_{12})	-	0.2246	0.2192	0.2164
Poisson's Ratio in YZ (μ_{23})	-	0.3447	0.3202	0.3006
Poisson's Ratio in XZ (μ_{31})	-	0.3447	0.3202	0.3006
Density	g/cm^3	1.3233	1.3503	1.3710
Longitudinal Tensile Strength (X_t)	MPa	144.193	182.594	220.995
Transverse Tensile Strength (Y_t)	MPa	40.20	46.16	54.18
Longitudinal Compressive Strength (X_c)	MPa	144.193	182.594	220.995
Transverse Compressive Strength (Y_c)	MPa	40.20	46.16	54.18
In Plane Shear Strength (S)	MPa	32.16	36.93	43.34

Fig.1. Meshed model of PALF/Epoxy composite laminate with hemispherical impactor

The impactor's initial impact velocity (V_I) is defined as the speed at which the impactor begins to move toward the target from a specific height. As the impactor strikes the plate, either it rebounds or penetrates where the velocity will reduce which is called residual velocity (V_R).

Kinetic energies, the initial kinetic energy (KE_I) of the impactors striking the target, and residual kinetic energy (KE_R) of the impactor are calculated by using Eq. (1) and (2). The mass of the impactor is m.

$$KE_I = \frac{1}{2}\, m\, V_I^2 \quad (1)$$

$$KE_R = \frac{1}{2}\, m\, V_R^2 \quad (2)$$

The difference between the initial kinetic energy and the residual kinetic energy computed by equation (3) is the energy absorbed (E_a) by the laminate

$$E_a = KE_I - KE_R \quad (3)$$

3. Results and Discussion

Energy Absorption. The PALF/Epoxy bio-composites are impacted by a rigid hemispherical shape impactor with a velocity of 2.21, 2.88, 3.87, 4.72, and 5.55 m/s which results in the level of impact energy of 3, 5, 10, 15, 20 J respectively. As the impactor strike a composite plate it reduces the impact energy by decimation in form of damage. This quantification of dissipation of energy is termed energy absorption. The residual velocity and absorbed energy of 30PE, 40PE, and 50PE PALF/Epoxy composites at altered impact velocities and impact energy are presented in Table 2.

Table 2 Residual velocity and energy absorbed of PALF/Epoxy composites at a different impact energy level

Composition	Impact Velocity (m/s)	Residual Velocity (m/s)	Velocity Drop (m/s)	Impact Energy (J)	Absorbed Energy (J)	Energy Absorption Ratio (%)
30PE	2.21	1.538	0.672	3	1.38	46.01
	2.88	1.727	1.153	5	2.98	59.50
	3.87	1.134	2.736	10	7.75	77.51
	4.72	-1.261	5.981	15	10.72	71.50
	5.55	-3.355	8.905	20	9.86	49.32
40PE	2.21	1.582	0.628	3	1.33	44.32
	2.88	1.853	1.027	5	2.76	55.17
	3.87	1.134	2.736	10	6.35	63.49
	4.72	-1.261	5.981	15	12.21	81.37
	5.55	-2.418	7.968	20	12.89	64.45
50PE	2.21	1.591	0.619	3	1.30	43.41
	2.88	1.841	1.039	5	2.80	56.10
	3.87	2.211	1.659	10	5.56	55.61
	4.72	1.675	3.045	15	10.91	72.77
	5.55	-1.826	7.376	20	14.19	70.96

Figure 2 shows the variance in energy absorption of PLAF/Epoxy composites at various levels of impact energy. It is observed that for 20 J of impact energy, a rise in the content of fiber from 30 to 40 and 40 to 50 improved the energy absorption by 30.7 and 10.1 % respectively. Maximum energy absorption for 30PE, 40PE, and 50PE is observed at 15, 20, and 20 J respectively. This is because higher fiber content restricts damage to laminate at a low level of impact energy.

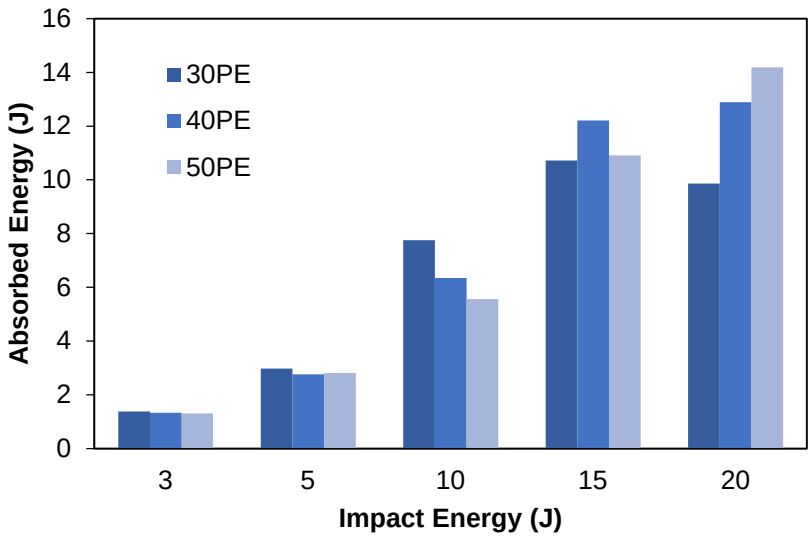

Fig. 2. Variation of absorbed energy of PALF/Epoxy composites with different impact energy

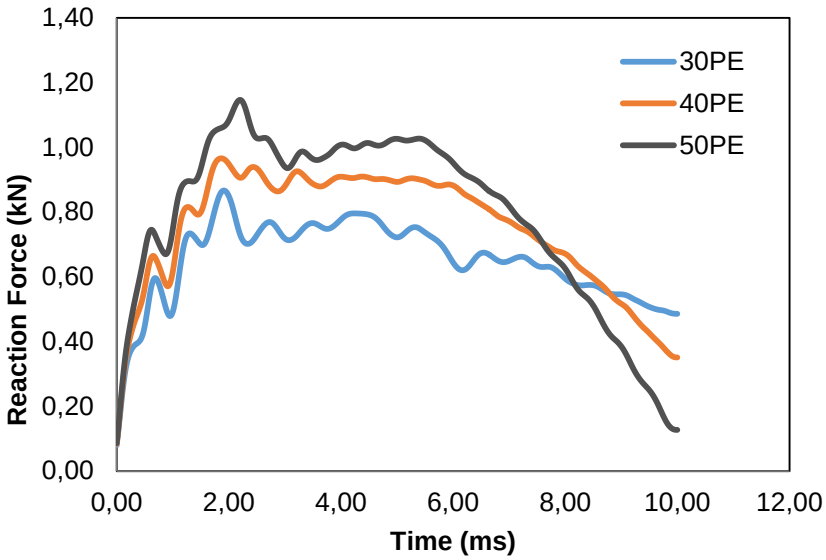

Fig. 3. Variation of the reaction force of PALF/Epoxy composites at 10 J impact energy

Force-time Response. A variation of impacted force concerning time is the force-time response of PALF/Epoxy composite. The force-time response of 30, 40 and 50PE configurations are obtained at different impact energy level (3, 5, 10, 15, 20 J) i.e. changing velocity (2.21, 2.88, 3.87, 4.72, 5.55 m/s). Figure 3 depicts the force-time response of PALF/Epoxy composites at 10J impact energy. The force increases up to peak value for a time of 2 ms and then decreases it represents the maximum resistance force (Pmax). The value of Pmax shows the ability of composite material to resist impact loading [6]. Curve before and after peak force indicates fracture initiation and fracture propagation region respectively. Forces increase initially and drop before reaching a value of Pmax is called critical force (Pcrc), this is a change in the stiffness of the composite due to damage evolution. The maximum reaction force of 0.867, 0.966, and 1.15 kN is observed for 30, 40, and 50PE composite respectively. The improvement of about 11.41 % and 19.04 % in resistance to impact is seen when the volume fraction of fiber rises from 0.3 to 0.4 and 0.4 to 0.5 respectively[7]. The deviation of peak force of PALF/Epoxy bio-composites with altered impact energy levels is depicted in Fig. 4. When impact energy is raised from 3 to 10 J and 10 to 20 J, the improvement in peak force is 12.9 and 5.2 % respectively for 30PE composites.

At all energy levels, an increase in the content of fiber raises the peak force of the reaction. For 50PE composites peak force of 1.1942 kN was observed at 15 J impact energy and then it drops to 1.1071 kN when impacted with 20 J energy. It shows the saturation of impact resistance force beyond 15J energy.

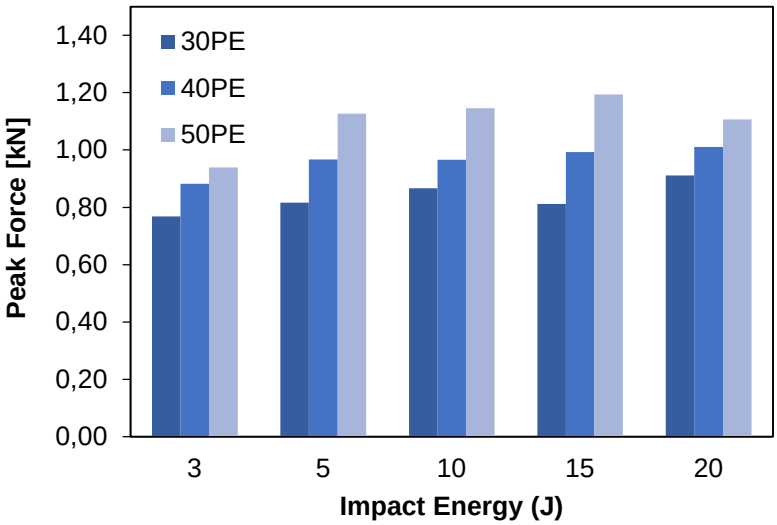

Fig. 4. Peak forces of PALF/Epoxy composites as a function of impact energy

Force-displacement Response. Figure 5 depicts the variation of reaction force against displacement of 30PE, 40PE, and 50PE composites. In all compositions of PLAF/Epoxy composites, curves attempted to form a closed loop in which it reached peak force and tried to return to the initial point. For 50PE composition shows higher area under the curve, indicating energy transformations of the impactor to plate. At low impact energy, the curve has close movement toward the initial point but at higher impact energy curve moves away from the initial point [30].

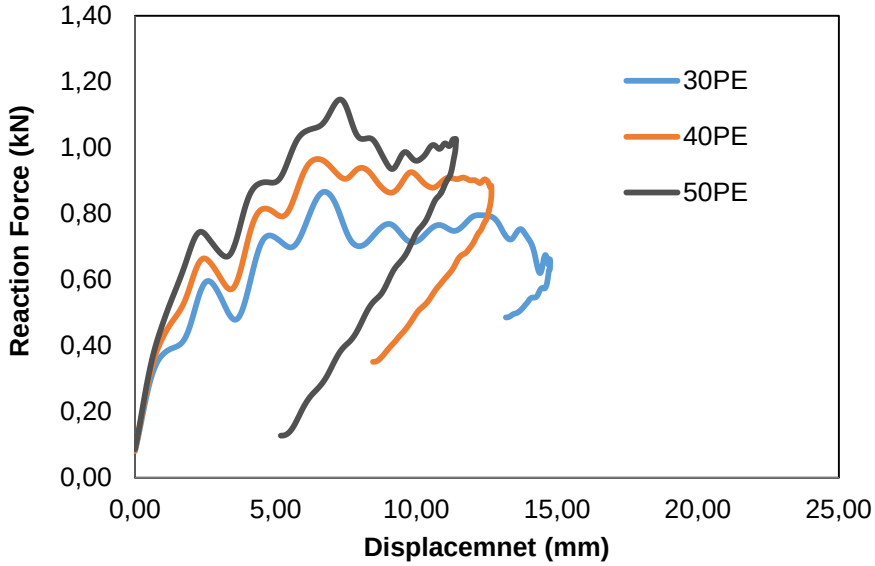

Fig. 5. Variation of reaction force against displacement of PALF/Epoxy composites at 10J impact energy

Figure 6 depicts the maximum displacement of 30PE, 40PE, and 50PE PALF/Epoxy composites with different levels of impact energy. The maximum displacement of 30PE, 40PE, and 50PE increases by 142.1, 133.1, and 130.4 %, respectively, when the impact energy is increased from 3 to 10 J. An increase in impact energy increases the maximum displacement but it is restricted by an increase in the content of fiber [14].

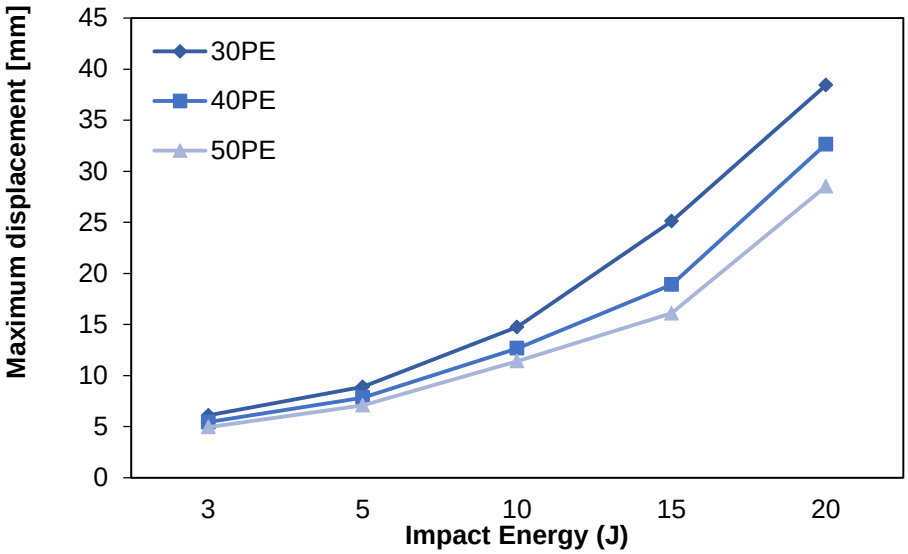

Fig. 6. Maximum displacements of PALF/Epoxy composites with impact energy

Damage Characterization. This section discusses damage caused in 30PE, 40PE, and 50PE PLAF/Epoxy composites at the impact of different impact energy levels. The damage counters were obtained under different failure modes of the first lamina of laminates viz. fibre failure under tensile and compression mode and matrix failure under tensile and compression mode. Figures 7 and 8 depict the contours of matrix damage on the first laminate under compressive and tensile mode respectively of 30PE, 40PE, and 50PE PALF/Epoxy composites at an impact energy of 3 to 20 J. The value 1 (counter colour blue) means the laminate is fully intact whereas the value 0 (counter colour red) means the laminate has failed. For 30 PE composites, an increase in impact energy level increase the damaged area of the matrix but the shape of damage for compressive and tensile mode is h-shaped and cross (+) shaped respectively. At 15 J impact energy level, the 30 PE composite is failed and the impactor penetrated through it but 40PE and 50PE sustained. The area of damage depicts that as the content of fibre increases from 30 % to 50 %, the intensity of damage is reduced in both failure modes.

Figures 9 and 10 depict the contours of fiber damage on the first laminate under compressive and tensile mode respectively of 30PE, 40PE, and 50PE PALF/Epoxy composites at the impact energy of 3 to 20 J. The shape of damage of fiber under compression and tensile mode is cross (+) but the intensity has a small deviation. This is because failure strain for PALF fibre under compression and tension mode is equal i.e.1.6 %. The 30PE PLAF/Epoxy composite sustained till 10J energy whereas 40PE and 50PE till 15J impact energy.

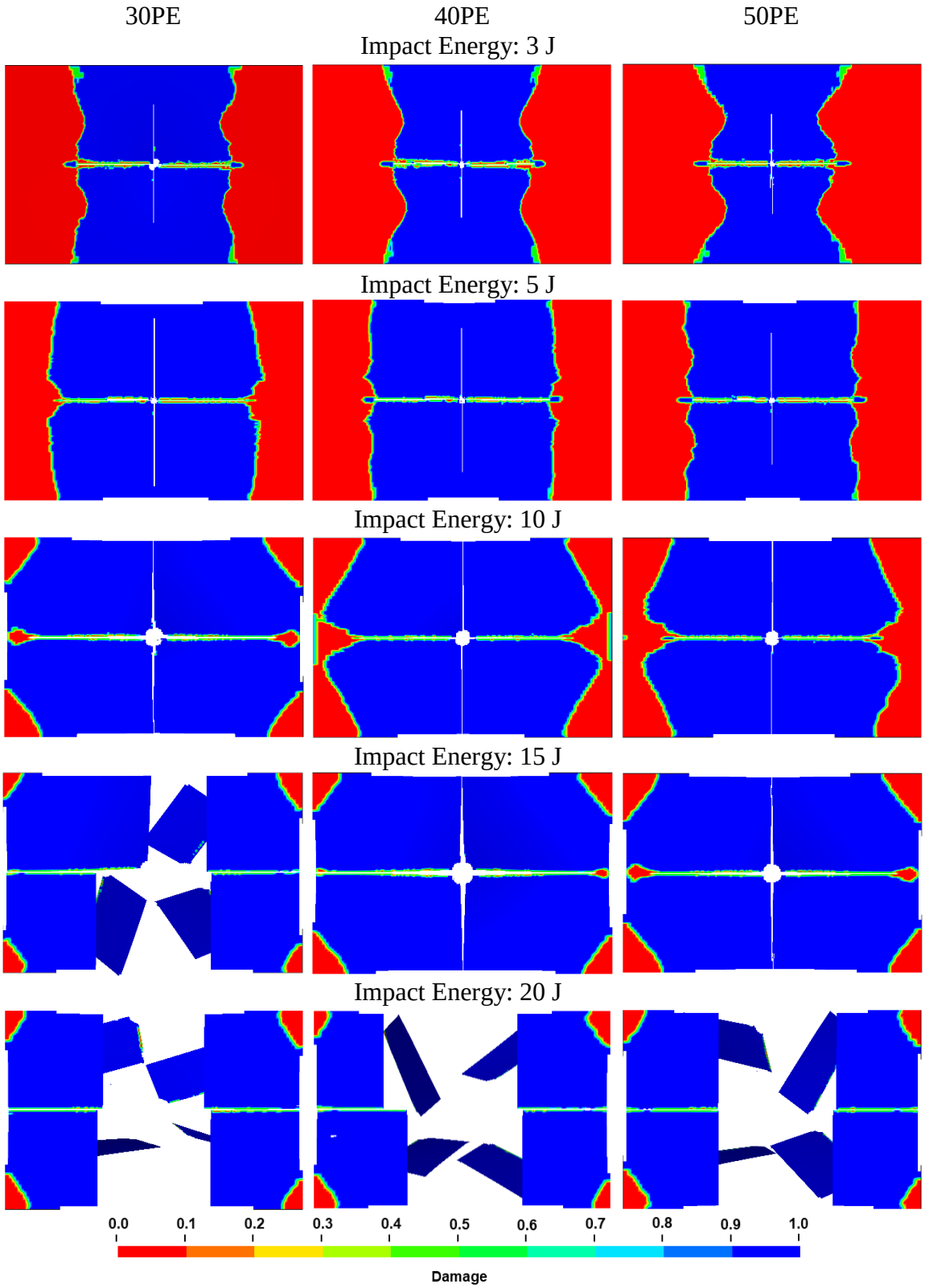

Fig. 7. Contours of matrix compressive damage on first laminate

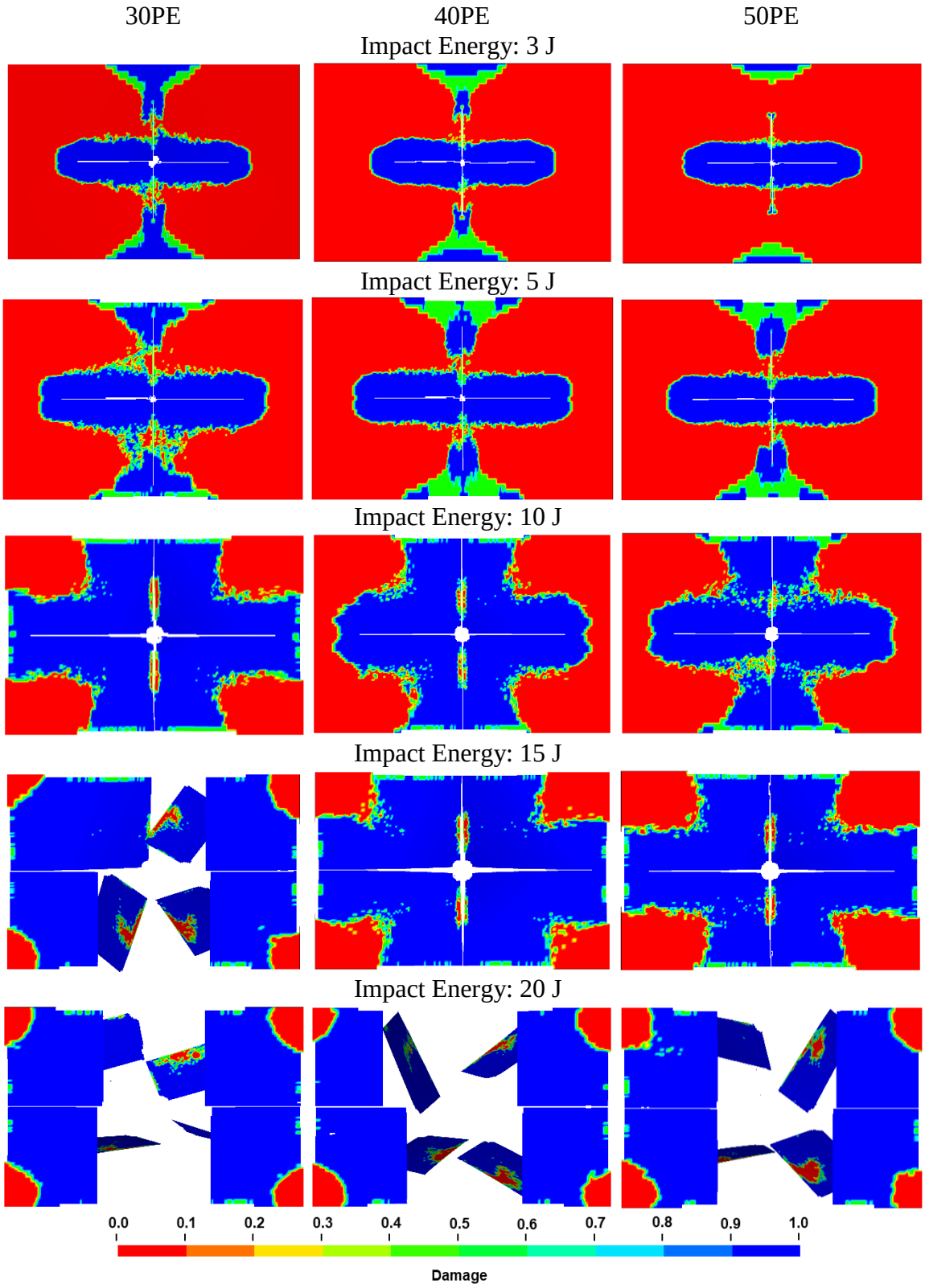

Fig. 8. Contours of matrix tensile damage on first laminate

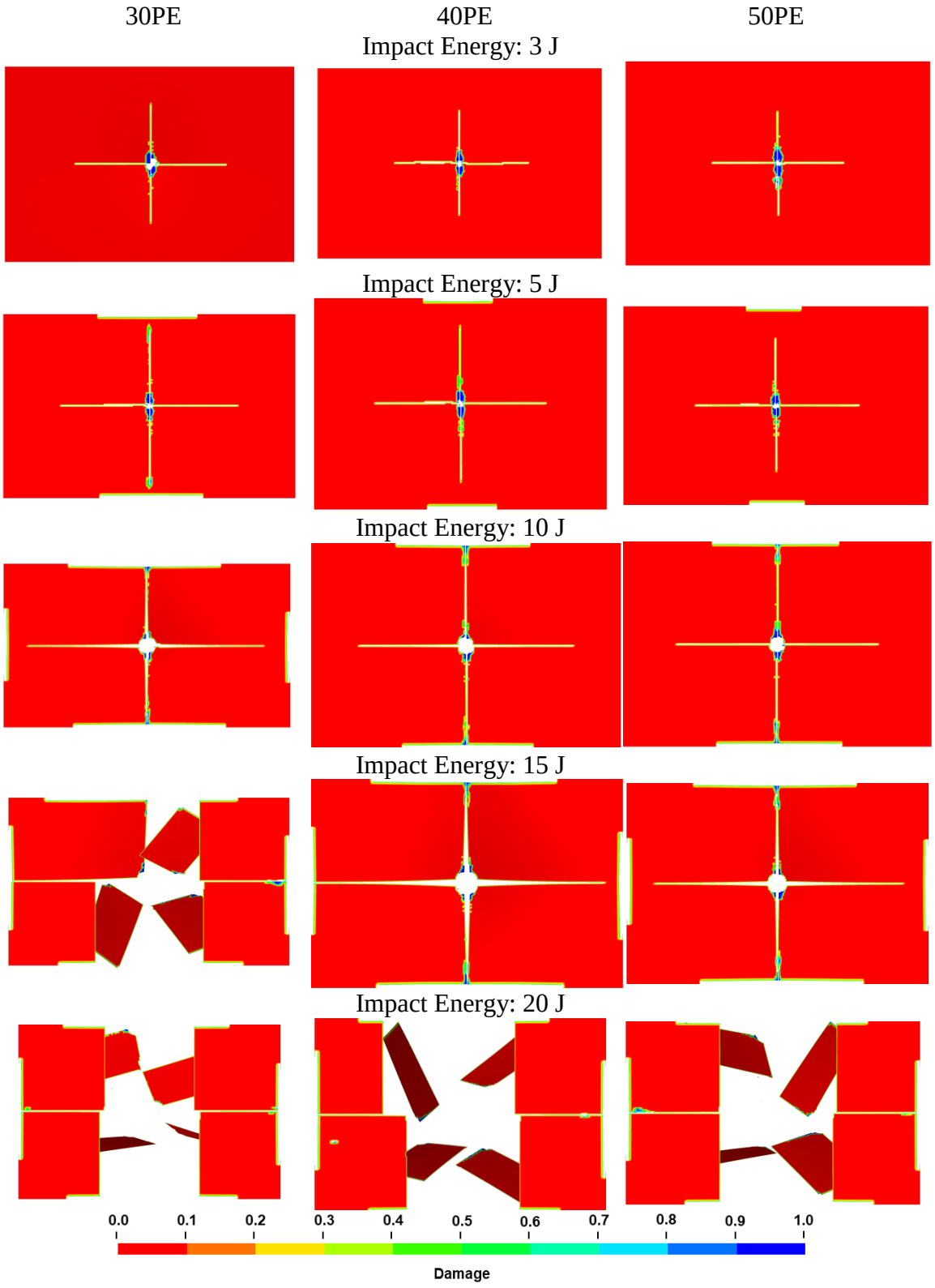

Fig. 9. Contours of fibre compressive damage on the first laminate

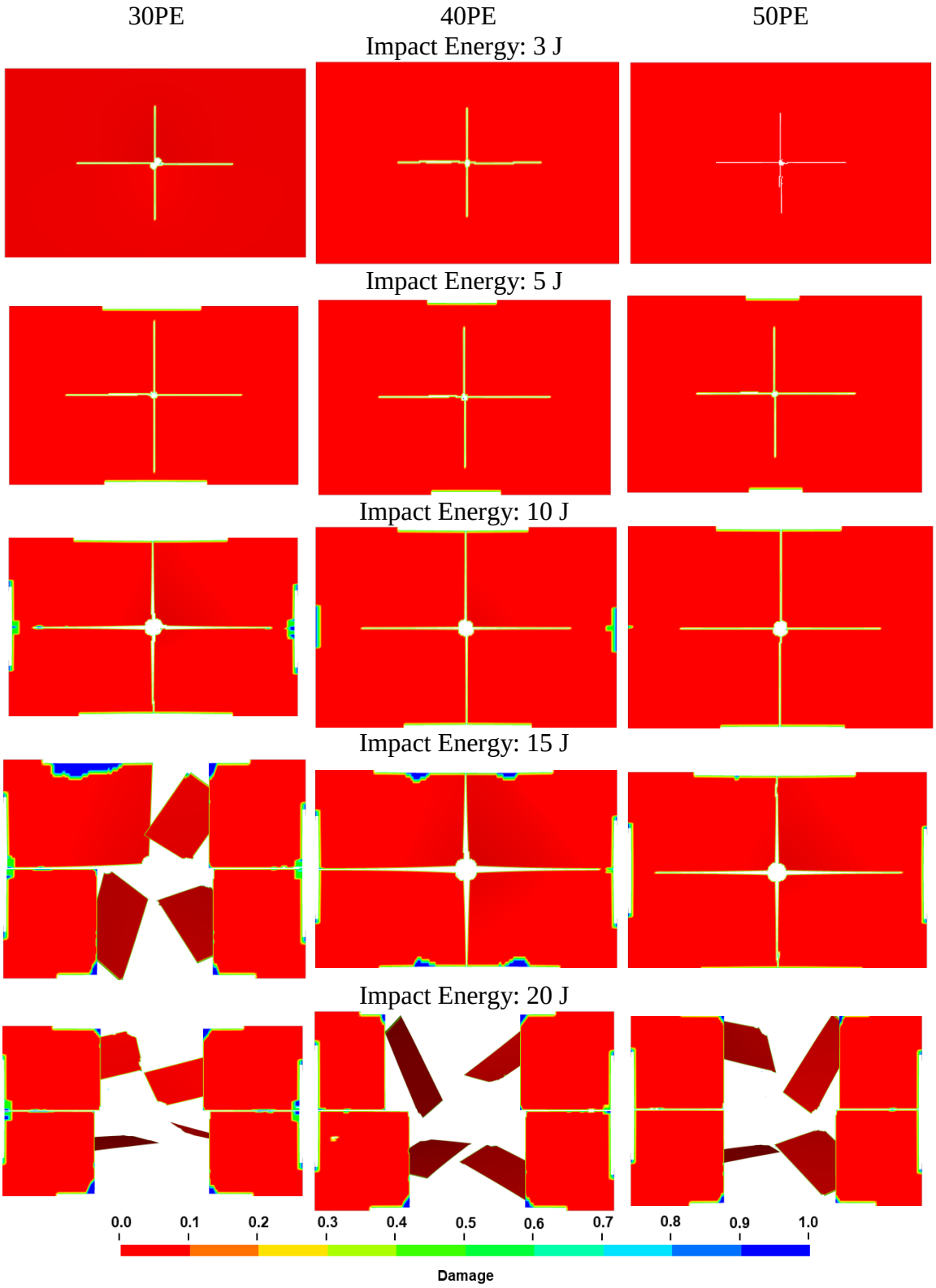

Fig. 10. Contours of fiber tensile damage on the first laminate

4. Conclusions

In the current research work, numerical simulation of PLAF/Epoxy composites under drop weight low-velocity impact has been carried out. The impact response of PLAF/Epoxy by varying impact energy levels has been simulated and the following conclusions are drawn,

- Energy absorption for 30PE, 40PE, and 50PE PLAF/Epoxy composites improved with an increase in impact energy up to 10J, 15J, and 15J respectively. After this impactor penetration was seen.
- Amongst all compositions, 50PE composites show the maximum energy absorption of 14.19 J when it is impacted with a 20 J energy level.
- For 30 PE composites, an increase in impact energy from 3 to 10 J and 10 to 20 J raises the maximum peak force by 12.9 and 5.2 % respectively.
- The peak of reaction force rises with an increase in the level of impact energy. For 50PE bio-composites maximum peak force of 1.1942 kN was observed at 15J impact energy.
- At 3 J impact energy; the maximum displacement of 30PE, 40PE and 50PE composites was 6.09, 5.43, and 4.94 mm. The increase in impact energy raises the maximum displacement of composites but it is restricted by a rise in fiber content.
- Damage characteristics of a matrix under tensile and compression mode are different i.e. cross (+) and h shaped but it is identical (cross-shaped) for fiber.

References

1. Faruk O, Bledzki AK, Fink HP, Sain M. Biocomposites reinforced with natural fibers: 2000-2010. *Prog. Polym. Sci.* 2012;37(11): 1552-1596.
2. Mathivanan NR, Jerald J. Experimental Investigation of Woven E-Glass Epoxy Composite Laminates Subjected to Low-Velocity Impact at Different Energy Levels. *J. Miner. Mater. Charact. Eng.* 2010;9(7): 643-652.
3. Al-Hajaj Z, Sy BL, Bougherara H, Zdero R. Impact properties of a new hybrid composite material made from woven carbon fibres plus flax fibres in an epoxy matrix. *Compos. Struct.* 2019;208: 346-356.
4. Ahmed KS, Vijayarangan S, Kumar A. Low velocity impact damage characterization of woven jute-glass fabric reinforced isothalic polyester hybrid composites. *J. Reinf. Plast. Compos.* 2007;26(10): 959-76.
5. Mahesh V, Joladarashi S, Kulkarni SM. Influence of laminate thickness and impactor shape on low velocity impact response of jute-epoxy composite: FE study. *Mater. Today Proc.* 2019;28: 545-550.
6. Mahesh V, Nilabh A, Joladarashi S, Kulkarni SM. Analysis of impact behaviour of sisal-epoxy composites under low velocity regime. *Rev. Des. Compos. Des. Mater. Av.* 2021;31(1): 57-63.
7. Mahesh V, Joladarashi S, Kulkarni SM. An experimental investigation on low-velocity impact response of novel jute/rubber flexible bio-composite. *Compos. Struct.* 2019;225: 111190.
8. Militello C, Bongiorno F, Epasto G, Zuccarello B. Low-velocity impact behaviour of green epoxy biocomposite laminates reinforced by sisal fibers. *Compos. Struct.* 2020;253: 112744.
9. Sheikh Md Fadzullah SH, Ramli SNN, Mustafa Z, Razali AS, Sivakumar D, Ismail I. Low velocity impact behaviour of pineapple leaf fibre reinforced polylactic acid biocomposites. *J. Adv. Manuf. Technol.* 2020;14(1): 1-12.
10. Dhakal HN, Skrifvars M, Adekunle K, Zhang ZY. Falling weight impact response of jute/methacrylated soybean oil bio-composites under low velocity impact loading. *Compos. Sci. Technol.* 2014;92: 134-141.
11. Mahesh V, Harausampath D, Mahesh V. An experimental study on ballistic impact response of jute reinforced polyethylene glycol and nano silica based shear thickening fluid composite. *Def Technol.* 2022;18(3): 401-409.

12. Hassan CS, Pei Q, Sapuan SM, Abdul Aziz N, Mohamed Yusoff MZ. Crash Performance of Oil Palm Empty Fruit Bunch (OPEFB) Fibre Reinforced Epoxy Composite Bumper Beam using Finite Element Analysis. *Int. J. Automot. Mech. Eng.* 2018;15: 5826-5836.
13. Yahaya R, Sapuan SM, Jawaid M, Leman Z, Zainudin ES. Measurement of ballistic impact properties of woven kenaf-aramid hybrid composites. *Meas. J. Int. Meas. Confed*. 2016;77: 335-343.
14. Majid DL, Mohd Jamal Q, Manan NH. Low-velocity Impact Performance of Glass Fiber, Kenaf Fiber, and Hybrid Glass/Kenaf Fiber Reinforced Epoxy Composite Laminates. *BioResources*. 2018;13(4): 8839-8852.
15. Mahesh V, Joladarashi S, Kulkarni SM. Comparative study on energy absorbing behavior of stiff and flexible composites under low velocity impact. *AIP Conf. Proc*. 2019;2057(1): 020025.
16. Dutta S, Chanda A, Rahman MZ, Das R, Bhattacharyya D. A numerical model to simulate the impact response of Flax-PP composites. In: *ICCM Int Conf Compos Mater.* 2019.
17. Panciroli R, Giannini O. Comparing the impact resistance of flax/epoxy and glass/epoxy composites through experiments and numerical simulations. *Compos. Struct*. 2021;264: 113750.
18. Deng J, Gong X, Xue P, Yin Q, Wang X. A comprehensive analysis of damage behaviors of composite sandwich structures under localized impact [preprint]. To be published in *Mech. Adv. Mater. Struct.* 2022. Available from: https://doi.org/10.1080/15376494.2022.2070937.
19. Patil S, Reddy DM, Naveen J, Swamy SS, Vignesh P, Venkatachalam G. Low-Velocity Impact and Compression after Impact Properties of Hemp and Jute Fiber Reinforced Epoxy Composites [preprint]. To be published in *J. Nat. Fibers*. 2022. Available from: https://doi.org/10.1080/15440478.2022.2057383.
20. Nayak S, Nayak RK, Panigrahi I. Effect of nano-fillers on low-velocity impact properties of synthetic and natural fibre reinforced polymer composites- a review [preprint]. To be published in *Adv. Mater. Process. Technol.* 2021. Available from: https://doi.org/10.1080/2374068X.2021.1945293.
21. Aji IS, Zainudin ES, Khairul MD, Abdan K, Sapuan SM. Electron beam cross-linking of hybridized kenaf/pineapple leaf fiber-reinforced high-density polyethylene composite with and without cross-linking agents. *J. Reinf. Plast. Compos*. 2011;30(21): 1827-1838.
22. Glória GO, Altoé GR, Moraes YM, Loyola RL, Margem FM, Monteiro SN. Tensile properties of epoxy composites reinforced with continuous palf fibers. *Charact Miner. Met. Mater*. 2015;2016: 139-144.
23. Her SC, Liang YC. The finite element analysis of composite laminates and shell structures subjected to low velocity impact. *Compos Struc.t* 2004;66(1-4): 277-285.
24. Kelkar AD, Chandekar GS, Thatte BS. On the behavior of fiberglass epoxy composites under low velocity impact loading. *Adv. Mech. Eng.* 2010;2. Available from: https://doi.org/10.1155/2010/621406.
25. Gungor E, Topa A. Numerical Investigation of Innovative Honeycomb-composite Sandwich Structure under Bird-strike Event. In: *Proc. 6th ICAME*. 2021. p.818-831.
26. Ansari MNM, Vinoth KS, Nordin A, Bassam A, Topa A. Tensile properties of hybrid kenaf/glass fiber reinforced epoxy composites with different stacking sequence using experimental and FEA simulation method. *IOP Conf. Ser. Mater. Sci Eng*. 2021;1128: 012023.
27. Bokhoeva LA, Baldanov AB, Rogov VE, Chermoshentseva AS, Topa Ameen. The Effect of The Addition of Nano powders on The Strength of Multilayer Composite Materials. *Ind. Lab. Diagnostics Mater.* 2021;87: 42-50.
28. Chang FK, Chang KY. A Progressive Damage Model for Laminated Composites Containing Stress Concentrations. *J. Compos. Mater*. 1987;21(9): 834-855.

29. Tsai SW, Wu EM. A General Theory of Strength for Anisotropic Materials. *J. Compos. Mater.* 1971;5(1): 58-80.
30. Najeeb MI, Sultan MTH, Shah AUM, Amir SMM, Safri SNA, Jawaid M, Shari MR. Low-velocity impact analysis of pineapple leaf fiber (Palf) hybrid composites. *Polymers.* 2021;13(18): 1-18.

THE AUTHORS

Raut Pavan
e-mail: raut.pavan@gmail.com
ORCID: 0000-0002-0842-0232

Anerao Prashant
e-mail: prashant.anerao@viit.ac.in
ORCID: 0000-0003-0353-7420

Topa Ameen
e-mail: ameen.topa@hotmail.com
ORCID: 0000-0001-5579-1514

Munde Yashwant
e-mail: yashwant.munde@gmail.com
ORCID: 0000-0002-1044-6415

Avinash Shinde
e-mail: avinash.shinde@cumminscollege.in
ORCID: 0000-0002-5048-837X

Siva Irulappasamy
e-mail: isiva@klu.ac.in
ORCID: 0000-0001-7505-127

Materials Physics and Mechanics. 2022;50(1): 141-157
Research article
http://dx.doi.org/10.18149/MPM.5012022_11

Submitted: December 6, 2021
Approved: June 21, 2022
Accepted: June 24, 2022

Modeling of unsteady elastic diffusion transverse vibrations of the isotropic simply supported Timoshenko plate

V.A. Vestyak[1], A.V. Zemskov[1]✉, D.V. Tarlakovskii[2]

[1]Moscow Aviation Institute (National Research University), 4 Volokolamskoe shosse, Moscow, Russia

[2]Lomonosov Moscow State University, GSP-1, Leninskie Gory, Moscow, 119991, Russia

✉ azemskov1975@mail.ru

Abstract. The unsteady problem of a homogeneous isotropic Timoshenko plate bending taken into account diffusion is considered. The initial mathematical formulation includes a system of equations of rectangular isotropic plate unsteady vibrations, obtained from a general model of elastic diffusion for continuum using the d'Alembert variational principle. An initial-boundary value problem is formulated, and Green's functions are found in the problem of a simply supported Timoshenko plate bending. In the example of a three-component rectangular plate under the action of a pair of bending moments, the interaction effects of mechanical and diffusion fields and the influence of relaxation processes on the kinetics of mass transfer are modelled. The calculation results are presented in analytical and graphical forms

Keywords: Timoshenko plate, elastic diffusion, unsteady problems, coupled problem, multicomponent continuum, Green's functions

Acknowledgements*. The reported study was funded by RFBR (Project No 20-08-00589).*

Citation: Vestyak VA, Zemskov AV, Tarlakovskii DV. Modeling of unsteady elastic diffusion transverse vibrations of the isotropic Timoshenko plate. *Materials Physics and Mechanics*. 2022;50(1): 141-157. DOI: 10.18149/MPM.5012022_11.

1. Introduction

The paper considers an unsteady problem of elastic diffusion vibrations of a plate, based on the Timoshenko plate model. This model is a refinement of the classical Kirchhoff-Love plate model by taking into account shear deformations and the influence of inertial forces when the normal is rotated relative to the middle surface.

The classical Kirchhoff-Love plate model often provides sufficient accuracy in solving many engineering problems. However, taking shear deformations into account can be essential for rods and plates made of an anisotropic material with a shear modulus much lower than Young's modulus. Some fibrous and composite materials, in particular human bones, have such properties. It is also important to consider shear deformations in the problems of three-layer rods and plate stability, where two bearing layers are made of thin, high-strength rigid material, and between them is a light and less durable filler. On the other hand, when the stiffness characteristics of the filler layer are significantly lower than the stiffness characteristics of the bearing layers, a simplified calculation using the classical Kirchhoff-Love model can lead to significant errors in determining the critical loads. This, in

turn, leads to a decrease in the economic efficiency of structures of technical systems or underestimates the potential resources of biological systems.

An equally important problem in the design of structures, under the action of multifactorial unsteady external influences, is the question of different physical field's interaction in a continuum. As early as the beginning of the 20th century, it was experimentally proved that, due to beams and plate bending, a deformation gradient initiates the process of ascending diffusion [1-3]. This leads to the formation of a concentration gradient and, consequently, to the redistribution of the solute atoms. As a result, the matter from areas of compression in the area of tension is transferred. This phenomenon is called the Gorsky effect. The result of scientific research was published in 1936 [1]. In the same way, the mechanical field, the temperature, and electromagnetic fields are interconnected.

A review of publications in this sphere shows that the problem of analyzing the interaction of mechanical and diffusion fields in thin-walled structural elements is also relevant today. Among the few publications on this topic are articles [4, 5]. They investigate the influence of diffusion processes on the bearing capacity of a smooth transversely isotropic shell. The contact interaction of a rod with an elastic half-space is considered in the works [6,7]. Publications [8-10] are devoted to the study of elastic diffusion processes in plates. The calculation of spherical shells taking into account diffusion is considered in [11].

It should be noted that all these problems are solved in a stationary formulation. The problems formulations of unsteady elastic diffusion beams and plate vibrations and methods for their solution are absent in the publications known to date. In the presented study, the mutual influence of mechanical and diffusion fields on each other in a Timoshenko plate under the action of external unsteady perturbations is investigated.

2. Problem formulation

The unsteady vibrations problem of a rectangular isotropic multicomponent Tymoshenko plate under the action of mechanical and diffusion perturbations are considered. A diagram of the applied forces and bending moments and the axes orientation of a rectangular Cartesian coordinate system is in Fig. 1.

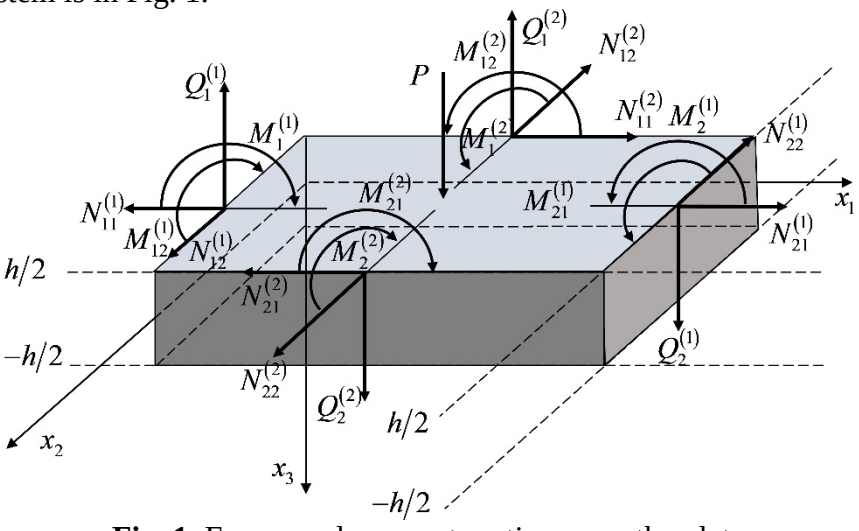

Fig. 1. Forces and moments acting upon the plate

For the problem formulation, we use the coupled elastic diffusion continuum model in a rectangular Cartesian coordinate system, which has the following form [12 - 15]:

$$\ddot{u}_i = \frac{\partial \sigma_{ij}}{\partial x_j} + F_i, \quad \dot{\eta}^{(q)} = -\frac{\partial J_i^{(q)}}{\partial x_i} + Y^{(q)}, \quad \eta^{(N+1)} = -\sum_{j=1}^{N} \eta^{(j)} \quad \left(q = \overline{1, N}\right), \tag{1}$$

where σ_{ij} and $J_i^{(q)}$ are components of the stress tensor and the diffusion flux vector, which are defined as follows

$$\sigma_{ij} = C_{ijkl}\frac{\partial u_k}{\partial x_l} - \sum_{r=1}^{N}\alpha_{ij}^{(r)}\eta^{(r)}, \quad J_i^{(q)} + \tau_q \dot{J}_i^{(q)} = -\sum_{t=1}^{N} D_{ij}^{(qt)}\frac{\partial \eta^{(t)}}{\partial x_j} + \Lambda_{ijkl}^{(q)}\frac{\partial^2 u_k}{\partial x_j \partial x_l} \quad \left(q = \overline{1,N}\right). \tag{2}$$

Here the dots denote the time derivative. All quantities in (1), (2) are dimensionless. We accepted the following notation

$$x_i = \frac{x^*_i}{l}, u_i = \frac{u^*_i}{l}, \tau = \frac{ct}{l}, C_{ijkl} = \frac{C^*_{ijkl}}{C^*_{1111}}, C^2 = \frac{C^*_{1111}}{\rho}, \alpha_{ij}^{(q)} = \frac{\alpha_{ij}^{*(q)}}{C^*_{1111}}, l_m = \frac{l^*_m}{l}, D_{ij}^{(qt)} = D_{ij}^{(t)} g^{(qt)},$$
$$D_{ij}^{(q)} = \frac{D_{ij}^{*(q)}}{Cl}, \Lambda_{ijkl}^{(q)} = \frac{m^{(q)} D_{ij}^{*(q)} \alpha_{kl}^{*(q)} n_0^{(q)}}{\rho R T_0 C l}, F_i = \frac{F_i^*}{C^*_{1111}}, Y^{(q)} = \frac{l Y^{*(q)}}{C}, h = \frac{h^*}{l}, \tau_q = \frac{c\tau^{(q)}}{l}, \tag{3}$$

where t is time; x_i^* are rectangular Cartesian coordinates; u_i^* are displacement vector components; l are characteristic linear dimensions in the problem; l_1^*, l_2^* is the plate length and width; h^* is the plate thickness; $\eta^{(q)} = n^{(q)} - n_0^{(q)}$ is the concentration increment of q-th component in the multicomponent continuum; $n^{(q)}$ and $n_0^{(q)}$ is the current and initial concentrations (mass fractions) of q-th component; C^*_{ijkl} are components of the elastic constant tensor; ρ is the medium density; $\alpha_{ij}^{*(q)}$ are coefficients characterizing the medium volumetric changes due to diffusion; $D_{ij}^{*(q)}$ are the self-diffusion coefficients; R is the universal gas constant; T_0 is initial temperature; $m^{(q)}$ is the molar mass q-th component; $\tau^{(q)}$ is relaxation time of diffusion perturbations; $g^{(qt)}$ is the Darken's thermodynamic coefficients.

The initial conditions are assumed to be zero (the continuum is unperturbed):

- the mechanical part

$$u_i\big|_{\tau=0} = 0, \quad \dot{u}_i\big|_{\tau=0} = 0, \tag{4}$$

- the diffusion part

$$\eta^{(q)}\Big|_{\tau=0} = 0, \quad \dot{\eta}^{(q)}\Big|_{\tau=0} = 0 \quad q = \overline{1,N}. \tag{5}$$

Boundary conditions (the domain G is bounded; n_i are components of the outer normal unit vector to the surface ∂G):

- the mechanical part ($\partial G = \Pi_u \bigcup \Pi_\sigma$; $\Pi_u \cap \Pi_\sigma = \varnothing$)

$$u_i\big|_{\Pi_u} = U_i, \quad \sigma_{ij} n_j\big|_{\Pi_\sigma} = P_i \quad (\tau > 0), \tag{6}$$

- the diffusion part ($\partial G = \Pi_\eta \bigcup \Pi_J$; $\Pi_\eta \cap \Pi_J = \varnothing$)

$$\eta^{(q)}\Big|_{\Pi_\eta} = N^{(q)}, \quad \left(J_i^{(q)} + \tau_q \dot{J}_i^{(q)}\right)\Big|_{\Pi_J} = I_i^{(q)} \left(\tau > 0,\ q = \overline{1,N}\right). \tag{7}$$

The quantities on the boundary conditions right sides are surface kinematic U_i, $N^{(q)}$ and dynamic P_i, $I_i^{(q)}$ perturbations.

3. Model of elastic diffusion vibrations of a Timoshenko plate

To construct the equations for the bending of the plate, relations (1) - (7) using the d'Alembert variational principle are written in the form of the following variational equality:

$$\int\limits_G \left(\ddot{u}_i - \frac{\partial \sigma_{ij}}{\partial x_j} - F_i \right) \delta u_i dG + \sum_{q=1}^{N} \int\limits_G \left(1 + \tau_q \frac{\partial}{\partial \tau} \right) \left(\dot{\eta}^{(q)} + \frac{\partial J_i^{(q)}}{\partial x_i} - Y^{(q)} \right) \delta \eta^{(q)} dG +$$
$$+ \iint\limits_{\Pi_\sigma} \left(\sigma_{ij} n_j - P_i \right) \delta u_i dS + \sum_{q=1}^{N} \iint\limits_{\Pi_J} \left(\dot{J}_i^{(q)} + \tau_q \ddot{J}_i^{(q)} - I_i^{(q)} \right) n_i \delta \eta^{(q)} dS = 0, \tag{8}$$

where δu_i are virtual displacement, $\delta \eta^{(q)}$ are virtual concentrations increments.

Further, we assume that:

1) The domain G has the form $G = D \times [-h/2, h/2]$, where $D = [0, l_1] \times [0, l_2]$ is the rectangular region of the plate's middle surface $x_3 = 0$, $\Gamma = \partial D$ is the middle surface boundary (fig.1)

2) The plate surface has the form $\Pi = \Pi_- \cup \Pi_+ \cup \Pi_b$, where Π_- is bottom surface corresponds $x_3 = -h/2$, Π_+ is top surface corresponds $x_3 = h/2$, $\Pi_b = \Pi_{11} \cup \Pi_{21} \cup \Pi_{12} \cup \Pi_{22}$ are side surface. The surface Π_{1k} corresponding $x_k = 0$, the surface Π_{2k} corresponding $x_k = l_k$, $k = 1,2$. We assume that the plate side surface is free from mechanical loads and mass transfer

$$\sigma_{ij} n_j \Big|_{\Pi_-} = \sigma_{ij} n_j \Big|_{\Pi_+} = 0. \tag{9}$$
$$\left(J_i^{(q)} + \tau_q \dot{J}_i^{(q)} \right) \Big|_{\Pi_-} = \left(J_i^{(q)} + \tau_q \dot{J}_i^{(q)} \right) \Big|_{\Pi_+} = 0.$$

3) Plate material is an isotropic perfect solid solution

$$C_{ijkl} = \lambda \delta_{ij} \delta_{kl} + \mu \left(\delta_{ik} \delta_{jl} + \delta_{il} \delta_{jk} \right), \quad \Lambda_{ijkl}^{(q)} = \delta_{ij} \delta_{kl} \Lambda_q, \quad \alpha_{ij}^{(q)} = \delta_{ij} \alpha_q, \quad D_{ij}^{(qr)} = \delta_{ij} D_{qr}. \tag{10}$$

Here λ and μ are dimensionless elastic Lamé constants, δ_{ij} is the Kronecker symbol.

4) Transverse plate deflections are considered small. We also consider that a straight fibre normal to the middle surface after deformation remains straight to the middle surface (the Timoshenko plate theory). Then the linearization of the unknown quantities concerning the variable x_3 will have the form (the approximate equality is replaced by the exact)

$$\begin{aligned} u_1(x_1, x_2, x_3, \tau) &= u(x_1, x_2, \tau) - x_3 \chi_1(x_1, x_2, \tau), \\ u_2(x_1, x_2, x_3, \tau) &= v(x_1, x_2, \tau) - x_3 \chi_2(x_1, x_2, \tau), \\ u_3(x_1, x_2, x_3, \tau) &= w(x_1, x_2, \tau) + x_3 \psi(x_1, x_2, \tau), \\ \eta^{(q)}(x_1, x_2, x_3, \tau) &= N_q(x_1, x_2, \tau) + x_3 H_q(x_1, x_2, \tau). \end{aligned} \tag{11}$$

5) Taking into account (9), we assume that there are no deformations along the axis Ox_3. Then [16-20]:

$$\varepsilon_{33} = \frac{\partial u_3}{\partial x_3} = \psi = 0 \Rightarrow \psi = 0.$$

Hence:

$$\begin{aligned} u_1(x_1, x_2, x_3, \tau) &= u(x_1, x_2, \tau) - x_3 \chi_1(x_1, x_2, \tau), \\ u_2(x_1, x_2, x_3, \tau) &= v(x_1, x_2, \tau) - x_3 \chi_2(x_1, x_2, \tau), \quad u_3(x_1, x_2, x_3, \tau) = w(x_1, x_2, \tau), \\ \eta^{(q)}(x_1, x_2, x_3, \tau) &= N_q(x_1, x_2, \tau) + x_3 H_q(x_1, x_2, \tau). \end{aligned} \tag{12}$$

In this case, in accordance with (2), (10), and (11), the components of the stress tensor and the diffusion flux vector will be written as

$$\sigma_{11} = \frac{\partial u}{\partial x_1} - x_3 \frac{\partial \chi_1}{\partial x_1} + \lambda \left(\frac{\partial v}{\partial x_2} - x_3 \frac{\partial \chi_2}{\partial x_2} \right) - \sum_{j=1}^{N} \alpha_j \left(N_j + x_3 H_j \right),$$

$$\sigma_{22}=\lambda\left(\frac{\partial u}{\partial x_1}-x_3\frac{\partial \chi_1}{\partial x_1}\right)+\frac{\partial v}{\partial x_2}-x_3\frac{\partial \chi_2}{\partial x_2}-\sum_{j=1}^{N}\alpha_j\left(N_j+x_3H_j\right),$$
$$\sigma_{33}=\lambda\left(\frac{\partial u}{\partial x_1}-x_3\frac{\partial \chi_1}{\partial x_1}\right)+\lambda\left(\frac{\partial v}{\partial x_2}-x_3\frac{\partial \chi_2}{\partial x_2}\right)-\sum_{j=1}^{N}\alpha_j H_j,$$
$$\sigma_{12}=\mu\left(\frac{\partial u}{\partial x_2}+\frac{\partial v}{\partial x_1}-x_3\frac{\partial \chi_1}{\partial x_2}-x_3\frac{\partial \chi_2}{\partial x_1}\right),\quad \sigma_{13}=\mu\left(-\chi_1+\frac{\partial w}{\partial x_1}\right),\quad \sigma_{23}=\mu\left(-\chi_2+\frac{\partial w}{\partial x_2}\right), \tag{13}$$
$$J_1^{(q)}+\tau_q\dot{J}_1^{(q)}=-\sum_{r=1}^{N}D_q g^{(qr)}\left(\frac{\partial N_r}{\partial x_1}+x_3\frac{\partial H_r}{\partial x_1}\right)+\Lambda_q\left(\frac{\partial^2 u}{\partial x_1^2}-x_3\frac{\partial^2 \chi_1}{\partial x_1^2}+\frac{\partial^2 v}{\partial x_1\partial x_2}-x_3\frac{\partial^2 \chi_2}{\partial x_1\partial x_2}\right),$$
$$J_2^{(q)}+\tau_q\dot{J}_2^{(q)}=-\sum_{r=1}^{N}D_q g^{(qr)}\left(\frac{\partial N_r}{\partial x_2}+x_3\frac{\partial H_r}{\partial x_2}\right)+\Lambda_q\left(\frac{\partial^2 u}{\partial x_1\partial x_2}-x_3\frac{\partial^2 \chi_1}{\partial x_1\partial x_2}+\frac{\partial^2 v}{\partial x_2^2}-x_3\frac{\partial^2 \chi_2}{\partial x_2^2}\right),$$
$$J_3^{(q)}+\tau_q\dot{J}_3^{(q)}=-\sum_{r=1}^{N}D_q g^{(qr)}H_r-\Lambda_q\left(\frac{\partial \chi_1}{\partial x_1}+\frac{\partial \chi_2}{\partial x_2}\right)\ \ \left(q=\overline{1,N}\right).$$

Substituting equalities (12) and (13) in (8), we obtain models of longitudinal and transverse vibrations of the plate [20]. The equations of longitudinal vibrations are similar in form to the two-dimensional equations of elastic diffusion for continuum and are not presented here.

The transverse vibration equations have the form

$$\ddot{\chi}_1=\frac{\partial^2 \chi_1}{\partial x_1^2}+\mu\frac{\partial^2 \chi_1}{\partial x_2^2}+\mu k_T^2\left(\frac{\partial w}{\partial x_1}-\chi_1\right)+(\lambda+\mu)\frac{\partial^2 \chi_2}{\partial x_1\partial x_2}+\sum_{j=1}^{N}\alpha_j\frac{\partial H_j}{\partial x_1}-\frac{12}{h^3}m_1,$$
$$\ddot{\chi}_2=\mu\frac{\partial^2 \chi_2}{\partial x_1^2}+\frac{\partial^2 \chi_2}{\partial x_2^2}+\mu k_T^2\left(\frac{\partial w}{\partial x_2}-\chi_2\right)+(\lambda+\mu)\frac{\partial^2 \chi_1}{\partial x_1\partial x_2}+\sum_{j=1}^{N}\alpha_j\frac{\partial H_j}{\partial x_2}-\frac{12}{h^3}m_2, \tag{14}$$
$$\ddot{w}=\mu k_T^2\left(\frac{\partial^2 w}{\partial x_1^2}-\frac{\partial \chi_1}{\partial x_1}\right)+\mu k_T^2\left(\frac{\partial^2 w}{\partial x_2^2}-\frac{\partial \chi_2}{\partial x_2}\right)+\frac{q}{h},$$
$$\dot{H}_q+\tau_q\ddot{H}_q=\sum_{r=1}^{N}D_q g^{(qr)}\left(\frac{\partial^2 H_r}{\partial x_1^2}+\frac{\partial^2 H_r}{\partial x_2^2}\right)+\Lambda_q\left(\frac{\partial^3 \chi_1}{\partial x_1^3}+\frac{\partial^3 \chi_2}{\partial x_1^2\partial x_2}+\frac{\partial^3 \chi_1}{\partial x_1\partial x_2^2}+\frac{\partial^3 \chi_2}{\partial x_2^3}\right)+\frac{12}{h^3}z_q,$$

where k_T coefficient taking into account the uneven distribution of shear stresses over the thickness of the plate.

If the shear stresses are distributed according to the Zhuravsky formula, then for a plate of thickness h we have [16,17,20]

$$k_T^2=\frac{5}{6}.$$

The remaining quantities in (14) are defined as follows:

1) $m_1=\int\limits_{-h/2}^{h/2}x_3F_1dx_3-\int\limits_{-h/2}^{h/2}\sigma_{13}dx_3$ and $m_2=\int\limits_{-h/2}^{h/2}x_3F_2dx_3-\int\limits_{-h/2}^{h/2}\sigma_{23}dx_3$, where m_1 and m_2 are the surface distributed moment,

2) $q=\int\limits_{-h/2}^{h/2}F_3dx_3$ is the surface distributed transverse load,

3) $z_q=\int\limits_{-h/2}^{h/2}Y^{(q)}x_3dx_3$ is the surface density of bulk mass transfer sources.

Equations (14) are supplemented by boundary conditions, which are also obtained from the variational equation (8). In the simply support case of the plate on all sides, they have the form

$$\left(\frac{\partial\chi_1}{\partial x_1}+\lambda\frac{\partial\chi_2}{\partial x_2}+\sum_{j=1}^{N}\alpha_j H_j\right)\Bigg|_{x_1=0}=-\frac{12}{h^3}M_1^{(1)},\quad \left(\frac{\partial\chi_1}{\partial x_1}+\lambda\frac{\partial\chi_2}{\partial x_2}+\sum_{j=1}^{N}\alpha_j H_j\right)\Bigg|_{x_1=l_1}=-\frac{12}{h^3}M_2^{(1)},$$

$$\left(\lambda\frac{\partial\chi_1}{\partial x_1}+\frac{\partial\chi_2}{\partial x_2}+\sum_{j=1}^{N}\alpha_j H_j\right)\Bigg|_{x_2=0}=-\frac{12}{h^3}M_1^{(2)},\quad \left(\lambda\frac{\partial\chi_1}{\partial x_1}+\frac{\partial\chi_2}{\partial x_2}+\sum_{j=1}^{N}\alpha_j H_j\right)\Bigg|_{x_2=l_2}=-\frac{12}{h^3}M_2^{(2)},$$

$$\chi_2\big|_{x_1=0}=\mathrm{X}_{21}^{(1)},\ \chi_2\big|_{x_1=l_1}=\mathrm{X}_{22}^{(1)},\ \chi_1\big|_{x_2=0}=\mathrm{X}_{11}^{(2)},\ \chi_1\big|_{x_2=l_2}=\mathrm{X}_{12}^{(2)},\qquad(15)$$

$$w\big|_{x_1=0}=W_1^{(1)},\ w\big|_{x_1=l_1}=W_2^{(1)},\ w\big|_{x_2=0}=W_1^{(2)},\ w\big|_{x_2=l_2}=W_2^{(2)},$$

$$H_q\big|_{x_1=0}=H_{q1}^{(1)},\ H_q\big|_{x_1=l_1}=H_{q2}^{(1)},\ H_q\big|_{x_2=0}=H_{q1}^{(2)},\ H_q\big|_{x_2=l_2}=H_{q2}^{(2)}.$$

Here $M_k^{(l)}$ are bending moments shown in Fig. 1; $\mathrm{X}_{ij}^{(l)}$, $W_i^{(l)}$ и $H_{q1}^{(1)}$ are given boundary kinematic characteristics of the required physical fields.

In accordance with (4), and (5), the initial conditions are assumed to be zero.

4. Integral representation of the solution

The solution to the problem (14), and (15) will be sought in the form

$$\chi_1(x_1,x_2,\tau)=\sum_{k=1}^{N+2}\int_0^{l_2}\int_0^{\tau}\left[G_{1k1}(x_1,x_2,\zeta,\tau-t)\,f_{k11}(\zeta,t)-G_{1k1}(l_1-x_1,x_2,\zeta,\tau-t)\,f_{k12}(\zeta,t)\right]dtd\zeta+$$
$$+\sum_{k=1}^{N+2}\int_0^{l_1}\int_0^{\tau}\left[G_{1k2}(x_1,x_2,\xi,\tau-t)\,f_{k21}(\xi,t)+G_{1k2}(x_1,l_2-x_2,\xi,\tau-t)\,f_{k22}(\xi,t)\right]dtd\xi$$

$$\chi_2(x_1,x_2,\tau)=\sum_{k=1}^{N+2}\int_0^{l_2}\int_0^{\tau}\left[G_{2k1}(x_1,x_2,\zeta,\tau-t)\,f_{k11}(\zeta,t)+G_{2k1}(l_1-x_1,x_2,\zeta,\tau-t)\,f_{k12}(\zeta,t)\right]dtd\zeta+$$
$$+\sum_{k=1}^{N+2}\int_0^{l_1}\int_0^{\tau}\left[G_{2k2}(x_1,x_2,\xi,\tau-t)\,f_{k21}(\xi,t)-G_{2k2}(x_1,l_2-x_2,\xi,\tau-t)\,f_{k22}(\xi,t)\right]dtd\xi,$$

$$w(x_1,x_2,\tau)=\sum_{k=1}^{N+2}\int_0^{l_2}\int_0^{\tau}\left[G_{3k1}(x_1,x_2,\zeta,\tau-t)\,f_{k11}(\zeta,t)+G_{3k1}(l_1-x_1,x_2,\zeta,\tau-t)\,f_{k12}(\zeta,t)\right]dtd\zeta+\qquad(16)$$
$$+\sum_{k=1}^{N+2}\int_0^{l_1}\int_0^{\tau}\left[G_{3k2}(x_1,x_2,\xi,\tau-t)\,f_{k21}(\xi,t)+G_{3k2}(x_1,l_2-x_2,\xi,\tau-t)\,f_{k22}(\xi,t)\right]dtd\xi,$$

$$H_q(x_1,x_2,\tau)=\sum_{k=1}^{N+2}\int_0^{l_2}\int_0^{\tau}\left[G_{q+3,k1}(x_1,x_2,\zeta,\tau-t)\,f_{k11}(\zeta,t)+G_{q+3,k1}(l_1-x_1,x_2,\zeta,\tau-t)\,f_{k12}(\zeta,t)\right]dtd\zeta+$$
$$+\sum_{k=1}^{N+2}\int_0^{l_1}\int_0^{\tau}\left[G_{q+3,k2}(x_1,x_2,\xi,\tau-t)\,f_{k21}(\xi,t)+G_{q+3,k2}(x_1,l_2-x_2,\xi,\tau-t)\,f_{k22}(\xi,t)\right]dtd\xi,$$

where the functions G_{ikl} are the Green's functions of the problem (14), (15), which satisfy the equations

$$\ddot{G}_{1kl}=\frac{\partial^2 G_{1kl}}{\partial x_1^2}+\mu\frac{\partial^2 G_{1kl}}{\partial x_2^2}+\mu k_T^2\left(\frac{\partial G_{3kl}}{\partial x_1}-G_{1kl}\right)+(\lambda+\mu)\frac{\partial^2 G_{2kl}}{\partial x_1\partial x_2}+\sum_{j=1}^{N}\alpha_j\frac{\partial G_{j+3,kl}}{\partial x_1},$$

$$\ddot{G}_{2kl}=\mu\frac{\partial^2 G_{2kl}}{\partial x_1^2}+\frac{\partial^2 G_{2kl}}{\partial x_2^2}+\mu k_T^2\left(\frac{\partial G_{3kl}}{\partial x_2}-G_{2kl}\right)+(\lambda+\mu)\frac{\partial^2 G_{1kl}}{\partial x_1\partial x_2}+\sum_{j=1}^{N}\alpha_j\frac{\partial G_{j+3,kl}}{\partial x_2},$$

$$\ddot{G}_{3kl}=\mu k_T^2\left(\frac{\partial^2 G_{3kl}}{\partial x_1^2}-\frac{\partial G_{1kl}}{\partial x_1}+\frac{\partial^2 G_{3kl}}{\partial x_2^2}-\frac{\partial G_{2kl}}{\partial x_2}\right), \tag{17}$$

$$\dot{G}_{q+3,kl}+\tau_q\ddot{G}_{q+3,kl}=\sum_{r=1}^{N}D_{qr}\left(\frac{\partial^2 G_{r+3,kl}}{\partial x_1^2}+\frac{\partial^2 G_{r+3,kl}}{\partial x_2^2}\right)+\Lambda_q\left(\frac{\partial^3 G_{1kl}}{\partial x_1^3}+\frac{\partial^3 G_{2kl}}{\partial x_1^2\partial x_2}+\frac{\partial^3 G_{1kl}}{\partial x_1\partial x_2^2}+\frac{\partial^3 G_{2kl}}{\partial x_2^3}\right)$$

and the following boundary conditions

$$\left(\frac{\partial G_{1kl}}{\partial x_1}+\lambda\frac{\partial G_{2kl}}{\partial x_2}+\sum_{j=1}^{N}\alpha_j G_{j+3,kl}\right)\Bigg|_{x_1=0}=\delta_{1k}\delta_{1l}\delta(\tau)\delta(x_2-\zeta),$$

$$\left(\lambda\frac{\partial G_{1kl}}{\partial x_1}+\frac{\partial G_{2kl}}{\partial x_2}+\sum_{j=1}^{N}\alpha_j G_{j+3,kl}\right)\Bigg|_{x_2=0}=\delta_{1k}\delta_{2l}\delta(\tau)\delta(x_1-\xi),$$

$$\left(\frac{\partial G_{1kl}}{\partial x_1}+\lambda\frac{\partial G_{2kl}}{\partial x_2}+\sum_{j=1}^{N}\alpha_j G_{q+3,kl}\right)\Bigg|_{x_1=l_1}=0,\quad \left(\lambda\frac{\partial G_{1kl}}{\partial x_1}+\frac{\partial G_{2kl}}{\partial x_2}+\sum_{j=1}^{N}\alpha_j G_{j+3,kl}\right)\Bigg|_{x_2=l_2}=0, \tag{18}$$

$$G_{2kl}\big|_{x_1=0}=\delta_{2k}\delta_{1l}\delta(\tau)\delta(x_2-\zeta),\quad G_{2kl}\big|_{x_1=l_1}=0,\quad G_{1kl}\big|_{x_2=0}=\delta_{2k}\delta_{2l}\delta(\tau)\delta(x_1-\xi),\quad G_{1kl}\big|_{x_2=l_2}=0,$$

$$G_{3kl}\big|_{x_1=0}=\delta_{3k}\delta_{1l}\delta(\tau)\delta(x_2-\zeta),\quad G_{3kl}\big|_{x_1=l_1}=0,\quad G_{3kl}\big|_{x_2=0}=\delta_{3k}\delta_{2l}\delta(\tau)\delta(x_1-\xi),\quad G_{3kl}\big|_{x_2=l_2}=0,$$

$$G_{q+3,kl}\big|_{x_1=0}=\delta_{q+3,k}\delta_{1l}\delta(\tau)\delta(x_2-\zeta),\quad G_{q+3,kl}\big|_{x_1=l_1}=0,$$

$$G_{q+3,kl}\big|_{x_2=0}=\delta_{q+3,k}\delta_{2l}\delta(\tau)\delta(x_1-\xi),\quad G_{q+3,kl}\big|_{x_2=l_2}=0.$$

The functions f_{klm} define edge disturbances, which, in accordance with (15), have the form:

$$f_{111}(x_2,\tau)=-\frac{12}{h^3}M_1^{(1)}(x_2,\tau),\quad f_{112}(x_2,\tau)=-\frac{12}{h^3}M_2^{(1)}(x_2,\tau),$$

$$f_{121}(x_1,\tau)=-\frac{12}{h^3}M_1^{(2)}(x_1,\tau),\quad f_{122}(x_1,\tau)=-\frac{12}{h^3}M_2^{(2)}(x_1,\tau),$$

$$f_{211}(x_2,\tau)=\mathrm{X}_{21}^{(1)}(x_2,\tau),\ f_{212}(x_2,\tau)=\mathrm{X}_{22}^{(1)}(x_2,\tau),\ f_{221}(x_1,\tau)=\mathrm{X}_{11}^{(2)}(x_1,\tau),\ f_{222}(x_1,\tau)=\mathrm{X}_{12}^{(2)}(x_1,\tau),$$

$$f_{311}(x_2,\tau)=W_1^{(1)}(x_2,\tau),\ f_{312}(x_2,\tau)=W_2^{(1)}(x_2,\tau),\ f_{321}(x_1,\tau)=W_1^{(2)}(x_1,\tau),\ f_{322}(x_1,\tau)=W_2^{(2)}(x_1,\tau),$$

$$f_{q+2,11}(x_2,\tau)=H_{q1}^{(1)}(x_2,\tau),\quad f_{q+2,12}(x_2,\tau)=H_{q2}^{(1)}(x_2,\tau),$$

$$f_{q+2,21}(x_1,\tau)=H_{q1}^{(2)}(x_1,\tau),\quad f_{q+2,22}(x_1,\tau)=H_{q2}^{(2)}(x_1,\tau). \tag{19}$$

5. Algorithm for finding Green's functions

We will assume that the plate material is an ideal solid solution. In this case [12-15]

$$g^{(qr)}=\delta_{qr},\quad D_{qr}=D_q g^{(qr)}=\begin{cases}D_q, & r=q\\ 0, & r\neq q\end{cases}$$

Applying the Laplace transform to (17), (18), we obtain (s is Laplace transform parameter, superscript L denotes the Laplace transform):

$$
\begin{aligned}
&s^2 G^L_{1kl} = \frac{\partial^2 G^L_{1kl}}{\partial x_1^2} + \mu \frac{\partial^2 G^L_{1kl}}{\partial x_2^2} + \mu k_T^2 \left(\frac{\partial G^L_{3kl}}{\partial x_1} - G^L_{1kl} \right) + (\lambda + \mu) \frac{\partial^2 G^L_{2kl}}{\partial x_1 \partial x_2} + \sum_{j=1}^{N} \alpha_j \frac{\partial G^L_{j+3,kl}}{\partial x_1}, \\
&s^2 G^L_{2kl} = \mu \frac{\partial^2 G^L_{2kl}}{\partial x_1^2} + \frac{\partial^2 G^L_{2kl}}{\partial x_2^2} + \mu k_T^2 \left(\frac{\partial G^L_{3kl}}{\partial x_2} - G^L_{2kl} \right) + (\lambda + \mu) \frac{\partial^2 G^L_{1kl}}{\partial x_1 \partial x_2} + \sum_{j=1}^{N} \alpha_j \frac{\partial G^L_{j+3,kl}}{\partial x_2}, \\
&s^2 G^L_{3kl} = \mu k_T^2 \left(\frac{\partial^2 G^L_{3kl}}{\partial x_1^2} - \frac{\partial G^L_{1kl}}{\partial x_1} + \frac{\partial^2 G^L_{3kl}}{\partial x_2^2} - \frac{\partial G^L_{2kl}}{\partial x_2} \right), \\
&s G^L_{q+3,kl} + \tau_q s^2 G^L_{q+3,kl} = D_q \left(\frac{\partial^2 G^L_{q+3,kl}}{\partial x_1^2} + \frac{\partial^2 G^L_{q+3,kl}}{\partial x_2^2} \right) + \Lambda_q \left(\frac{\partial^3 G^L_{1kl}}{\partial x_1^3} + \frac{\partial^3 G^L_{2kl}}{\partial x_1^2 \partial x_2} + \frac{\partial^3 G^L_{1kl}}{\partial x_1 \partial x_2^2} + \frac{\partial^3 G^L_{2kl}}{\partial x_2^3} \right);
\end{aligned}
\tag{20}
$$

$$
\begin{aligned}
&\left(\frac{\partial G^L_{1kl}}{\partial x_1} + \lambda \frac{\partial G^L_{2kl}}{\partial x_2} + \sum_{j=1}^{N} \alpha_j G^L_{j+3,kl} \right)\Bigg|_{x_1=0} = \delta_{1k} \delta_{1l} \delta(x_2 - \zeta), \\
&\left(\lambda \frac{\partial G^L_{1kl}}{\partial x_1} + \frac{\partial G^L_{2kl}}{\partial x_2} + \sum_{j=1}^{N} \alpha_j G^L_{j+3,kl} \right)\Bigg|_{x_2=0} = \delta_{1k} \delta_{2l} \delta(x_1 - \xi), \\
&\left(\frac{\partial G^L_{1kl}}{\partial x_1} + \lambda \frac{\partial G^L_{2kl}}{\partial x_2} + \sum_{j=1}^{N} \alpha_j G^L_{j+3,kl} \right)\Bigg|_{x_1=l_1} = 0, \quad \left(\lambda \frac{\partial G^L_{1kl}}{\partial x_1} + \frac{\partial G^L_{2kl}}{\partial x_2} + \sum_{j=1}^{N} \alpha_j G^L_{j+3,kl} \right)\Bigg|_{x_2=l_2} = 0, \\
&G^L_{2kl}\Big|_{x_1=0} = \delta_{2k} \delta_{1l} \delta(x_2 - \zeta), \quad G^L_{2kl}\Big|_{x_1=l_1} = 0, \quad G^L_{1kl}\Big|_{x_2=0} = \delta_{2k} \delta_{2l} \delta(x_1 - \xi), \quad G^L_{1kl}\Big|_{x_2=l_2} = 0, \\
&G^L_{3kl}\Big|_{x_1=0} = \delta_{3k} \delta_{1l} \delta(x_2 - \zeta), \quad G^L_{3kl}\Big|_{x_1=l_1} = 0, \quad G^L_{3kl}\Big|_{x_2=0} = \delta_{3k} \delta_{2l} \delta(x_1 - \xi), \quad G^L_{3kl}\Big|_{x_2=l_2} = 0, \\
&G^L_{q+1,kl}\Big|_{x_1=0} = \delta_{q+3,k} \delta_{1l} \delta(x_2 - \zeta), \quad G^L_{q+1,kl}\Big|_{x_1=l_1} = 0, \\
&G^L_{q+1,kl}\Big|_{x_2=0} = \delta_{q+3,k} \delta_{2l} \delta(x_1 - \xi), \quad G^L_{q+1,kl}\Big|_{x_2=l_2} = 0.
\end{aligned}
\tag{21}
$$

Multiplying the first equation in (20) by $\cos\lambda_n x_1 \sin\mu_m x_2$, the second equation by $\sin\lambda_n x_1 \cos\mu_m x_2$, the third and fourth by equation $\sin\lambda_n x_1 \sin\mu_m x_2$, $\lambda_n = \pi n / l_1$, $\mu_m = \pi m / l_2$ and integrating into the rectangle $D = [0, l_1] \times [0, l_2]$ taking into account conditions (21), we obtain

$$
\begin{aligned}
&k_{1nm}(s) G^{LF}_{1klnm}(\xi, \zeta, s) + K_{nm} G^{LF}_{2klnm}(\xi, \zeta, s) - \\
&- \mu k_T^2 \lambda_n G^{LF}_{3klnm}(\xi, \zeta, s) - \lambda_n \sum_{j=1}^{N} \alpha_j G^{LF}_{j+3,klnm}(\xi, \zeta, s) = F_{1klnm}(\xi, \zeta) \\
&K_{nm} G^{LF}_{1klnm}(\xi, \zeta, s) + k_{2nm}(s) G^{LF}_{2klnm}(\xi, \zeta, s) - \\
&- \mu k_T^2 \mu_m G^{LF}_{3klnm}(\xi, \zeta, s) - \mu_m \sum_{j=1}^{N} \alpha_j G^{LF}_{j+3,klnm}(\xi, \zeta, s) = F_{2klnm}(\xi, \zeta), \\
&- \mu k_T^2 \left[\lambda_n G^{LF}_{1klnm}(\xi, \zeta, s) + \mu_m G^{LF}_{2klnm}(\xi, \zeta, s) \right] + k_{3nm}(s) G^{LF}_{3klnm}(\xi, \zeta, s) = F_{3klnm}(\xi, \zeta), \\
&- M_{1qnm} G^{LF}_{1klnm}(\xi, \zeta, s) - M_{2qnm} G^{LF}_{2klnm}(\xi, \zeta, s) + k_{q+3,nm}(s) G^{LF}_{q+3,klnm}(\xi, \zeta, s) = F_{q+3,klnm}(\xi, \zeta),
\end{aligned}
\tag{22}
$$

where

$$
\begin{aligned}
&k_{1nm}(s) = s^2 + \mu k_T^2 + \lambda_n^2 + \mu \mu_m^2, \quad k_{2nm}(s) = s^2 + \mu k_T^2 + \mu \lambda_n^2 + \mu_m^2, \quad \Lambda_q^* = \Lambda_q (\lambda - 1), \\
&k_{3nm}(s) = s^2 + \mu k_T^2 (\lambda_n^2 + \mu_m^2), \quad k_{q+3,nm}(s) = s + \tau_q s^2 + D_q (\lambda_n^2 + \mu_m^2), \\
&M_{1qnm} = \Lambda_q \lambda_n (\lambda_n^2 + \mu_m^2), \quad M_{2qnm} = \Lambda_q \mu_m (\lambda_n^2 + \mu_m^2), \quad K_{nm} = (\lambda + \mu) \lambda_n \mu_m,
\end{aligned}
$$

$$F_{1klnm}(\xi,\zeta)=-\frac{4}{l_1l_2}\left(\delta_{1k}+\mu k_T^2\delta_{3k}\right)\delta_{1l}\sin\mu_m\zeta+\frac{4\mu\mu_m}{l_1l_2}\left(\delta_{1l}\cos\mu_m\zeta+\delta_{2l}\cos\lambda_n\xi\right)\delta_{2k},$$

$$F_{2klnm}(\xi,\zeta)=-\frac{4}{l_1l_2}\left(\delta_{1k}+\mu k_T^2\delta_{3k}\right)\delta_{2l}\sin\lambda_n\xi+\frac{4\mu\lambda_n}{l_1l_2}\left(\delta_{1l}\cos\mu_m\zeta+\delta_{2l}\cos\lambda_n\xi\right)\delta_{2k},$$

$$F_{3klnm}(\xi,\zeta)=\frac{4\mu k_T^2}{l_1l_2}\left(\lambda_n\delta_{1l}\sin\mu_m\zeta+\mu_m\delta_{2l}\sin\lambda_n\xi\right)\delta_{3k},$$

$$F_{q+3,klnm}(\xi,\zeta)=\frac{4\Lambda_q}{l_1l_2}\left(\lambda_n\delta_{1l}\sin\mu_m\zeta+\mu_m\delta_{2l}\sin\lambda_n\xi\right)\delta_{1k}+\frac{4\lambda_n\mu_m\Lambda_q^*}{l_1l_2}\left(\delta_{1l}\cos\mu_m\zeta+\delta_{2l}\cos\lambda_n\xi\right)\delta_{2k}+$$

$$+\frac{4\lambda_n}{l_1l_2}\left(D_q\delta_{q+3,k}-\Lambda_q\sum_{j=1}^{N}\alpha_j\delta_{j+3,k}\right)\delta_{1l}\sin\mu_m\zeta+\frac{4\mu_m}{l_1l_2}\left(D_q\delta_{q+3,k}-\Lambda_q\sum_{j=1}^{N}\alpha_j\delta_{j+3,k}\right)\delta_{2l}\sin\lambda_n\xi;$$

$$G_{1klnm}^{LF}(\xi,\zeta,s)=\frac{4}{l_1l_2}\int_0^{l_1}\int_0^{l_2}G_{1kl}^{L}(x_1,x_2,\xi,\zeta,s)\cos\lambda_n x_1\sin\mu_m x_2dx_2dx_1,$$

$$G_{2klnm}^{LF}(\xi,\zeta,s)=\frac{4}{l_1l_2}\int_0^{l_1}\int_0^{l_2}G_{2kl}^{L}(x_1,x_2,\xi,\zeta,s)\sin\lambda_n x_1\cos\mu_m x_2dx_2dx_1, \qquad (23)$$

$$G_{pklnm}^{LF}(\xi,\zeta,s)=\frac{4}{l_1l_2}\int_0^{l_1}\int_0^{l_2}G_{pkl}^{L}(x_1,x_2,\xi,\zeta,s)\sin\lambda_n x_1\sin\mu_m x_2dx_2dx_1,$$

$$G_{1kl}^{L}(x_1,x_2,\xi,\zeta,\tau)=\sum_{n=0}^{\infty}\sum_{m=1}^{\infty}G_{1klnm}^{LF}(\xi,\zeta,\tau)\cos\lambda_n x_1\sin\mu_m x_2,$$

$$G_{2kl}^{L}(x_1,x_2,\xi,\zeta,\tau)=\sum_{n=1}^{\infty}\sum_{m=0}^{\infty}G_{2klnm}^{LF}(\xi,\zeta,\tau)\sin\lambda_n x_1\cos\mu_m x_2,$$

$$G_{pkl}^{L}(x_1,x_2,\xi,\zeta,\tau)=\sum_{n=1}^{\infty}\sum_{m=1}^{\infty}G_{pklnm}^{LF}(\xi,\zeta,\tau)\sin\lambda_n x_1\sin\mu_m x_2,\quad p\ge 3.$$

The solution of the system (22) has the form $\left(q,p=\overline{1,N},\ \ k=\overline{1,N+3},\ \ l=1,2\right)$

$$G_{iklnm}^{LF}(\xi,\zeta,s)=\frac{P_{iklnm}(\xi,\zeta,s)}{P_{nm}(\xi,\zeta,s)}\ \ (i=1,2), \qquad (24)$$

$$G_{3klnm}^{LF}(\xi,\zeta,s)=\frac{4\mu k_T^2}{l_1l_2}\frac{\left(\lambda_n\delta_{1l}\sin\mu_m\zeta+\mu_m\delta_{2l}\sin\lambda_n\xi\right)\delta_{3k}}{k_{3nm}(s)}+\frac{P_{3klnm}(\xi,\zeta,s)}{Q_{3nm}(\xi,\zeta,s)},$$

$$G_{q+3,klnm}^{LF}(\xi,\zeta,s)=\frac{P_{q+3,klnm}(\xi,\zeta,s)}{Q_{q+3,nm}(\xi,\zeta,s)}+\frac{4}{l_1l_2}\frac{\Lambda_q\left(\lambda_n\delta_{1l}\sin\mu_m\zeta+\mu_m\delta_{2l}\sin\lambda_n\xi\right)\delta_{1k}}{k_{q+3,nm}(s)}+$$

$$+\frac{4\lambda_n\mu_m\Lambda_q^*}{l_1l_2}\frac{\left(\delta_{1l}\cos\mu_m\zeta+\delta_{2l}\cos\lambda_n\xi\right)\delta_{2k}}{k_{q+3,nm}(s)}+$$

$$+\frac{4}{l_1l_2}\frac{\lambda_n\left(D_q\delta_{q+3,k}-\Lambda_q\sum_{j=1}^{N}\alpha_j\delta_{j+3,k}\right)\delta_{1l}\sin\mu_m\zeta+\mu_m\left(D_q\delta_{q+3,k}-\Lambda_q\sum_{j=1}^{N}\alpha_j\delta_{j+3,k}\right)\delta_{2l}\sin\lambda_n\xi}{k_{q+3,nm}(s)},$$

where

$$P_{nm}(s)=\left[k_{1nm}(s)k_{2nm}(s)-K_{nm}^2\right]k_{3nm}(s)\Pi_{nm}(s)-$$
$$-\mu^2k_T^4\left[\mu_m^2k_{1nm}(s)+\lambda_n^2k_{2nm}(s)-2K_{nm}\mu_m\lambda_n\right]\Pi_{nm}(s)-$$
$$-k_{3nm}(s)\sum_{j=1}^{N}\alpha_j\left\{\left[\mu_mk_{1nm}(s)-\lambda_nK_{nm}\right]M_{2jnm}+\left[\lambda_nk_{2nm}(s)-\mu_mK_{nm}\right]M_{1jnm}\right\}\Pi_{jnm}(s),$$
$$Q_{pnm}(s)=k_{pnm}(s)P_{nm}(s),\quad p\geq 3,$$
$$\Pi_{nm}(s)=\prod_{j=1}^{N}k_{j+3,nm}(s),\quad \Pi_{jnm}(s)=\prod_{r=1,r\neq j}^{N}k_{r+3,nm}(s),\quad \Pi_{ijnm}(s)=\prod_{r=1,r\neq i,j}^{N}k_{r+3,nm}(s).$$
$$S_{1nm}(s)=k_{2nm}(s)k_{3nm}(s)-\mu^2k_T^4\mu_m^2,\quad S_{2nm}(s)=k_{1nm}(s)k_{3nm}(s)-\mu^2k_T^4\lambda_n^2,$$
$$S_{3nm}(s)=K_{nm}k_{3nm}(s)-\mu^2k_T^4\mu_m\lambda_n.$$

The rest of the polynomials $P_{iklnm}(\xi,\zeta,s)$, included in the solution in solution (24) are defined as:

$$P_{111nm}(\xi,\zeta,s)=-\frac{4}{l_1l_2}\left[S_{1nm}(s)\Pi_{nm}(s)-\mu_mk_{3nm}(s)\sum_{j=1}^{N}\alpha_jM_{2jnm}\Pi_{jnm}(s)\right]\sin\mu_m\zeta+$$
$$+\frac{4\lambda_n}{l_1l_2}\left[\lambda_nS_{1nm}(s)-\mu_mS_{3nm}(s)\right]\sum_{j=1}^{N}\alpha_j\Lambda_j\Pi_{jnm}(s)\sin\mu_m\zeta,$$
$$P_{112nm}(\xi,\zeta,s)=\frac{4}{l_1l_2}\left[S_{3nm}(s)\Pi_{nm}(s)-\lambda_nk_{3nm}(s)\sum_{j=1}^{N}\alpha_jM_{2jnm}\Pi_{jnm}(s)\right]\sin\lambda_n\xi+$$
$$+\frac{4\mu_m}{l_1l_2}\left[\lambda_nS_{1nm}(s)-\mu_mS_{3nm}(s)\right]\sum_{j=1}^{N}\alpha_j\Lambda_j\Pi_{jnm}(s)\sin\lambda_n\xi,$$
$$P_{121nm}(\xi,\zeta,s)=\frac{4}{l_1l_2}\mu\left[\mu_mS_{1nm}(s)-\lambda_nS_{3nm}(s)\right]\Pi_{nm}(s)\cos\mu_m\zeta+$$
$$+\frac{4\mu}{l_1l_2}k_{3nm}(s)\left(\lambda_n^2-\mu_m^2\right)\sum_{j=1}^{N}\alpha_jM_{2jnm}\Pi_{jnm}(s)\cos\mu_m\zeta+$$
$$+\frac{4\lambda_n\mu_m}{l_1l_2}\left[\lambda_nS_{1nm}(s)-\mu_mS_{3nm}(s)\right]\sum_{j=1}^{N}\alpha_j\Lambda_j^*\Pi_{jnm}(s)\cos\mu_m\zeta,$$
$$P_{122nm}(\xi,\zeta,s)=\frac{4}{l_1l_2}\mu\left[\mu_mS_{1nm}(s)-\lambda_nS_{3nm}(s)\right]\Pi_{nm}(s)\cos\lambda_n\xi+$$
$$+\frac{4\mu}{l_1l_2}k_{3nm}(s)\left(\lambda_n^2-\mu_m^2\right)\sum_{j=1}^{N}\alpha_jM_{2jnm}\Pi_{jnm}(s)\cos\lambda_n\xi+$$
$$+\frac{4\lambda_n\mu_m}{l_1l_2}\left[\lambda_nS_{1nm}(s)-\mu_mS_{3nm}(s)\right]\sum_{j=1}^{N}\alpha_j\Lambda_j^*\Pi_{jnm}(s)\cos\lambda_n\xi,$$
$$P_{131nm}(\xi,\zeta,s)=\frac{4}{l_1l_2}\mu k_T^2\left[\mu k_T^2\lambda_n\left(\lambda_nk_{2nm}(s)-\mu_mK_{nm}\right)-S_{1nm}(s)\right]\Pi_{nm}(s)\sin\mu_m\zeta+$$
$$+\frac{4}{l_1l_2}\mu k_T^2\mu_mk_{3nm}(s)\sum_{j=1}^{N}\alpha_jM_{2jnm}\Pi_{jnm}(s)\sin\mu_m\zeta,$$
$$P_{132nm}(\xi,\zeta,s)=\frac{4}{l_1l_2}\mu k_T^2\left[S_{3nm}(s)+\mu k_T^2\mu_m\left(\lambda_nk_{2nm}(s)-\mu_mK_{nm}\right)\right]\Pi_{nm}(s)\sin\lambda_n\xi+$$
$$-\frac{4}{l_1l_2}\mu k_T^2\lambda_nk_{3nm}(s)\sum_{j=1}^{N}\alpha_jM_{2jnm}\Pi_{jnm}(s)\sin\lambda_n\xi,$$

$$P_{1,q+3,1nm}(\xi,\zeta,s)=\frac{4\alpha_q\lambda_n}{l_1l_2}\left[\lambda_n S_{1nm}(s)-\mu_m S_{3nm}(s)\right]\left[D_q\Pi_{qnm}(s)-\Lambda_q\sum_{j=1}^{N}\alpha_j\Pi_{jnm}(s)\right]\sin\mu_m\zeta,$$

$$P_{1,q+3,2nm}(\xi,\zeta,s)=\frac{4\alpha_q\mu_m}{l_1l_2}\left[\lambda_n S_{1nm}(s)-\mu_m S_{3nm}(s)\right]\left[D_q\Pi_{qnm}(s)-\Lambda_q\sum_{j=1}^{N}\alpha_j\Pi_{jnm}(s)\right]\sin\lambda_n\xi,$$

$$P_{211nm}(\xi,\zeta,s)=\frac{4}{l_1l_2}\left[S_{3nm}(s)\Pi_{nm}(s)-\mu_m k_{3nm}(s)\sum_{j=1}^{N}\alpha_j M_{1jnm}\Pi_{jnm}(s)\right]\sin\mu_m\zeta+$$
$$+\frac{4\lambda_n}{l_1l_2}\left[\mu_m S_{2nm}(s)-\lambda_n S_{3nm}(s)\right]\sum_{j=1}^{N}\alpha_j\Lambda_j\Pi_{jnm}(s)\sin\mu_m\zeta,$$

$$P_{212nm}(\xi,\zeta,s)=-\frac{4}{l_1l_2}\left[S_{2nm}(s)\Pi_{nm}(s)-\lambda_n k_{3nm}(s)\sum_{j=1}^{N}\alpha_j M_{1jnm}\Pi_{jnm}(s)\right]\sin\lambda_n\xi+$$
$$+\frac{4\mu_m}{l_1l_2}\left[\mu_m S_{2nm}(s)-\lambda_n S_{3nm}(s)\right]\sum_{j=1}^{N}\alpha_j\Lambda_j\Pi_{jnm}(s)\sin\lambda_n\xi,$$

$$P_{221nm}(\xi,\zeta,s)=\frac{4}{l_1l_2}\mu\left[\lambda_n S_{2nm}(s)-\mu_m S_{3nm}(s)\right]\Pi_{nm}(s)\cos\mu_m\zeta+$$
$$+\frac{4\mu}{l_1l_2}\left(\mu_m^2-\lambda_n^2\right)k_{3nm}(s)\sum_{j=1}^{N}\alpha_j M_{1jnm}\Pi_{jnm}(s)\cos\mu_m\zeta+$$
$$+\frac{4\lambda_n\mu_m}{l_1l_2}\left[\mu_m S_{2nm}(s)-\lambda_n S_{3nm}(s)\right]\sum_{j=1}^{N}\alpha_j\Lambda_j^*\Pi_{jnm}(s)\cos\mu_m\zeta,$$

$$P_{222nm}(\xi,\zeta,s)=\frac{4\mu}{l_1l_2}\left[\lambda_n S_{2nm}(s)-\mu_m S_{3nm}(s)\right]\Pi_{nm}(s)\cos\lambda_n\xi+$$
$$+\frac{4\mu}{l_1l_2}\left(\mu_m^2-\lambda_n^2\right)k_{3nm}(s)\sum_{j=1}^{N}\alpha_j M_{1jnm}\Pi_{jnm}(s)\cos\lambda_n\xi+$$
$$+\frac{4\lambda_n\mu_m}{l_1l_2}\left[\mu_m S_{2nm}(s)-\lambda_n S_{3nm}(s)\right]\sum_{j=1}^{N}\alpha_j\Lambda_j^*\Pi_{jnm}(s)\cos\lambda_n\xi,$$

$$P_{231nm}(\xi,\zeta,s)=\frac{4\mu}{l_1l_2}k_T^2\left[S_{3nm}(s)+\mu k_T^2\lambda_n\left(\mu_m k_{1nm}(s)-\lambda_n K_{nm}\right)\right]\Pi_{nm}(s)\sin\mu_m\zeta-$$
$$-\frac{4\mu}{l_1l_2}k_T^2\mu_m k_{3nm}(s)\sum_{j=1}^{N}\alpha_j M_{1jnm}\Pi_{jnm}(s)\sin\mu_m\zeta,$$

$$P_{232nm}(\xi,\zeta,s)=\frac{4\mu}{l_1l_2}k_T^2\left[\mu k_T^2\mu_m\left(\mu_m k_{1nm}(s)-\lambda_n K_{nm}\right)-S_{2nm}(s)\right]\Pi_{nm}(s)\sin\lambda_n+$$
$$+\frac{4\mu}{l_1l_2}k_T^2\lambda_n k_{3nm}(s)\sum_{j=1}^{N}\alpha_j M_{1jnm}\Pi_{jnm}(s)\sin\lambda_n\xi,$$

$$P_{2,q+3,1nm}(\xi,\zeta,s)=\frac{4\alpha_q}{l_1l_2}\lambda_n\left[\mu_m S_{2nm}(s)-\lambda_n S_{3nm}(s)\right]\left[D_q\Pi_{qnm}(s)-\Lambda_q\sum_{j=1}^{N}\alpha_j\Pi_{jnm}(s)\right]\sin\mu_m\zeta,$$

$$P_{2,q+3,2nm}(\xi,\zeta,s)=\frac{4\alpha_q}{l_1l_2}\mu_m\left[\mu_m S_{2nm}(s)-\lambda_n S_{3nm}(s)\right]\left[D_q\Pi_{qnm}(s)-\Lambda_q\sum_{j=1}^{N}\alpha_j\Pi_{jnm}(s)\right]\sin\lambda_n\xi,\qquad(25)$$

$$P_{3klnm}(\xi,\zeta,s)=\mu k_T^2\left[\lambda_n P_{1klnm}(\xi,\zeta,s)+\mu_m P_{2klnm}(\xi,\zeta,s)\right],$$
$$P_{q+3,klnm}(\xi,\zeta,s)=M_{1qnm}P_{1klnm}(\xi,\zeta,s)+M_{2qnm}P_{2klnm}(\xi,\zeta,s).$$

The Laplace originals of the functions in (24) have the form [21] ($i,l=1,2$, $q=\overline{1,N}$, $j=\overline{1,2N+6}$, $k=\overline{1,N+3},$)

$$G^F_{iklnm}(\xi,\zeta,\tau)=\sum_{j=1}^{2N+6}A^{(j)}_{1klnm}(\xi,\zeta)e^{s_{jnm}\tau},$$

$$G^F_{3klnm}(\xi,\zeta,\tau)=\sum_{j=1}^{2N+8}A^{(j)}_{3klnm}(\xi,\zeta)e^{s_{jnm}\tau}+\frac{4\mu k_T^2}{l_1l_2}\sum_{j=2N+7}^{2N+8}\frac{(\lambda_n\delta_{1l}\sin\mu_m\zeta+\mu_m\delta_{2l}\sin\lambda_n\xi)\delta_{3k}}{k'_{3nm}(s_{jnm})}e^{s_{jnm}\tau},$$

$$G^F_{q+3,1lnm}(\xi,\zeta,\tau)=\sum_{j=1}^{2N+6}A^{(j)}_{q+3,1lnm}(\xi,\zeta)e^{s_{jnm}\tau}+\sum_{j=1}^{2}A^{(2N+6+j)}_{q+3,1lnm}(\xi,\zeta)e^{\gamma^{(q)}_{jnm}\tau}+$$
$$+\frac{4\Lambda_q}{l_1l_2}\sum_{j=1}^{2}\frac{\lambda_n\delta_{1l}\sin\mu_m\zeta+\mu_m\delta_{2l}\sin\lambda_n\xi}{k'_{q+3,nm}(\gamma^{(q)}_{jnm})}e^{\gamma^{(q)}_{jnm}\tau},$$

$$G^F_{q+3,2lnm}(\xi,\zeta,\tau)=\sum_{j=1}^{2N+6}A^{(j)}_{q+3,2lnm}(\xi,\zeta)e^{s_{jnm}\tau}+\sum_{j=1}^{2}A^{(2N+6+j)}_{q+3,2lnm}(\xi,\zeta)e^{\gamma^{(q)}_{jnm}\tau}+$$
$$+\frac{4\Lambda^*_q\lambda_n\mu_m}{l_1l_2}\sum_{j=1}^{2}\frac{\delta_{1l}\cos\mu_m\zeta+\delta_{2l}\cos\lambda_n\xi}{k'_{q+3,nm}(\gamma^{(q)}_{jnm})}e^{\gamma^{(q)}_{jnm}\tau}, \qquad (26)$$

$$G^F_{q+1,p+3,lnm}(\xi,\zeta,\tau)=\sum_{j=1}^{2N+6}A^{(j)}_{q+3,p+3,lnm}(\xi,\zeta)e^{s_{jnm}\tau}+\sum_{j=1}^{2}A^{(2N+6+j)}_{q+3,p+3,lnm}(\xi,\zeta)e^{\gamma^{(q)}_{jnm}\tau}+$$
$$+\frac{4}{l_1l_2}(D_q\delta_{qp}-\alpha_p\Lambda_q)(\delta_{1l}\lambda_n\sin\mu_m\zeta+\delta_{2l}\mu_m\sin\lambda_n\xi)\sum_{j=1}^{2}\frac{e^{\gamma^{(q)}_{jnm}\tau}}{k'_{q+3,nm}(\gamma^{(q)}_{jnm})},$$

$$A^{(j)}_{1klnm}(\xi,\zeta)=\frac{P_{iklnm}(\xi,\zeta,s_{jnm})}{P'_{nm}(s_{jnm})},\quad A^{(r)}_{3klnm}(\xi,\zeta)=\frac{P_{iklnm}(\xi,\zeta,s_{rnm})}{Q'_{3nm}(s_{rnm})},\quad r=\overline{1,2N+8},$$

$$A^{(j)}_{q+3,kl}(\lambda_n,\mu_m,\xi,\zeta)=\frac{P_{q+1,klnm}(\xi,\zeta,s_{jnm})}{Q'_{q+3,nm}(s_{jnm})},\quad A^{(2N+6+i)}_{q+3,klnm}(\xi,\zeta)=\frac{P_{q+1,klnm}(\xi,\zeta,\gamma^{(q)}_{jnm})}{Q'_{q+3,nm}(\gamma^{(q)}_{jnm})},$$

where s_{jnm}, $j=\overline{1,2N+6}$ are zeros of the polynomial $P_{nm}(s)$, $s_{2N+6+i,nm}$ are additional zeroes of the polynomial $Q_{3nm}(s)$, $\gamma^{(q)}_{jnm}$ are additional zeroes of the polynomial $Q_{q+3,nm}(s)$

$$s_{2N+7,nm}=-ik_T\sqrt{\mu(\lambda_n^2+\mu_m^2)},\quad s_{2N+8,nm}=ik_T\sqrt{\mu(\lambda_n^2+\mu_m^2)},$$
$$\gamma^{(q)}_{1nm}=\frac{-1-\sqrt{1-4\tau_qD_q(\lambda_n^2+\mu_m^2)}}{2\tau_q},\quad \gamma^{(q)}_{2nm}=\frac{-1+\sqrt{1-4\tau_qD_q(\lambda_n^2+\mu_m^2)}}{2\tau_q}.$$

6. Example

For calculation, we consider a rectangular three-component ($N=3$) plate (independent components zinc and copper, which diffuse in duralumin), with the following characteristics [22].

$$\lambda^*=6.93\cdot10^{10}\frac{N}{m^2},\ \mu^*=2.56\cdot10^{10}\frac{N}{m^2},\ \rho=2700\frac{kg}{m^3},\ D^{*(2)}_{11}=D^{*(2)}_{22}=2.89\cdot10^{-14}\frac{m^2}{sec},\ T_0=700\,K,$$

$$\alpha^{*(1)}_{11}=\alpha^{*(1)}_{22}=1.55\cdot10^7\frac{J}{m^3},\quad \alpha^{*(2)}_{11}=\alpha^{*(2)}_{22}=6.14\cdot10^7\frac{J}{m^3},\quad D^{*(1)}_{11}=D^{*(1)}_{22}=2.62\cdot10^{-12}\frac{m^2}{sec},$$

$$n^{(1)}_0=0.0084,\quad n^{(2)}_0=0.045,\quad m^{(1)}=0.065\frac{kg}{mol},\quad m^{(2)}=0.064\frac{kg}{mol},\quad l=h^*=5\cdot10^{-4}\,m.$$

We assume that the plate has the following dimensions: $l^*_1=0.01m$, $l^*_2=0.01m$, $h^*=0.0005\,m$.

Let us set the following load parameters in the boundary conditions (15) (other $f_{mkl}=0$ in (19))

$$f_{111}(x_2,\tau)=-\frac{12}{h^3}M_1^{(1)}(x_2,\tau)=H(\tau)\sin(\mu_1 x_2),$$
$$f_{112}(x_2,\tau)=-\frac{12}{h^3}M_2^{(1)}(x_2,\tau)=H(\tau)\sin(\mu_1 x_2). \qquad (27)$$

Calculating convolutions (16), taking into account (23) - (26), we obtain

$$\chi_1(x_1,x_2,\tau)=\sum_{k=1}^{N+2}\int_0^{l_2}\int_0^{\tau}\left[G_{111}(x_1,x_2,\zeta,\tau-t)-G_{111}(l_1-x_1,x_2,\zeta,\tau-t)\right]H(t)\sin(\mu_1\zeta)dtd\zeta=$$
$$=l_2\sin(\mu_1 x_2)\sum_{n=1}^{\infty}\sin\frac{\lambda_n}{2}\cos\lambda_n\left(\frac{1}{2}-x_1\right)\sum_{j=1}^{2N+6}\frac{e^{s_{jn1}\tau}-1}{s_{jn1}}\frac{\tilde{P}_{111n1}(s_{jn1})}{P'_{n1}(s_{jn1})},$$

$$\chi_2(x_1,x_2,\tau)=\sum_{k=1}^{N+2}\int_0^{l_2}\int_0^{\tau}\left[G_{211}(x_1,x_2,\zeta,\tau-t)-G_{211}(l_1-x_1,x_2,\zeta,\tau-t)\right]H(t)\sin\mu_1\zeta dtd\zeta=$$
$$=l_2\sin(\mu_1 x_2)\sum_{n=1}^{\infty}\sin\frac{\lambda_n}{2}\cos\lambda_n\left(\frac{1}{2}-x_1\right)\sum_{j=1}^{2N+6}\frac{e^{s_{jn1}\tau}-1}{s_{jn1}}\frac{\tilde{P}_{211n1}(s_{jn1})}{P'_{n1}(s_{jn1})},$$

$$w(x_1,x_2,\tau)=\sum_{k=1}^{N+2}\int_0^{l_2}\int_0^{\tau}\left[G_{311}(x_1,x_2,\zeta,\tau-t)+G_{311}(l_1-x_1,x_2,\zeta,\tau-t)\right]H(t)\sin(\mu_1\zeta)dtd\zeta=$$
$$=l_2\sin(\mu_1 x_2)\sum_{n=1}^{\infty}\sin\frac{\lambda_n}{2}\cos\lambda_n\left(\frac{1}{2}-x_1\right)\sum_{j=1}^{2N+8}\frac{e^{s_{jn1}\tau}-1}{s_{jn1}}\frac{\tilde{P}_{311n1}(s_{jn1})}{Q'_{3n1}(s_{jn1})},$$

$$H_q(x_1,x_2,\tau)=\sum_{k=1}^{N+2}\int_0^{l_2}\int_0^{\tau}\left[G_{q+3,11}(x_1,x_2,\zeta,\tau-t)+G_{q+3,11}(l_1-x_1,x_2,\zeta,\tau-t)\right]H(t)\sin(\mu_1\zeta)dtd\zeta=$$
$$=l_2\sin(\mu_1 x_2)\sum_{n=1}^{\infty}\sin\frac{\lambda_n}{2}\cos\left[\lambda_n\left(\frac{1}{2}-x_1\right)\right]\sum_{j=1}^{2N+6}\frac{e^{s_{jn1}\tau}-1}{s_{jn1}}\frac{\tilde{P}_{q+1,11n1}(s_{jn1})}{Q'_{q+3,n1}(s_{jn1})}+$$
$$+l_2\sin(\mu_1 x_2)\sum_{n=1}^{\infty}\sin\frac{\lambda_n}{2}\cos\left[\lambda_n\left(\frac{1}{2}-x_1\right)\right]\sum_{j=1}^{2}\frac{e^{\gamma^{(q)}_{jn1}\tau}-1}{\gamma^{(q)}_{jn1}}\frac{\tilde{P}_{q+1,11n1}(\gamma^{(q)}_{jn1})}{Q'_{q+3,n1}(\gamma^{(q)}_{jn1})}+$$
$$+\frac{4\Lambda_q}{l_1}\sin(\mu_1 x_2)\sum_{n=1}^{\infty}\lambda_n\sin\frac{\lambda_n}{2}\cos\left[\lambda_n\left(\frac{1}{2}-x_1\right)\right]\sum_{j=1}^{2}\frac{e^{\gamma^{(q)}_{jn1}\tau}-1}{k'_{q+3,n1}(\gamma^{(q)}_{jn1})\gamma^{(q)}_{jn1}},$$

where according to (3.8)

$$\tilde{P}_{m11n1}(s)=\frac{P_{m11n1}(\xi,\zeta,s)}{\sin\mu_m\zeta},\quad \tilde{P}_{q+1,11n1}(s)=M_{1qn1}\tilde{P}_{111n1}(s)+M_{2qn1}\tilde{P}_{211n1}(s)\ \ (m=1,2,3).$$

The calculation results are shown in Figs. 2-9. 20 series terms are used for calculation. Further increasing does not lead to visible changes in the results. E.g., the difference between 10 and 20 terms of series for deflections and concentration increments is less than 1%, and for rotations of normal fibres it is about 3%.

Figures 2, and 3 show the rotations of a normal fibre, and Figs. 4, 5 show the deflections of the plate. The result obtained in terms of deflections is in satisfactory agreement with the result obtained for the Kirchhoff-Love plate [18,19].

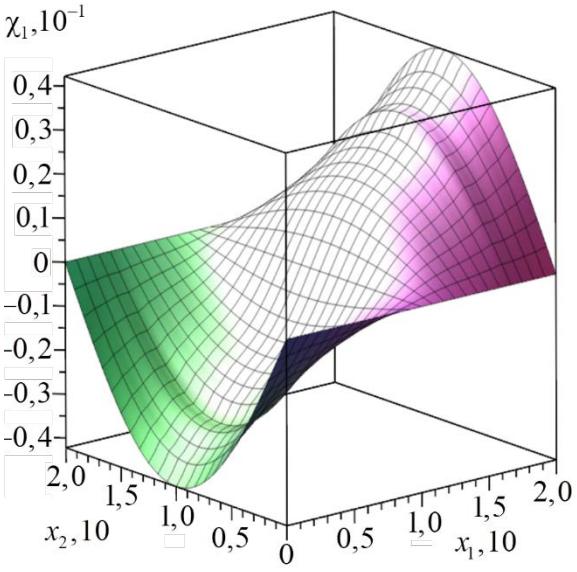

Fig. 2. The angle of rotation $\chi_1\left(x_1, x_2, 6.5 \cdot 10\right)$

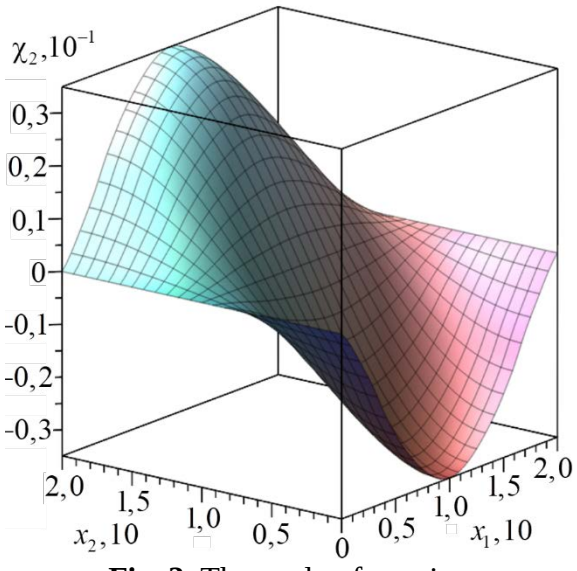

Fig. 3. The angle of rotation $\chi_2\left(x_1, x_2, 6.5 \cdot 10\right)$

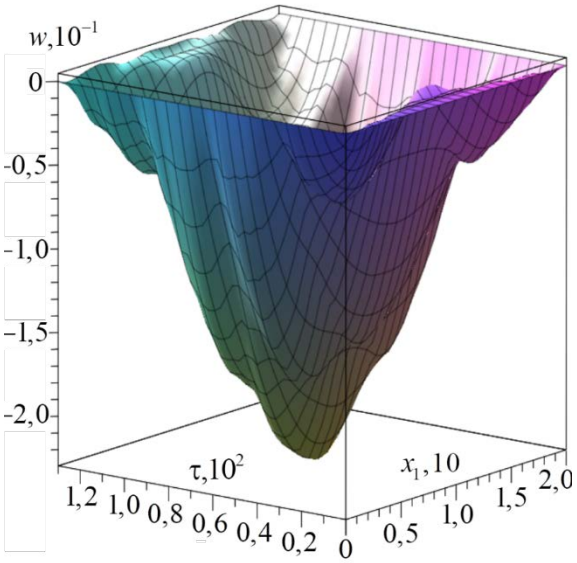

Fig. 4. The plate deflection $w\left(x_1, 0.5 l_2, \tau\right)$

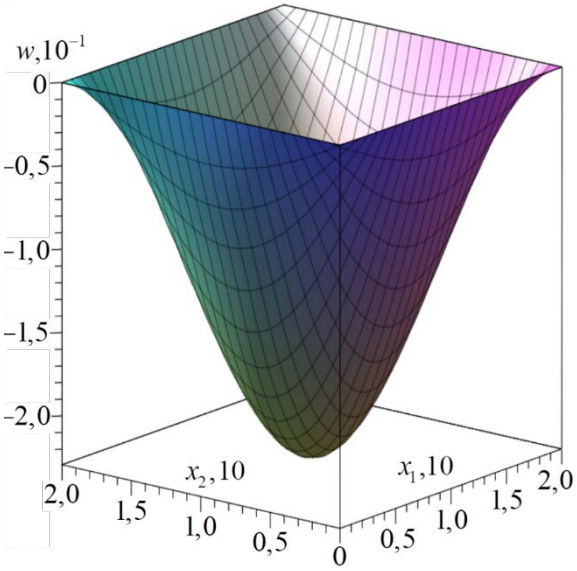

Fig. 5. The plate deflection $w\left(x_1, x_2, 6.5 \cdot 10\right)$

A comparison of the results for the elastic diffusion model and elastic model (at $\alpha_{ij}^{*(q)} = 0$) shows that the influence of diffusion on the mechanical field at given boundary conditions is negligibly small.

Figures 6, 7 show the surface density of the concentration increment of zinc (Fig. 6) and copper (Fig. 7), which are initiated by bending moments (27) applied to the edges of the plate $x_1 = 0$ and $x_1 = l_1$. These increments have small values, which is confirmed by experimental studies [23], according to which the effect of mechanical loads on the diffusion field begins to manifest itself significantly, mainly during plastic deformations. Thus, elastic deformations have little effect on the kinetics of mass transfer.

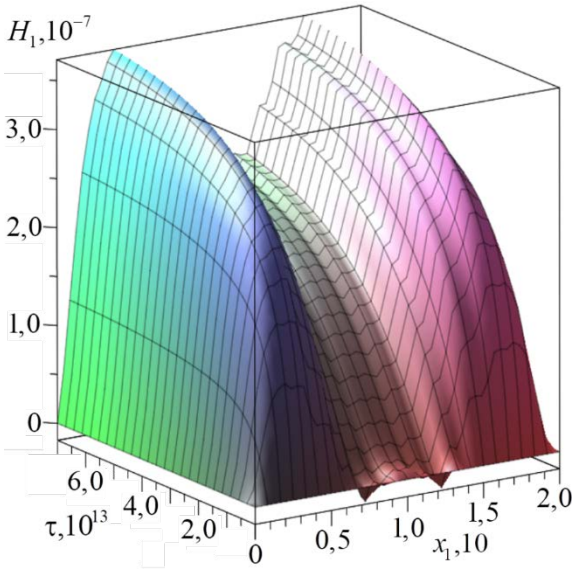

Fig. 6. Surface density of the concentration increment $H_1\left(x_1, 0.5l_2, \tau\right)$

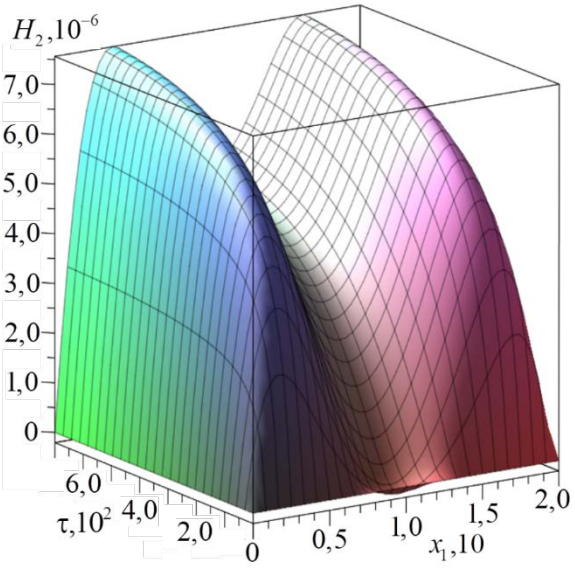

Fig. 7. Surface density of the concentration increment $H_2\left(x_1, 0.5l_2, \tau\right)$

Figures 8, and 9 show the effect of relaxation processes on the kinetics of mass transfer. It is shown that the effects associated with considering the finite velocity of propagation of diffusion fluxes are significantly manifested in a finite time interval, commensurate with the relaxation time $\tau^{(q)}$ and then decay (Fig. 9).

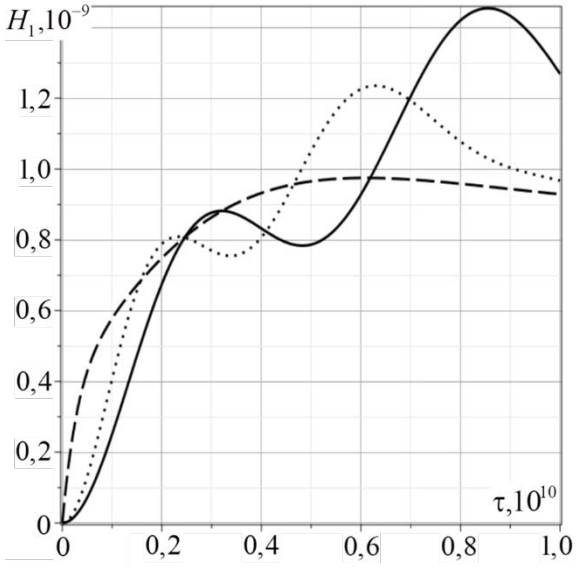

Fig. 8. Surface density of the concentration increment $H_1\left(0.1l_1, 0.5l_2, \tau\right)$, $\tau \in \left[0, 10^{10}\right]$ at different relaxation times. The solid line corresponds to $\tau^{(q)} = 200$ *sec.*, the dotted line to $\tau^{(q)} = 100$ *sec.*, the dashed line $\tau^{(q)} = 0$

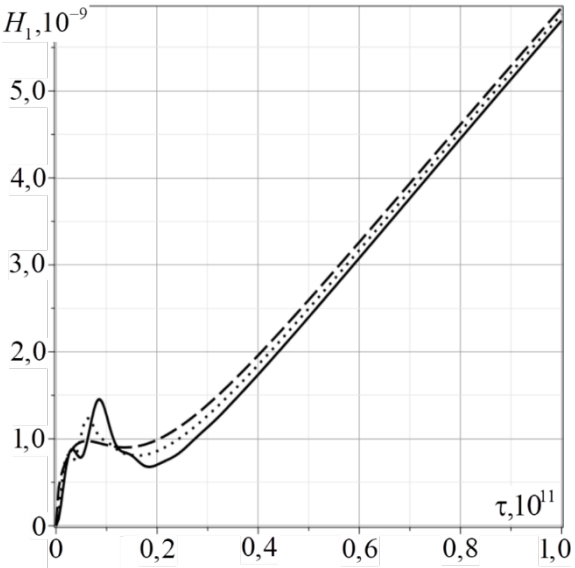

Fig. 9. Surface density of the concentration increment $H_1\left(0.1l_1, 0.5l_2, \tau\right)$, $\tau \in \left[0, 10^{11}\right]$ at different relaxation times. The solid line corresponds to $\tau^{(q)} = 200$ *sec.*, the dotted line to $\tau^{(q)} = 100$ *sec.*, the dashed line $\tau^{(q)} = 0$

6. Conclusions

Using the d'Alembert variational principle, a mathematical model of unsteady elastic diffusion transverse vibrations of a rectangular isotropic Timoshenko plate was constructed, which describes the relationship between mechanical and diffusion fields in a continuum. Furthermore, the model considers the relaxation diffusion effects, which determine the final velocity of diffusion disturbance propagation.

A method for finding Green's functions in the problem of unsteady elastic diffusion transverse vibrations of a simply supported plate is proposed. This method applies the integral Laplace transform and the expansion in the double trigonometric Fourier series. Found Green's functions made it possible to obtain an analytical solution to the problem of a simply supported plate bending under the action of moments suddenly applied to the plate's edges.

The calculation performed for a three-component plate makes it possible to modeling the nature of the mechanical and diffusion fields' interaction in a bent plate and the influence of relaxation processes on the kinetics of mass transfer.

It should be mentioned that the algorithm suggested is not a universal method of coupled initial boundary value problems solution, and in particular of mechanical diffusion problems for plates. In the work [14] it is shown that a solution in the form of Fourier series is possible only under certain boundary conditions. These include simple support. In other cases, for example, for cantilever restraint, the method of equivalent boundary conditions is used. It is tested on the example of one-dimensional problems of mechanical diffusion [14], as well as for cantilever Bernoulli-Euler beams taking diffusion into account [25]. Solution of analogous problems for plates using the method mentioned transcends the scope of this work because of its awkwardness.

Reference

1. Gorskij VS. Study of elastic aftereffect in Cu-Au alloy with an ordered lattice. *Zhurnal e'ksperimental'noj i teoreticheskoj fiziki*. 1936;6(3): 272-276. (In Russian)

2. Nachtrieb NH, Handler GS. A relaxed vacancy model for diffusion incrystalline metals. *Acta Metallurgica*. 1954;2(6): 797-802.

3. Petit J, Nachtrieb NH. Self-Diffusion in Liquid Gallium. *Journal of Chemical Physics*. 1956;24: 1027.

4. Shvets RN, Flyachok VM. The equations of mechanothermodiffusion of anisotropic shells taking account of transverse strains. *Matematicheskie metody' i fiziko-mexanicheskie polya.* 1984;20: 54-61. (In Russian)

5. Shvets RN, Flyachok VM. A variational approach to solving dynamic problems of mechanothermal diffusion of anisotropic shells. *Matematicheskaya fizika i nelinejnaya mexanika*. 1991;16: 39-43. (In Russian)

6. Aouadi M, Copetti MIM. Analytical and numerical results for a dynamic contact problem with two stops in thermoelastic diffusion theory. *ZAMM Zeitschrift fur Angewandte Mathematik und Mechanik.* 2015: 1-24. Available from: DOI 10.1002/zamm.201400285.

7. Copetti MIM, Aouadi M. A quasi-static contact problem in thermoviscoelastic diffusion theory. *Applied Numerical Mathematics.* 2016;109: 157–183.

8. Aouadi M. Miranville A. Smooth attractor for a nonlinear thermoelastic diffusion thin plate based on Gurtin-Pipkin's model. *Asymptotic Analysis.* 2015;95: 129-160.

9. Aouadi M. On thermoelastic diffusion thin plate theory. *Applied Mathematics and Mechanics (English Edition)* 2015;36(5): 619-632.

10. Aouadi M, Miranville A. Quasi-stability and global attractor in nonlinear thermoelastic diffusion plate with memory. *Evolution Equations and Control Theory*. 2015;4(3): 241-263.

11. Bhattacharya D., Kanoria M. The influence of two temperature generalized thermoelastic diffusion inside a spherical shell. *International Journal of Engineering and Technical Research (IJETR).* 2014;2(5): 151-159.
12. Knyazeva AG. *Introduction to the thermodynamics of irreversible processes. Lectures about models Model of medium with diffusion and internal surfaces and some applied problems.* Tomsk: Ivan Fedorov publishing house; 2014. (In Russian)
13. Eremeev VS. *Diffusion and stresses*. Moscow: Energoatomizdat; 1984 (In Russian)
14. Zemskov AV, Tarlakovskij DV. *Modeling of mechanodiffusion processes in multicomponent bodies with flat boundaries*. Moscow: Fizmatlit; 2021. (In Russian)
15. Igumnov LA, Tarlakovskii DV, Zemskov AV. A two-dimensional nonstationary problem of elastic diffusion for an orthotropic one-component layer. *Lobachevskii Journal of Mathematics.* 2017;38(5): 808-817.
16. Mikhailova EY, Tarlakovskii DV, Fedotenkov GV. *Obshchaya teoriya uprugikh obolochek.* Moscow: MAI; 2018. (In Russian)
17. Timoshenko S. *Strength of Materials, 3rd edition. Part 1. Elementary Theory and Problems*. Melbourne (Florida): Krieger Publishing Company; 1976.
18. Zemskov AV, Tarlakovskii DV. Unsteady elastic diffusion vibrations of an orthotropic rectangular Kirchhoff-Love plate considering a diffusion fluxes relaxation. *Lobachevskii Journal of Mathematics*. 2021;42(8): 2064-2075.
19. Zemskov AV, Tarlakovskii DV. Modelling of rectangular Kirchhoff plate oscillations under unsteady elastodiffusive perturbations. *Acta Mechanica*. 2021;232: 1785-1796.
20. Zemskov A, Tarlakovskii D, Grigorevskiy N. Modeling an unsteady elastic diffusion processes in a Timoshenko plate. In: *9th edition of the International Conference on Computational Methods for Coupled Problems in Science and Engineering (COUPLED PROBLEMS 2021)*. Available from: https://www.scipedia.com/public/Zemskov_et_al_2021a.
21. Ditkin VA, Prudnikov AP. *Operational Calculus Handbook*. Moscow: Izdatel`stvo Vy`sshaya shkola; 1965. (In Russian)
22. Babichev AP, Babushkina NA, Bratkovsky AM. *Physical quantities*: *reference manual.* Moscow: Energoatomizdat; 1991. (In Russian)
23. Nirano K, Cohen M, Averbach V, Ujiiye N. Self-Diffusion in Alpha Iron During Compressive Plastic Flow. *Transactions of the Metallurgical Society of AIME*. 1963;227: 950.
24. Zemskov AV, Tarlakovskii DV, Faykin GM. Unsteady bending of a cantilevered Euler-Bernoulli beam with diffusion. *Computational continuum mechanics.* 2021;14(1): 40-50.

THE AUTHORS

Vestyak V.A.
e-mail: v.a.vestyak@mail.ru
ORCID: 0000-0002-9434-5477

Zemskov A.V.
e-mail: azemskov1975@mail.ru
ORCID: 0000-0002-2653-6378

Tarlakovskii D.V.
e-mail: tdvhome@mail.ru
ORCID: 0000-0002-5694-9253

Materials Physics and Mechanics. 2022;50(1): 158-165
Research article
http://dx.doi.org/10.18149/MPM.5012022_12

Submitted: May 24, 2022
Approved: July 14, 2022
Accepted: August 3, 2022

Instability of plastic deformation in crystalline alloys: the Portevin-Le Chatelier effect

G.F. Sarafanov[1]✉, Yu.G. Shondin[2]

[1]Mechanical Engineering Research Institute of the Russian Academy of Sciences – Branch of Federal Research Center "Institute of Applied Physics of the RAS", Nizhny Novgorod

[2]Kozma Minin Nizhny Novgorod State Pedagogical University, Minina 1, 603000 Nizhny Novgorod, Russia

✉ gf.sarafanov@yandex.ru

Abstract. A mechanism of the plastic deformation instability of crystalline alloys is considered in an autowave model of the Portevin-Le Chatelier effect. The model is defined by a system of differential equations for deforming stress, dislocation velocity, the concentration of dissolved impurity atoms interacting with moving dislocations, and forming an "atmosphere" of atoms around them, which provides braking of dislocations. In the model, the distribution of impurity atoms at a certain dislocation rate is considered to be stationary, which is typical for elevated temperatures. In this case, it is shown that the braking force at a dislocation velocity above the critical one has a region of negative sensitivity to the deformation rate, as a result of which the Portevin-Le Chatelier effect is realized. The numerical solution of the original system under the assumptions made showed that the effect manifests itself in the form of relaxation self-oscillations of the deforming stress and the rate of plastic deformation. An expression for the oscillation period is obtained, which is inversely proportional to a given rate of plastic deformation and temperature.
Keywords: Portevin-Le Chatelier effect, alloys, serrated deformation, high temperatures, relaxation self-oscillation

Acknowledgements. *The Russian Science Foundation supported this work, project No. 22-22-00749.*

Citation: Sarafanov GF, Shondin YuG. Instability of plastic deformation in crystalline alloys: the Portevin-Le Chatelier effect. *Materials Physics and Mechanics*. 2022;50(1): 158-165. DOI: 10.18149/MPM.5012022_12.

1. Introduction

The mechanics of crystalline alloy deformation in a certain interval of elevated temperatures reveals experimentally features associated with serrated deformation [1,2]. In the literature, this phenomenon is called the Portevin-Le Chatelier effect after the French researchers, who first observed this effect in 1923.

The serrated deformation is especially clearly manifested in crystalline alloys with a BCC structure, where atoms of a solute substance are embedded in the internodes of an octahedral structure. In solid substitution solutions, the Portevin-Le Chatelier effect is somewhat weaker distinguished from the ordinary background deformation hardening [3].

The effect is the repeated occurrence of localized or spreading deformation bands, causing short-term jumps of deformation in the crystal. When deformation occurs at a

constant rate, this manifests itself macroscopically in the form of jumps of the deforming stress due to the elastic response of the machine-sample system. Sometimes a fairly smooth change in the load is observed (usually for FCC crystals), but more often the dynamics of jumps in the form of the relaxation oscillations take place.

The Portevin-Le Chatelier effect, as a manifestation of the instability of plastic flow, can be observed for a wide class of alloys under arbitrary types of loading in certain ranges of deformation rates and temperatures. In experiments on uniaxial loading, the effect is manifested at low deformation rates and elevated temperature: the loading-deformation diagram acquires a sawtooth shape (Fig. 1).

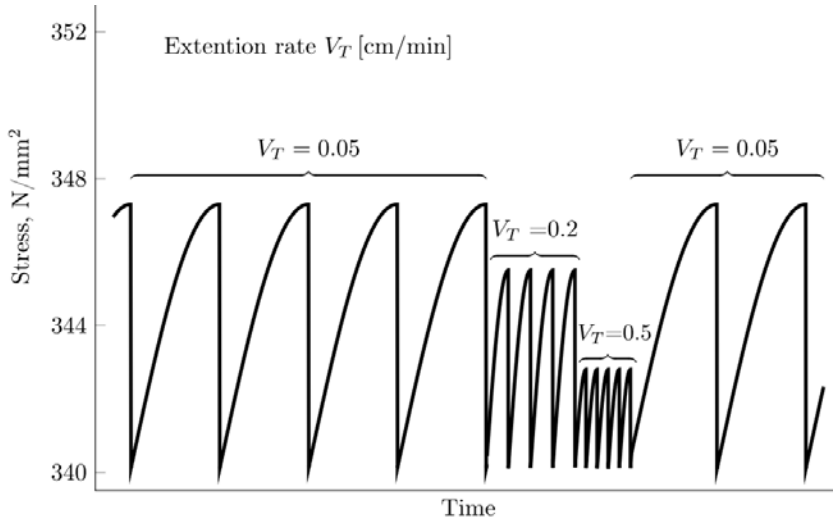

Fig. 1. Experimental dependence of the applied to the sample stresses on time at different values of the deformation rate. Tensile tests were carried out (V_T is the rod velocity) for the alloy $Al-Mg5-Mn0.8$ at the temperature $T = 395K$ [4]

Usually, there are three main types of manifestation of the Portevin-Le Chatelier effect [5,6,7]: type A – the appearance and movement of a single (solitary) Luders deformation band along the axis of the sample, which can occur repeatedly; type B – deformation bands appear and disappear in an oscillating or intermittent mode, spreading along the sample; type C – Luders bands occur randomly along the length of the sample.

The analysis of experimental data allows us to conclude that the manifestation of the Portevin-Le Chatelier effect [8-11] is directly related to the formation of "atmospheres" of dissolved atoms [1, 3] on mobile dislocations. This leads to a negative velocity sensitivity of the flow stress and, as a consequence, to the instability of plastic deformation in the form of Luders bands and the Portevin-Le Chatelier effect.

Due to the recent increase in interest in this effect [12-15], a large number of various models [10,16-18] have been proposed in the literature. However, a complete theory has not yet been built.

First of all, this is due to the phenomenological nature of many models and, accordingly, the lack of rigor in the formulation of the problem. For example, when analyzing from a mathematical point of view the serrated deformation characteristic to the Portevin-Le Chatelier effect, one should take into account the inertial terms (the effective mass of dislocations) in the original system of equations. This makes the model mathematically more correct. In this situation, it is advisable to formulate a model for mesoscopic variables: deforming stress and dislocation velocity, within the framework of the model [19], taking into account the dynamics of clouds of impurity atoms in the vicinity of moving dislocations.

In this article, an autowave model is formulated, which allows us to give a possible explanation of the Portevin -Le Chatelier effect and the formation of deformation bands (Luders bands)from a single position. Within the framework of the model under consideration, the article assumes obtaining the dependence of the deforming stress and dislocation velocity on time in the form of relaxation oscillations. Other unstable modes of plastic deformation based on the proposed model will be investigated in subsequent works.

2. The model of unstable deformation in alloys

Let us consider the behavior of an ensemble of dislocations in a slip band of width w. Let us choose the $0x$ axis in the direction of a given dislocation sliding system at some angle to the axis of the tensile test specimen. Let the distribution of dislocations in the slip band be characterized by their densities $\rho_+(\mathbf{r},t)$ and $\rho_-(\mathbf{r},t)$, and $\rho_+^0 = \rho_-^0 = \rho_0/2$ in equilibrium. Denote the velocity of dislocations by $v(\mathbf{r},t)$. Accordingly, the rate of plastic deformation in the slip strip is defined as $\dot{\varepsilon} = b\rho_0 v$ (b is the module of the Burgers dislocation vector).

In general, the movement of dislocations with an atmosphere of dissolved atoms (for example, Cottrell's atmosphere) is a complex two-dimensional problem. For this reason, we first consider the one-dimensional case to clarify the features of the nonlinear dynamics of dislocations and impurity atoms. We assume that the deviation of the dislocation density from the stationary value is insignificant, then the process of plastic deformation in the shear band in the loading regime with a given rate $\dot{\varepsilon}_0$ of plastic deformation can be described by the following system of equations

$$m^*\left(\frac{\partial v}{\partial t} + v\frac{\partial v}{\partial x}\right) = b(\tau + \tau^{int}) - F(v), \tag{1}$$

$$\frac{\partial \tau^{int}}{\partial t} = -\frac{\tau^{int}}{t_a} + \gamma_1 \frac{\partial^2 \dot{\varepsilon}}{\partial x^2}, \tag{2}$$

$$\frac{\partial \tau}{\partial t} = G^*\left[\dot{\varepsilon}_0 - \frac{b\rho_0}{L_p}\int_0^{L_p} v(x,t)dx\right], \tag{3}$$

$$\frac{\partial c}{\partial t} = D_c\frac{\partial^2 c}{\partial x^2} + \frac{D_c}{kT}\frac{\partial}{\partial x}\left(c\frac{\partial W}{\partial x}\right) + v\frac{\partial c}{\partial x}, \tag{4}$$

$$F(v) = -\int_{-\infty}^{\infty} c\frac{\partial W}{\partial x}dx, \tag{5}$$

where equation (1) is the equation of dislocation motion, m^* is its effective mass, $\tau = \tau_e - \tau_i$ is the shear deforming stress in the current sliding system, τ_e is the external stress component in the current sliding system, τ_i is the dry friction stress (the internal friction from randomly located dislocations and Hall-Petch stress), τ^{int} is the field of internal stresses from a system of dislocation charges at the grain boundaries. τ^{int} is defined by equation (2), which takes into account the fact that elastic fields induced at the boundaries (in accordance with the continuum limit of the Ballou-Bilby formula $\tau^{int} = \gamma_1\partial_{xx}^2\varepsilon$) relax due to accommodative adjustments. The parameter $\gamma_1 \approx \alpha_g G d^2$ serves as a measure of elastic grain correlation ($\alpha_g \approx 1$, d is grain size), and t_a is a characteristic time of plastic accommodation [19].

The equation (3) is the Gilman-Johnston equation for the active loading regime [19,20], which takes into account the dynamics of load changes under the condition of the stretching rate constancy of the crystal sample, G^* is the effective modulus of elasticity, L_p is the length of the plastic deformation zone.

The diffusion and drift of solute atoms in one-dimensional approximation are determined by the equation (4), where $c(t,x)$ is the number of impurity atoms per unit area, D_c is the diffusion coefficient of dissolved atoms. $F(v)$ is the nonlinear braking force of dislocation per unit length is due to the interaction of impurity atoms with dislocation, which is determined by the interaction energy

$$W = \frac{\beta}{(b^2 + x^2)^{1/2}}, \tag{6}$$

where β is the interaction constant in the dimensional effect [3]. The energy $W(x)$ in the one-dimensional approximation creates a cloud of impurity atoms in the vicinity of the dislocation similar to the Cottrell atmosphere in the two-dimensional case [1,3].

The original system (1)-(5) is quite complex and contains a large variety of possible solutions. For this reason, in this paper, we restrict ourselves by the following approximations: (i) let the time of plastic accommodation t_a in the equation (3) is significantly less than the characteristic time scale of changing the variable τ^{int}, then $\tau^{int} \propto \partial^2_{xx}\dot{\varepsilon}$ [7,19], (ii) we neglect in the diffusion equation (4) by the time derivative (i.e. we consider the stationary case, when the formation time of the atmosphere of impurity atoms is less than the time of characteristic changing of the variables τ and v). As a result, we have

$$m^*(\frac{\partial v}{\partial t} + v\frac{\partial v}{\partial x}) = b(\tau + \tau^{int}) - F(v), \tag{7}$$

$$\tau^{int} \approx t_a\gamma_1 \frac{\partial^2 \dot{\varepsilon}}{\partial x^2} = \eta \frac{\partial^2 v}{\partial x^2}, \tag{8}$$

$$\frac{\partial \tau}{\partial t} = G^*[\dot{\varepsilon}_0 - \frac{b\rho_0}{L_p}\int_0^{L_p} v(x,t)dx], \tag{9}$$

$$D_c\frac{\partial^2 c}{\partial x^2} + \frac{D_c}{kT}\frac{\partial}{\partial x}(c\frac{\partial W}{\partial x}) + v\frac{\partial c}{\partial x} = 0, \tag{10}$$

$$F(v) = -\int_{-\infty}^{\infty} c\frac{\partial W}{\partial x}dx, \tag{11}$$

where $\eta = b\rho_0 t_a \gamma_1$.

In these approximations, since equations (10) and (11) determine the behavior of the system (7)-(9), we consider first the diffusion problem and find the braking force $F(v)$. Solving (10) and (11) numerically, we obtain the following results, shown in Fig. 2.

The dependence of the braking force $F(v)$ on dislocation velocity has a characteristic nonlinear appearance with a descending part corresponding to the negative velocity sensitivity of the flow stress (Fig. 2 *a*). The function $F(v)$ has a maximum at some velocity $v = v_a$, which can be evaluated as follows.

From a physical point of view, the mobility of dislocations is determined by the diffusion of dissolved atoms, if the relaxation time x_1/v for displacement during dislocation drift over a certain distance x_1 is less than the relaxation time x_1^2/D_c for diffusion over the same distance, where $x_1 = \beta/kT$ is the effective width of the dislocation potential (6).

At the maximum point, the nature of the dislocation movement changes from diffusion to drift i.e. $x_1/v \approx x_1^2/D_c$ must be performed, or, taking into account $x_1 = \beta/kT$, we get

$$v_a \approx \frac{D_c kT}{\beta} = v_t. \tag{12}$$

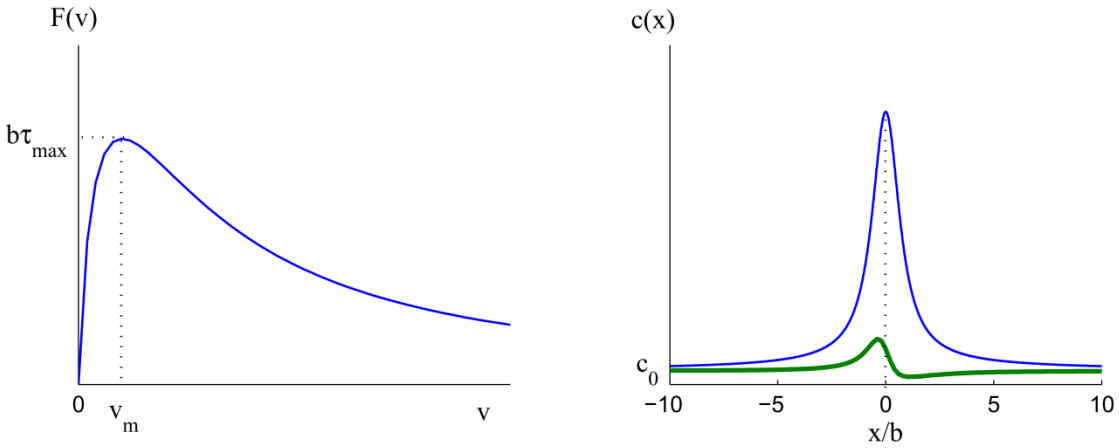

a *b*

Fig. 2. The dependence of the braking force $F(v)$ on the dislocation velocity (a) in the case of braking by the atmosphere determined by the solution of the equation (10). In the figure (b) the symmetric curve corresponds to the atmosphere $c = c_0 \exp(W(x)/kT)$ at $v = 0$ and the asymmetric curve to the atmosphere at $v >> v_a$ (T is temperature, k is the Boltzmann constant, c_0 is the impurity concentration at $x = \pm\infty$)

It was observed in [11], that with diffusion dynamics ($v < v_a$), the distribution of dissolved impurity atoms around a moving dislocation is approximately the same as with $v = 0$, i.e.

$$c \approx c_0 \exp(W/kT). \tag{13}$$

In this case, using the theorem about dissipation [3]

$$Fv = \frac{kT}{D_c}\int_{-\infty}^{\infty} \frac{v^2 (c - c_0)^2}{c}\, dx, \tag{14}$$

which follows from (11), and considering (13) for $\beta < 2bkT$ and $v = v_t$ we get

$$b\tau_{max} = \frac{4kTc_0 v}{D_c}\int_{-\infty}^{\infty} \mathrm{sh}^2 \frac{\beta}{2kT\sqrt{b^2 + x^2}}\, dx \approx 6\pi c_0 \beta / b. \tag{15}$$

Then, at low velocities, the deforming stress depends linearly on the velocity, i.e. $\tau = Bv$, where the mobility is defined as

$$B = \frac{\tau_{max}}{v_t} = \frac{6\pi c_0 \beta^2}{D_c b^2 kT}, \tag{16}$$

which, up to a numerical coefficient, coincides with the Cottrell-Jesvon[11] formula.

3. The Portevin-Le Chatelier effect

From the analysis of the solution for the braking force $F(v)$, it follows that at $v > v_a$, the braking force decreases with increasing velocity. This is due to the fact that, as the velocity increases, the dislocation gradually loses the atmosphere of dissolved atoms (Fig. 2*b*), at some critical velocity [3]

$$v_c = D_c \beta / kTb^2 \tag{17}$$

the atmosphere disappears and at $v > v_c$ the braking is caused only by the statistically distributed atoms of the solute. For this domain ($v > v_c$), we consider the mechanism proposed by Hirt and Lote in the field of solute atoms [3]. They found that the flow stress is determined in this case by the ratio

$$\tau = 2vc_0kT/D_cb. \quad (18)$$

For further analysis, we introduce the function

$$f(v) = F(v)/b + 2vc_0kT/D_cb, \quad (19)$$

which is the sum of the function $F(v)/b$ with the stress τ (18). The graph of $f(v)$ has the form of a nonlinear N-shaped figure, shown in Fig. 3.

Depending on the specified loading conditions of the sample ($\dot{\varepsilon} = \dot{\varepsilon}_0$), the straight line $v = v_0 = \dot{\varepsilon}_0/b\rho_0$ corresponding to the homogeneous stationary solution of the systems (7)-(9) can intersect the curve $\tau = f(v)$ differently.

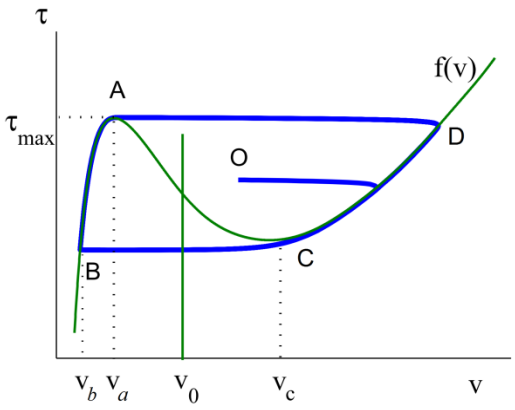

Fig. 3. Phase diagram for the variables τ and v. The straight line $v - v_0 = 0$ located on the descending branch of the function $f(v)$

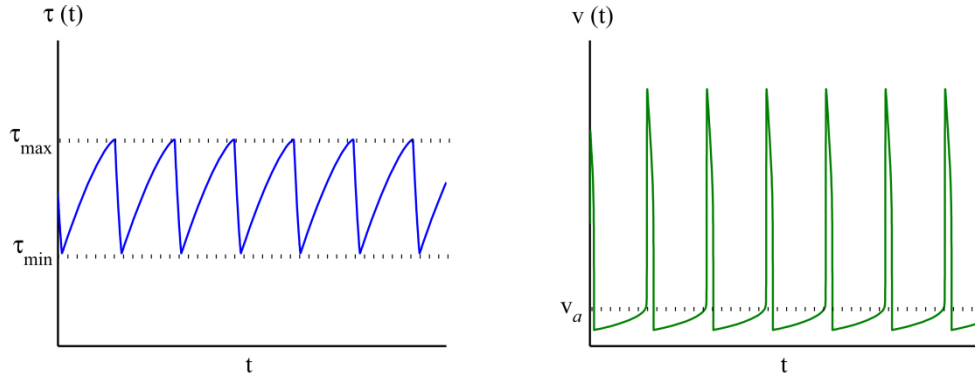

Fig. 4. The form of the obtained relaxation self-oscillations of the deforming stress $\tau(t)$ and the dislocation velocity $v(t)$ in the slip band as a function of time t

If it intersects $f(v)$ in the stable region ($f'(v)|_{v=v_0} > 0$), then the plastic deformation process develops through the propagation of the excitation fronts of the deformation rate (Luders bands) [19], if in an unstable ($f'(v)|_{v=v_0} < 0$), then, additionally with the propagation of the wavefronts, a jump-like self-oscillating mode of the unstable flow is established, which manifests itself as the Portevin-Le Chatelier effect. Let us consider this particular case.

We assume that the time of spontaneous formation of deformation bands at the lateral boundary of the sample is significantly less than the time of propagation of the bands through the cross-section. In this case, the load change does not have time to adjust to the specified regime of plastic deformation and the deformation bands fill the entire sample space almost instantly.

We consider for this case solution of the system of equations (7)-(9) with the replacement $F(v)$ by $bf(v)$. Numerical analysis of this system has shown that the flow stress $\tau(t)$ and the dislocation velocity $v(t)$ change periodically over time.

A self-oscillating process on the plane of variables (τ, v) corresponds to the phase trajectory $\tau(v)$, shown in Fig. 3. Under any initial conditions (for example, corresponding to the point O), the system goes to the limit cycle $ABCD$ regime, consisting of segments of fast and slow movements. Meanwhile, the system performs relaxation self-oscillations (Fig. 4).

4. Conclusions

It can be noted, that the system (7)-(9) has a small parameter with the time derivative of velocity, the smallness of which is due to the extreme smallness of the effective dislocation mass ($m^* \approx 10^{-15}$ g/cm). Then the analysis of the solution of the system (7)–(9) can be carried out by standard asymptotic methods, dividing the system into the subsystem of fast movements

$$m^*\left(\frac{\partial v}{\partial t} + v\frac{\partial v}{\partial x}\right) = \eta\frac{\partial^2 v}{\partial x^2} + b\tau - bf(v), \quad \tau = const, \tag{20}$$

and the subsystem of slow movements

$$\frac{\partial \tau}{\partial t} = G^*\left[\dot{\varepsilon}_0 - \frac{b\rho_0}{L_p}\int_0^{L_p} v(x,t)dx\right], \quad \tau = f(v). \tag{21}$$

The subsystem of fast movements actually coincides with that considered in [19] and is a mathematical model of the formation and propagation of Luders bands.

From equation (21), it is possible to determine the oscillation period T_0 by calculating the time of movement along the limit cycle. Meanwhile, the time of fast movements can be neglected.

The main contribution to the oscillation period is made by the segment $A-B$ of slow movements (see Fig. 4), on which the average dislocation velocity

$$\bar{v} = \frac{1}{L_p}\int_0^{L_p} v(x,t)dx \tag{22}$$

coincides approximately with the velocity of dislocations in the slip band ($\bar{v} \approx v$). Then from (21), we find

$$T_0 = \frac{1}{G^* b\rho_0}\int_{v_b}^{v_a}\frac{f'(v)}{v_0 - v}dv \approx \frac{6\pi c_0\beta^2}{G^*\dot{\varepsilon}_0 D_c b^2 kT}. \tag{23}$$

Expression for the oscillation period (23) is obtained under the assumption of an approximation of $f(v)$ on the segment $A-B$ by a linear function for $v_0 > v_a$, and using also relations (12) and (15). Thus, the oscillation period is T_0 inversely proportional to the rate of plastic deformation $\dot{\varepsilon}_0$ [4] (see Fig. 1) and decreases with increasing temperature T [6].

References

1. Cottrell AH. *Dislocations and Plastic Flow in Crystals*. Oxford Univ. Press, London; 1953.
2. Friedel J. *Dislocations*. Oxford: Pergamon; 1964.
3. Hirth JP, Lothe J. *Theory of dislocations*. New York: John Wiley; 1968.
4. Korbel A, Dybiec H. The problem of the negative strain - rate sensitivity of metals under the Portevin-Le Chatelier deformation conditions. *Acta Metall.* 1981;29(1): 89-93.
5. Maj P, Zdunek J, Mizera J, Kurzydlowski KJ. The effect of a notch on the Portevin-Le Chatelier phenomena in an Al-3Mg model alloy. *Mater. Charact.* 2014;96: 46-53.

6. Kubin LP, Estrin Y. Evolution of dislocation densities and the critical conditions for the Portevin-Le Chatelier effect. *Acta Metall. Mater.* 1990;38(5): 679-695.
7. Lebedkin MA, Brecher Y, Estrin Y, Kubin LP. Statistical behavior and regularities of localization of deformations in the Portevin-LeChatelier effect. *Phys. Rev. Lett.* 1995;74(23): 4758-4761.
8. Brechet Y, Estrin Y. On the influence of precipitation on the Portevin-Le Chatelier effect. *Acta Metal. Mater.* 1995;43(3): 955-963.
9. Halmer P. On the physics of the Portevin-Le Chatelier effect part 1: The statistics of dynamic strain ageing. *Materials Science and Engineering A.* 1996;207(2): 208-215.
10. MacCormick PG. The Portevin-Le Chatelier effect in an Al-Mg-Si alloy. *Acta Metall.* 1971;19(5): 463-471.
11. Cottrell AH. A note on the Portevin-Le Chatelier effect. *Philosophical Magazine.* 1953;44(335): 829-832.
12. Chen H, Chen Z, Wang C et al. The effect of TiB2 ceramic particles on Portevin–Le Chatelier behavior of TiB2/Al-Mg metal. *Journal of Materials Research and Technology.* 2021;14: 2302-2311.
13. Cui CY, Zhang R, Zhou YZ. Portevin-Le Chatelier effect in wrought Ni-based superalloys: experiments and mechanisms. *J. Mater. Sci. Technol.* 2020;51: 16-21.
14. GengYX, Zhang D, Zhang JS, Zhuang L. Zn/Cu regulated critical strain and serrated flow behavior in Al-Mg alloys. *Mater. Sci. Eng. A.* 2020;795: 139991-139997.
15. Wang, XG, Wang L, Huang MX. Kinematic and thermal characteristics of Luders and Portevin-Le Chatelier bands in a medium Mn transformation-induced plasticity steel. *Acta Materialia*. 2017;124: 17-29.
16. Kubin LP, Estrin Y. The Portevin Le Chatelier effect in deformation with constant stress rate. *Acta Metall.* 1985;33(3): 397-407.
17. MacCormick PG. Theory of flow localisation due to dynamic strain ageing. *Acta Metall.* 1989;36(12): 3061-3067.
18. Hahner P. Modelling of propagative plastic instabilities. *Scripta Metall.* 1993;29: 1171-1176.
19. Sarafanov GF, Shondin YuG. Deformation instability in crystalline alloys: Luders bands. *Materials Physics and Mechanics*. 2021;47(3): 431-437.
20. Johnston WG, Gilman J. Dislocation velocities, dislocation densities and plastic flow in lithium fluoride crystals. *J. Appl Phys.* 1959;30(2): 129-143.

THE AUTHORS

Sarafanov G.F.
e-mail: gf.sarafanov@yandex.ru
ORCID: -

Shondin Yu.G.
e-mail: yu.shondin@yandex.ru
ORCID: 0000-0002-1246-8503

Materials Physics and Mechanics. 2022;50(1): 166-183
Research article
http://dx.doi.org/10.18149/MPM.5012022_13

Submitted: April 30, 2022
Approved: July 12, 2022
Accepted: August 12, 2022

The effect of phase lags and fractional parameters on waves across an elastic and thermoelastic medium

Puneet Bansal[1], Vandana Gupta[2]✉

[1]University Institute of Engineering and Technology, Kurukshetra University Kurukshetra, Haryana, India

[2]Department of Mathematics, IGN College, Ladwa, Haryana, India

✉ vandana223394@gmail.com

Abstract. In this paper, three-phase lag heat transfer model Roychoudhari [1] is employed to study the problem of reflection and transmission of thermoelastic waves of an obliquely incident plane P or SV wave at the interface between an elastic solid and a fractional order thermoelastic solid subjected to continues boundary conditions. The amplitude reflection and amplitude transmission coefficients are derived by using the potential method. It was found that the energy ratios and amplitude ratios of waves depend upon the incident angle and the frequency of the incident wave. The problem is illustrated by computing numerical values of amplitude ratios and energy ratios for the copper material. Graphical results for two-phase lag are compared with the corresponding results for three-phase lag theory of thermoelasticity. The effect of fractional order on the energy ratios is also discussed graphically. The present derivation is used to study the energy conservation among the incident, reflected, and transmitted waves. It is verified that in this process there is no energy dissipation at the interface.

Keywords: amplitude; fractional, reflection, transmission, three-phase lag, elastic waves, energy ratio

Acknowledgements*. No external funding was received for this study.*

Citation: Bansal P, Gupta V. The effect of phase lags and fractional parameters on waves across an elastic and thermoelastic medium. *Materials Physics and Mechanics*. 2022;50(1): 166-183. DOI: 10.18149/MPM.5012022_13.

1. Introduction

The field of fractional calculus studies fractional derivatives, fractional integrals, and their properties. Fractional calculus is the mathematical study that takes the traditional definitions of integral and derivative operators of calculus to the fractional integral and derivatives. Although there was not any geometrical and physical representation of fractional order integral and derivatives for more than 300 years. Igor Podlubny showed the geometric interpretation and physical representation as "Shadows on the walls" and "Shadows of the past" respectively.

Fractional calculus is used in many desirable models to review the physical processes considerably among with heat conduction, diffusion, viscoelasticity, solid mechanics, electrical networks, fluid flow and electromagnetic theory, etc. which involves integrals

and derivatives of fractional order. In many cases the use of fractional order theory is very useful in situations where the heat conduction law depending upon classical theory fails.

Abel [2] was the first to use fractional calculus for the tautochrone problem. It can be stated that the theory of fractional derivatives and integrals was established after the 1950's. Caputo and Mainardi [3-4] and Caputo [5] experimentally verified the use of fractional derivatives for viscoelastic materials and proved the connection between fractional derivatives and linear viscoelasticity. Miller and Ross [6] established a collection of various developments and applications in the field of fractional calculus.

The path of transformation in the heat equation law of classical theory to the parabolic type heat conduction equation was opened by Lord and Shulman [7]. A further modification was made by Green and Naghdi [8-10] by the introduction of three distinct theories. Chandrasekharaiah [11] introduced the dual phase lag theory of thermoelasticity. This theory supported the theory proposed by Tzou [12-13] where the heat conduction equation becomes hyperbolic. In this model heat conduction equation involves two-phase lags to study the microstructural effects that occur during the heat transfer. The theory given by Roychoudhuri [1] was the modification of the previous generalized theories of thermoelasticity and it involves a Fourier law having three phase lags.

Achenbach [14] described the different aspects of elastodynamics and wave propagation phenomenon for thermoelastic solid medium. Borcherdt [15] studied the reflection and refraction of waves in elastic and anelastic solid mediums. Sherief and Saleh [16] using the Laplace Transform technique studied a half-space problem in a generalized thermoelastic diffusion medium. Kumar and Gupta [17-18] in their work used the methodology of fractional calculus and dual-phase-lags. Wang, Liu, Wang & Zhou [19] derived the basic equations for anisotropic temperature-dependent generalized thermoelastic medium with fractional order parameters.

Raslan [20] using the Laplace transform technique solved a one-dimensional problem having fractional derivative and computed the results for temperature change, displacement, and stress distribution. Abbas [21] studied the coupling of plasma, elastic and thermal waves using the eigenvalue approach. He also depicted the difference between the classical, Lord-Shulman and the dual phase lag theory. Lata [22] studied the thermomechanical interactions in a thick circular plate under the two temperature theory of thermoelasticity with fractional order derivative. Kumar, Vashisth, and Ghangas [23] investigated the effect of phase lag, two-temperature, and void on waves in the anisotropic thermoelastic medium.

Atwa and Ibrahim [24] studied the effect of two temperatures and diffusion and also depicted the effect of three-phase lag and Green Nagdhi type III theories of thermoelasticity. Nonlocal theory having fractional derivative heat transfer thermoelastic medium with voids was studied by Bachher and Sarkar [25].

Waves in a thermoelastic medium with dual-phase-lag and voids were studied by Mondal, Sarkar, and Sarkar [26]. Said [27] used fractional order parameters to study the plane wave propagation and computed the fundamental solution.

Abouelregal [28] used the theory of fractional calculus and derived a new model of three-phase-lag thermoelastic heat conduction of higher-order time-fractional derivatives that includes high-order time-fractional derivative approximations of three-phase-lags in the heat flux vector, the temperature gradient and in the thermal displacement gradient.

Abouelregal and Ahmad [29] constructed a fractional order thermoelastic model with phase lags. Saidi and Abouelregal [30] studied the thermoelastic model for an infinitely long cylinder with two phase-lags having higher-order time-derivatives.

Kulkarni and Mittal [31] applied the two-temperature theory to a homogeneous isotropic generalized dual phase lag fractional order thermoelastic medium. He obtained

thermal displacement, stresses, conductive temperature, and thermomechanical temperature using the State space approach.

Abouelregal et al. [32] established a generalized thermoelastic model by considering two-fractional thermal conduction and multi-phase-lags. They also extracted several models of generalized thermoelasticity including fractional derivatives from the considered model.

Abouelregal et al. [33] presented a new fractional model of non-Fourier heat conduction that includes phase delays and two fractional orders using the Laplace transform approach. Sharma [34] studied the effect of phase-lags and voids on thermoelastic interactions in a nonlocal elastic hollow cylinder.

The present paper is concerned with the reflection and transmission phenomena of the P and SV waves striking at the plane interface between an elastic solid half-space and a thermoelastic half-space with fractional order derivative. The three-phase lag thermoelastic model [1] is used to discuss the effects of the incident angle and the frequency of the incident wave on the reflection and transmission coefficients in the forms of amplitude ratios and energy ratios, respectively. Finally, comparisons have been made to study the effect of the fractional order parameters, two-phase lag, and three-phase lag theory of thermoelasticity. It is verified that there is no energy dissipation at the interface.

2. Governing Equations

Following Kumar and Gupta [17], the equations of motion, Stress-Strain and temperature relation, and Strain displacement relation are:

$$\left(\lambda+2\mu\right)\nabla\left(\nabla.\mathrm{u}\right)-\mu\left(\nabla\times\nabla\times\mathrm{u}\right)-\beta_1\nabla T=\rho\ddot{\mathrm{u}}, \tag{1}$$

$$\sigma_{ij}=2\mu e_{ij}+\left(\lambda e_{kk}-\gamma T\right)\delta_{ij}, \tag{2}$$

$$e_{ij}=\frac{1}{2}\left(u_{i,j}+u_{j,i}\right). \tag{3}$$

The heat conduction equation for three-phase lag thermoelastic medium with time-fractional derivative is

$$\left[K^*\left(1+\frac{\left(\tau_\nu\right)^\alpha}{\alpha!}\frac{\partial^\alpha}{\partial t^\alpha}\right)+K\frac{\partial}{\partial t}\left(1+\frac{\left(\tau_T\right)^\alpha}{\alpha!}\frac{\partial^\alpha}{\partial t^\alpha}\right)\right]\nabla^2T=\left(1+\frac{\left(\tau_q\right)^\alpha}{\alpha!}\frac{\partial^\alpha}{\partial t^\alpha}+\frac{\left(\tau_q\right)^{2\alpha}}{\left(2\alpha\right)!}\frac{\partial^{2\alpha}}{\partial t^{2\alpha}}\right)\left(\rho C_E\ddot{T}+\gamma T_0\ddot{e}_{kk}\right), \tag{4}$$

where λ,μ are the Lame's constants, ρ is the density assumed to be independent of time, u is displacement vector, α denotes the fractional order parameter, K is the coefficient of thermal conductivity, C_E is the specific heat at constant strain, $T=\Theta-T_0$ is small temperature increment, Θ is the absolute temperature of the medium; T_0 is the reference temperature of the body chosen such that $\left|\left(T/T_0\right)\right|<<1$, σ_{ij},e_{ij} are the components of the stress and strain respectively, e_{kk} is the dilatation, $\beta_1=\left(3\lambda+2\mu\right)\nu_t,\nu_t$ is the coefficient of thermal linear expansion, τ_q,τ_T and τ_ν respectively, are the phase lag of heat flux, phase lag of temperature gradient and phase lag of thermal displacement gradient.

3. Fractional-order derivative and integral

Following Caputo [35] and Miller and Ross [6]:

$$\frac{d^{\alpha}}{dt^{\alpha}} f(t) = I^{1-\alpha} f'(t),$$

where fractional order $\alpha \in (0,1]$ (5)

$$I^{\alpha} f(t) = \int_0^t \frac{(t-\tau)^{\alpha-1}}{\Gamma(\alpha)} f(\tau)\, d\tau, \quad \alpha > 0. \tag{6}$$

Here $f(t)$ is an absolutely continuous function.

4. Definition and formulation of the problem

We consider a plane interface along the x_1-axis between an isotropic elastic solid half-space $x_3 < 0$ (Medium I) and a thermoelastic solid half-space $x_3 > 0$ (Medium II) with x_3-axis points vertically downwards into the thermoelastic solid medium. The reflection and transmission problem investigated here is in the two-dimensional $x_1 - x_3$ plane. The geometry of the paper is shown in Fig. 1.

Let a plane harmonic wave (P or SV) traveling through the isotropic elastic solid half-space be incident at the interface $x_3 = 0$. The incident wave will give rise to:

(i) Two homogeneous waves (P and SV), reflected in isotropic elastic solid half-space.
(ii) Three inhomogeneous waves (P, T and SV), transmitted in isotropic thermoelastic solid half-space.

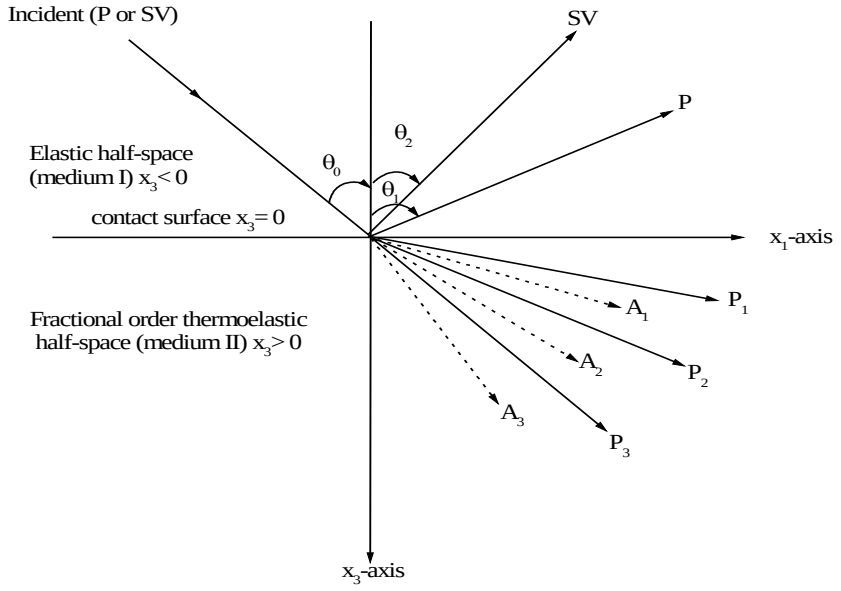

Fig. 1. Geometry of the problem

The displacement vector $\mathbf{u}^{e}$ of elastic solid half-space and $\mathbf{u}$ of thermoelastic half-space are

$$\mathbf{u}^{e} = (u_1^{e}, 0, u_3^{e}), \mathbf{u} = (u_1, 0, u_3). \tag{7}$$

The dimensionless quantities are introduced as

$$x_i' = C_0\eta x_i, u_i' = C_0\eta u_i, u_i'^e = C_0\eta u_i^{\ e}, t' = C_0^{\ 2}\eta t, T' = \frac{T}{T_0}, \sigma_{ij}' = \frac{\sigma_{ij}}{\rho C_0^2}, \sigma_{ij}'^e = \frac{\sigma_{ij}^{\ e}}{\rho C_0^2}, P^{*e'} = \frac{P^{*e}}{C_0},$$

$$P_{ij}^{*'} = \frac{P_{ij}^*}{C_0}, \tau_q' = C_0^{\ 2}\eta\tau_q, \tau_T' = C_0^{\ 2}\eta\tau_T, \tau_\nu' = C_0^{\ 2}\eta\tau_\nu, C_T = \frac{1}{C_0}\sqrt{\frac{K^*}{\rho C_E}}, C_K = \sqrt{\frac{\eta K}{\rho C_E}}, \tag{8}$$

$$C_0^{\ 2} = \frac{\lambda + 2\mu}{\rho}, i = 1,3.$$

Using Helmholtz representation, the non-dimensional displacement components u_1^e, u_3^e, u_1, u_3 are related by the potential functions as

$$u_1 = \left(\partial\phi / \partial x_1\right) - \left(\partial\psi / \partial x_3\right), u_3 = \left(\partial\phi / \partial x_3\right) + \left(\partial\psi / \partial x_1\right),$$

$$u_1^e = \left(\partial\phi^e / \partial x_1\right) - \left(\partial\psi^e / \partial x_3\right), u_3^e = \left(\partial\phi^e / \partial x_3\right) + \left(\partial\psi^e / \partial x_1\right). \tag{9}$$

Assuming plane harmonic waves in x_1x_3 – plane as

$$\left\{\phi, \psi, T, \phi^e, \psi^e\right\}\left(x_1, x_3, t\right) = \left\{\bar{\phi}, \bar{\psi}, \bar{T}, \bar{\phi}^e, \bar{\psi}^e\right\} e^{-i\omega t}, \tag{10}$$

Where ω is the angular frequency.

Taking $\bar{\phi} = \bar{\phi}_1 + \bar{\phi}_2$, these potentials $\bar{\phi}_1, \bar{\phi}_2$ satisfy the wave equations

$$\left.\begin{aligned}\left[\nabla^2 + \left(\omega^2 / V_1^2\right)\right]\bar{\phi}_1 = 0\\ \left[\nabla^2 + \left(\omega^2 / V_2^{\ 2}\right)\right]\bar{\phi}_2 = 0\end{aligned}\right\} \tag{11}$$

Here V_1, V_2 are the velocities P and T wave in medium 2 and are characteristic roots of the equation

$$FV^4 - E\omega^2V^2 + D\omega^4 = 0, \tag{12}$$

where

$$F = \beta^2\omega^4 C, E = \beta^2\omega^2 C + \beta^2\omega^2\left(C_T^2 A - i\omega B C_K^2\right) + b \in C\omega^2, D = C_T^2 A - i\omega B C_K^2,$$

$$A = \left(1 + \left(-i\omega\right)^\alpha \frac{\left(\tau_\nu\right)^\alpha}{\alpha!}\right), B = \left(1 + \left(-i\omega\right)^\alpha \frac{\left(\tau_T\right)^\alpha}{\alpha!}\right), C = \left(1 + \left(-i\omega\right)^\alpha \frac{\left(\tau_q\right)^\alpha}{\alpha!} + \left(-i\omega\right)^{2\alpha} \frac{\left(\tau_q\right)^{2\alpha}}{2\alpha!}\right),$$

$$\in = \frac{\gamma}{\rho C_E}, \beta^2 = \frac{\lambda + 2\mu}{\mu}, b = \frac{\gamma T_0}{\mu}.$$

The potential functions $\bar{\psi}, \bar{\phi}^e, \bar{\psi}^e$ satisfy the equations

$$\left[\nabla^2 + \left(\omega^2 / V_3^{\ 2}\right)\right]\bar{\psi} = 0, \tag{13}$$

$$\left(\nabla^2 + \omega^2 / v_p^2\right)\bar{\phi}^e = 0, \tag{14}$$

$$\left(\nabla^2 + \omega^2 / v_s^2\right)\bar{\psi}^e = 0, \tag{15}$$

where $V_3 = \frac{1}{\beta}$ is the velocity of SV wave in medium 2.

$v_p^e = \sqrt{\frac{\left(\lambda^e + 2\mu^e\right)}{\rho^e}}$ and $v_s^e = \sqrt{\frac{\mu^e}{\rho^e}}$ are the velocities of P and SV wave in medium 1.

The potential functions in elastic solid half-space(medium 1) are taken as

$$\phi^e = A_0^e \exp\left[i\omega\left\{\left(\left(x_1\sin\theta_0 + x_3\cos\theta_0\right)/v_p\right) - t\right\}\right] + A_1^e \exp\left[i\omega\left\{\left(\left(x_1\sin\theta_1 - x_3\cos\theta_1\right)/v_p\right) - t\right\}\right], \tag{16}$$

$$\psi^e = B_0^e \exp\left[i\omega\left\{\left(\left(x_1\sin\theta_0 + x_3\cos\theta_0\right)/v_s\right) - t\right\}\right] + B_1^e \exp\left[i\omega\left\{\left(\left(x_1\sin\theta_2 - x_3\cos\theta_2\right)/v_s\right) - t\right\}\right]. \tag{17}$$

where the coefficients $A_0^e\left(B_0^e\right), A_1^e$ and B_1^e are respectively the amplitudes of incident P or incident SV, reflected P, and reflected SV waves.

Following (Borcherdt [15]), in thermoelastic solid half-space (medium 2), the wave field for the transmitted wave is

$$\left\{\phi, T\right\} = \sum_{i=1}^{2}\left\{1, n_i\right\} B_i exp\left(\mathrm{A}_i.\mathrm{r}\right) exp\left\{i\left(\mathrm{P}_i.\mathrm{r} - \omega t\right)\right\}, \left(\ i = 1,2\right) \tag{18}$$

$$\psi = B_3 exp\left(\mathrm{A}_3.\mathrm{r}\right) exp\left\{i\left(\mathrm{P}_3.\mathrm{r} - \omega t\right)\right\}. \tag{19}$$

Here n_i denotes the constants specified in Appendix 1.

The coefficients B_1, B_2, and B_3 are the transmitted P, T, and SV wave amplitudes.

The propagation and attenuation vectors are

$$\mathrm{P}_i = \xi_R \hat{x}_1 + dV_{iR}\hat{x}_3, \mathrm{A}_i = -\xi_I \hat{x}_1 - dV_{iI}\hat{x}_3,, \left(\ i = 1,2,3\right), \tag{20}$$

$$dV_i = dV_{iR} + i dV_{iI} = p.v.\left(\left(\omega^2/V_i^2\right) - \xi^2\right), \left(\ i = 1,2,3\right), \tag{21}$$

$$\xi = \xi_R + i\xi_I .$$

Here p.v. denotes the principal value.

$$\xi = \left|\mathrm{P}_i\right|\sin\theta_i' - i\left|\mathrm{A}_i\right|\sin\left(\theta_i' - \gamma_i\right), \tag{22}$$

where

$\gamma_i, i = 1,2,3$ are the angle between propagation and attenuation vector, $\theta_i', i = 1,2,3$ are the angle of refraction.

5. Boundary conditions

At interface x_3 =0,

1. **Mechanical conditions**

Continuity of stress and displacement components

$$\sigma_{33}{}^e = \sigma_{33}, \tag{23}$$

$$\sigma_{31}{}^e = \sigma_{31}, \tag{24}$$

$$u_1{}^e = u_1, \tag{25}$$

$$u_3{}^e = u_3, \tag{26}$$

2. **Thermal condition**

$$\frac{\partial T}{\partial x_3} + hT = 0. \tag{27}$$

where h denotes the coefficient of heat transfer, $h \to 0$ and $h \to \infty$ are respectively for the insulated, and isothermal boundary.

where in equations (23) and (24):

$$\sigma_{31}=\mu\left(u_{1,3}+u_{3,1}\right)/\rho C_0^2,\qquad \sigma_{33}=\left[\left(\lambda+2\mu\right)u_{3,3}+\lambda u_{1,1}-\rho c_1^2 T-\rho c_1^2 C\right]/\rho C_0^2,$$
$$\sigma_{31}^e=\mu\left(u_{1,3}^e+u_{3,1}^e\right)/\rho C_0^2,\qquad \sigma_{33}^e=\left[\left(\lambda+2\mu\right)u_{33}^e+\lambda u_{1,1}^e\right]/\rho C_0^2. \tag{28}$$

Using the (16)-(19) in the above equations, we have

$$\sum_{j=1}^{5} d_{ij} Z_j = g_i, \tag{29}$$

and Snell's law

$$\xi_R=\omega\sin\theta_0/V_0=\omega\sin\theta_1/v_p=\omega\sin\theta_2/v_s, \tag{30}$$

Here Z_1, Z_2 denotes the amplitude ratios of reflected P and reflected SV wave and Z_3, Z_4, Z_5 denotes the amplitude ratios of transmitted P, T and SV waves to that of the incident wave.

Also $d_{ij}, (i, j = 1,2,3,4,5)$ are specified in Appendix 2.

$$\begin{aligned} & V_0 = v_p^e, \text{when P-wave is incident} \\ \text{and} \quad & V_0 = v_s^e, \text{when SV-wave is incident} \\ & \xi_I = 0 \end{aligned} \tag{31}$$

The coefficients g_i in the equation (29) are

$$g_i=\begin{cases}(-1)^i d_{i1}, & \textit{for incident P wave}\\ (-1)^{i+1} d_{i2}, & \textit{for incident SV wave}\end{cases};\ i=1,2,3,4$$
$$g_i=0;\ i=5.$$

6. Energy partition

It is physically important to consider the energy partition of the incident wave among the various reflected and refracted waves at the plane interface. The rate of energy transmission per unit area is given by Achenbach [14]:

$$\left.\begin{aligned}\left\langle P^{*e}\right\rangle &= \mathrm{Re}\left\langle\sigma\right\rangle_{13}^{e}.\mathrm{Re}\left\langle\dot{u}_1^e\right\rangle+\mathrm{Re}\left\langle\sigma\right\rangle_{33}^{e}.\mathrm{Re}\left\langle\dot{u}_3^e\right\rangle\left(\textit{elastic medium}\right)\\ \left\langle P_{ij}^{*}\right\rangle &= \mathrm{Re}\left\langle\sigma\right\rangle_{13}^{(i)}.\mathrm{Re}\left\langle\dot{u}_1^{(j)}\right\rangle+\mathrm{Re}\left\langle\sigma\right\rangle_{33}^{(i)}.\mathrm{Re}\left\langle\dot{u}_3^{(j)}\right\rangle\left(\textit{thermoelastic medium}\right)\end{aligned}\right\} \tag{32}$$

Using equations (16)-(19) in equation (32) with the aid of (9) and (28), we have the energy ratio of reflected P and SV waves as

$$E_i=-\left\langle P_i^{*e}\right\rangle/\left\langle P_0^{*e}\right\rangle;\qquad i,j=1,2, \tag{33}$$

and

$$E_{ij}=\left\langle P_{ij}^{*}\right\rangle/\left\langle P_0^{*e}\right\rangle;\qquad i,j=1,2,3, \tag{34}$$

are the energy ratios of transmitted P, T, and SV waves respectively.

The non-diagonal entries

$$E_{RR}=\sum_{i=1}^{3}\left(\sum_{j=1}^{3}E_{ij}-E_{ii}\right). \tag{35}$$

denotes the sharing of interaction energy in all transmitted waves.

Also

$$\left\langle P_1^{*e}\right\rangle=\frac{1}{2}\frac{\omega^4\rho^e c_0^2}{\alpha}\left|A_1^e\right|^2\mathrm{Re}\left(\cos\theta_1\right),\left\langle P_2^{*e}\right\rangle=\frac{1}{2}\frac{\omega^4\rho^e c_0^2}{\beta}\left|B_1^e\right|^2\mathrm{Re}\left(\cos\theta_2\right),$$

$$\left\langle P_0^{*e}\right\rangle = \begin{cases} \left\langle P_0^{*e}\right\rangle = -\dfrac{1}{2}\dfrac{\omega^4\rho^e c_0^2}{\alpha}\left|\mathrm{A}_0^e\right|\cos\theta_0, (\text{for incident P}-\text{wave}) \\ \left\langle P_0^{*e}\right\rangle = -\dfrac{1}{2}\dfrac{\omega^4\rho^e c_0^2}{\beta}\left|B_0^e\right|\cos\theta_0, (\textit{ for } \text{incident SV}-\text{wave}) \end{cases},$$

$$\left\langle P_{ij}^*\right\rangle = -\frac{\omega^4}{2}\mathrm{Re}\left[\left\{2\mu\frac{dV_i}{\omega}\frac{\xi_R}{\omega}\frac{\overline{\xi}_R}{\omega}+\lambda\left(\frac{\xi_R}{\omega}\right)^2\left(\frac{d\overline{V}_j}{\omega}\right)+\rho c_0^2\left(\frac{dV_i}{\omega}\right)^2\left(\frac{d\overline{V}_j}{\omega}\right)+\frac{\gamma n_i T_0}{\omega^2}\left(\frac{d\overline{V}_j}{\omega}\right)\right\}B_i\overline{B}_j\right], i, j = 1,2,3$$

$$\left\langle P_{i3}^*\right\rangle = -\frac{\omega^4}{2}\mathrm{Re}\left[\left\{-2\mu\frac{dV_i}{\omega}\frac{d\overline{V}_3}{\omega}\frac{\xi_R}{\omega}+\lambda\left(\frac{\xi_R}{\omega}\right)^2\left(\frac{\overline{\xi}_R}{\omega}\right)+\rho c_0^2\left(\frac{dV_i}{\omega}\right)^2\left(\frac{\overline{\xi}_R}{\omega}\right)+\frac{\gamma n_i T_0}{\omega^2}\left(\frac{\overline{\xi}_R}{\omega}\right)\right\}B_i\overline{B}_3\right],$$

$$\left\langle P_{3j}^*\right\rangle = -\frac{\omega^4}{2}\mathrm{Re}\left[\left\{\mu\left(\left(\frac{\xi_R}{\omega}\right)^2\frac{\overline{\xi}_R}{\omega}-\frac{\overline{\xi}_R}{\omega}\left(\frac{dV_3}{\omega}\right)^2\right)-\lambda\frac{\xi_R}{\omega}\frac{dV_3}{\omega}\frac{d\overline{V}_j}{\omega}+\rho c_0^2\frac{\xi_R}{\omega}\frac{dV_3}{\omega}\frac{d\overline{V}_j}{\omega}\right\}\overline{B}_j B_3\right],$$

$$\left\langle P_{33}^*\right\rangle = -\frac{\omega^4}{2}\mathrm{Re}\left[\left\{\mu\left(\left(\frac{dV_3}{\omega}\right)^2-\left(\frac{\xi_R}{\omega}\right)^2\right)\frac{d\overline{V}_3}{\omega}-2\mu\frac{\xi_R}{\omega}\frac{\overline{\xi}_R}{\omega}\frac{dV_3}{\omega}\right\}B_3\overline{B}_3\right], \text{ i , j =1, 2.} \quad (36)$$

The law of conservation of energy is also verified i.e.

$$E_1 + E_2 + E_{11} + E_{22} + E_{33} + E_{RR} = 1. \quad (37)$$

7. Numerical results and discussion

Using the physical data for copper material in a thermoelastic medium (medium 2) are taken from Sherief and Saleh [16] and granite in an elastic medium (medium 1) is taken from Bullen [36].

For thermoelastic medium

$\lambda = 7.76\times10^{10}\, Kgm^{-1}s^{-2}$, $\mu = 3.86\times10^{10}\, Kgm^{-1}s^{-2}$, $T_0 = 0.293\times10^3 K$,

$C_E = .3831\times10^3\, JKg^{-1}K^{-1}$, $\alpha_t = 1.78\times10^{-5}K^{-1}$

$h = 0$, $\rho = 8.954\times10^3\, Kgm^{-3}$, $K = 0.383\times10^3 Wm^{-1}K^{-1}$.

$C_T = 0$ for two and three phase lag model and $C_K = 1$.

For elastic medium

$\rho^e = 2.65\times10^3\, Kgm^{-3}$, $\alpha^e = 5.27\times10^3\, ms^{-1}$, $\beta^e = 3.17\times10^3\, ms^{-1}$

and frequency $\omega = 2\times\pi\times100\ Hz$ is kept fixed.

In Figures 2-7 and Figures 8-13, the energy ratios $E_i, i = 1,2$ and the energy matrix defined in the previous section are calculated and plotted with respect to the angle of incidence $\theta_0 = 0°$ to $\theta_0 = 90°$ for two and three-phase lag models and fractional orders α =0.5 and α =1.5 respectively.

In all figures, the slant and horizontal lines correspond to fractional orders α =0.5 and α =1.5 respectively for three-phase lag model. The horizontal squares and slant squares correspond to fractional orders α =0.5 and α =1.5 respectively for two-phase lag model. The graphs are plotted in 3D to clearly depict the effect of fractional orders and phase lag models.

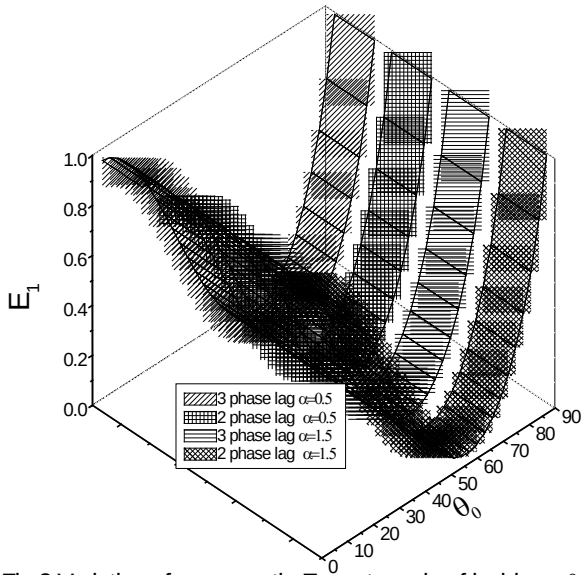

Fig. 2. Variation of energy ratio E_1 w.r.t. angle of incidence θ_0 for P wave

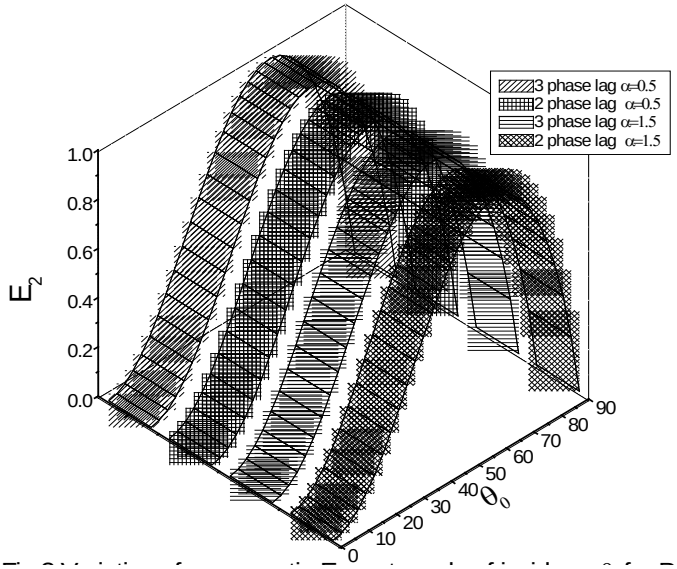

Fig. 3. Variation of energy ratio E_2 w.r.t. angle of incidence θ_0 for P wave

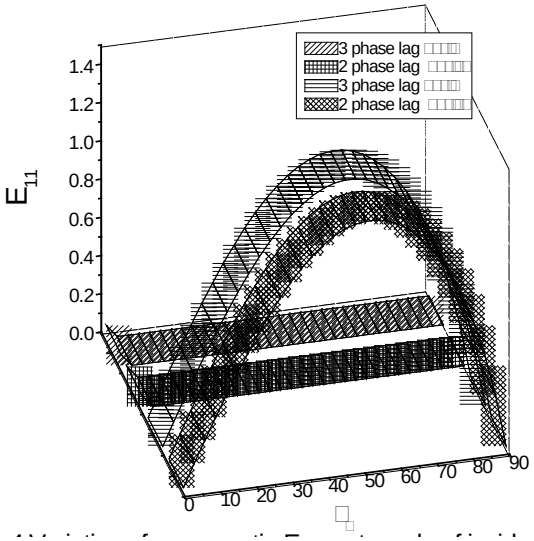

Fig. 4. Variation of energy ratio E_{11} w.r.t. angle of incidence θ_0 for P wave

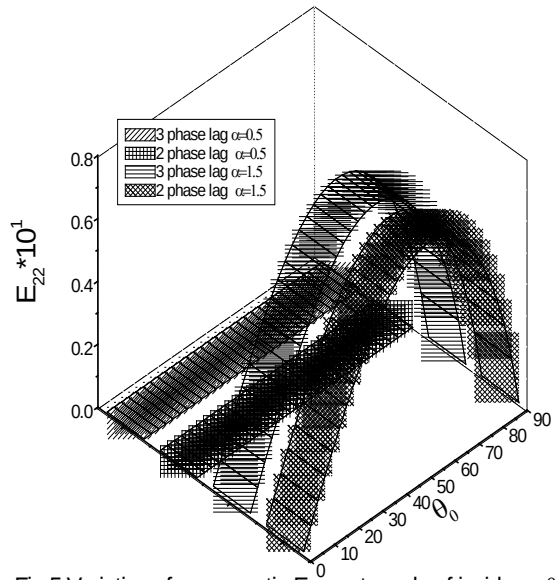

Fig. 5. Variation of energy ratio E_{22} w.r.t. angle of incidence θ_0 for P wave

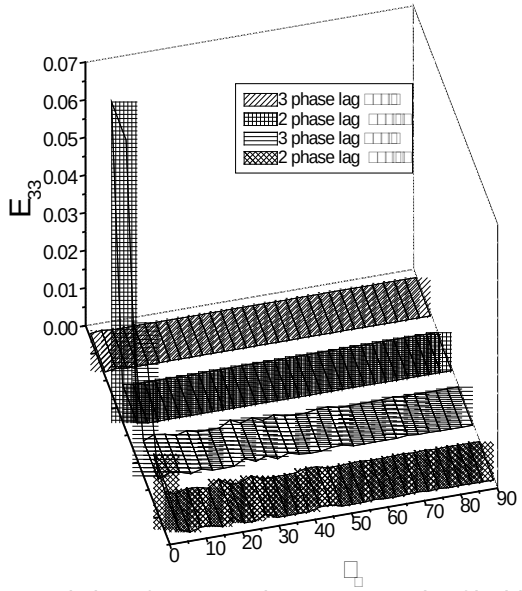

Fig. 6. Variation of energy ratio E_{33} w.r.t. angle of incidence θ_0 for P wave

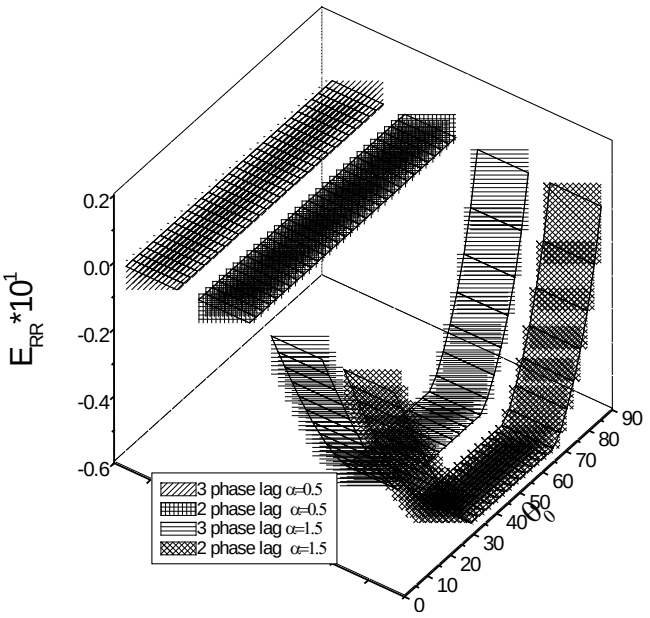

Fig.7. Variation of energy ratio E_{RR} w.r.t. angle of incidence θ_0 for P wave

Incident P wave

Figure 2 depicts that for two and three-phase lag models, for θ_o varies from 0 to 63°, E_1 decreases with increase in θ_o after that E_1 increases with further increase in the values of θ_o up to 90°. But Figure 3 almost depicts the different behavior. Here first E_2 increases in the range $0 \le \theta_o \le 69°$ of θ_o and then decrease in the values of θ_o up to 90°.

Figure 4 indicates that for α =0.5, for both models E_{11} decreases when $0 \le \theta_o \le 5°$ and then attains minima. Due to the small values of E_{11}, its values are magnified after multiplication by 10^6. On the other hand for α =1.5, for both models, E_{11} increases for $0 \le \theta_o \le 69°$ and then decreases continuously. Figure 5 depicts that for α =0.5, for both models E_{22} attains the minimum value. Figure 6 depicts that E_{33} attains the minimum value, nearly to zero in the range $10° \le \theta_o \le 90°$ and in range $0 \le \theta_o \le 10°$ values of E_{33} are higher in the case of two-phase model with α =0.5. The values of E_{33} are magnified by multiplying the original value with 10^{25}. Figure7 depicts that for α =0.5, the energy ratio E_{RR} attains a value nearly equal to zero for both phase models and for α =1.5, E_{RR} decreases in the range $0 \le \theta_o \le 30°$ and attains a constant value in the range $30° \le \theta_o \le 60°$ and further increases rapidly for both phase models. Also from figures, the law of conservation of energy is also verified.

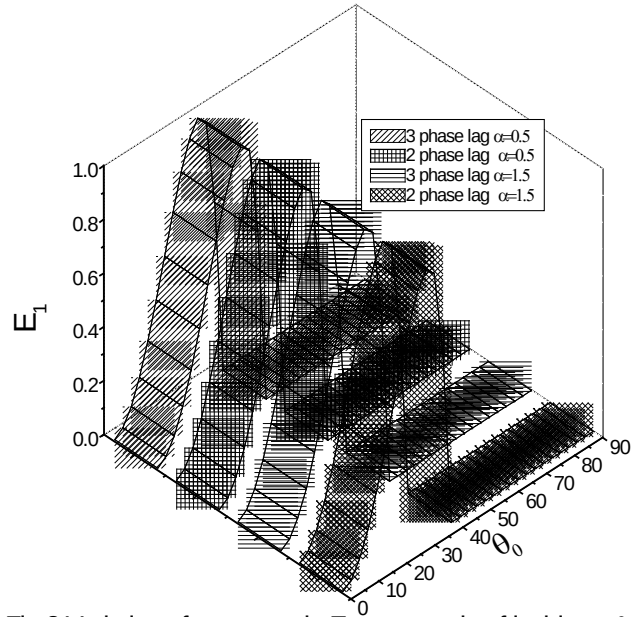

Fig. 8. Variation of energy ratio E_1 w.r.t. angle of incidence θ_0 for SV wave

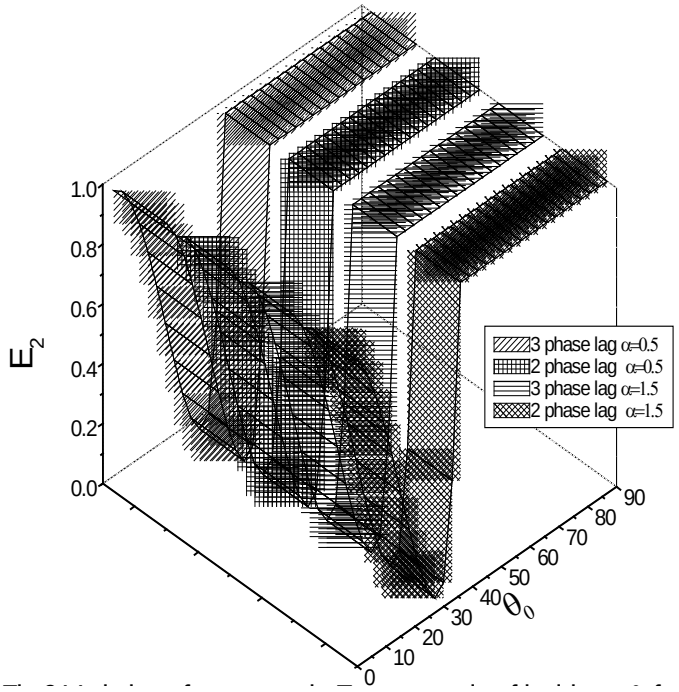

Fig.9. Variation of energy ratio E_2 w.r.t. angle of incidence θ_0 for SV wave

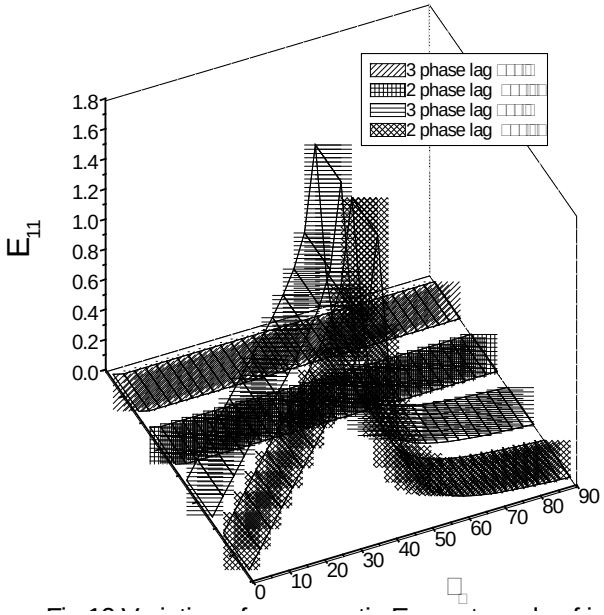

Fig.10. Variation of energy ratio E_{11} w.r.t. angle of incidence θ_0 for SV wave

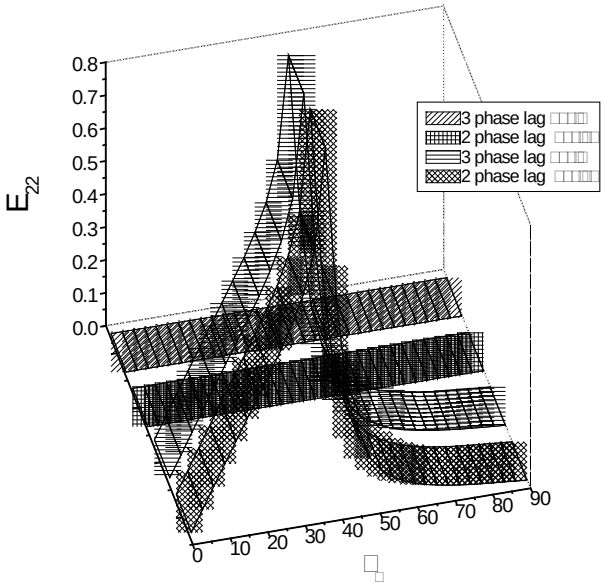

Fig.11. Variation of energy ratio E_{22} w.r.t. angle of incidence θ_0 for SV wave

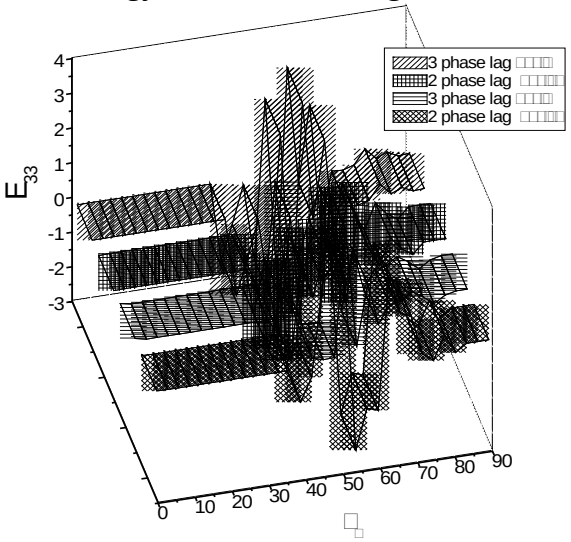

Fig.12. Variation of energy ratio E_{33} w.r.t. angle of incidence θ_0 for SV wave

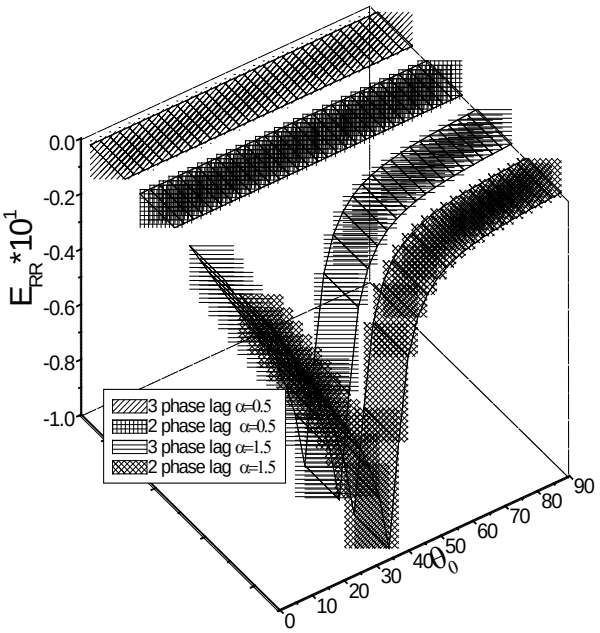

Fig.13. Variation of energy ratio E_{RR} w.r.t. angle of incidence θ_0 for SV wave

Incident SV wave

From Figure 8, it is evident that for both phase models and fractional orders E_1 increases rapidly for $0 \le \theta_o \le 30°$, attains a maximum at $\theta_o = 30°$ and decreases rapidly for $30° \le \theta_\circ \le 40°$, and thereafter attains minimum value nearly to zero in the range $40° \le \theta_o \le 90°$. From Figure 9 it is clear that the trend of E_2 is opposite to E_1 in the range $40° \le \theta_o \le 90°$. E_{11} and E_{22} shows the same variation for both phase models and fractional orders. Both attain a maximum value of α =1.5 in the range $30° \le \theta_o \le 40°$. The values of E_{11} and E_{22} are magnified by multiplying the original values with 10^6. Figure 12 indicates that E_{33} attains a value nearly to zero in the range $0 \le \theta_o \le 40°$ and then fluctuates for $40° \le \theta_o \le 90°$ and attains maximum and minimum values in the range $40° \le \theta_o \le 60°$. The energy ratios E_{33} are magnified by multiplying the original value with 10^{22}. Figure 13 indicates that for α =0.5 (Two and three-phase lag models) values of E_{RR} are nearly to zero and α =1.5 (Two and three phase lag model), E_{RR} decreases smoothly when $0 \le \theta_o \le 35°$, attains minima at $\theta_o = 35°$ and then increases rapidly in the range $35° \le \theta_o \le 90°$. The law of conservation of energy is verified.

8. Conclusion

1. The reflection/ transmission coefficients of oblique incidence of P (or SV) wave are derived.
2. Reflection/transmission coefficients changes with change in the material parameters and angle of incidence.
3. The results obtained indicate the significant effect of phase lags and fractional parameters on the reflection/transmission characteristics of waves.
4. The energy ratios are numerically calculated and plotted graphically and sum of energy ratios of reflected, and transmitted waves and interference between transmitted waves is proved to be unity which shows that there is no dissipation of energy.

5. Significant effect of fractional orders and phase lag models has been observed on energy ratios.
6. This problem of reflection and transmission of waves has applications in many fields like geophysics, seismology, non-destructive evaluation, etc.

References

1. Roychoudhary SK. On thermoelastic three phase lag model. *Journal of Thermal Stresses*. 2007;30(3): 231-238.
2. Abel NH. Solution de quelques problems a l'aide d'integrales defines. *Werke*. 1823;1: 10
3. Caputo M, Mainardi F. A new dissipation model based on memory mechanism. *Pure and Applied Geophysics*. 1971;91: 134-147.
4. Caputo M, Mainardi F. Linear model of dissipation in anelastic solids. *Rivis ta del Nuovo cimento*. 1971;1: 161-198.
5. Caputo M. Vibrations of an infinite viscoelastic layer with a dissipative memory. *The Journal of the Acoustical Society of America*. 1974;56(3): 897-904.
6. Miller KS, Ross B. *An introduction to the fractional integrals and derivatives, theory and applications*. New York: John Wiley and Sons Inc.; 1993.
7. Lord HW, Shulman Y. A generalized dynamical theory of thermoelasticity. *Journal of the Mechanics and Physics of Solids*. 1967;15(5): 299-309.
8. Green AE, Naghdi PM. A re-examination of the basic postulates of thermomechanics. *Proceedings of Royal Society of America. Math. Mathematical, Physical and Engineering Sciences.* 1991;432(1885): 171-194.
9. Green AE, Naghdi PM. On undamped heat waves in an elastic solid. *Journal of Thermal Stresses.* 1992;15(2): 253-264.
10. Green AE, Naghdi PM. Thermoelasticity without energy dissipation. *Jounal of Elasticity*. 1993;31(3): 189-208.
11. Chandrasekharaiah DS. Hyperbolic Thermoelasticity: A review of recent literature. *Applied Mechanics Reviews.* 1998;51: 705-729.
12. Tzou DY. A unified field approach for heat conduction from macro to micro Scales. *Journal of Heat Transfer*. 1995;117: 8-16.
13. Tzou DY. *Macro-to microscale heat transfer: the lagging behavior*. Washigton: Taylor and Francis; 1996.
14. Achenbach JD. *Wave propagation in elastic solids.* North–Holland: Amstendam; 1973.
15. Borcherdt RD. Reflection-refraction of general P and type-I S waves in elastic and anelastic solids. *Geophysical Journal of the Royal Astronomical Society*. 1982;70: 621-638.
16. Sherief HH, Saleh HA. A half space problem in the theory of thermoelastic diffusion. *International Journal of Solids and Structures*. 2005:42: 4484-4493.
17. Kumar R, Gupta V. Wave propagation at the boundary surface of an elastic and thermoelastic diffusion media with fractional order derivative. *Applied Mathematical Modelling*. 2015;39: 1674-1688.
18. Kumar R, Gupta V. Dual-phase-lag model of wave propagation at the interface between elastic and thermoelastic diffusion media. *Journal of Engineering Physics and Thermophysics*. 2015;88: 247-259.
19. Wang YZ, Liu D, Wang Q, Zhou JZ. Fractional Order Theory of Thermoelasticity for Elastic Medium with Variable Material Properties. *Journal of Thermal Stresses*. 2015;38(6): 665-676.
20. Raslan WE. Application of fractional order theory of thermoelasticity to a 1D problem for a spherical shell. *Journal of Theoretical and Applied Mechanics*. 2016;54(1): 295-304.

21. Abbas IA. A dual phase lag model on photothermal interaction in an unbounded semiconductor medium with cylindrical cavity. *International Journal of Computational Materials Science and Engineering*. 2016;5(3): 1650016.
22. Lata P. Fractional order thermoelastic thick circular plate with two temperatures in frequency domain. *Applications and Applied Mathematics*. 2018;13(2): 1216-1229.
23. Kumar R, Vashisth AK, Ghangas S. Waves in anisotropic thermoelastic medium with phase lag, two-temperature and void. *Materials Physics and Mechanics*. 2018;35(1): 126-138.
24. Atwa SY, Ibrahim E. Two temperature effect on a rotational thermoelastic medium with diffusion due to three-phase-lag model. *Journal of Nanotechnology and Advanced Materials*, 2019;7(1): 1-15.
25. Bachher M, Sarkar N. Nonlocal theory of thermoelastic materials with voids and fractional derivative heat transfer. *Waves in Random and Complex Media*. 2019;29(4): 595-613.
26. Mondal S, Sarkar N, Sarkar N. Waves in dual-phase-lag thermoelastic materials with voids based on Eringen's nonlocal elasticity. *Journal of Thermal Stresses*. 2019;42(8): 1035-1050.
27. Said SM. Fractional derivative heat transfer for rotating modified couple stress magneto-thermoelastic medium with two temperatures. *Waves in Random and Complex Media*. 2020;32: 1517-1534.
28. Abouelregal AE. Three-phase-lag thermoelastic heat conduction model with higher-order time-fractional derivatives. *Indian Journal of Physics*. 2020;94: 1949-1963.
29. Abouelregal AE, Ahmad H. A modified thermoelastic fractional heat conduction model with a single-lag and two different fractional-orders. *Journal of Applied and Computational Mechanics*. 2021;7(3): 1676-1686.
30. Saidi A, Abouelregal A. Thermoelastic model with higher-order time-derivatives and two phase-lags for an infinitely long cylinder under initial stress and heat source. *Journal of Applied and Computational Mechanics*. 2021;7(1): 277-291.
31. Kulkarni V, Mittal G. Two temperature dual-phase-lag fractional thermal investigation of heat flow inside a uniform rod. *Applications and Applied Mathematics: An International Journal*. 2021;16(1): 762-775.
32. Abouelregal A, Soleiman A, Sedighi HM, Khalil K, Nasr M. Advanced thermoelastic heat conduction model with two fractional parameters and phase-lags. *Physica Scripta*. 2021;96(12): 124048.
33. Abouelregal A, Alesemi M, Alfadil H. Thermoelastic reactions in a long and thin flexible viscoelastic cylinder due to non-uniform heat flow under the non-fourier model with fractional derivative of two different ordersJ.. *AIMS Mathematics*. 2022;7(5): 8510-8533.
34. Sharma D. Effect of phase-lags model on thermoelastic interactions of nonlocal elastic hollow cylinder with voids material in the presence of time-dependent heat flux. *Proceedings of the National Academy of Sciences, India Section A: Physical Sciences*. 2022;92: 343-352.
35. Caputo M. Caputo Lineal model of dissipation whose *q* is almost frequency independent II. *Geophysical Journal of the Royal Astronomical Society*. 1967;13: 529-539.
36. Bullen KE. *An introduction to the theory of seismology*. England: Cambridge University Press; 1963.

THE AUTHORS

Puneet Bansal
e-mail: puneet4u@gmail.com
ORCID: 0000-0003-2366-5868

Vandana Gupta
e-mail: vandana223394@gmail.com
ORCID: 0000-0003-2366-5868

Appendix 1

$$n_i = \frac{\beta^2 \omega^4 C\bar{\phi}}{\left(\omega^2 C V_i^2 - \omega^2\left(C_T^2 A - i\omega B C_K^2\right)\right)}, \text{ i=1,2.}$$

Appendix 2

$$d_{11} = 2\mu^e\left(\frac{\xi_R}{\omega}\right)^2 - \rho^e {c_0}^2, d_{12} = 2\mu^e \frac{\xi_R}{\omega}\frac{dV_\beta}{\omega}, d_{15} = 2\mu\frac{\xi_R}{\omega}\frac{dV_3}{\omega}, d_{21} = 2\mu^e\frac{\xi_R}{\omega}\frac{dV_\alpha}{\omega},$$

$$d_{22} = \mu^e\left[\left(\frac{dV_\beta}{\omega}\right)^2 - \left(\frac{\xi_R}{\omega}\right)^2\right], d_{25} = \mu\left[\left(\frac{\xi_R}{\omega}\right)^2 - \left(\frac{dV_3}{\omega}\right)^2\right], d_{31} = \frac{\xi_R}{\omega}, d_{32} = \frac{dV_\beta}{\omega},$$

$$d_{35} = \frac{dV_3}{\omega}, d_{41} = -\frac{dV_\alpha}{\omega}, d_{42} = \frac{\xi_R}{\omega}, d_{45} = -\frac{\xi_R}{\omega}, d_{51} = d_{52} = d_{55} = 0,$$

$$d_{1j} = \lambda\left(\frac{\xi_R}{\omega}\right)^2 + \rho {c_0}^2\left(\frac{dV_j}{\omega}\right)^2 + \gamma n_j \frac{T_0}{\omega^2}, d_{2j} = 2\mu\frac{\xi_R}{\omega}\frac{dV_j}{\omega}, d_{3j} = -\frac{\xi_R}{\omega}, d_{4j} = -\frac{dV_j}{\omega},$$

$$d_{5j} = in_j\frac{dV_j}{\omega} + n_j\frac{h}{\omega}, j = 3,4, \frac{dV_\alpha}{\omega} = \left(\frac{1}{\alpha^2} - \left(\frac{\xi_R}{\omega}\right)^2\right)^{\frac{1}{2}} = \left(\frac{1}{\alpha^2} - \frac{\sin^2\theta_0}{{V_0}^2}\right)^{\frac{1}{2}},$$

$$\frac{dV_\beta}{\omega} = \left(\frac{1}{\beta^2} - \frac{\sin^2\theta_0}{{V_0}^2}\right)^{\frac{1}{2}}, \frac{dV_j}{\omega} = p.v.\left(\frac{1}{{V_j}^2} - \frac{\sin^2\theta_0}{{V_0}^2}\right)^{\frac{1}{2}}, \ j = 1, 2, 3.$$

Materials Physics and Mechanics. 2022;50(1): 184-191
Research article
http://dx.doi.org/10.18149/MPM.5012022_14

Submitted: January 21, 2021
Approved: June 29, 2022
Accepted: August 23, 2022

Designing aspects of photoacoustic cell for crystalline solids

A.P. Sarode[1]✉, O.H. Mahajan[2]

[1]Dr. A.G.D. Bendale Girls College, Jhilla Road, Jalgaon 425002, India

[2]M.J. College, Jalgaon 425001, India

✉ abhisarode@rediffmail.com

Abstract. Today, non-destructive analysis techniques for solids are playing an important role in industrial applications and scientific as well as technological research. Photoacoustic method is one of such non-destructive methods, in which generation of acoustic waves takes place due to the absorption of the modulated incident radiation. Photoacoustic cell is a base for photoacoustic research. Hence design and performance optimization play an important role in determining the efficiency of that cell. The design of the photoacoustic cell depends on various aspects like mode of operation, thermal diffusion, nature of the radiation source, and type of the detector. In this paper, designing aspects of a new photoacoustic cell for crystalline solids are presented. A mathematical expression for population density of absorbing molecules in the excited state of a crystalline solid during photoacoustic interaction in terms of the radiative and collisional time constants is also determined.

Keywords: crystalline solids, photoacoustic transducers, photoacoustic testing, photoacoustic effect, photoacoustic cell

Acknowledgements. *Granted in VCRM Scheme of K.B.C.N.M. University, Jalgaon, India.*

Citation: Sarode AP, Mahajan OH. Designing aspects of photoacoustic cell for crystalline solids. *Materials Physics and Mechanics*. 2022;50(1): 184-191. DOI: 10.18149/MPM.5012022_14.

1. Introduction

Photoacoustic effect is based on the absorption of electromagnetic radiation by analyte molecules [1]. Non-radiative relaxation processes, such as collisions with other molecules, lead to local warming of the sample matrix [2,3]. Pressure fluctuations are then generated by thermal expansion, which can be detected in the form of acoustic or ultrasonic waves. In other words, the transformation of an optical event to an acoustic one takes place in photoacoustic effect. A fraction of the radiation falling upon the sample is absorbed and results in excitation, the type of which is being dependent upon the energy of the incident radiation.

Photoacoustic technique is applicable to solids, liquids, and gases. It is a robust and sensitive technique used today for analysis. The cells used in this technique are widely studied by researchers in the last decade. Chrobak and Malinski presented design of a new photoacoustic cell and its performance optimisation in 2013 [4]. Photoacoustic cell based on Helmholtz resonances was demonstrated by M.N. Popovik et al. in 2016 [5]. In the same year, design framework for an open photoacoustic cell was given by B. Lang and A. Bergman [6]. In 2017, Bluvshtein et al. presented calibration of a multiple pass photoacoustic cell using light-absorbing aerosols [7]. Optical frequency comb photoacoustic detection was presented by Sadiek et al. in 2018 [8]. In recent years, Cotterell et al. gave optimisation of the performance of aerosol photoacoustic cells in 2019 [9]. In the same year, Sathiyamoorthy and

Kolios demonstrated experimental design and numerical investigation of a photoacoustic cell for microscopic applications [10]. Last year, Said El-busaidy et al. presented modelling of open photoacoustic cell [11].

The cells in photoacoustic spectroscopy are small cylindrical cavities where the radiation interacts with the target material [12]. The radius of the cavity is limited by the size of the infrared beam. The length of the photoacoustic cell is generally as small as possible. On the other hand, a longer absorption length would lead to a larger signal and better signal-to-noise ratio. The photoacoustic cell design also affects the signal generation by defining the heat conduction out of the cell. Therefore it is essential to consider the thermal effects in the cell. The other important aspects are mode of operation, shape of the cell, modulation scheme, and heat absorption in the crystal.

2. Processes in photoacoustic cell

Non-radiative de-excitation processes which normally occur in the cell, give rise to the generation of thermal energy within the sample [13]. If the incident radiation is modulated then the generation of thermal energy within the sample will also be periodic and a thermal wave or a pressure wave will be produced having the same frequency as this modulation. Energy is transferred by the thermal wave or the pressure wave towards the sample boundary, where a periodic temperature change is generated [14]. The periodic variation in the temperature at the surface of the sample results in the generation of an acoustic wave in the gas immediately adjacent and this wave propagates through the volume of the gas to the detector (microphone, piezoelectric transducers, or optical method) where a signal is produced [15]. This detector or microphone signal, when plotted as a function of wavelength, will give a spectrum proportional to the absorption spectrum of the sample.

3. Aspects of designing

The important aspects of designing of a photoacoustic cell for a solid crystal are

1) Mode of Operation
2) Scheme of Excitation
3) Shape of the cell
4) Heat Absorption in the crystal

Mode of operation. In a closed photoacoustic cell, the enclosed air surrounding the crystal will vibrate as per the modulating frequency of the source of incident radiation. When the mode of operation is resonant, one of the resonant frequencies of the signal in the cavity will be the modulation frequency of the incident source. The pressure fluctuations in the cell will generate an acoustic wave whose amplitude will be amplified at the frequency of modulation of the incident radiation. The amplification of the signal will be proportional to quality factor Q. Quality factor represents relation between resonant frequency of the signal and its bandwidth. To amplify only the modulating frequency of the generated signal inside the cell, a large separation should be kept between the adjacent resonance frequencies along with a high-quality factor [16]. The amplification of all other remaining resonant frequencies will be inversely proportional to the subtraction between the square of the modulating frequency and the square of the resonant frequency of the generated signal.

If the mode of operation of photoacoustic cell used is resonant then implemented modulation frequencies are relatively high, around 3 kHz. The purpose of this selection is to minimize the noise depending on the reciprocal of the frequency. The associated noises are external acoustic noise, noise due to amplification, and intrinsic noise of the detector. The cavity length is shorter for higher frequencies. Hence while selecting the resonant frequency, an intermediate value between a longer absorption length and shorter cavity length should be

preferable. Generally, a smaller cavity length is preferred so as to have a compact cell having a shorter response time [17].

Scheme of excitation. As mentioned earlier, the photoacoustic effect is based on the sample heating produced by optical absorption. In order to generate acoustic waves, which can be detected by pressure-sensitive transducers, periodic heating and cooling of the sample is necessary to generate pressure fluctuations.

Modulated excitation. In modulated excitation schemes, radiation sources are employed whose intensity fluctuates periodically in the form of a square or a sine wave, resulting in a 50% duty cycle. This can be realized for example by the mechanical chopping of a light source. A way to overcome the 50% duty cycle is to modulate the phase instead of the amplitude of the emitted radiation. On the other hand, chopped or modulated lamps or IR sources from commercial spectrometers are used for the determination of UV or IR absorption spectra of opaque solid crystals [18]. Modulated continuous wave lasers are the most common sources for photoacoustic analysis. Photoacoustic cell play an important role in photoacoustic effect. This fact can be utilized for signal enhancement by acoustic resonance. Thus, acoustic resonance curves must be considered in photoacoustic cell design.

Pulsed excitation. In pulsed photoacoustic spectroscopy, laser pulses with durations in the nanosecond range are usually employed for excitation. Since the repetition rates are in the range of a few Hz, the result is a short illumination followed by a much longer dark period: a low-duty cycle. This leads to a fast and adiabatic thermal expansion of the sample medium resulting in a short shock pulse. Data analysis in this case is performed in the time domain. Therefore, the signal is recorded by oscilloscopes, boxcar systems, or fast A to D converters. Transformation of the signal pulse into the frequency domain results in a wide spectrum of acoustic frequencies up to the ultrasonic range [19]. Thus, laser beams modulated in the form of a sine wave excite one single acoustic frequency, whereas short laser pulses are broadband acoustic sources.

Shape of the cell. Resonant photoacoustic cell is fabricated according to the required dimensions of the internal cavity suitable to the acoustic wavelength [20]. A schematic diagram of cylindrical photoacoustic cell for a solid crystal is shown in Fig. 1. The structure of the cell is modified by connecting additional buffers to the central part as shown. Addition of buffers is useful in the prevention of noise due to the coupling of the cell with the other measurement devices.

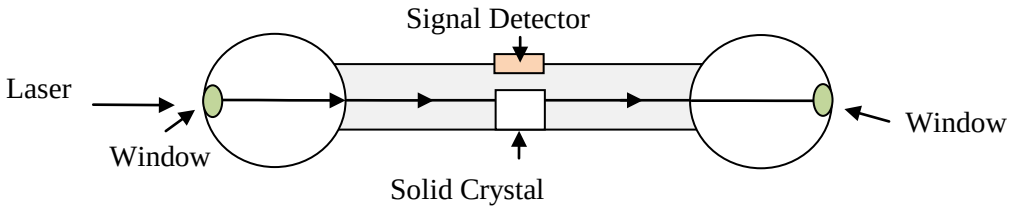

Fig. 1. A schematic diagram of a newly designed photoacoustic cell for a crystalline solid

A resonator with short dimensions oriented in the perpendicular direction with respect to the propagating acoustic signal represents a one-dimensional photoacoustic cell. When the propagating sound waves are reflected back in the cell, standing acoustic waves generated by the excited sound signals are amplified if the difference in phase of the waves is 2π or in its multiple. The reflections of the waves at the ends of the cell as well as acoustic path length are the important factors on which phase difference depends. At the closed end of the cell, a pressure antinode will be formed. The reason for this is the higher acoustic impedance of the cell material than air [21].

The most used shape of the photoacoustic cell is a cylindrical shape because it matches the symmetry of the laser beam. For a small size acoustic sensor or a microphone, the measured signal is proportional to the amplitude of acoustic signal at its location. Unwanted sound signals generated in resonance from the external sources are reduced by placing the sensor at the node of the generated amplified wave. The desired value of the Q factor for a cylindrical photoacoustic cell can be designed up to 900.

Heat absorption in the crystal. For absorbing samples the optical absorption length is an important parameter and may be taken as the depth into the sample at which essentially all of the incident radiation has been absorbed. The thermal wave produced in the sample is heavily damped and may be considered to be fully damped out within a distance of $2\pi\mu_s$, where μ_s is the thermal diffusion length. It is normally assumed that only those thermal waves originating from a depth less than or equal to us will make an appreciable contribution to the photoacoustic signal measured.

The observed photoacoustic signal is a complex quantity having a magnitude and phase relative to the modulation of incident radiation. Being a function of the absorption coefficient, modulation frequency, and thermal characteristics of the sample as well, the photoacoustic signal is directly proportional to the incident power of the radiation and also depends upon the characteristics of the gas in contact with the sample surface and the properties of the backing material upon which the sample is positioned [22].

To describe the absorption of light in a crystalline solid, consider a two-level system, in which energy transfers take place. A schematic representation of a two-level system in a crystal in photoacoustic interaction is shown in Fig. 2. These energy transfers are radiative and non-radiative. Let us consider two states i and j. Also, consider the coefficients r_{ij} and c_{ij}. The radiative transition rate is r_{ij} and c_{ij} is non-radiative transition rate c_{ij} is also called collision-induced energy transfer. Now, introduce Einstein coefficients for stimulated and spontaneous emission, B_{ij} and A_{ij}. Consider ρ_ω as the spectral energy density at the frequency of the transition between E_0 and E_3. Einstein coefficients can be expressed as

$$r_{ij} = \rho_\omega B_{ij} + A_{ij}, \quad (1)$$

where ρ_ω is the spectral energy density at the frequency of the transition between E_0 and E_3. The quantity ρ_ω measures the radiant energy per volume per unit frequency and can be expressed in terms of units Js / m^3.

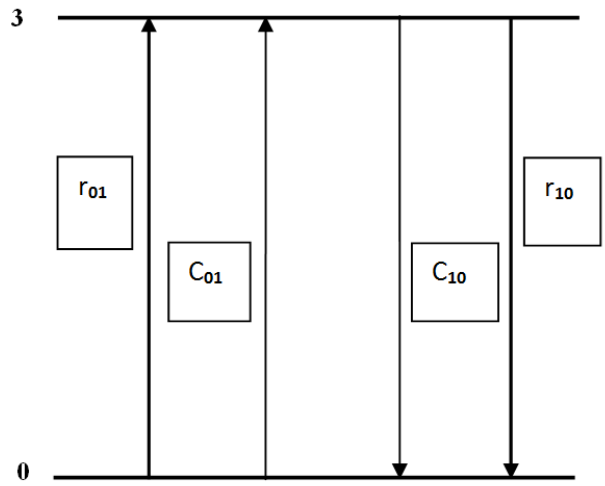

Fig. 2. A schematic representation of a two-level system in a crystal

Note that $B_{ij} = B_{ji}$ so that $B_{03} = B_{30}$. But $A_{03} = 0$ because spontaneous emission from a state of lower energy to any one of higher energy does not occur.

Hence, $r_{03} = \rho_\omega B_{03}$.

Also, $r_{30} = \rho_\omega B_{03} + A_{30}$.

Again, the probability of excitation due to collision from E_0 to E_3 is very low. Therefore, approximately we can say,

$c_{03} \sim= 0$.

Let us determine the rate of transition. For this calculation, we must distinguish the population densities of absorbing molecules in the ground and excited states. Consider these population densities as n_0 and n_3, respectively corresponding to energies E_0 and E_3. To calculate the rate of change of population in the upper state, we must consider the difference between the number of molecules entering and leaving the excited state.

$$\dot{n}_3 = (r_{03} + c_{03}) n_0 - (r_{30} + c_{30})\, n_3,$$

$$\dot{n}_3 = \rho_\omega B_{03} n_0 - (\rho_\omega B_{03} + A_{30} + c_{30})\, n_3,$$

$$\dot{n}_3 = \rho_\omega B_{03} n_0 - \rho_\omega B_{03} n_3 - (A_{30} + c_{30})\, n_3,$$

$$\dot{n}_3 = \rho_\omega B_{03} (n_0 - n_3) - (A_{30} + c_{30}) n_3. \tag{2}$$

Let the radiative and collision time constants be $T_r = \dfrac{1}{A_{30}}$ and $T_c = \dfrac{1}{C_{30}}$ respectively. The total time constant is, then the addition of radiative and collision time constants.

$T = T_r + T_c$.

Now, equation (3) can be written as

$$\dot{n}_3 = \rho_\omega B_{03} (n_0 - n_3) - \left(\frac{1}{T_r} + \frac{1}{T_c}\right) n_3. \tag{3}$$

Let us follow a similar process to calculate $\dot{n}_0$ as

$$\dot{n}_0 = (r_{30} + c_{30})\, n_3 - (r_{03} + c_{03})\, n_0,$$

$$\dot{n}_0 = (\rho_\omega B_{03} + A_{30} + c_{30})\, n_3 - \rho_\omega B_{03} n_0,$$

$$\dot{n}_0 = \rho_\omega B_{03} (n_3 - n_0) + (A_{30} + c_{30})\, n_3,$$

$$\dot{n}_0 = \rho_\omega B_{03} (n_3 - n_0) + (+)\, n_3,$$

$$\dot{n}_0 = \rho_\omega B_{03} (n_3 - n_0) + \left(\frac{T_r + T_c}{T_r T_c}\right) n_3. \tag{4}$$

Hence,

$$\dot{n}_3 - \dot{n}_0 = \rho_\omega B_{03} (n_0 - n_3) - \left(\frac{1}{T_r} + \frac{1}{T_c}\right) n_3 - \left[\rho_\omega B_{03} (n_3 - n_0) + \left(\frac{T_r + T_c}{T_r T_c}\right) n_3\right],$$

$$\dot{n}_3 - \dot{n}_0 = \rho_\omega B_{03} (n_0 - n_3) - \left(\frac{1}{T_r} + \frac{1}{T_c}\right) n_3 - \rho_\omega B_{03} (n_3 - n_0) - \left(\frac{T_r + T_c}{T_r T_c}\right) n_3,$$

$$\dot{n}_3 - \dot{n}_0 = \rho_\omega B_{03} n_0 - \rho_\omega B_{03} n_3 - \left(\frac{1}{T_r} + \frac{1}{T_c}\right) n_3 - \rho_\omega B_{03} n_3 + \rho_\omega B_{03} n_0 - \left(\frac{T_r + T_c}{T_r T_c}\right) n_3,$$

$$\dot{n}_3 - \dot{n}_0 = 2\rho_\omega B_{03} n_0 - 2\rho_\omega B_{03} n_3 - 2\left(\frac{T_r + T_c}{T_r T_c}\right) n_3,$$

$$\dot{n}_3 - \dot{n}_0 = -2\left\{\rho_\omega B_{03}\left(n_3 - n_0\right) + \left(\frac{T}{T_r T_c}\right) n_3\right\}. \quad (5)$$

To consider an interchange adiabatically in upper and lower population in steady state condition, intensity, I should vary slowly. In such situation, we can say that

$\dot{n}_3 - \dot{n}_0 = 0.$

So equation (5) becomes

$$0 = -2\left\{\rho_\omega B_{03}\left(n_3 - n_0\right) + \left(\frac{T}{T_r T_c}\right) n_3\right\}.$$

We know that total molecular density is

$N = n_0 + n_3,$

$n_3 = N - n_0,$

$$0 = -2\left\{\rho_\omega B_{03}\left(N - n_0 - n_0\right) + \left(\frac{T}{T_r T_c}\right) n_3\right\},$$

$$0 = -2\left\{\rho_\omega B_{03}\left(N - 2n_0\right) + \left(\frac{T}{T_r T_c}\right) n_3\right\},$$

$$0 = -2\rho_\omega B_{03}\left(N - 2n_0\right) - 2\left(\frac{T}{T_r T_c}\right) n_3,$$

$$0 = -2\rho_\omega B_{03} N + 4\rho_\omega B_{03} n_0 - 2\left(\frac{T}{T_r T_c}\right) n_3,$$

$$4\rho_\omega B_{03} n_0 = 2\rho_\omega B_{03} N + 2\left(\frac{T}{T_r T_c}\right) n_3,$$

$$n_0 = \left\{2\rho_\omega B_{03} N + 2\left(\frac{T}{T_r T_c}\right) n_3\right\} \Big/ 4\rho_\omega B_{03},$$

$$n_0 = \left\{\rho_\omega B_{03} N + \left(\frac{T}{T_r T_c}\right) n_3\right\} \Big/ 2\rho_\omega B_{03}, \quad (6)$$

and,

$$n_3 = \left\{4\rho_\omega B_{03} n_0 - 2\rho_\omega B_{03} N\right\} \Big/ 2\left(\frac{T}{T_r T_c}\right),$$

$$n_3 = \left\{2\rho_\omega B_{03} n_0 - \rho_\omega B_{03} N\right\} \Big/ \left(\frac{T}{T_r T_c}\right). \quad (7)$$

Thus, population density of absorbing molecules in the excited state during photoacoustic interaction of a solid crystal is exactly determined.

4. Conclusions

Thus, a mathematical expression for population density of absorbing molecules in the excited state during photoacoustic interaction in terms of the radiative and collisional time constants for a crystalline solid is exactly determined. This expression allows the calculation of various parameters of photoacoustic signal related with solid crystal in the designed photoacoustic cell. The cell designing in terms of heat absorption in the crystal, mode of operation, scheme of excitation, and shape of the cell is theoretically presented. This theoretical approach constitutes an important step towards determination of various aspects of new designs of

photoacoustic cells for solid crystals. This work will be useful in photoacoustic research for scientific and industrial applications in various fields in the future.

References

1. Rosencwaig A, Gersho A. Theory of Photoacoustic effects in solid. *Journal of Applied Physics*. 1976;47(1): 64-67.
2. West G, Barrett JJ, Siebert DR, Reddy KV. Photoacoustic Spectroscopy.*Review of Scientific Instruments.* 1983;54(7): 797-817.
3. McDonald FA, Wetsel GC. Generalized Theory of the Photoacoustic Effect. *Journal of Applied Physics*. 1978;49(4): 2313-2322.
4. Chrobak L, Malinski M. Design and optimization of the photoacoustic cell for nondestructive photoacoustic spectroscopy. *Nondestructive Testing and Evaluation.* 2013;28(1): 17-27.
5. Popovic MN, Nesic MV, Ciric-Kostic S, Zivanov M, Markushev DD, Rabasovic MD, Galovic SP. Helmholtz Resonances in Photoacoustic Experiment with Laser-Sintered Polyamide Including Thermal Memory of Samples. *Int J Thermophys.* 2016;37: 116.
6. Lang B, Bergmann A. Design framework for a gas sensor based on an open photoacoustic resonator. *IEEE Sensors.* 2016;4: 1-3.
7. Bluvshtein N, Flores JM, He Q, Segre E, Segev L, Hong N, Donohue A, Hilfiker JN, Rudich Y. Calibration of a multi-pass photoacoustic spectrometer cell using light-absorbing aerosols. *Atmos. Meas. Tech.* 2017;10(3): 1203-1213.
8. Sadiek I, Mikkonen T, Vainio M, Toivonen J, Foltynowicz A. Optical frequency comb photoacoustic spectroscopy. *Physical Chemistry Chemical Physics.* 2018;20(44): 27849-27855.
9. Cotterell MI, Ward GP, Hibbins AP, Wilson A, Langridge JM. Optimizing the performance of aerosol photoacoustic cells: Method validation and application to single-resonator multipass cells. *Aerosol Science and Technology*. 2019;53(10): 1107-1127.
10. Sathiyamoorthy K, Kolios MC. Experimental design and numerical investigation of a photoacoustic sensor for a low-power, continuous-wave, laser-based frequency-domain photoacoustic microscopy. *Journal of Biomedical Optics*. 2019;24(12): 121912.
11. El-Busaidy SAS, Baumann B, Wolff M, Duggen L. Modelling of open photoacoustic resonators. *Photoacoustics*. 2020;18: 100161-100164.
12. Wolff M, Harde H. Photoacoustic Spectrometer Based on a Planckian Radiator with Fast Time Response. *Infrared Physics & Technology*. 2003;44(1): 51-55.
13. Kottmann J, Rey JM, Sigrist MW. New photoacoustic cell design for studying aqueous solutions and gels. *Rev. Sci. Instrum*. 2011;82(8): 084903.
14. Malinski M. Determination of air-tightness of the packaging of electronic devices by the thermoacoustic method. *Arch. Acoust.* 2005;30(3): 345-355.
15. Wilcken K, Kauppinen J. Optimization of a Microphone for Photoacoustic Spectroscopy. *Applied Spectroscopy.* 2003;59(9): 1087-1092.
16. Tavakoli M, Tavakoli A, Taheri M, Saghafifar H. Design, simulation and structural optimization of a longitudinal acoustic resonator for trace gas detection using laser photoacoustic spectroscopy. *Opt. Laser Technology.* 2012;42(5): 828-838.
17. Raghu O, Philip J. A dual channel photoacoustic cell for imaging experiments on solid samples. *Journal of the Instrument Society of India.* 2003;33(3): 155-158.
18. Chrobak L, Malinski M. Transmission and absorption based photoacoustic methods of determination of the optical absorption spectra of Si samples – comparison. *Solid State Commun*. 2009;149(39-40): 1600-1604.
19. Rabasovic MD, Nikolic JD, Markushev DD, Jovanovic KJ. Pulsed photoacoustic gas cell design for low pressure studies. *Opt. Mater*. 2008;30(7): 1197-1200.

20. Jorge MPPM, Mendes FJ, Oliveira AC, Braga AJP, Cesar CL, Morato SP, Vieira JrND, Vieira MMF. Resonant photoacoustic cell for low temperature measurements. *Cryogenics.* 1999;39(3): 193-195.
21. Yehya F, Chaudhary AK. Designing and modeling of efficient resonant photoacoustic sensors for spectroscopic applications. *Journal of Modern Physics*. 2011;2: 200-209.
22. Schmid T. Photoacoustic Spectroscopy for Process Analysis. *Analytical and Bioanalytical Chemistry.* 2006;384: 1071-1072.

THE AUTHORS

Sarode A.P.
e-mail: abhisarode@rediffmail.com
ORCID: 0000-0003-4638-1614

Mahajan O.**H.**
e-mail: abhi.jjit@rediffmail.com
ORCID: 0000-0001-6651-8089

Submission of papers:
Manuscript should be submitted (**both MS Word and PDF**) by e-mail to: **mpmjournal@spbstu.ru**
After a confirmation of the paper acceptation, the authors should send the signed hard copy of the "Transfer of Copyright Agreement" form (available at http://www.mpm.spbstu.ru section "Authors") by regular post to "Materials Physics and Mechanics" editorial office:
Periodicals Editorial Office, Institute of Advanced Manufacturing Technologies, Peter the Great St.Petersburg Polytechnic University, Polytechnicheskaya, 29, St.Petersburg 195251, Russia.
The scanned copy of the signed "Transfer of Copyright Agreement" should be send by e-mail to: mpmjournal@spbstu.ru.

Filetype:
Authors are invited to send their manuscripts **as MS Word file with PDF format copy.**
MS Word file should be prepared according to the general instructions bellow; we are kindly asking the authors to look through the detail instruction at: http://www.mpm.spbstu.ru.

Length:
Papers should be limited to 30 typewritten pages (including Tables and Figures placed in the proper positions in the text).

Structure of the manuscript:

PAPER TITLE: CENTERED,

TIMES NEW ROMAN 14 BOLD, CAPITAL LETTERS

A.B. Firstauthor[1], C.D. Secondauthor[2*] –Times New Roman 12, bold, centered

[1]Affiliation, address, country - Times New Roman 10, centered

*e-mail: e-mail of the corresponding author - Times New Roman 10, centered

Abstract. Times New Roman 12 font, single line spacing. Abstract should not exceed 12 lines.
Keywords: please, specify paper keywords right after the abstract.

Paper organization. Use Times New Roman 12 font with single line spacing. Use *Italic* font in order to stress something; if possible, please, use **bold** for headlines only.

Page numbering. Please, do not use page numbering.

Tables, Figures, Equations. Please, see the sample file at http://www.mpm.spbstu.ru for more details.

References
References should be subsequently numbered by Arabic numerals in square brackets, e.g. [1,3,5-9], following the sample style below:
[1] Koch CC, Ovid'ko IA, Seal S, Veprek S. *Structural Nanocrystalline Materials: Fundamentals and Applications*. Cambridge: Cambridge University Press; 2007.
[2] Hull D, Bacon DJ. *Introduction to Dislocations*. 5nd ed. Amsterdam: Butterworth-Heinemann; 2011 Available from: https://www.sciencedirect.com/science/book//
9780080966724?via%3Dihub [Accessed 19th June 2018].
[3] Romanov AE, Vladimirov VI. Disclinations in crystalline solids. In: Nabarro FRN (ed.) *Dislocations in Solids*. Amsterdam: North Holland; 1992;9. p.191-402.
[4] Mukherjee AK. An examination of the constitutive equation for elevated temperature plasticity. *Materials Science and Engineering: A*. 2002;322(1-2): 1-22.

[5] Soer WA, De Hosson JTM, Minor AM, Morris JW, Stach EA. Effects of solute Mg on grain boundary and dislocation dynamics during nanoindentation of Al–Mg thin films. *Acta Materialia*. 2004;52(20): 5783-5790.
[6] Matzen ME, Bischoff M. A weighted point-based formulation for isogeometric contact. *Computer Methods in Applied Mechanics and Engineering*. 2016;308: 73-95. Available from: doi.org/10.1016/j.cma.2016.04.010.
[7] Joseph S, Lindley TC, Dye D. Dislocation interactions and crack nucleation in a fatigued near-alpha titanium alloy. To be published in *International Journal of Plasticity. Arxiv.* [Preprint] 2018. Available from: https://arxiv.org/abs/1806.06367 [Accessed 19th June 2018].
[8] Pollak W, Blecha M, Specht G. *Process for the production of molded bodies from silicon-infiltrated, reaction-bonded silicon carbide*. US4572848A (Patent) 1983.
[9] Brogan C. *Experts build pulsed air rig to test 3D printed parts for low carbon engines*. Available from: http://www.imperial.ac.uk/news/186572/experts-build-pulsed-test-3d-printed/ [Accessed 19th June 2018].

Правила подготовки статей:

Рукопись (**английский язык, MS Word и копия PDF**) должна быть направлена в редакцию журнала по электронной почте: **mpmjournal@spbstu.ru**.

После подтверждения принятия статьи в печать, авторы должны отправить подписанные:

1. Соглашение о передаче авторских прав (http://www.mpm.spbstu.ru, раздел «Авторам»);
2. Экспертные заключения о том, что материалы статьи не содержат сведений, составляющих государственную тайну, и информацию, подлежащую экспортному контролю; по адресу:

Россия, 195251, Санкт-Петербург, Политехническая, д. 29, Санкт-Петербургский политехнический университет Петра Великого, Институт передовых производственных технологий, Редакция периодических изданий.

Скан-копии подписанных документов просим направить по электронной почте: mpmjournal@spbstu.ru

Тип файла:

Редакция принимает **файлы MS Word с копией в формате PDF**. Статья должна быть подготовлена в соответствии с настоящей инструкцией, мы просим авторов также следовать более подробным инструкциям на сайте журнала http://www.mpm.spbstu.ru в разделе «Авторам».

Длина статьи:

Статья не должна превышать 30 страниц формата А4, включая Таблицы и Рисунки, размещенные непосредственно в соответствующих местах.

Общие правила оформления статьи:

НАЗВАНИЕ СТАТЬИ: ВЫРОВНЯТЬ ПО ЦЕНТРУ, ШРИФТ, TIMES NEW ROMAN 14 BOLD, ЗАГЛАВНЫЕ БУКВЫ

Автор(ы): **А.Б. Первыйавтор[1], В.Г. Автор[2*]**- шрифт Times New Roman 12, bold, по центру

[1]Наименование организации, адрес, страна - шрифт Times New Roman 10, по центру

* e-mail автора, представившего статью - шрифт Times New Roman 10, по центру

Аннотация. Аннотация статьи составляет не более 12 строк. Используйте шрифт Times New Roman 12, одинарный межстрочный интервал.

Ключевые слова: укажите ключевые слова после аннотации.

Как организовать текст статьи. Используйте шрифт Times New Roman 12, одинарный межстрочный интервал. При необходимости выделить какую-либо информацию используйте *курсив*. Используйте **полужирный** шрифт только для заголовков и подзаголовков.

Номера страниц. Пожалуйста, не используйте нумерацию страниц

Таблицы, Рисунки, Уравнения. Подробные правила оформления данных элементов статьи приведены в инструкции на сайте журнала http://www.mpm.spbstu.ru

Литература

Ссылки приводятся в тексте в квадратных скобках [1,3,5-9]. Стиль оформления ссылок:

[1] Koch CC, Ovid'ko IA, Seal S, Veprek S. *Structural Nanocrystalline Materials: Fundamentals and Applications*. Cambridge: Cambridge University Press; 2007.

[2] Hull D, Bacon DJ. *Introduction to Dislocations*. 5nd ed. Amsterdam: Butterworth-Heinemann; 2011 Available from: https://www.sciencedirect.com/science/book//9780080966724?via%3Dihub [Accessed 19th June 2018].

[3] Romanov AE, Vladimirov VI. Disclinations in crystalline solids. In: Nabarro FRN (ed.) *Dislocations in Solids*. Amsterdam: North Holland; 1992;9. p.191-402.

[4] Mukherjee AK. An examination of the constitutive equation for elevated temperature plasticity. *Materials Science and Engineering: A*. 2002;322(1-2): 1-22.

[5] Soer WA, De Hosson JTM, Minor AM, Morris JW, Stach EA. Effects of solute Mg on grain boundary and dislocation dynamics during nanoindentation of Al–Mg thin films. *Acta Materialia*. 2004;52(20): 5783-5790.
[6] Matzen ME, Bischoff M. A weighted point-based formulation for isogeometric contact. *Computer Methods in Applied Mechanics and Engineering*. 2016;308: 73-95. Available from: doi.org/10.1016/j.cma.2016.04.010.
[7] Joseph S, Lindley TC, Dye D. Dislocation interactions and crack nucleation in a fatigued near-alpha titanium alloy. To be published in *International Journal of Plasticity. Arxiv.* [Preprint] 2018. Available from: https://arxiv.org/abs/1806.06367 [Accessed 19th June 2018].
[8] Pollak W, Blecha M, Specht G. *Process for the production of molded bodies from silicon-infiltrated, reaction-bonded silicon carbide*. US4572848A (Patent) 1983.
[9] Brogan C. *Experts build pulsed air rig to test 3D printed parts for low carbon engines*. Available from: http://www.imperial.ac.uk/news/186572/experts-build-pulsed-test-3d-printed/ [Accessed 19th June 2018].

МЕХАНИКА И ФИЗИКА МАТЕРИАЛОВ

50 (1) 2022

Учредители: Санкт-Петербургский политехнический университет Петра Великого,

Институт проблем Машиноведения Российской академии наук

Издание зарегистрировано федеральной службой по надзору в сфере связи,

информационных технологий и массовых коммуникаций (РОСКОМНАДЗОР),

свидетельство ПИ №ФС77-69287 от 06.04.2017 г.

Телефон редакции

+7(812)552 77 78, доб. 224

E-mail: mpmjournal@spbstu.ru

Компьютерная верстка А.Ю. Ромашкина

Подписано в печать 31.10.2022 г. Формат 60x84/8. Печать цифровая
Усл. печ. л. 10,0. Тираж 100. Заказ____.

Отпечатано с готового оригинал-макета, предоставленного автором
в Издательско-полиграфическом центре Политехнического университета Петра Великого. 195251, Санкт-Петербург, Политехническая ул., 29.
Тел.: +7(812)552 77 78, доб. 224.

MPM SCIENTIFIC JOURNAL

MPM, Vol. 50, No. 1, 2022